Self-induced Electrochemical Promotion of Noble Metal Nanoparticles for Environmentally Important Reaction Systems

Rima Isaifan

Thesis submitted to the
Faculty of Graduate and Postdoctoral Studies
In partial fulfillment of the requirements for the degree of

Doctorate in Philosophy

in the
Department of Chemical and Biological Engineering
Faculty of Engineering
University of Ottawa

Abstract

Volatile organic compounds (VOCs) and carbon monoxide are considered the main greenhouse gas pollutants from either automotive engines or stationary sources. The increased concentration of these pollutants in air severely affects human health and causes changes in earth climate and vegetation growth rates. Ethylene is one of the VOCs closely related with photocatalytic pollution when it reacts with nitrogen oxides in the presence of sun light to form ground-level ozone. It is also responsible for quick repining of fruits and vegetables. Carbon monoxide, on the other hand, is a poisonous gas mainly released by vehicle emissions, and when inhaled in high concentrations, it causes severe health problems related to the respiratory system leading to significant rates of deaths annually in Europe and North America. Globally, The World Health Organization (WHO) estimates that seven million people die yearly due to poor air quality-related reasons which urges current and future stringent regulations to control air pollution emissions.

In the past four decades, several equipment modifications and processes have been studied for reducing these emissions. Among them is the phenomenon of Electrochemical Promotion of Catalysis (EPOC) which was first reported in the early 1980s. EPOC has been successfully shown to convert automotive, indoor and industrial air pollutants such as VOCs, CO and nitrogen oxides (NO_x) to harmless gases. It involves reversible changes in the catalytic properties of catalysts deposited on solid electrolytes when a small electric current or potential is applied. More recently, it was demonstrated that EPOC can be thermally induced without any electrical polarization, in analogy to the well-known phenomenon of metal-support interaction, by using noble metal nanocatalysts supported on ionically conducting materials such as yttria-stabilized zirconia (YSZ).

The objective of this research is to gain deeper understanding of the factors affecting metal-support interaction between the active metal and the support to enhance their catalytic activity for environmentally-important reaction systems; specifically, ethylene and carbon monoxide oxidation as well as hydrogen fuel purification by carbon monoxide methanation. First, the activity of platinum nanoparticles deposited on carbon black, which is a conventional support used in catalysis, is studied. The effect of particle size of four Pt/C

nanoparticles synthesized using a modified reduction method for ethylene (C_2H_4) complete catalytic oxidation is investigated. These catalysts show high activity towards C_2H_4 oxidation which is found to be a strongly size-dependent reaction. Full conversion of ~1000 ppm C_2H_4 is achieved over the smallest nanoparticles (1.5 nm) at 100^oC while higher temperature ~170^oC is required to completely oxidize ethylene over the largest nanoparticle (6.3 nm).

The second stage of this research compares the catalytic activity of platinum and ruthenium nanoparticles when deposited on ionic or mixed ionic conductive vs. non ionic conductive supports for CO and VOCs oxidation. The Pt and Ru nanoparticles are deposited on yttria-stabilized zirconia (8% Y_2O_3-stabilised ZrO_2), cerium (IV) oxide (CeO_2), samarium-doped ceria (SDC), gamma-alumina (γ-Al_2O_3), carbon black and on novel perovskite group $Sm_{1-x}Ce_xFeO_3$ (x = 0, 1, 5) resulting in $\leq$ 1 wt. (weight) % of Pt and Ru on each support. It is found that the nanocatalysts deposited on ionic conductive or mixed ionic conductive supports outperformed the catalysts deposited on non ionic conductors due to strong metal-support interaction that greatly affects the electronic and catalytic properties of the catalysts. The enhanced catalytic activity towards CO and C_2H_4 oxidation reactions is shown by earlier catalytic activity and complete conversion, lower activation energies, greater turnover frequencies and higher intrinsic rates per active surface area.

To further investigate the effect of ionic conductivity of the supports and the exchange of O^{2-} (oxygen vacancy) between the support and the catalyst surface, complete oxidation of pollutants is studied in the absence of oxygen in the gas phase. For the first time, complete oxidation of CO and C_2H_4 in an oxygen-free environment at low temperatures (< 250^oC) is achieved, which represents the main novel finding in this research. The idea of pollutant removal in the absence of oxygen is extended to a practical reaction for fuel cells application which is hydrogen fuel purification from CO impurities at temperatures < 100^oC. Moreover, the effect of particle size, pollutant concentration, operating conditions and support nature in the absence of oxygen in the gas feed is studied. It is proposed that the metal nanoparticles and the solid electrolyte form local nano-galvanic cells at the vicinity of the three-phase boundary where the anodic reaction is CO or C_2H_4 oxidation and the cathodic reaction is the surface partial reduction of the support. A systematic catalyst reactivation process is suggested and the catalytic activity of these nano-catalysts is studied which can be further investigated

for air pollution control applications such as in vehicle catalytic converters, indoor air quality units and power plant emissions.

Résumé

Les composés organiques volatils (COVs) et le monoxyde de carbone (CO) sont considérés comme les principaux gaz à effet de serre provenant des moteurs de véhicules et de sources stationnaires. L'augmentation de la concentration de ces polluants dans l'air a un effet négatif considérable sur la santé humaine, influence le climat terrestre et affecte la vitesse de croissance de la flore. L'éthylène est un des COVs étroitement reliés avec la pollution photocatalytique lorsqu'il réagit avec les oxydes d'azotes (NOx) en présence de rayons solaires pour produire de l'ozone au niveau du sol. De plus, le CO est un gaz toxique produit en grande partie par les émissions de véhicules qui, lorsqu'inhalées à haute concentration, peuvent causer des problèmes de santé sévères liés au système respiratoire provoquant un nombre élevé de décès annuellement en Europe et en Amérique du Nord. L'Organisation mondiale de la santé (OMS) estime qu'au total sept millions de personnes meurent annuellement dues à la pauvre qualité de l'air. Ces raisons démontrent un besoin imminent de règles strictes sur les émissions de gaz polluants.

Au cours des quatre dernières décennies, de nombreuses pièces d'équipement ont été modifiées et plusieurs procédés ont été étudiés afin de réduire ces émissions. Parmi ceux-ci figure le phémonène de "Electrochemical Promotion of Catalysis" (EPOC) qui fut reporté pour la première fois au début des années 1980. EPOC a été utilisé avec succès pour convertir les COVs, le CO et les NOx provenant de différentes sources (automobile, intérieure ou industrielle) en gaz inoffensifs. Ce processus consiste en l'obtention de changement réversible des propriétés catalytiques de catalyseurs déposés sur des électrolytes solides par l'application d'un petit courant électrique. Récemment, on a démontré que EPOC pouvait être induit de façon thermique sans aucune polarisation électrique simplement en utilisant un catalyseur à base de métal noble supporté sur un matériel conducteur d'ions comme "yttria-stabilized zirconia" (YSZ).

L'objectif de cette recherche est d'obtenir une compréhension plus profonde des facteurs affectant l'interaction métal-support entre le métal actif et le support améliorant leur activité catalytique pour des réactions environnementalement importantes; spécifiquement pour l'oxydation d'éthylène (C_2H_4) et du CO et pour la purification de l'hydrogène par la

méthanation du CO. Premièrement, l'activité des nanoparticules de platine déposé sur du noir de carbone, qui est un support conventionnellement utilisé en catalyse, est étudiée. L'effet de la grosseur des nanoparticules métalliques de quatre catalyseurs de Pt/C synthétisé utilisant une méthode de réduction modifiée sur l'oxydation catalytique complète de C_2H_4 est étudié. Ces catalyseurs démontrent une haute activité envers l'oxydation de C_2H_4 qui dépendant de la grosseur des nanoparticules. Une conversion complète de ~ 1000 ppm de C_2H_4 est obtenue sur les plus petites nanoparticules (1.5 nm) à 100^{o}C alors qu'une température d'environ ~ 170^{o}C est nécessaire pour la même conversion sur les plus grosses nanoparticules (6.3 nm).

La deuxième étape de cette recherche compare l'activité catalytique des nanoparticules de platine et celles de ruthénium lorsque déposée sur des conducteurs ioniques ou électroniques et ioniques à leur déposition sur des matériaux non conducteurs d'ions pour l'oxydation de COVs et du CO. Les nanoparticules de Pt et de Ru sont déposées sur du YSZ, de l'oxyde de cérium (IV) (CeO_2), du samarium-doped ceria (SDC), de l'alumine gamma (γ-Al_2O_3), du noir de carbone et sur le groupe de perovskites innovateur de la forme $Sm_{1-X}Ce_XFeO_3$ (x = 0, 1, 5) entraînant une charge de moins de 1% par masse de Pt et de Ru sur chaque support. On observe que le nanocatalyseur déposé sur des supports qui sont des conducteurs ioniques ou électroniques et ioniques performaient mieux que les nanocatalyseurs déposés sur des supports qui ne sont pas de conducteurs ioniques dus à l'interaction métal-support fort qui affecte grandement les propriétés électroniques et catalytiques du catalyseur. L'augmentation de l'activité catalytique envers les réactions d'oxydation du monoxyde de carbone et de C_2H_4 est démontrée par une augmentation d'activité catalytique et une plus haute conversion à plus basse température, par une énergie d'activation plus basse, par une fréquence de renouvellement plus élevée et par un taux de réaction intrinsèque plus élevé par aire de surface active.

Pour étudier en profondeur l'effet de la conductivité ionique des supports et l'échange de O^{2-} (déficience d'oxygène) entre le support et la surface du catalyseur, l'oxydation complète des polluants est étudiée en l'absence d'oxygène dans la phase gazeuse. Pour la première fois, l'oxydation complète du CO et de C_2H_4 est obtenue dans un environnement sans oxygène à basse température (< 250^{o}C) ce qui représente la découverte principale de cette recherche. L'idée de la suppression de polluants dans un environnement sans oxygène peut être appliqué

à des fins pratiques dans les piles à combustibles pour la purification de l'hydrogène en retirant les traces de CO à des températures < 100^{o}C. De plus, l'effet de la taille des particules, de la concentration des polluants, des conditions d'opérations et de la nature du support en l'absence d'oxygène dans la phase gazeuse sont étudiées. On propose que les nanoparticules métalliques et l'électrolyte solide forment des cellules nanogalvaniques locales près de la frontière entre les trois phases où la réaction anodique est l'oxydation du CO ou de C_2H_4 et la réaction cathodique est la réduction partielle de la surface du support. Un procédé de réactivation systématique est proposé et l'activité catalytique de ces nanoparticules est étudiée. Une étude plus poussée pourrait permettre le développement d'applications concernant le contrôle de la pollution de l'air tel que dans les catalyseurs de véhicules, les purificateurs d'air intérieurs et les émissions de centrales électriques.

Acknowledgement

First and foremost, I would like to express my sincere gratitude and appreciation to my thesis supervisor Dr. Elena A. Baranova who taught me the little I know about catalysis, electrochemistry and nanotechnology. Without her patience, guidance, advice and innovative ideas, none of this work would be possible.

I am deeply grateful to my Qatari friend and mentor Eng. Jassim Al-Emadi whose support and guidance made a great transformation in my career and personal life ever since we worked together in 2004.

I would like to express my gratitude to the technical staff in the Department of Chemical and Biological Engineering: Louis Tremblay, Gerard Nina, and, Franco Ziroldo for the enormous effort and prompt assistance whenever I needed throughout my experimental coursework.

I am grateful to my wonderful friend Enshirah Da'na for all the great years we spent together and the sincere friendship we shared. I am also thankful to Joanne Gamage for the continuous support and encouragement throughout the past years. Additionally, I am thankful for the opportunity to meet and work with many talented and friendly researchers in our lab for which special thanks go to Dr. Spyridon, Dr. Anis, Holly, Evans, and Michele. Special thanks to Nicolas Brazeau for the time and effort he put in translating the abstract of my thesis into French.

A great thanks and love go to my wonderful husband Hassan and my kids Sadiq and Faisal who lighten my life with love and patience. You are the joy and happiness that shadow my days and without you, this work would have not been completed.

Finally, I am grateful and indebted to my parents Jamal and Khalida whose infinite love and profound admiration for science and research motivated me since the childhood to be what I am now. I am also thankful to my sisters, brothers and my family in law for their continuous love and support which made our far distance so close.

To my family.....

Statement of Contributions of Collaborators

I hereby declare that I am the sole author of this thesis. I conducted the experimental work, performed data analysis and wrote all the chapters and appendices presented in this work under the scientific supervision of Dr. Elena A. Baranova. I have acknowledged other sources of information, experimental work and assistance in analyses where applicable at the end of each chapter. The continuous scientific guidance throughout the project and editorial comments for the written work were provided by my supervisor Dr. Elena A. Baranova.

Table of contents

List of Figures

List of Tables

List of Abbreviations

ADF: annular dark field

BET: Brunauer-Emmett-Teller theory

DFT: density functional theory

EDX: energy dispersive x-ray

EG: ethylene glycol

EPOC: electrochemical promotion of catalysis

FWHM: full width at half maxima

FW3/4M: full width at three quarter maxima

GC: gas chromatography

GDC: gadolinia-doped ceria

ICP: inductively coupled plasma

NEB: nudged elastic band

NEMCA: non-faradaic modification of catalysis

NDIR: non-dispersive infrared

PEEM: photoemission electron microscopy

PEMFC: proton exchange membrane fuel cell

PM: precious metal

PRM: polyol reduction method

PROX: preferential oxidation

SDC: samarium-doped ceria

SMSI: strong metal-support interaction

SOFC: solid oxide fuel cells

STEM: scanning transmission electron microscopy

TEM: transmission electron microscopy

TGA: thermal gravimetric analysis

TOF: turn over frequency

tpb: three-phase boundary

TPD: temperature-programmed desorption

TWC: three-way catalytic converter

UHP: ultra high pressure

VOC: volatile organic compound

WMSI: weak metal-support interaction

XAS: x-ray absorption spectra

XPS: x-ray photoelectron spectroscopy

XRD: x-ray diffraction

YSZ: yttria-stabilized zirconia

List of Symbols

Roman

a_s: specific surface area ($m^2 \cdot g^{-1}$)

C_{AS}: gas concentration of component A at the catalyst surface ($kmol \cdot m^{-3}$)

C_{WP}: Weisz-Prater coefficient for internal mass diffusion

d_{nm}: particle diameter (nm)

D_e: effective gas phase diffusivity ($m^2 \cdot s^{-1}$)

E_a: activation energy ($J \cdot mol^{-1}$)

F: Faraday constant; magnitude of electron charge per mole electrons ($C \cdot mol^{-1}$)

F: gas flowrate ($mol \cdot min^{-1}$)

H_r: heat of reaction ($J \cdot mol^{-1}$)

I: electric current (A)

k: reaction rate constant ($mol \cdot s^{-1}$)

M: molecular weight ($g \cdot mol^{-1}$)

n: charge of the applied ion in Faraday's law (C)

n_T: total number of moles (mol)

Na: Avogadro number; number of atoms per mole (6.022×10^{23} mol^{-1})

N_G: moles of active metal sites (mol)

r: rate of oxidation or electrooxidation ($mole \cdot s^{-1}$)

r: electro-promoted catalytic rate ($mol \cdot s^{-1}$)

r_o: unpromoted catalytic rate (open circuit catalytic rate) ($mol \cdot s^{-1}$)

R: universal gas constant ($J \cdot mol^{-1} \cdot K^{-1}$)

R: radius of particle (m)

T: temperature (K)

w: mass of catalysts (g)

Greek

Λ: apparent Fradaic efficiency

γ: intrinsic rate per active metal surface area ($mol \cdot s^{-1} \cdot m^{-2}$)

μ: micrometer (μm)

σ: conductivity ($S \cdot cm^{-1}$)

ρ: solid catalyst density ($kg \cdot m^{-3}$)

θ: Bragg angle (^{o})

λ: wavelength of electromagnetic radiation (m)

SECTION I: INTRODUCTION

1 General Introduction

1.1 Introduction

Heterogeneous catalysis refers to the form of catalysis where the phase of the catalyst differs from that of the reactants. A heterogeneous catalyst can be composed of one bulk catalyst or two major components: the active metal particles and the support. In concept, the reactants diffuse to the catalyst surface and are adsorbed onto it physically or by the formation of a chemisorption bond. After reaction, the products desorp and diffuse away from the surface.

The research in heterogeneous catalysis is of tremendous importance for the chemical industry. It aims at the design of tailored ultra-high selective catalysts to promote green chemistry, of which supported metals constitute an important class of these materials [1,2]. The properties of supported metal particles can be tuned by (i) the control of particle size and (ii) the use of metal-support interaction [2]. Most recent catalysts utilize metal particles in the nano-meter size deposited on high surface area supports. The support has been claimed to promote specific electronic properties and/or geometrical features of the nano-sized supported metal particles in what is known as the phenomenon of strong metal-support interaction (SMSI) [2-4].

The electrochemical promotion of catalysis (EPOC) was first reported in the 1980s [5]. It is a phenomenon where the catalytic activity of conductive catalysts deposited on solid electrolytes can be altered in a very pronounced and reversible way by applying very small currents (μA) or potentials (typically up to ± 2 V) between the catalysts and an electronic conductor (counter electrode), also deposited on the solid electrolyte [5-8]. The resulting increase in catalytic rate often exceeds by several orders of magnitude the increase anticipated from Faraday's Law. The phenomenon of EPOC combined with classical heterogeneous catalysis is not limited to any particular electrolyte, conductive catalyst or type of reaction, and together they could be utilized for the regeneration and activation of metals (Pt, Pd, Ru, Ir, Pd, etc.) and metal oxides (RuO_2, IrO_2, etc.), which are currently used for purification of

automotive exhaust [9-11]. Due to the high cost and limited availability of these metals, it is important to use as low metal concentration as possible in these catalytic converters. This is accomplished by using nanoparticles instead of micro films and by keeping the active metals at high degree of dispersion.

On the other hand, it has been recently found that the backspillover of the ionic species from the support to the gas-exposed catalyst surface can be thermally induced without any electrical polarization by using nanoparticles supported on ionic or mixed ionic conductive ceramics such as yittria-stabilized zirconia (YSZ), cerium oxide (CeO_2) and titanium oxide (TiO_2) in what is called self-induced electrochemical promotion (self-induced EPOC) [8,9].

In this thesis, further investigation of self-induced EPOC over noble metal nanoparticles, the effect of nanoparticle size and support nature on their catalytic activity for carbon monoxide and ethylene oxidation in oxygen-rich and oxygen-free environment is conducted. Moreover, stability over time, catalyst regeneration and mechanism of pollutants electrooxidation in the absence of oxygen in the gas feed are proposed.

1.2 Thesis structure

This dissertation is comprised of seven main sections. *Section I* includes three chapters: the current one which is a general introduction, Chapter 2, a literature review and background related to this research and Chapter 3 which highlights main research objectives. *Section II* includes Chapter 4 which details nanocatalyst synthesis, characterization and experimental setup. *Section III* presented by Chapter 5 discusses nanoparticle activity when supported on a conventional non ionic conductive support for ethylene oxidation. *Section IV* includes Chapter 6 through Chapter 8 which discusses the phenomenon of metal-support interaction by comparing the activity of nanoparticles when deposited on ionic and mixed ionic conductive vs. non ionic conductive supports for volatile organic compounds (VOCs) oxidation. *Section V* sheds more light on the effect of oxygen vacancy in the ionic and mixed ionic conductors when oxidation of VOCs is carried out in oxygen-free environment. This section includes Chapter 9 through Chapter 11 and it presents the main novel findings in this research. The conclusions and general discussions related to the entire thesis are summarized in *Section VI* in Chapter 12. The last part is *Section VII* (Appendices A, B and C). Appendix A

and B are the supporting information submitted with the articles related to the work presented in Chapter 8 and 10, respectively. Appendix C summarizes the main scholar and scientific contributions of the author during the research conducted in this thesis. There are seven research articles contained in the main body of this dissertation, of which four are published in scholarly journals. The four published articles appear in this thesis with permission of the respective publishers holding the copyrights. The remaining articles have been submitted or to be submitted for publication soon. In addition, there is a published refereed transaction paper related to the work presented in Chapter 6.

Further discussion concerning thesis structure, including a detailed description of the contents of each chapter, is presented below. The associated scientific contributions are also listed, including the impact factor (IF) of the relevant journals in which publications were made.

Chapter 1: Introduction

A general overview and discussion related to the research is provided and the framework for the thesis is outlined.

Chapter 2: Background and literature review

The aim of this chapter is to provide the reader with specific background and literature review related to the undertaken scope and objectives of this research. It summarizes the main concepts in self-induced electrochemical promotion phenomenon, the factors affecting nanoparticle activity towards volatile organic compound oxidation and metal-support interaction overview. The latest achievements and applications of this phenomenon in environmental pollution control are also summarized.

Chapter 3: Research motivation and objectives

This chapter highlights the main motivation of this research and what is needed to be investigated under the scope of this work.

Chapter 4: Catalyst synthesis, characterization and experimental setup

This chapter describes the procedure of the synthesis of at least twenty nanocatalysts using a modified polyol reduction method. Detailed characterization of the particle size,

composition, morphology, metal loading, oxidation state and specific surface area are presented. The experimental setup is as well described.

Chapter 5: Particle size effect on catalytic activity of carbon-supported Pt nanoparticles for complete ethylene oxidation

The effect of Pt nanoparticle size (< 10 nm) was studied for the first time for ethylene oxidation. Carbon black with large surface area is used as well for the first time as a support for platinum nanoparticles for this reaction. The catalytic activity of four Pt/C catalysts with different particle sizes is studied to investigate the structure sensitivity of ethylene oxidation over these catalysts. Moreover, detailed x-ray photoelectron spectroscopy study is conducted to support the observed trend of increased catalytic activity as the nanoparticle size decreases for ethylene oxidation at low temperatures (25 - 220^{o}C).

Contributions

(a) Published paper

R. J. Isaifan, S. Ntais, E. A. Baranova, " Particle size effect on catalytic activity of carbon-supported Pt nanoparticles for complete ethylene oxidation", Applied Catalysis A: General 464 - 465 (2013) 87- 94. (IF (2013) = 3.674).

(b) Invited seminar presentation

(i) Centre for Catalysis Research and Innovation Technical Seminar, UOttawa, Canada, 2013.

Chapter 6: Metal-support interaction of Pt nanoparticles with ionically and non-ionically conductive supports for CO oxidation

Yttria-stabilized zirconia (YSZ), an interesting ionic conductive ceramic, is investigated as a potential support for metals in heterogeneous catalysis. Self-induced electrochemical promotion is studied over platinum nanoparticles (~ 2.5 nm) synthesized with a modified polyol reduction method and deposited on YSZ. The catalytic activity of Pt/YSZ was compared with Pt nanoparticles deposited on carbon black and alumina as well as with a commercial catalyst synthesized by the traditional wet impregnation method for CO oxidation in the temperature range of 25 - 250^{o}C.

Contributions

(a) Published paper

R. J. Isaifan, H. A. Dole, E. Obeid, L. Lizarraga, P. Vernoux, E. A. Baranova, "Metal-support interaction of Pt nanoparticles with ionically and non-ionically conductive supports for CO oxidation", Electrochemical and Solid State Letters 15(3) (2012) E14-E17. (IF (2012) = 2.01).

(b) Published refereed journal transaction

R. J. Isaifan, H. A. Dole, E. Obeid, L. Lizarraga, E. A. Baranova, P. Vernoux, "Catalytic carbon monoxide oxidation over size-controlled Pt nanoparticles in the gas phase and elevated temperatures", Electrochemical Society Transactions 35 (28) (2011) 43-57.

(c) Conference presentations

(i) The 219th Electrochemical Society Conference, Montreal, Canada, 2011.

(ii) The 7th International Conference on Environmental Catalysis, Lyon, France, 2012.

(d) Invited seminar presentations

(i) The Annual Meeting of the Center for Catalysis Research and Innovation (CCRI), University of Ottawa, Ottawa, Canada, 2011.

Chapter 7: Effect of ionically conductive supports on the catalytic activity of platinum and ruthenium nanoparticles for ethylene complete oxidation

The catalytic activity of ruthenium nanoparticles is compared with platinum nanoparticles of the same particle size each deposited on four supports and is studied for complete oxidation of ethylene. Ruthenium, being a noble metal ten times cheaper than platinum, shows comparable activity in the temperature range of experiments (25 - 220^{o}C). Ru/YSZ nanoparticles are used for the first time as a catalyst for ethylene oxidation and show high activity at low temperatures. Moreover, the complete oxidation of ~ 0.1% ethylene in the absence of oxygen in the gas feed over Ru/YSZ is compared to that of Pt/YSZ. At the end, the mechanism of self-induced EPOC is discussed and compared to the electrochemical promotion phenomenon EPOC and a comparative scheme is presented.

Contributions

(a) Accepted paper

R. J. Isaifan, E. A. Baranova, "Effect of ionically conductive supports on the catalytic activity of platinum and ruthenium nanoparticles for ethylene complete oxidation", Journal of Catalysis Today (2014) CATTOD-S-14-00030 (in press). (IF (2014) = 3.309).

(b) Conference presentation

(i) The 11th European Congress on Catalysis, EuropaCat-XI, Lyon, France, 2013.

(c) Invited seminar presentation

(i) The 2nd Electrochemical Society Symposium, Montreal, Canada, 2012.

Chapter 8: Pt nanoparticles supported on $SmFeO_3$ perovskite group for carbon monoxide and ethylene oxidation

A novel group of perovskites is used for the first time as catalysts and as supports for Pt nanoparticles for the complete oxidation of carbon monoxide and ethylene at low temperatures (25 - 350^{o}C). The effect of doping the perovskites with 1 – 5 % cerium is investigated. The catalytic activity of the blank perovskites is also compared to other blank supports such as yttria stabilized zirconia and alumina. Moreover, the perovskites are used as supports to platinum nanoparticles and show higher activity depicted by the lowest activation energies and the earlier light off curves compared to other perovskite groups reported earlier in literature for similar catalytic reactions and conditions.

Contributions:

(a) Submitted paper

R. J. Isaifan, W. D. Penwell, J. O. C. Filizzola, J. B. Giorgi, E. A. Baranova, "Platinum nanoparticles supported on $SmFeO_3$ novel perovskite group for carbon monoxide and ethylene oxidation", submitted to the Journal of Applied Catalysis B: Environmental, APCATB-S-14-02169 (2014), *under review*. (IF (2014) = 6.007.

Chapter 9: Catalytic electrooxidation of volatile organic compounds by oxygen-ion conducting ceramics in oxygen-free gas environment

The content of this chapter presents the main novel part of this research which is the complete oxidation of volatile organic compounds in the absence of oxygen in the gas feed over noble metal nanoparticles deposited on ionic and mixed ionic conductive supports. The catalytic activity of these materials is compared with the catalytic activity of the noble metals when supported on non ionic conductive supports and with blank supports as well. The mechanism of nano-galvanic cells formation at the three-phase boundary is proposed to explain the observed activity. Finally, the stability of the catalyst over time and effect of pollutant concentration are studied in oxygen-free gas environment.

Contributions:

(a) Published paper:

R. J. Isaifan, E. A. Baranova, "Catalytic electrooxidation of volatile organic compounds by oxygen-ion conducting ceramics in oxygen-free gas environment", Journal of Electrochemistry Communications 27 (2013) 164–167. (IF (2013) = 4.287).

(b) Conference presentations

(i) The 7th International Conference on Environmental Catalysis, Lyon, France, 2012.

(ii) The 62nd Canadian Chemical Engineering Conference, Vancouver, Canada, 2012.

(c) Invited seminar presentation

(i) Centre for Catalysis Research and Innovation Technical Seminar, UOttawa, Canada, 2013.

Chapter 10: Size-dependent activity of Pt/yttria-stabilized zirconia catalyst for wireless electrooxidation of ethylene and carbon monoxide in oxygen-free environment

This chapter presents an extended study to the novel part presented in chapter 9. The size effect of four platinum nanocatalysts deposited on yttria-stabilized zirconia is studied for the complete oxidation of carbon monoxide and ethylene in the absence of oxygen in the gas phase. Detailed characterization using annular dark field-scanning transmission spectroscopy

and x-ray photoelectron spectroscopy show the effect of a strong metal-support interaction (self-induced EPOC) between Pt and YSZ which dramatically enhances the catalytic activity of these catalysts in the presence and absence of oxygen in the gas feed.

(a)Submitted paper to:

R. J. Isaifan, S. Ntais, M. Couillard, E. A. Baranova, "Size-dependent activity of Pt/yttria-stabilized zirconia catalyst for wireless electrooxidation of ethylene and carbon monoxide in oxygen free environment", submitted to the Journal of Catalysis, JCAT-14-609 (2014), *under review*. (IF (2014) = 6.073).

(b) Conference presentation

(i) International workshop for ionically conductive ceramics for catalysis, Lyon, France, 2013.

Chapter 11: Particle size effect of Pt/yttria-stabilized zirconia on carbon monoxide methanation and preferential electrooxidation for hydrogen gas purification at low temperatures

This chapter presents a practical application of the novel part of this research which is related to fuel cells operating at low temperatures and in preferable oxygen-lean environment. The methanation of 1000 ppm carbon monoxide in hydrogen-rich stream is studied over four particle sizes of Pt/YSZ in the absence of oxygen in the gas phase. The effect of nanocatalyst particle size, CO concentration and stability over time is investigated. Moreover, the catalyst selectivity towards methane formation is discussed at temperatures below 100^{o}C.

Contributions:

(a) A paper to be submitted to: the Journal of Power Sources.

Chapter 12: General discussion, conclusions and recommendations

This chapter presents general discussion and conclusions for the work presented in this dissertation. The novelty of this research and original contributions to knowledge are highlighted. To this end, recommendations for future work related to applications in air pollution control are suggested.

Appendix A: Supporting information for the article submitted in Chapter 8

In this Appendix, the catalytic activity as light-off curves in terms of conversion vs. temperature for all the catalysts discussed in Chapter 8 is presented. Moreover, detailed heat and mass transfer limitation calculations are shown for every experimental run.

Appendix B: Supporting information for the article presented in chapter 10

In this Appendix, spatially-resolved energy dispersive x-ray spectroscopy (EDX) spectra is presented and discussed. The catalytic activity as light-off curves in terms of conversion vs. temperature for all the catalysts discussed in chapter 10 is presented. In addition, detailed heat and mass transfer limitation calculations are shown for every experimental run. Moreover, a calculation sample for the length of the three-phase boundary of the nanocatalysts is given.

Appendix C: Scholarly contributions

Scholarly contributions made during the course of this doctoral research are detailed which include the following metrics (excluding submitted papers): publication of 6 peer-reviewed articles in scholarly journals and one refereed transaction article, participation in 13 conference presentations, and delivery of one invited presentation and one seminar. These contributions include collaborative research that was conducted in parallel to the scope of the current thesis.

1.3 References

[1] R. Jin, *Nanotechnol. Rev.* 1 (2012) 31.

[2] B. Coq, *NATO Sci. Ser.* 546 (2000) 49.

[3] S. Tauster, *Acc. Chem. Res.* 20 (1987) 389.

[4] S. Tauster, S. Fung, R. Garten, *J. Am. Chem. Soc.* 100 (1978) 170.

[5] M. Stoukides, C. G. Vayenas, *J. Catal.* 70 (1981) 137.

[6] S. Bebelis, *J. Catal.* 118 (1989) 125.

[7] N. Anastasijevic, *Catal. Today.* 146 (2009) 308.

[8] C. G. Vayenas, S. Bebelis, C. Pliangos, S. Brosda, D. Tsiplakides, Electrochemical Activation of Catalysis, Promotion, Electrochemical Promotion and Metal-support Interactions, Kluwer Academic/Plenum Publisher, New York, 2001.

[9] J. B. Hunter, *Platin. Met. Rev*. 1 (1968) 2.

[10] G. Acres, *Platin. Met. Rev.* 3 (1970) 74.

[11] M. Shelef, R. W. McCabe, *Catal. Today.* 62 (2000) 35.

2 Background and Literature Review

2.1 Introduction to heterogeneous catalysis

Catalysis is a complex science which integrates chemistry, materials science, and chemical reaction engineering. It has an enormous impact on the world economy, since more than 90% of chemical manufacturing processes utilize catalysts [1]. As a general definition, a catalyst is a substance, added in small amounts, which can speed up chemical reactions without being consumed in the reaction process. The power of a catalyst lies in its capability in accelerating chemical reactions by decreasing the activation energy needed for the reaction to take place [2].

Catalysis, including heterogeneous, homogeneous, and enzymatic catalysis, is vitally important for the development of modern society. The main focus in the 20^{th} century was to improve the activity of catalysts in terms of producing more product molecules per unit area per unit time, while achieving 100% selectivity in all catalyst-based chemical processes has been the target of catalysis science in the 21^{st} century [3][4]. This is evident by more than 10 Noble Prizes in Chemistry awarded for work pertaining to catalysis [5]. The 2007 Noble Prize in Chemistry was awarded to Prof. Ertl, a pioneer in introducing surface science techniques to the field of heterogeneous catalysis leading to a deeper understanding of how chemical reactions take place at surfaces [1].

Heterogeneous catalysis utilizing metal particles plays an essential role in the industrial, commercial and environmental applications. Therefore, the design of highly active catalysts in an efficient and cost-effective way is an important topic [1][6]. Industrial catalysis has been practiced for nearly a century; but its significance for the petrochemical industry was particularly realized when the oil crisis occurred in the 1970s. The importance of catalysis is also reflected in environmental protection and public health; a well-known example is the catalytic converters for removing toxic emissions of automobiles, which were first developed by General Motors Corporation and Ford Motor Company in 1974 [2][7].

In a typical heterogeneous catalytic process, the catalytic reaction occurs repeatedly by a sequence of elementary steps, including molecular adsorption, surface diffusion, chemical rearrangement (bond-breaking, bond-forming, molecular rearrangement) of the adsorbed reaction intermediates, and desorption of the products [6]. Since the catalytic reaction occurs when the reactants adsorb onto the catalyst surface, the reaction rate depends on the total surface area of the solid catalysts as well as the catalyst geometry which can have a deterministic effect on the selectivity of specific catalytic reactions (i.e. structure-sensitive reactions). Therefore, it is preferable to increase the specific surface area of the catalyst by decreasing the particle size down to the nanoscale.

The rise of nanotechnology over the past two decades has opened the door to a revolution in catalysis science [1][6][8][9]. The new technology did not only help improve understanding of reaction mechanisms in industrial catalysis, but also provided new and novel catalysts with high activity and selectivity. It has been widely accepted that a higher catalytic activity could be achieved by increasing the surface area of the specific active phase of the catalyst through the reduction of the size of the corresponding catalytic particles. The fraction of atoms on particle surfaces increases dramatically as the size of particles decreases. This fraction is referred to as "dispersion" and it approaches 100% when the particle size reaches 1 nm, hence providing more active sites for catalytic reactions. Additionally, the catalytic selectivity could be improved by using nanocrystals with a specific shape that have specific desirable local bonding geometries [10].

2.2 Precious metal nanoparticles for air pollution control

In the Periodic Table, precious metals (PM), also called noble metals, refer to silver (Ag), gold (Au), osmium (Os), palladium (Pd), platinum (Pt), rhodium (Rh), iridium (Ir) and ruthenium (Ru), with the latter six elements known as the platinum group [2]. Heterogeneous catalysis of PM mostly involve very small particle form at the nanoscale (e.g., 1 – 100 nm in diameter), although in some cases microscale particles are also used (e.g., Ag particles of a few μm in size are used in industrial epoxidation of ethylene).

Due to the enormous impact of catalysis development on the commercial, industrial and environmental level, one area of catalysis that is developing at a rapid pace is

nanocatalysis. Striking novel catalytic properties have been reported for nanoparticle catalysts as compared to their bulk counterparts in terms of pronounced enhanced reactivities and selectivities [1].

Nanotechnology has been utilized recently in "Environmental Catalysis" which aims at reducing pollution contents in air and water [6][11]. Starting from this base, extensive studies have been reported to investigate various important aspects in this field such as: (i) the dilution of the active sites, (ii) the use of promoters and bimetallic, (iii) the use of well-crystallized surfaces and (iv) the influence of metal–support interactions. The objectives of these studies were to point out the vital influence of the experimental conditions and gas phase compositions which may induce very strong surface modifications of the initial metallic aggregates. Moreover, the catalytic activity was found to depend on the reaction type in addition to the nature of carriers effect such as the participation of the ionic species from the support [11]. Several recent reviews were published on nanocatalysis citing the tremendous development of these materials and their impact in the past few decades [1][2][7][5]. Many experimental studies have focused on correlating nanocatalysts activity with particle size, geometry, composition, oxidation state and chemical/physical environment which all play a role in determining nanoparticles reactivity [1].

The following two sections will shed light on the main findings and development of precious metal nanocatalysts for air pollution control related to their application in indoor air quality units and as automotive exhaust catalysts.

2.2.1 Precious metal nanoparticles for indoor air quality units

The indoor environment plays an important role in human health, because people generally spend more than 80% of their time in indoors, which contributes a higher risk from inhalation of pollutants than outdoors [12]. Indoor pollutants include carbon monoxide (CO), carbon dioxide (CO_2) and volatile organic compounds (VOCs). The main indoor resources for emitting VOCs are furnishing materials, hair sprays, air fresheners, paints, printers and tobacco. The major indoor VOC pollutant is formaldehyde (HCHO) which can cause nasal tumors, mucus membrane tract and skin irritation. In general, three methods are suggested to improve indoor air quality, namely: air pollution source control, ventilation process

improvement and air cleaning [12]. Source control has been applied to several consumer products such as manufacturing water-based paints instead of the oil-based ones which have been used for decades. Several ventilation processes have been developed such as implementing air conditioning with higher rates of fresh air circulation. In the context of this dissertation, indoor air quality control by air cleaning using heterogeneous catalysis will be summarized.

Most of the indoor air quality control catalysts utilize photocatalysis as the main process to oxidize pollutants inside the buildings. A very well established commercial photocatalyst is the nano titanium dioxide (TiO_2) smart coatings which decompose bacteria and micro-organic compound in indoor environment. Generally speaking, a photocatalyst is a substance that uses light irradiation to modify the rate of the reaction; in this case, oxidation of micro-organisms and volatile organic compounds is taking place as the main process. Moreover, titania-supported Au nanoparticles have been found to be active at ambient conditions for the oxidation of CO to CO_2 and hence can be used to reduce the levels of CO pollution in buildings by being incorporated into the paint covering the interior walls or as coatings in indoor air pollution control units [13].

2.2.2 Precious metal nanoparticles as automotive exhaust catalyst

In a recent status report from Johnson-Matthey PLC, heterogeneous catalysts with noble metals comprise over than 90% of the direct market with a total value at $15 billion, from which, roughly 40% is devoted to the automotive sector. Recent projections estimate that automotive emissions control catalysts will constitute a market value greater than $7 billion by 2015. Emissions treatment accounts for more than half of the gross demand for palladium and platinum, and more than 80% of the demand for rhodium as illustrated in Fig. 2-1.

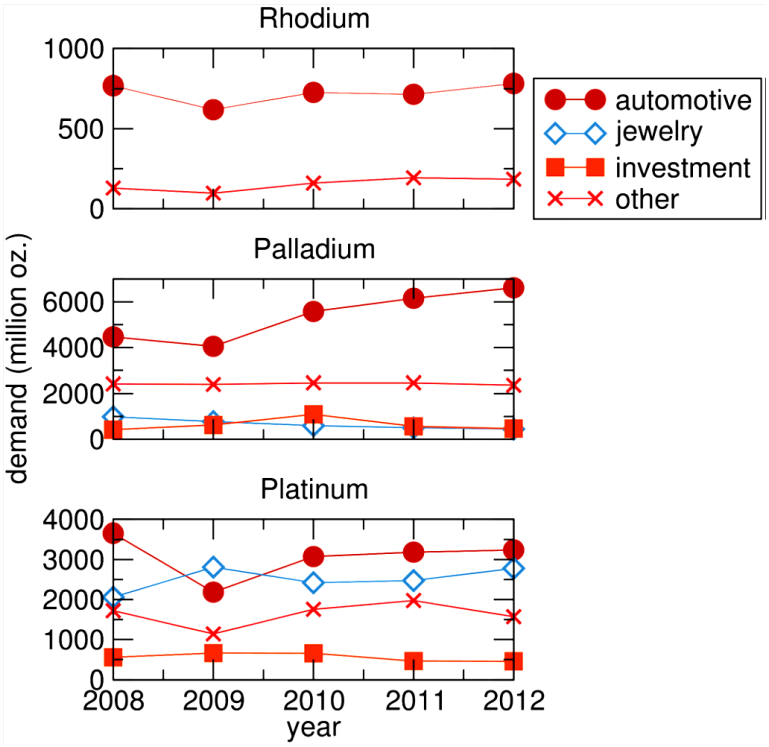

Figure 2-1: Recent usage of Rh, Pd, and Pt, showing the significant share of automotive catalysis. The data is from the Johnson-Matthey PLC document Platinum 2013, and was current to March 2013.

The amount and type of pollutants vary depending on the nature of fuel used for the vehicle. Fig. 2-2 shows the two main exhaust emissions from petrol and diesel automobiles.

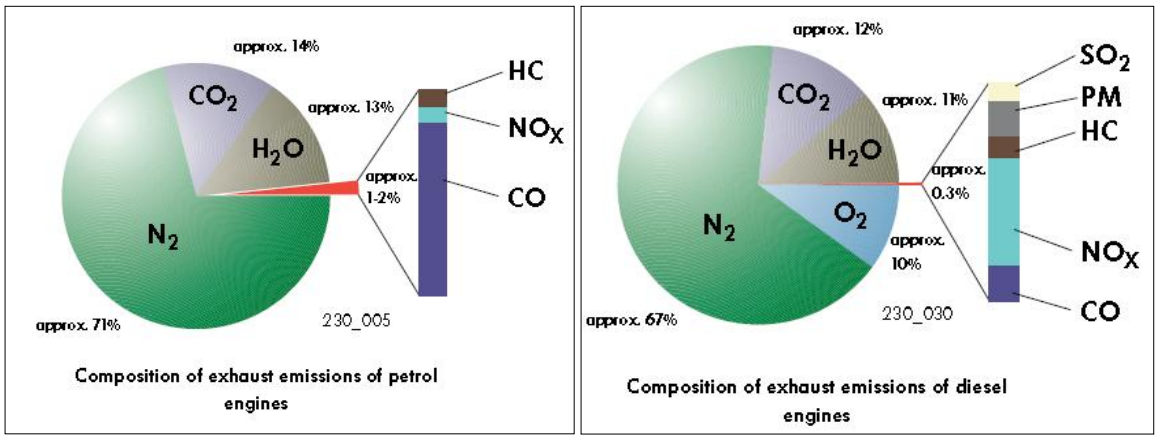

Figure 2-2: Types of motor vehicle exhaust emissions. Data is from self-study programme 230 by Audi and Volksvaagen [14].

The three-way catalytic (TWC) converter has been widely used to remove automotive exhaust pollutants specifically; carbon monoxide (CO), hydrocarbons (HC) and nitrogen oxides (NO_x) via the following reaction schemes:

1- oxidation of carbon monoxide

$$CO + 1/2\ O_2 \Rightarrow CO_2$$

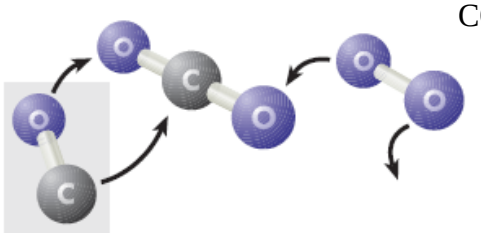

2- oxidation of hydrocarbons

$$C_xH_y + (x+(y/4))O_2 \Rightarrow xCO_2 + (y/2)\ H_2O$$

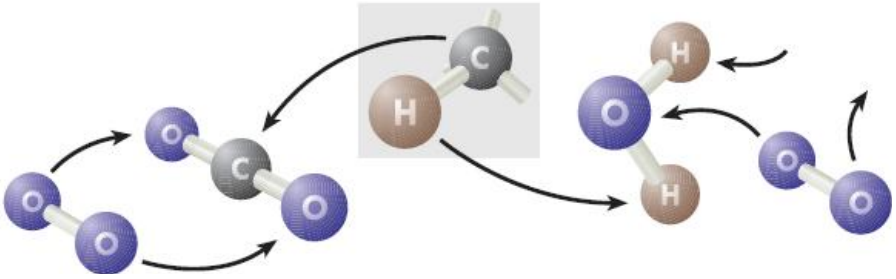

3-reduction of nitrogen oxides

$$2NO \Rightarrow O_2 + N_2$$

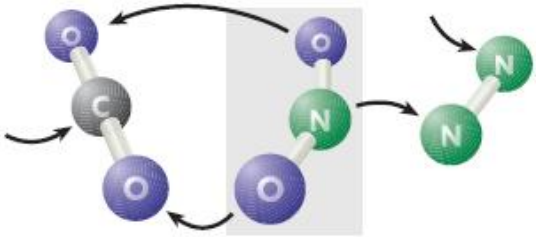

Figure 2-3: The catalytic cleaning processes in TWC. The schematics are from self-study programme 230 by Audi and Volkswagen [14].

The main components in TWCs are precious metals such as Pt, Pd or Rh as the active catalysts, and an inorganic oxide such as γ-alumina (Al_2O_3), CeO_2, and ceria-based composite oxides as supports which all operate at temperatures above 300^{o}C [2]. The phenomenon of metal-support interaction was substantial by many experiments and it plays an important role in the catalytic activity of TWCs. It depends on the support and metal type so that different

support and metal will lead to different interaction. The main metal-support interaction relations in automotive exhaust catalysts are shown in Fig. 2-4.

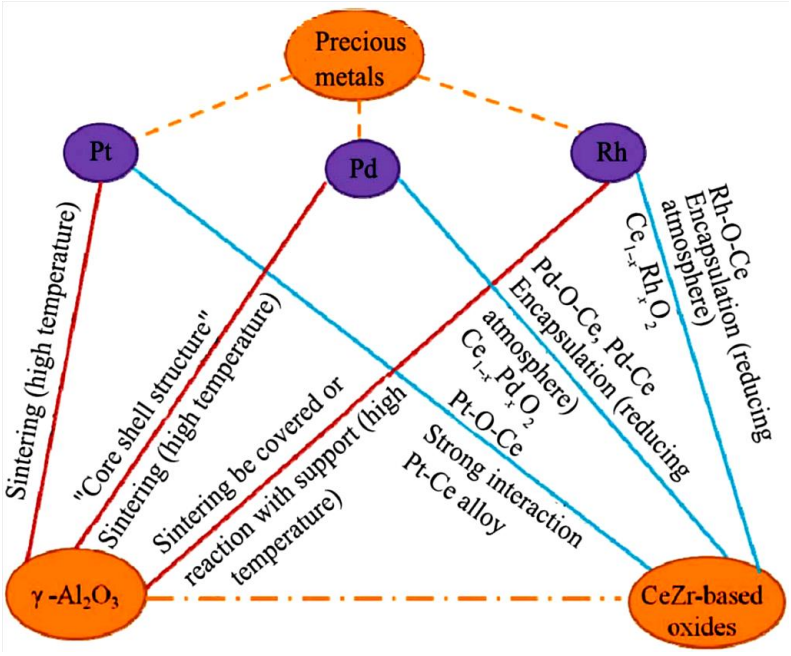

Figure 2-4: Schematic diagram of metal-support interaction in automotive exhaust catalysts [7].

The support used in the TWCs can improve the dispersion of precious metals and suppress the sintering of noble metals at high temperature, thus improving the catalytic performance and endurance ability. On the other hand, precious metals enhance the redox performance and oxygen storage capacity of the supports [7]. For example, Harrison et al. reported that Pt, Pd and Rh promoted the reduction of surface oxygen of CeO_2 [15]. In another study on the effect of noble metals of the support, 1 wt. % of Pt was supported on $Ce_xZr_{1-x}O_2$ and was reduced for three cycles. It was found that Pt favoured the structural reforming of ceria-zirconia into one cubic solid and prevented $CeAlO_3$ formation which is harmful to the catalytic performance. Moreover, Pt particles (2 – 3 nm) strongly interacted with ceria, and it highly dispersed on ceria-zirconia grains with diameter between 10 and 35 nm [16]. It is known that ceria-based oxide is suitable for Pt to achieve a good balance between catalytic activity and the sintering suppression. On the other hand, for Rh catalysts, zirconia based oxide is verified to meet the requirements for similar mechanism. Based on this, a new TWC with a noble metal sintering suppression technology based on the support anchoring effect was

designed, separating Pt and Rh metals while supporting the former on ceria-based and the latter on zirconia based oxides [17]. Fig. 2-5 shows the catalytic activity of this catalyst design upon engine test after ageing in terms of the temperature at which 50% conversion of target pollutant is achieved. Compared to the conventional catalyst, this developed catalyst exhibits a very high catalytic activity presented by much lower light off temperatures, although it contains less precious metal than the conventional one. As a matter of fact, this catalyst has been used practically-adopted in gasoline-fueled engine automobiles since 2005 [7][17].

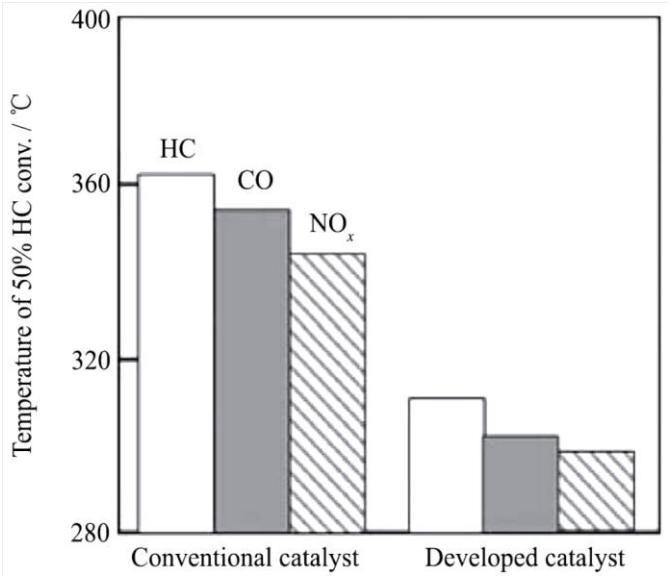

Figure 2-5: Performance of the developed catalyst applying the Pt support- interaction concept in engine bench test after the engine ageing [17].

2.3 Heterogeneous catalysis on platinum group metal nanoparticles for environmentally important reaction systems

A general trend in the studies conducted on supported noble metal nanoparticles found that particle synthesis methods, particle size, particle shape and crystallographic planes greatly affect the catalytic rates of various reactions [18]. To better understand the role of active sites in heterogeneous catalysis, tremendous account of studies has been published contributing to this topic as illustrated in Fig. 2-6.

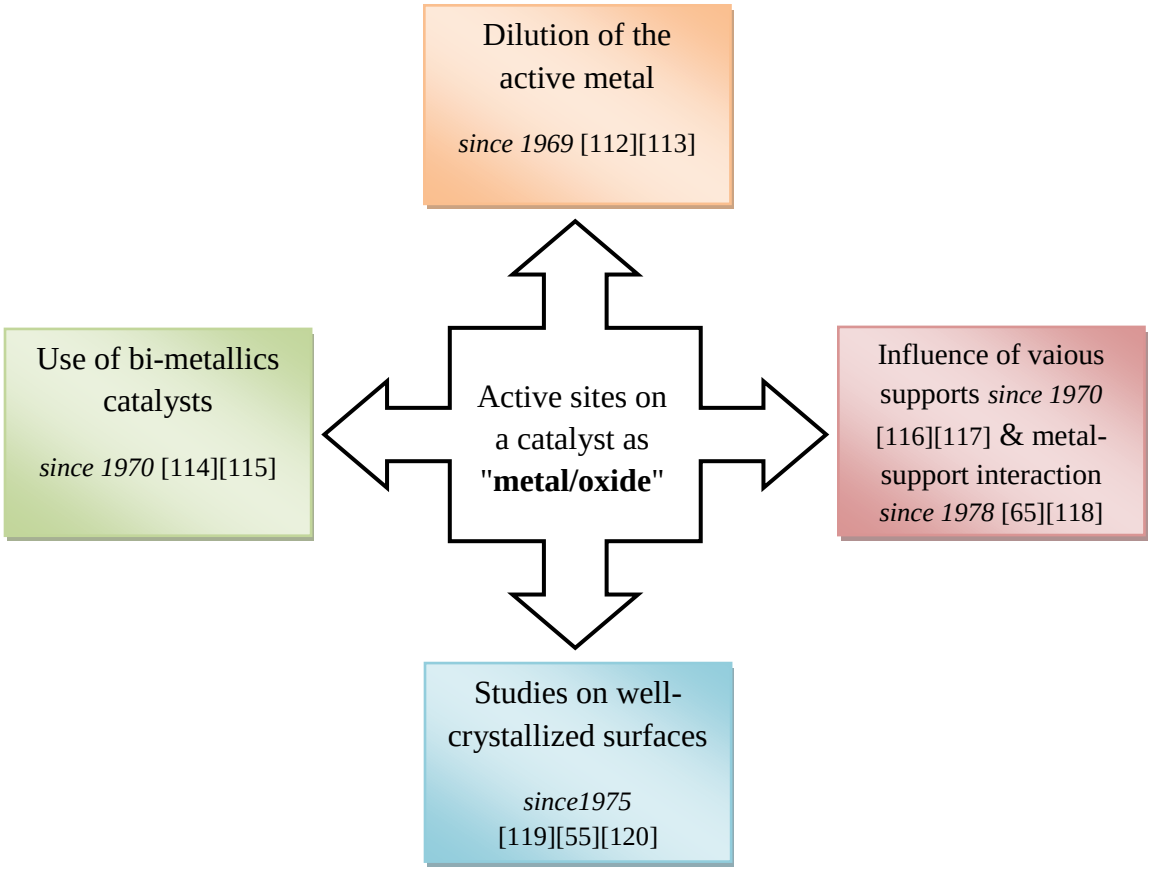

Figure 2-6: Convergent studies to approach a better understanding of the active sites in heterogeneous catalysis, adapted from [19].

To closely focus on the main applications of nanoparticles in air pollution control within the scope of this work, the following sub-sections will highlight mainly the use of noble metal nanoparticles for the effective removal of pollutants, more specifically: carbon monoxide oxidation, ethylene oxidation and carbon monoxide methanation.

2.3.1 Heterogeneous catalysis on platinum group nanoparticles for carbon monoxide oxidation

The catalytic oxidation of CO to CO_2 on platinum group metals is a well studied reaction for its environmental and industrial importance [20][21]. It is chosen as the model reaction in this research to study the catalytic activity of the synthesized catalysts as well as for being the main pollutant target for automotive exhaust pollution control. The reaction of

CO oxidation on Pt group metals was studied extensively and it has been established that it follows Langmuir-Hinshelwood mechanism in which the reactants enter the reaction from an adsorbed state as shown in Fig. 2-7.

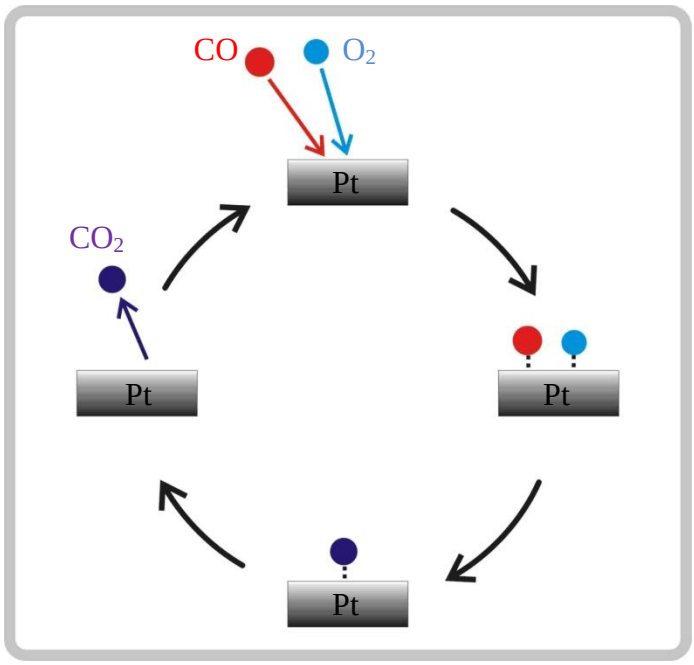

Figure 2-7: Schematic representation of CO chemisorption on Pt group metals following Langmuir- Hinshelwood mechanism.

The Langmuir /Hinshelwood reaction between CO_{ads} and O_{ads} is well established as the dominant reaction mechanism [22–25] as per the following reaction steps :

$$CO_{(g)} \Rightarrow CO_{ads} \quad (2.1)$$

$$O_{2(g)} \Rightarrow 2O_{ads} \quad (2.2)$$

$$CO_{ads} + O_{ads} \Rightarrow CO_{2(g)} \quad (2.3)$$

where the reverse of reaction 2.2 (desorption of adsorbed O_{ads}) atoms and the reverse of reaction 2.3 (the dissociative chemisorption of CO_2) are neglected [26]. The kinetics of CO oxidation have the order of +1.0 with respect to oxygen and -0.5 with respect to carbon monoxide over Pt surfaces [27].

Regardless of the sample type (supported, polycrystalline, different orientations of single crystals) and pressure region (from atmospheric pressure to ultrahigh vacuum), the reaction rate exhibits in all cases similar features being structure-insensitive reaction over platinum surfaces [28][29]. Haneda et al. [30] conducted a detailed study to investigate the effect of Pt/Al_2O_3 nanoparticles dispersion on their catalytic activity for CO oxidation. They prepared six catalysts with dispersion values from 0.07 - 0.81 and found that although CO conversion increased with increasing catalyst dispersion, the turn over frequency of CO over these catalysts was independent of catalyst dispersion, indicating structure insensitivity of this reaction as shown in Fig. 2-8.

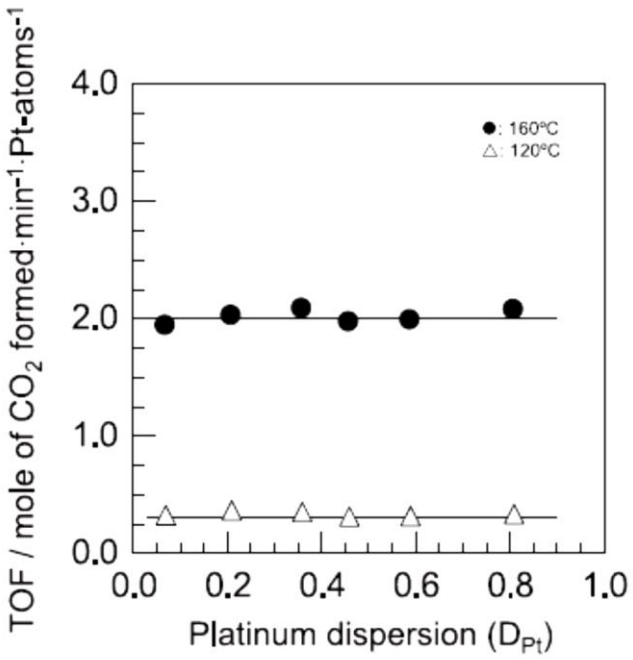

Figure 2-8: Change in TOF of CO oxidation at 120 and 160°C on Pt/Al_2O_3 as a function of Pt dispersion [30].

Since the TOF at 120 and 160°C was almost identical in the entire range of Pt dispersion, all the Pt atoms located at face, corner and edge sites would be the catalytically active sites for CO oxidation on supported Pt catalysts [30]. In other words, although Pt dispersion was changed, the fact that almost steady TOF values were obtained for CO oxidation on Pt/Al_2O_3 suggests that surface electronic state of Pt particles is almost identical as catalytically active sites for CO oxidation.

On the other hand, Joo et al. [31] studied the effect of Ru nanoparticle size on CO oxidation. They prepared six Ru nanoparticles sizes of the range 2.1 - 6 nm and found out that CO turn over frequency increased as Ru nanoparticle size increased as shown in Fig. 2-9.

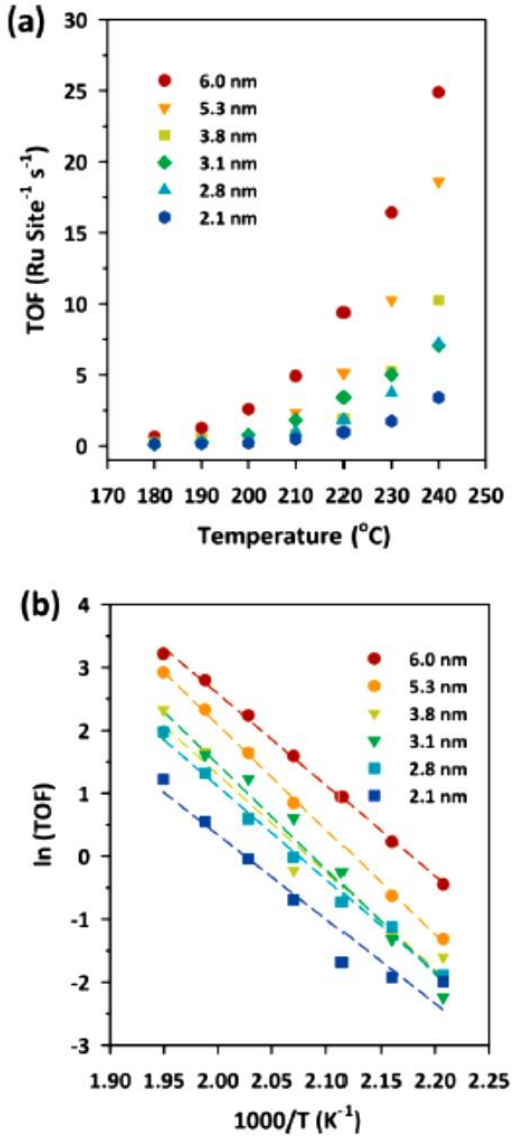

Figure 2-9: CO oxidation activity on Ru NPs: (a) change of CO oxidation activity with temperature and (b) Arrhenius plots for CO oxidation [31].

The origin of size dependence of CO oxidation rate over Ru nanoparticles have been attributed to various factors, including structural effects, electronic effects, metal-support interactions, and presence of an active surface oxide layer. Particularly, the role of the surface

oxide layer surrounding the metal core has been suggested as the catalytically active species, which was identified by advanced *in-situ* analytical techniques [31]. The authors conclusion is in agreement with number of studies reported previously by Assmann et al. who investigated active species and structural deactivation behavior of various types of Ru catalysts in bulk single crystals [32], polycrystalline micrometer-scale powders [33] and in supported nanoparticles [34]. The summary of their findings indicate that under oxidizing reaction conditions, the metallic Ru surface converts to a catalytically active thin ruthenium oxide layer. They claimed that the stability of the core-shell structure where the catalytically active RuO_2 shell layer is formed on the Ru metallic core is controlled by kinetics. An active oxide layer on the Ru single crystals or reduced RuO_2 powder is maintained under oxidizing conditions whereas such an active oxide on the supported Ru NPs is unstable, which indicates that the stability of catalytically active oxide layer appears to increase with the size of Ru catalysts. Therefore, it is reasonable that the stability of Ru NPs changes in a similar manner suggested by Assmann et al. studies that smaller Ru NPs would be subject to a higher degree of oxidation than larger ones, thus exposing a larger portion of catalytically inactive species on their surfaces. Consequently, the stability of Ru NPs can be correlated with the size dependence found in Joo et al. study [31]. By contrast, CO oxidation showed opposite trend of size dependence with Pt [35] and Ir [36] nanoparticles with more studies needed over Pt nanoparticles to investigate size effect.

2.3.2 Heterogeneous catalysis on platinum group nanoparticles for ethylene oxidation

Ethylene is a low molecular weight volatile organic compound (VOC) and is considered as a harmful molecule that contributes to photochemical pollution. Moreover, complete ethylene oxidation is of specific interest due to the global need to decrease the hydrocarbon content of stationary and automotive emissions [37]. The mechanism of ethylene oxidation on Pt metal group surfaces is well studied and it is found to follow Langmuir-Hinshelwood mechanism.

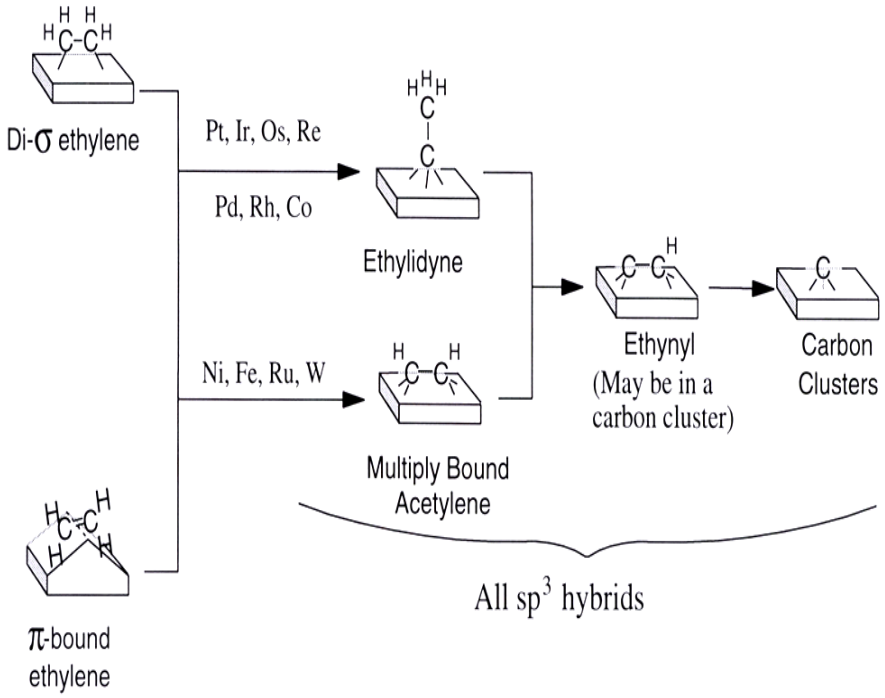

Figure 2-10: The mechanism of ethylene decomposition on different transition metals (After Yagasaki and Masel [1994]).

Very few studies are published for ethylene oxidation. One of the early studies was reported by Pliangos et al. [38] where they chose the case of ethylene oxidation to study induced metal-support interaction effects on the activity of automotive exhaust catalyst. Various degrees of metal-support interaction was observed when catalysts of combinations of one of three metals, Pt, Pd or Rh supported on five different supports, that is, SiO_2, γ-Al_2O_3, YSZ, TiO_2 or TiO_2 (W^{6+}) were studied for ethylene complete oxidation at atmospheric pressure in the temperature range of 150 - 500^oC. Figure 2-11 shows the turnover frequency of the fifteen catalysts understudy at 320^oC.

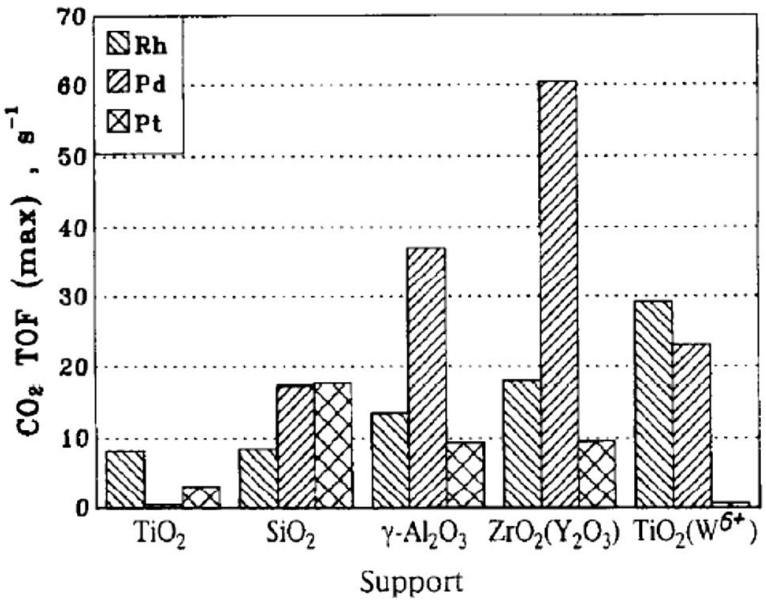

Figure 2-11: Comparison of the turnover activity of the fifteen model catalysts investigated for ethylene oxidation reaction at 320°C [38].

Comparison of the activity results presented above reveals generally that Pd-supported catalysts have higher activity compared to Rh and Pt for this reaction. On the other hand, the best supports for the three different metals were TiO_2 (W^{6+}) for Rh, YSZ for Pd and SiO_2 for Pt. These conclusions marked important for the development of improved automotive exhaust catalytic converters [38]. The turnover frequency variation was attributed to the metal-support interaction between the metal and the carrier. In the case of TiO_2 (W^{6+}) for Rh, YSZ for Pd being the best supports, it is suggested that strong metal-support induced back spillover of oxygen ions (O^{2-}) originating from the carrier to the metal surface which is responsible for the improved catalytic activity of the overall catalysts. In fact, supports like TiO_2 (W^{6+}) and YSZ are known in the literature to have significant oxygen storage capacity [39] that gives higher turnover frequency for hydrocarbon oxidations. On the other hand, in the case of Pt, SiO_2 was the best support since it has the highest surface area which improved Pt dispersion and hence enhanced the catalyst for ethylene oxidation which is known to be structure sensitive over Pt metal [40][41]. Deihl et al. [42] studied catalytic oxidation of ethylene over 1 wt. % Pt nanoparticles (1 nm) deposited on aluminum oxide (Al_2O_3) to study the molecule structure effect on its reactivity in the temperature range of 100 - 400°C. They compared structure reactivity relationship in alkanes and alkenes and concluded as reported earlier in literature,

that contrary to alkanes, alkenes adsorption on Pt does not require a preliminary C–H bond cleavage. Alkenes can adsorb via π- bonding between the C=C bond and the platinum atoms [43][44]. The second step is the transformation of this π-coordinated alkene-Pt species into a di-σ species which leads to C–C bond scission and reaction with adsorbed oxygen.

It is worth mentioning that there is scarcity in studies related to C_2H_4 oxidation on Ru nanoparticles (being ten times less expensive than Pt) which will be one of the targets studied in this research.

2.3.3 Heterogeneous catalysis on platinum group nanoparticles for hydrogen stream purification from carbon monoxide impurities

Fuel cells are considered to be one of the promising technologies for efficient power generation. A variety of fuel cells have been developed in the past 170 years [45][46]: solid polymer fuel cells (SPFC), also known as proton-exchange membrane fuel cells (PEMFC) operating at 80^{o}C, alkaline fuel cells (AFC), operating at 100^{o}C, phosphoric acid fuel cells (PAFC) for 200^{o}C operation, molten carbonate fuel cells (MCFC) at 650^{o}C, solid oxide fuel cells (SOFC) for high temperature operation, 800-1100^{o}C. Except for the case of direct methanol fuel cells, the ideal fuel for these fuel cells is hydrogen with less than 50 ppm CO as impurity to avoid poisoning of Pt fuel cell catalyst [46].

PEMFC have attracted significant interest due to their low temperature of operation (80^{o}C), high power density, high efficiency, easy start up and the environmentally benign nature of their exhaust. Therefore, several studies are devoted to investigate PEMFC as a clean and efficient alternative to combustion of fuels for power generation in stationary and mobile applications [45][47].

The anode in PEMFC operating at low temperatures (80 - 100^{o}C) can be easily poisoned by traces of CO in the hydrogen-rich fuel feed. Therefore, it is critical to remove CO at low temperatures with minimum loss of hydrogen [48][49][45]. Several methods for CO removal from the hydrogen stream have been reported [45]:

i) Purification with hydrogen selective membrane,

ii) CO methanation,

iii) Pressure swing adsorption, and

iv) Preferential oxidation of CO (PROX).

All the above mentioned methods have their advantages and disadvantages, though among them, CO methanation is one of the most promising processes to remove small amounts of CO for the following reasons:

a) CO methanation does not require addition of oxygen (air) as the case in PROX. Addition of oxygen has its own disadvantages causing dilution, adding safety restriction and reducing hydrogen yield.

b) methane produced is inert to the fuel cell and can be used in the afterburner [50].

The selective CO methanation process (mainly eq. 2.4) includes the following reactions [45][51]:

$$CO + 3H_2 \rightarrow CH_4 + H_2O \qquad \Delta H^o_{298} = -206.2\ kJ{\cdot}mol^{-1} \qquad (2.4)$$

$$CO_2 + 4H_2 \rightarrow CH_4 + 2H_2O \qquad \Delta H^o_{298} = -164.9\ kJ{\cdot}mol^{-1} \qquad (2.5)$$

$$CO + 1/2O_2 \rightarrow CO_2 \qquad \Delta H^o_{298} = -283.6\ kJ{\cdot}mol^{-1} \qquad (2.6)$$

$$H_2 + 1/2O_2 \rightarrow H_2O \qquad \Delta H^o_{298} = -243.5\ kJ{\cdot}mol^{-1} \qquad (2.7)$$

$$CO_2 + H_2 \rightarrow CO + H_2O \quad (RWGS) \qquad \Delta H^o_{298} = 41.1\ kJ{\cdot}mol^{-1} \qquad (2.8)$$

However, current PROX systems operate at high temperatures (150 – 250^{o}C) and require the use of oxygen in order to oxidize CO to CO_2; this results in undesirable reaction of oxygen with hydrogen (eq. 2.7) and increase in reactor volume [47][49]. Therefore the development of an efficient and highly selective CO methanation catalytic systems with minimum O_2 concentration in the H_2 + CO mixture is imperative [52][49][53][54].

Methanation of CO over various metal catalysts has been widely investigated from the view point of synthesizing methane from syngas [55] and recently also for the purpose of residual CO removal for PEMFC applications [50][56][51]. Galletti et al. [51] studied the

effect of different loadings of Ru nanoparticles (3, 4 and 5 wt. %) supported over γ-Al_2O_3 for complete CO methanation in the temperature range of 180 - 440^{o}C. The results in Fig. 2-12 show that Ru/γ-Al_2O_3 is an active catalyst for CO methanation but at elevated temperatures, higher CO concentration is observed due to the reverse water gas shift reaction (eq. 2.8) which is thermodynamically favoured at higher temperature.

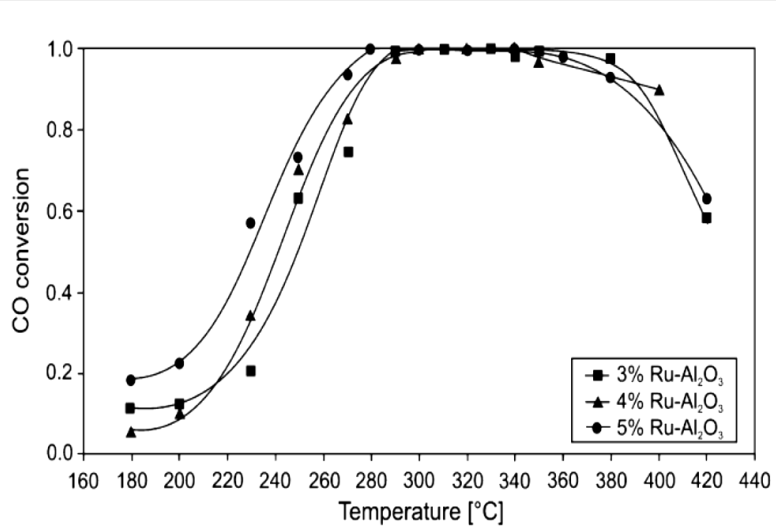

Figure 2-12: CO conversion vs. temperature for Ru-based catalysts on Al_2O_3 with different Ru loads [51].

Therefore, it is essential to study CO methanation at low temperature to avoid driving (eq. 2.8) forwards and under the lowest possible concentration of oxygen in the gas feed to avoid the loss of hydrogen through (eq. 2.7). This target is one of the main objectives of our research in this dissertation.

2.4 Classical promotion in heterogeneous catalysis

The performance of real industrial catalysts is often adjusted by modifiers (additives) [57][58]. A modifier is called a promoter when it increases the catalyst activity in terms of reaction rate per site. Modifiers may also affect a catalyst's performance in an undesired manner. In this case, the modifier acts as a catalyst poison. Promoters play a key role in heterogeneous catalysis and they can be divided mainly into structural promoters and electronic promoters [59][60]. Structural promoters enhance and stabilize the dispersion of the active phase on the catalyst support, while electronic promoters enhance the catalytic

properties of the active phase itself [59]. This is due to their ability to modify the chemisorptive properties of the catalyst surface and to significantly affect the chemisorptive bond strength of reactants and intermediates. As an example, the iron-based ammonia synthesis catalyst is promoted by alumina (Al_2O_3) and potassium oxide (K_2O). Alumina acts as a textural promoter, as it prevents the rapid sintering of pure iron metal. It may also act as a structural promoter by stabilizing more active sites on the iron surface. Potassium oxide, on the other hand, affects the adsorption kinetics and dissociation of dinitrogen and the binding energy of nitrogen on adjacent iron sites, hence acts as an electronic promoter [61].

In a recent study to investigate the influence of different promoters (Fe, Cu and Ce) on the catalytic activity of high performance palladium nanoparticles supported on purified attapulgite clay (Pd/PATP) for CO oxidation, Pd-Fe/PATP was found to have superior activity compared to the other two promoted catalysts under the same conditions. Figure 2-13 compares of the activity of these catalysts as per this study [62].

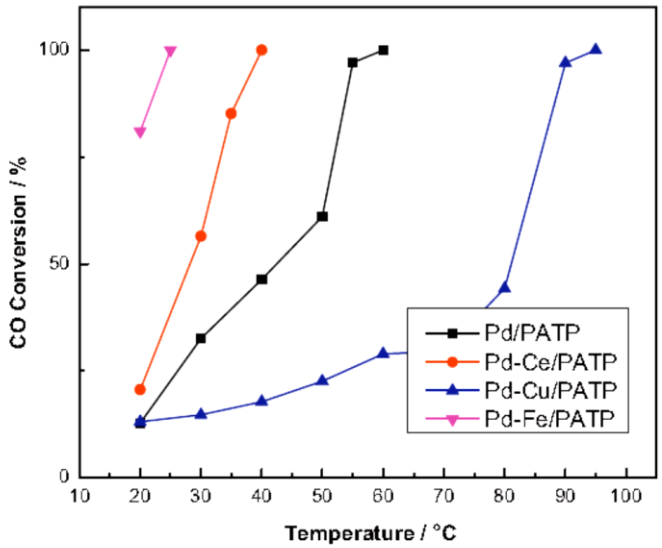

Figure 2-13: The effect of promoter type on CO oxidation [62].

Characterization of the four catalysts showed that Pd-Fe/PATP catalyst had the highest Pd dispersion and the minimum Pd size which are all factors conducive to CO oxidation reflected by full conversion of 1% CO at 25^{o}C over Pd-Fe/PATP. The authors further investigated the effect of Fe loading with four different values (3, 5, 10 and 15 wt. %) and found that the best catalyst was the sample with 10 wt. % Fe loading. They used x-ray

diffraction (XRD) and hydrogen temperature-programmed reduction (H_2-TPR) characterization to explain the promoting effect of Fe added for CO oxidation. XRD patterns showed the appearance of FeO(OH) peaks in the Fe-loading 10 wt. % sample, at $2\theta = 18.9^o$ and 27.7^o, respectively, corresponding to the (0 0 2) and (3 0 1) faces. When the Fe loading amount was 3 wt. %, 5 wt. % and 15 wt. %, the peaks of FeO(OH) had not appeared. That indicated that FeO(OH) species were the actual promoting species that enhanced the catalytic activity for CO oxidation. Moreover, The H_2-TPR traces showed a reduction peak of Pd oxide at 100^oC and a peak of Fe_2O_3 reduction at 462^oC in the 3 wt. % sample. As the Fe loading increases, the reduction peaks of Pd and Fe_2O_3 oxidation moved towards higher temperatures, but as the wt. % content reached 10 wt. %, an additional reduction peak for the intermediate product of Pd-Fe-PATP catalyst (beside Pd oxide and Fe_2O_3) was detected in the range of 200 - 250^oC which disappeared when Fe loading was 15 wt.%. This peak was ascribed to the reduction of weakly chemical-adsorbed oxygen which was more active and more easily reduced by hydrogen than the lattice oxygen of Fe_2O_3. So the weakly chemical-adsorbed oxygen was very important to enhance the activity of Pd-Fe/PATP catalysts due to which, the catalyst with 10 wt.% Fe loading had the highest activity [62].

In a study directly related to the effect of mixed oxides as promoters to the TWC catalysts in advanced automotive de-pollution applications, Kaspar et al. [63] reported a detailed review of the promotional effect of CeO_2-ZrO_2 mixed oxides utilized in catalytic converters. The main characteristic of CeO_2–ZrO_2 mixed oxides in current TWCs is the so-called oxygen storage/release capacity. The oxygen storage capacity (OSC) is the ability of CeO^{2-} containing oxides to adsorb and release oxygen under fuel-lean and fuel-rich conditions, respectively according to the reaction:

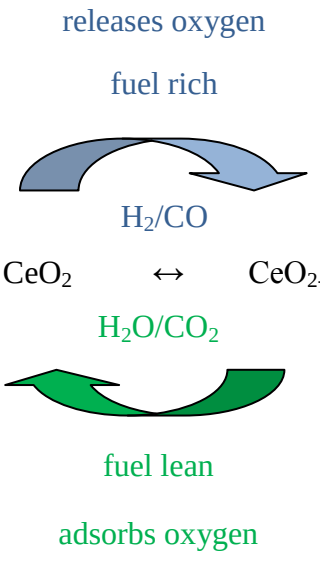

(2.9)

The OSC is a crucial property of the TWCs since it helps to cope with the air-to-fuel oscillations and maintains a stoichiometric composition of the exhaust at the noble metal catalyst to achieve the highest exhaust conversions. Deactivation of the TWCs by the loss of OSC property is largely recognized due to ageing at high temperatures, which leads to sintering of the OSC component. Thermal stabilization of the OSC component is therefore a major objective for developing advanced TWCs. Two factors were studied and found to be effective in stabilization of CeO_2-ZrO_2 mixed oxides for TWC catalyst, namely: the proper design of pore structure and the addition of Al_2O_3. Samples with higher pore size distribution showed less surface area collapse after sintering at 1273K for 5 hours. On the other hand, given the importance of the textural stability for practical application of the CeO_2-ZrO_2 in the TWCs, the design of nanocomposites where the CeO_2-ZrO_2 phase is dispersed over a stable inert support could represent a suitable way to improve thermal stability of these systems. This could be achieved by the addition of Al_2O_3 which enhances the thermal stability up to 1373K and improves reduction behavior of CeO_2-ZrO_2 mixed oxides.

An example of an electronic promoter can be presented by a recent study by Wang et al. [64] on the effect of adding Fe to Pt nanoparticles for the catalytic hydrogenation of organic molecules. It was found that the catalytic hydrogenation of ethylene is drastically accelerated on the surface of 2 nm PtFe bimetallic nanoparticles compared to pure Pt. In particular, the PtFe nanoparticles showed ~3 times higher activity at 25^{o}C and considerably lower activation energy than the Pt nanoparticles with a similar size. Sum frequency generation (SFG) vibrational spectroscopy under reaction conditions showed that incorporation of Fe into Pt nanoparticle catalysts weakens the adsorption of ethylidyne, an inactive spectator species, on the catalyst surface due to an effect of electronic structure modification when Fe is added to Pt surfaces. Similarly, the turnover frequency of cyclohexene hydrogenation is also significantly enhanced by incorporating Fe into Pt nanoparticle catalysts due to the displacing of inactive reaction intermediates on the catalyst surface [64].

2.5 Metal-support interaction effect (MSI) of different supports

2.5.1 Basics and introduction to metal-support interaction mechanism

In the early days of catalysis, the porous and high surface area support was thought to be inert. However, recently it became apparent that the catalytic activity depends on the catalyst crystallite size (referred to as the particle size effect) and the material of the supports (referred to as metal-support interaction). The particle size effect is pronounced for structure sensitive reactions where the rate is significantly different from one crystallographic plane to another. This type of reactions frequently occurs on catalytic sites consisting of surface atoms with specific geometry. Therefore, it is reasonable to expect different distribution of crystallographic planes as the crystallite size decreases, which affects the activity and selectivity of the catalyst. On the other hand, structure insensitive reactions (most hydrogenations and some oxidations) are less affected by dispersion or particle size effects.

The second phenomenon, i.e. metal support interaction, was first introduced by Tauster et al. [65]. This concept is well observed when the active phase has the same dispersion or average crystallite size on different supports. In this case, the support has a dramatic effect on the activity and selectivity of the active phase changing its catalytic activity in a very pronounced way.

Factors that affect the form and degree of metal-support interaction include the content of precious metal [66][67][68][69], the nature of support [69][70][71] and catalyst preparation methods [72][73]. Most reports in this field studied the metal-support interaction of metals on one support with different conditions such as Rh/-, Pt/- and Au/TiO_2 [74][75], Pt/C with different carbon materials [76][77], Pt/SnO_2 [78] and Pt/Al_2O_3 [79]. However, very few studies were conducted to investigate and compare ionic and mixed ionic conducting with non ionic conducting supports on the metal-support phenomenon [80].

Metal-support interactions have been classified into three main categories depending on the nature of the support [81]:

i- weak metal-support interaction (WMSI), generally accepted between metals and oxides such as SiO_2, Al_2O_3, carbon and graphite,

ii- medium metal-support interaction (MMSI), in the case of small metals supported on zeolites,

iii- strong metal-support interaction (SMSI), predominant in the case of metals supported on certain reducible oxides such as TiO_2 and V_2O_5.

SMSI was observed with considerable effects on the catalyst activity when Group VIII metals (platinum, iridium, palladium, rhodium, osmium and ruthenium) were deposited on reducible or partially reducible supports. Therefore, several models were proposed to explain the effect of metal-support interaction catalysts properties. Generally, the changes in the catalytic activity are ascribed to modification of the electronic properties of the metal particles. Electron transfer between the support oxygen atoms and the nearby metal particles is thought to increase the electron density on the metal particles [82]. The charge is transferred from the solid with the lower work function to the solid with the higher work function, hence modifying the catalyst activity. One of the early related articles published in Science reported that Tauster et al. [81] used molecular orbital and spectroscopic studies to show that the changes in chemisorptive, catalytic, and structural properties strongly suggest an electronic interaction at the metal-oxide interface due to SMSI. The dominant interaction, however, was found to be an ionic attraction as the result of a charge transfer from the reduced cation to the adjacent metal atom.

Recently, Fu and Wagner [83] summarized in their review the basic concepts for quantifying the electronic interaction at the metal/oxide interfaces and comparing them to the well-developed theories and calculation methods in this field. To further understand solid-gas phase reactions, the redox reaction at the metal/oxide interfaces was investigated with emphasis on the dependence of the reaction on the electronic structure of both the metal and the oxide [84][85]. In one of Fu and Wagners' previous works, the model system Pd/TiO_2 was used to evaluate the charge transfer between both solids. It was found that the charge transfer is induced from the support to the metal which has higher work function as shown in Fig. 2-14 [86].

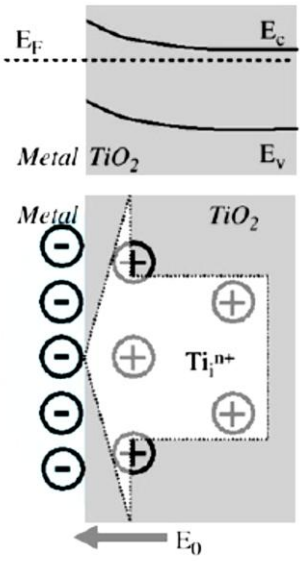

Figure 2-14: Upper panel: Schematic diagram showing the energy bands of a metal–TiO_2 interface in the case of work function of (Metal) > work function of TiO_2. Lower panel: Positive space charges at TiO_2 surface regions and the electric field E_0 produced by the interfacial charge transfer process, promoting the outward diffusion of Ti interstitial ions, Ti^{n+} (n < 4) [86].

2.6 Ionic conductive and non ionic conductive supports of metal catalysts

Metal heterogeneous catalysts are composed of two major components: the active metal particles and the support. The support is not only a carrier for active catalyst compounds but also can improve the dispersion of precious metals and suppress the sintering of precious metals at high temperatures as shown previously [7]. Typical supports used in catalysis can be classified as ionic conductive or mixed ionic conductive such as samarium-doped ceria (SDC) and titanium oxide (TiO_2), respectively and non-ionic conductive supports such as alumina (Al_2O_3), silica and carbon [87][88]. The term solid electrolyte, also referred to as fast ionic conductor or sometimes super ionic conductor, is used to describe solid materials whose conductivity is wholly due to ionic displacement. Ionic conductive supports play a significant role in the present and future applications. There are many commercial uses of these ceramics such as in sensor technology, batteries, solid oxide fuel cells (SOFC) and as supports in catalysis [87].

The classification of solid electrolytes is usually based on the ion mainly responsible for the conductivity. Some of them are:

- oxygen ion (O^{2-}) conductors such as yittria-stabilized zirconia (YSZ) that are widely used in oxygen sensors in the temperature range of 400 - 1200^{o}C,
- Na^{+} conductors such as β"-aluminas which exhibit high conductivity in the range of 150 – 300^{o}C,
- F^{-} conductors such as PbF_2 which are conductive at 500^{o}C [59].

Wagner was the first to propose the use of solid electrolytes in heterogeneous catalysis for the measurement of oxygen activity on metal and metal oxide catalysts in 1970 [89]. In oxygen ion conductive solid electrolytes, the ionic conductivity is induced by the addition of a lower-valent cation which is charge-compensated by the formation of oxygen vacancies. These oxygen vacancies are highly mobile at elevated temperatures. More details of some conventional, ionic conductive and mixed ionic conductive supports used in this research are herein presented:

2.6.1 Aluminum oxide

Aluminum oxide (Al_2O_3), or alumina is one of the most versatile ceramic oxides, as it is used in a wide range of applications. It is found in nature in topaz, amethyst, and emerald. On the commercial scale, alumina is extracted and purified from the more abundant ores such as bauxite and clays. It is the close packing of the aluminum and oxygen atoms within this structure that leads to its good mechanical and thermal properties.

Table 2-1: Properties of Alumina [90].

Property	**Value**
Grain size, μm	1-5
Density, g/cm^3	3.95
Thermal Conductivity at 20^{o}C,W·m^{-1}·K^{-1}	30-40
Melting point, ^{o}C	2072
Specific surface area, m^2/g	120

Nanocrystalline gamma-phase (γ) alumina is among many poly types of alumina that find extensive applications as a catalyst support. The most useful properties these aluminas provide as catalyst supports are high surface area compared to ionic and mixed ionic conductors and well defined porosity [91].

2.6.2 Carbon black

To date, three forms of carbon are used as supports for precious metal catalyst to provide optimum properties and performance for different applications in the chemical industry. The most important carbon support material is activated carbon, followed by carbon black and graphite materials [92]. Precious metal on carbon catalysts are mainly used in liquid phase hydrogenation, dehydrogenation, or oxidation reactions in the fine chemicals area [93]. Carbon blacks are manufactured by the pyrolysis of hydrocarbons such as natural gas or oil fractions from petroleum processing. The high specific surface area of carbon black (254 m^2/g) is probably its most important advantage for being used as a support. It enhances the dispersion of metal catalyst, which is a significant factor for volatile organic compound oxidations due to structure sensitivity of these reactions.

Table 2-2: Properties of carbon black Vulcan XC-72 [94].

Property	Value
Melting point, ^oC	3550
Density, g/cm^3	1.7-1.9
Particle size, nm	30-60
Specific surface area, m^2/g	254

2.6.3 Cerium oxide

Cerium (IV) oxide is a mixed ionic conductor ceramic used as a catalyst support because of its relatively high ionic conductivity [95]. The widespread interest in the catalytic properties of ceria results from its application in automotive catalysis being able to be oxidized and reduced providing high oxygen storage capacity [87]. In the doped form, ceria is of interest as a support in heterogeneous catalysis as well as in solid oxide fuel cells due to its

extended electrolytic region (area of predominant ionic conductivity), over that of pure ceria. Substituting a fraction of the ceria with gadolinium or samarium introduces oxygen vacancies in the crystal which results in a better electrolyte.

Table 2-3: Properties of CeO_2.

Property	Value *
Melting point, °C	2600
Density, g/cm^3	7.132
Conductivity at 830°C, mS/cm	24.18
Specific Surface Area, m^2/g	30-40

*Fact sheet from supplier.

Figure 2-15 shows that the ionic conductivity of ceria and ceria-based electrolytes is higher at lower temperatures (500 - 700°C) in comparison with yittria-stabilized zirconia (YSZ).

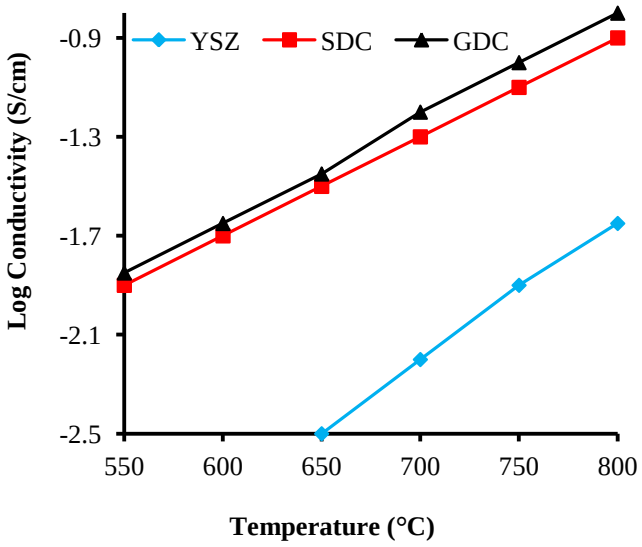

Figure 2-15: Ionic conductivity of samarium-doped (SDC) and gadolinia-doped (GDC) ceria compared to YSZ.

2.6.4 Perovskite-based mixed ionic conductors

The first perovskite material was discovered in the 1830's by the geologist Gustav Rose, who named it after the Russian mineralogist Lev Perovski [96]. In general, a perovskite-type oxide has an ABO_3 crystal structure wherein cations with a large ionic radius have twelve

coordination to oxygen atoms and occupy A-sites, and cations with a smaller ionic radius have six coordination and occupy B-sites as shown in Fig. 2-16. The catalytic properties of perovskites can be tuned by varying atom A or B or by insertion of dopings in their structure and they have been widely used in heterogeneous catalysis as electrodes and electrolytes [87][97][98].

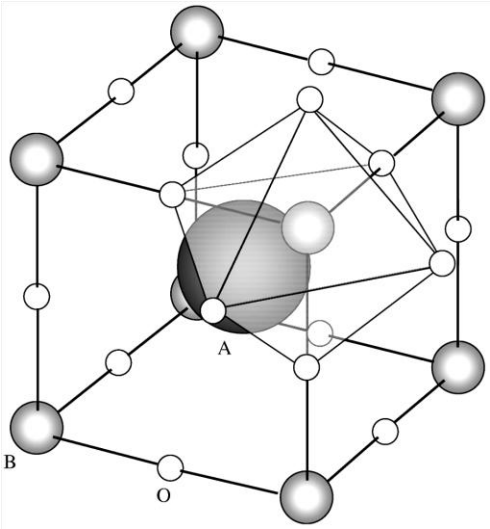

Figure 2-16: Structure of perovskite (ABO_3) [96].

2.6.5 Yttria-stabilized zirconia

Yttria-stabilized zirconia (YSZ) is a zirconium-oxide based ceramic, in which the particular crystal structure of zirconium oxide is made stable at room temperature by an addition of yttrium oxide. These oxides are commonly called "zirconia" (ZrO_2) and "yttria" (Y_2O_3), hence the name. The addition of yttria to pure zirconia replaces some of the Zr^{4+} ions in the zirconia lattice with Y^{3+} ions. This produces oxygen vacancies, since three O^{2-} ions replace four O^{2-} ions as shown in Fig. 2-17. It also permits yttria-stabilized zirconia to conduct O^{2-} ions, provided there is sufficient vacancy site mobility, which is a property that increases with temperature. This ability to conduct O^{2-} ions makes YSZ well suited to be used in solid oxide fuel cells, although it requires that they operate at high enough temperatures, usually above 600^{o}C.

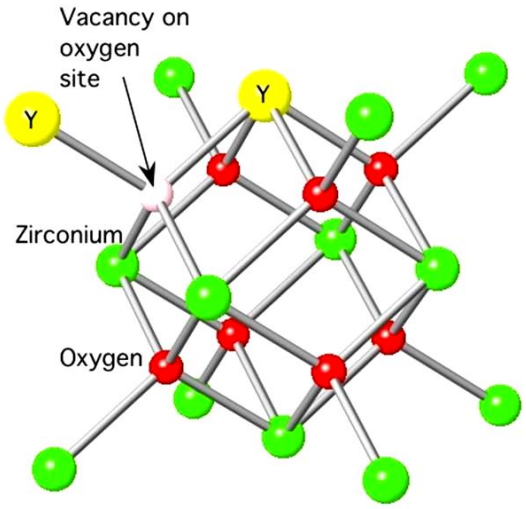

Figure 2-17: Oxygen vacancies in the cubic zirconia lattice [99].

Recently, YSZ has received attention as a catalytic support especially in studies of Electrochemical Promotion of Catalysis (EPOC) also called NEMCA (Non Faradaic Electrochemical Modification of the Catalytic Activity) effect [59] which will be explained in details in the following sections. Nevertheless, YSZ was not utilized efficiently as a support in heterogeneous catalysis which is one of the main scopes of this work.

Table 2-4: Properties of YSZ (8% Y_2O_3) [100][101].

Property	Value
Melting point, ^oC	2680
Density, g/cm^3	6
Conductivity at 300^{o}C, mS/cm	0.418
Specific surface area, m^2/g	13

2.7 Electrochemical promotion of catalysis (EPOC)

2.7.1 Definitions and basic quantities

The electrochemical promotion of catalysis (EPOC) is one of the most interesting discoveries in electrochemistry that has great impact on catalysis, especially in the field of heterogeneous catalysis. EPOC was first reported by Vayenas group in the early 1980s and has made a strong impact on modern electrochemistry and surface science [102]. This

phenomenon states that the catalytic activity of conductive catalysts deposited on solid electrolytes can be altered in a very pronounced, reversible and to some extent, predictable manner by applying small electrical currents or potentials (up to ±2V) between the catalyst and a second electronic conductor (counter electrode) also deposited on the solid electrolyte [103–105].

EPOC has been shown with more than 80 different catalytic systems, but in the last decade, it focused on the following four main areas [103]:

i- catalytic reactions with environmental impact, such as the oxidation of light hydrocarbons and reduction of NOx.

ii-mechanistic studies on the origin of EPOC using mainly oxygen ionic conductors

iii-scale up studies of EPOC for potential commercialization via the development of novel reactor designs

iv- application of EPOC in high or low temperature fuel cells

The basic experimental setup and operating principles used to investigate EPOC are shown in Fig. 2-18 in the case of ethylene oxidation. Platinum nanoporous metal catalyst electrode, typically 40 nm to 4 μm thick, is deposited on 8 mol% Y_2O_3-stabilised-ZrO_2 solid electrolyte [104]. In a typical EPOC experiment, the electrochemical cell can be represented by:

Gaseous reactant (working electrode)	catalyst	solid electrolyte	counter electrode	auxiliary gas
(e.g. C_2H_4+O_2)	*(e.g., Ru,etc)*	*(e.g. YSZ an O^{-2} conductor)*	*(e.g. Au)*	*(e.g. He)*

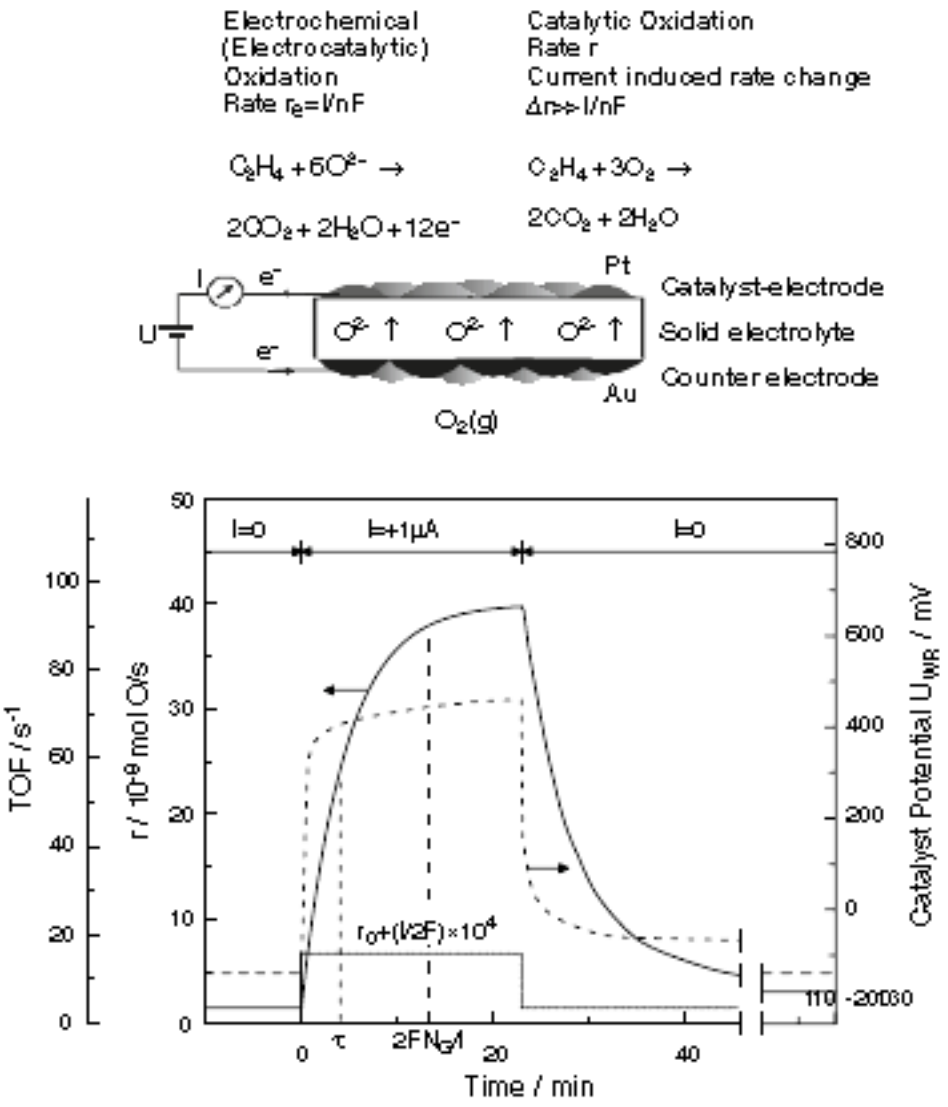

Figure 2-18: Basic experimental setup of EPOC and results for ethylene oxidation over platinum film deposited on yttria-stabilized zirconia ionic conductor [103].

There are two common parameters that quantify the magnitude of (EPOC):

1- The apparent Faradaic efficiency, Λ

$$\Lambda = \Delta r / (I/nF) \qquad (2.\ 10)$$

where Δr is the change in the catalytic reaction rate, I is the applied current, n is the charge of the applied ion and F is Faraday's constant [59].

2- The rate enhancement, ρ

$$\rho = r / r_o \qquad (2.\ 11)$$

where r is the electro-promoted catalytic rate and r_o is the unpromoted (open circuit) catalytic rate [59]. The whole electrochemical promotion process is related to the spillover-backspillover phenomenon which will be discussed in the following section.

2.7.2 Spillover –backspillover phenomenon

The effect of spillover-backspillover plays an important role in the electrochemical promotion of catalysis. Spillover is the migration of one or more species from the dispersed catalyst (e.g. Pt) to the support (e.g. YSZ) while backspillover is the migration of (O^{2-}) ions from the support to the metal catalyst. In the case of O^{2-} conductor supports, a general reaction scheme of oxygen spillover proposed by Delmon, Block and coworker [106] in catalytic systems is as follows:

$O_2 + 2D \longrightarrow 2O.D$	production of spillover O on donor D	(2. 12)
$2O{\cdot}D \longrightarrow O_2 + 2D$	recombination of O_2	(2. 13)
$A + O{\cdot}D \longrightarrow D + O{\cdot}A$	transfer of O between donor D and acceptor A	(2. 14)
$O{\cdot}A + B \longrightarrow C$	formation of active site C	(2. 15)
$R + C \longrightarrow P$	deactivation of active site C by reaction with R	(2. 16)

The term backspillover of the species migration from the support to the catalyst is used to distinguish it from the common spillover term used in catalytic systems to depict the migration of species in the opposite direction. These new species induced electrochemically onto the catalyst surface will change the catalytic properties of the catalyst surface, and even a seemingly inert material will acquire catalytic activity. Spillover, on the other hand, not only can improve the catalytic activity of the catalyst, but it can also increase the lifetime of that catalyst. This effect is induced through the formation of the effective double layer on the gas exposed catalyst surface [103].

According to EPOC, the backspillover species arriving at the three-phase boundary (tpb) migrate over the entire gas-exposed catalyst electrode surface (spillover) followed by either desorption to the gas phase or reaction with the co-adsorbed species. Recently, the

spreading of the backspilledover species was imaged by photoelectron emission microscopy (PEEM) on a dense Pt (111) thin film as shown in Fig. 2-19.

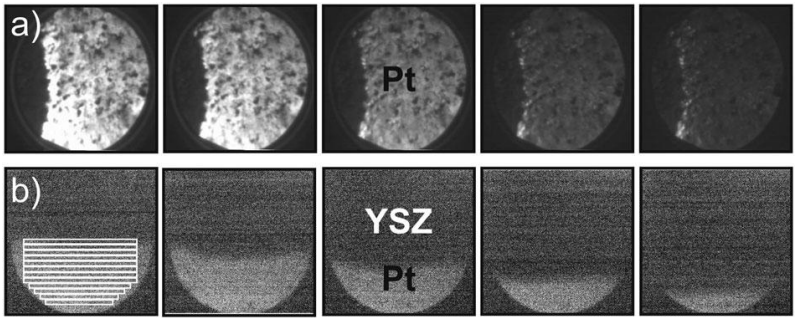

Figure 2-19: Sequence of PEEM images during polarization (a) Pt paste electrode (b) thin film Pt (111) electrode, field of view where grey level intensities extracted are shown as stripes [107].

2.8 Self-induced EPOC on platinum nanoparticles with ionic conductors

A major issue that faced the scientific community of EPOC was the thickness and morphology of the catalyst electrode. There has been a basic question on the suitable thickness of the electrode for an optimum behavior under electro-promoting conditions. The required low cost of the working electrode, together with the maximum dispersion leads to the utilization of nanoparticles instead of film catalysts.

The terminology "self-induced EPOC" was first proposed by Vernoux et al. [108] for the metal-support interaction phenomenon when the support is an ionic or mixed ionic conductor. The similarity between EPOC and metal-support interaction which will be discussed in the following section, is that in the former, electron transfer is induced between the catalyst and a counter electrode by applying electric polarization, while in the latter; the charge migration is induced thermally without any electrical polarization. Recently, Vernoux et al. [109] conducted a series of experiments (mainly temperature-programmed desorption experiments) to investigate the induced thermal migration of ionic species from the support towards the surface of the catalyst nanoparticles on Pt/YSZ under different conditions. The catalytic performance of these catalysts for propane deep oxidation were compared under various thermal pretreatments to show the effect of thermally induced backspillover of O^{2-} ionic species on catalytic performance.

The Pt nanoparticles were synthesized by impregnation and were deposited on YSZ to yield a 2.2 wt. % loading. To confirm the backspillover of the oxygen coming from the ionic conductive support, the authors adsorbed O_2 on the fresh Pt/YSZ and recorded 2 distinct oxygen peaks, which is unusual. This was compared with the single O_2 peak spectra when Pt is deposited on non-ionic conductive supports such as silica or alumina. Therefore, the authors attributed the first peak to gaseous oxygen adsorption and the second one to the electro-migrating $O^{\delta-}$ species. Furthermore, the area of the second peak was found to increase with the current intensity if a current was applied, confirming its relation with ionic oxygen species back spilled from the conductive support. This thermally induced migration of O^{2-} ionic species from YSZ to the Pt surface strongly promoted propane combustion which is in good agreement with previous EPOC experiments which confirmed that O^{-2} ionic species are effective promoters for alkane deep oxidation [110][111].

Numerous studies were conducted using surface spectroscopic and electrochemical techniques to prove that the backspillover is thermal in the case of metal-support interaction and electrochemically-assisted in the case of EPOC [59][111].

2.8.1 Experimental confirmation of the similarity between MSI and EPOC

Three independent systems were used by Nicole et al. to show that the mechanism of metal-support interaction is equivalent to EPOC [111]. In their work, ethylene oxidation on IrO_2, Pt and Rh was used as a model reaction to compare the rate enhancement and kinetic modification induced by:

(i) electrochemical promotion (EPOC) via electrochemical O^{2-} supply from YSZ and TiO_2 , and by

(ii) metal–support interactions obtained by interfacing IrO_2 with TiO_2 (with and without electrochemical promotion), or by

(iii) depositing dispersed Rh on TiO_2 and YSZ porous supports.

It was found that the addition of TiO_2, which is catalytically inactive, to IrO_2 sub-micrometer particles (which are moderately active for C_2H_4 oxidation) enhances the activity of IrO_2 for C_2H_4 oxidation by a factor of 12, and that the same maximum rate enhancement is obtained via electrochemical promotion of the IrO_2 catalyst (i.e., via electrochemical O^{2-}

supply to the IrO_2 catalyst from a YSZ solid electrolyte). Furthermore it was found that the IrO_2–TiO_2 catalyst mixtures can only be marginally promoted electrochemically.

These observations show conclusively that the mechanism of metal (IrO_2) – support (TiO_2) interaction in the system IrO_2–TiO_2 is identical to that of the electrochemically promoted IrO_2–YSZ system (i.e., continuous O^{2-} supply to the IrO_2 catalyst surface). In other words, the metal-support interaction between IrO_2 and TiO_2 can be seen as a "wireless" type of EPOC where TiO_2 continuously provides promoting O^{2-} species to the IrO_2 catalyst surface, and gaseous oxygen continuously replenishes spent O^{2-} in the TiO_2.

This conclusion is also supported by independent kinetic and x-ray photoelectron spectroscopy (XPS) of the electrochemical promotion of Pt utilizing TiO_2 (instead of YSZ) as the O^{2-} donor. The kinetics of C_2H_4 oxidation was investigated on Rh films interfaced with YSZ at various imposed potentials. The results show conclusively that electrochemical promotion is an *electrically-controlled* metal–support interaction and that at least certain types of metal–support interactions are induced by reverse spillover of oxygen anions from the support onto the surface of the metal crystallites as shown in Fig 2-20.

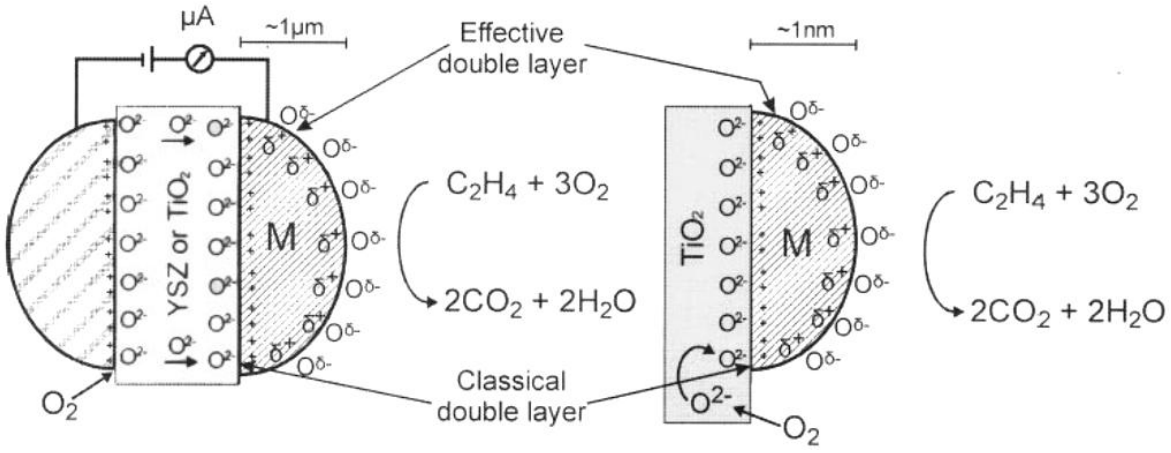

Electrochemical Promotion Metal-support Interaction

Figure 2-20: Schematic of a metal grain (~μm) in a metal catalyst film deposited on YSZ or TiO_2 under electrochemical promotion conditions (left), of a metal nanoparticle (~nm) deposited on a porous TiO_2 support (right) showing the locations of the classical double layers formed at the metal–support interface, and of the effective double layers formed at the metal–gas interface [111].

2.9 Conclusions

In summary, this chapter introduced the basic concepts in heterogeneous catalysts, electrochemical promotion of catalysis (EPOC) and discussed the similarity between EPOC and metal-support interaction. Main characteristics of the supports used in this research were summarized. The use of noble metal nanoparticles was highlighted as highly efficient and selective catalysts in various aspects of applications related to air pollution control. The new concept of self-induced EPOC introduced in 2009 as a type of metal-support interaction specifically with ionic or mixed ionic supports was introduced. The need to father investigate different factors affecting this phenomenon, i.e. particle size, type of support and operating conditions forms the frame to the goal of this thesis for the main application of these catalysts in vehicle exhaust catalytic converters and fuel cells to operate more efficiently at lower temperatures with the least noble metal content possible.

2.10 References

[1] B. R. Cuenya, *Thin Solid Films.* 518 (2010) 3127.

[2] R. Jin, *Nanotechnol. Rev.* 1 (2012) 31.

[3] G. A. Somorjai, K. McCrea, *Appl. Catal. A Gen.* 222 (2001) 3.

[4] G. A. Somorjai, Y. G. Borodko, *Catal. Letters.* 1 (2001) 76.

[5] J. A. Kurzman, L. M. Misch, R. Seshadri, *Dalton Trans.* 42 (2013) 14653.

[6] Q. Zhang, Y. Yin, *Pure Appl. Chem.* 86 (2014) 53.

[7] T. Zheng, J. He, Y. Zhao, W. Xia, J. He, *J. Rare Earths*. 32 (2014) 97.

[8] H. C. Zheng, *Acc. Chem. Res.* 46 (2013) 226.

[9] A. T. Bell, *Science.* 299 (2003) 1688.

[10] C. Burda, X. B. Chen, R. Narayanan, M. A. El-Sayed, *Chem. Rev.* 105 (2005) 1025.

[11] F. Garin, *Catal. Today.* 89 (2004) 255.

[12] L. Wang, M. Sakurai, H. Kameyama, *J. Hazard. Mater.* 167 (2009) 399.

[13] M. Daté, Y. Ichihashi, T. Yamashita, A. Chiorino, F. Boccuzzi, M. Haruta, *Catal. Surv. from Asia.* 72 (2002) 89.

[14] Volkswagen, Motor Vehicle Exhaust Emissions: composition, emission control, and standards., Wolfsburg, 2000.

[15] B. Harrison, A. Diwell, C. Hallett, Platin. *Met. Rev.* 32 (1988) 73.

[16] L. Liotta, A. Longo, G. Pantaleo, G. Di Carlo, G. Martorana, A. Cimino, S. Russo, G. Deganello, *Appl. Catal. B Environ.* 90 (2009) 470.

[17] H. Shinjoh, M. Hatanaka, Y. Nagai, T. Tanabe, N. Takahashi, T. Yoshida, Y. Miyake, *Top. Catal.* 52 (2009) 1967.

[18] C. -J. Jia, F. Schüth, *Phys. Chem. Chem. Phys.* 13 (2011) 2457.

[19] F. Garin, *Catal. Today.* 89 (2004) 255.

[20] M. Valden, *Science.* 281 (1998) 1647.

[21] C. Campblee, G. Ertl, H. Kuipers, J. Senger, *Surf. Sci.* 107 (1981) 207.

[22] T. Engel, G. Ertl, *Adv. Catal.* 28 (1979) 1.

[23] G. Ertl, *Surf. Sci.* 152-153 (1985) 328.

[24] M. Kawai, T. Onishi, K. Tamaru, *Appl. Surf. Sci.* 8 (1981) 361.

[25] G. Somorjai, *Appl. Surf. Sci.* 121 (1997) 1.

[26] A. Szabó, M. Henderson, J. T. Yates, *J. Chem. Phys.* 96 (1992) 6191.

[27] B. R. Shishu, *Platin. Met. Rev.* (1974) 58.

[28] M. Ehsasi, M. Matloch, O. Frank, J. H. Block, K. Christmann, F. S. Rys, W. Hirschwald, *J. Chem. Phys.* 91 (1989) 4949.

[29] A. K. Prashar, S. Maydevi, P. R. Rajamohanan, R. N. Devi, *Appl. Catal. A Gen.* 403 (2011) 91.

[30] M. Haneda, T. Watanabe, N. Kamiuchi, M. Ozawa, *Appl. Catal. B Environ.* 142-143 (2013) 8.

[31] S. H. Joo, J. Y. Park, J. R. Renzas, D. R. Butcher, W. Huang, G. A. Somorjai, *Nano Lett.* 10 (2010) 2709.

[32] J. Assmann, V. Narkhede, N. A. Breuer, M. Muhler, A. P. Seitsonen, M. Knapp, D. Crihan, A. Farkas, G. Mellau, H. Over, *J. Phys. Condens. Matter.* 20 (2008) 184017.

[33] J. Assmann, V. Narkhede, L. Khodeir, E. Lo, O. Hinrichsen, A. Birkner, H. Over, M. Muhler, *J. Phys. Chem. B.* 108 (2004) 14634.

[34] J. Assmann, D. Crihan, M. Knapp, E. Lundgren, E. Loffler, M. Muhler, V. Narkhede, H. Over, M. Schmid, A. P. Seitsonen, P. Varga, *Angew. Chem. Int. Ed. Engl.* 44 (2005) 917.

[35] E. McCarthy, J. Jahradnik, G. C. Kuczynski, J. J. Carberry, *J. Catal.* 39 (1975) 29.

[36] N. Cant, W. Hicks, P. C. Lennon, *J. Catal.* 54 (1978) 372.

[37] U. Ackelid, L. R. Wallenberg, L. Petersson, *Catal. Letters.* 39 (1996) 129.

[38] C. Pliangos, I. V. Yentekakis, V. G. Papadakis, C. G. Vayenas, X. E. Verykios, *Appl. Catal. B Environ.* 14 (1997) 161.

[39] E. C. Subbarao, H. S. Maiti, *Science.* 11 (1984) 317.

[40] G. H. Hatzikos, R. Masel, *Surf. Sci.* 185 (1987) 479.

[41] C. Vayenas, S. Bebelis, I. Yentekakis, H. Lintz, *Catal. Today.* 11 (1992) 303.

[42] F. Diehl, J. Barbier Jr., D. Duprez, I. Guibard, G. Mabilon, *Appl. Catal. B Environ*. 95 (2010) 217.

[43] Lawrence Berkeley Laboratory, Department of Chemistry, USA and Materials and Molecular Research Division, University of California, , Berkeley, California 94720, USA, Surf. Sci. 167 (1986) 150.

[44] F. Delbecq, P. Sautet, *Catal. Letters.* 28 (1994) 89.

[45] A. Mishra, R. Prasad, *Bull. Chem. Eng. Catal.* 6 (2011) 1.

[46] A. F. Ghenciu, *Solid-State Mater. Sci.* 6 (2002) 389.

[47] Y. H. Kim, E. D. Park, H. C. Lee, D. Lee, *Appl. Catal. A Gen.* 366 (2009) 363.

[48] A. M. Abdel-Mageed, S. Eckle, H. G. Anfang, R. J. Behm, *J. Catal.* 298 (2013) 148.

[49] L. Chang, N. Sasirekha, Y. Chen, W. Wang, *Ind. Eng. Chem. Res.* 45 (2006) 4927.

[50] R. A. Dagle, Y. Wang, G. -G. Xia, J. J. Strohm, J. Holladay, D. R. Palo, *Appl. Catal. A Gen.* 326 (2007) 213.

[51] C. Galletti, S. Specchia, G. Saracco, V. Specchia, *Chem. Eng. Sci.* 65 (2010) 590.

[52] I. H. Son, A. M. Lane, *Catal. Letters.* 76 (2001) 151.

[53] Y.-W. Chen, D. -S. Lee, H. -J. Chen, *Int. J. Hydrogen Energy.* 37 (2012) 15140.

[54] P. Panagiotopoulou, D. I. Kondarides, X. E. Verykios, *Appl. Catal. A Gen.* 344 (2008) 45.

[55] G. A. Somorjai, *Catal. Rev.* 23 (1981) 189.

[56] S. Takenaka, *Int. J. Hydrogen Energy.* 29 (2004) 1065.

[57] M. Kiskinova, Interaction of CO with single crystal metal surfaces, Chapter 2 in SSSC, vol. 64 (ed. L. Guczi), Elsevier, 1992.

[58] F. S. Stone, *J. Solid State Chem.* 12 (1975) 271.

[59] C. G. Vayenas, S. Bebelis, C. Pliangos, S. Brosda, D. Tsiplakides, Electrochemical Activation of Catalysis, Promotion, Electrochemical promotion and Metal-support Interactions, Kluwer Academic/Plenum Publisher, New York, 2001.

[60] R. J. Farrauto, C. H. Bartholomew, Fundamentals of Industrial Catalytic Processes, Chapman & Hall, London, 1997.

[61] N. Ozinger, Heterogeneous Catalysis and Solid Catalysts, Wiley-VCH Cerlag GmbH & Co. KGaA, Weinheim, 2009.

[62] W. Han, P. Zhang, X. Pan, Z. Tang, G. Lu, *J. Hazard. Mater.* 263 (2013) 299.

[63] J. Kašpar, P. Fornasiero, *J. Solid State Chem.* 171 (2003) 19.

[64] H. Wang, J. M. Krier, Z. Zhu, G. Melaet, Y. Wang, G. Kennedy, S. Alayoglu, K. An, G. A. Somorjai, *ACS Catal.* 3 (2013) 2371.

[65] S. Tauster, S. Fung, R. Garten, *J. Am. Chem. Soc.* 100 (1978) 170.

[66] A. S. Ivanova, E. M. Slavinskaya, R. V. Gulyaev, V. I. Zaikovskii, O. A. Stonkus, I. G. Danilova, L. M. Plyasova, A. I. Boronin, *Appl. Catal. B Environ.* 97 (2010) 57.

[67] L. L. Murrell, S. J. Tauster, D. R. Anderson, *Stud. Surf. Sci. Catal.* 75 (1993) 681.

[68] H. Miho, T. Naoki, T. Toshitaka, N. Yasutaka, D. Kazuhiko, A. Yuki, Y. Takeru, S. Hirofumi, *Appl. Catal. B Environ.* 99 (2010) 336.

[69] S. Hosokawa, M. Taniguchi, K. Utan, H. Kanai, S. Mamura, *Appl. Catal. A Gen.* 289 (2005) 115.

[70] B. R. Cuenya, S. H. Baeck, T. F. Jaramillo, E. W. McFarland, *J. Am. Chem. Soc.* 125 (2003) 12928.

[71] Â. Omil, J. M. Pintado, S. Bernal, J. J. Calvino, M. A. Cauqui, J. M. Gatica, C. Larese, J. A. Pe, A. Metalu, *Catal. Today.* 50 (1999) 175.

[72] S. Suhonen, M. Valden, M. Hietikko, R. Laitinen, A. Savimäki, M. Härkönen, *Appl. Catal. A Gen.* 218 (2001) 151.

[73] R. Strobel, S. E. Pratsinis, *Platin. Met. Rev.* 53 (2009) 11.

[74] J. Ohyama, A. Yamamoto, K. Teramura, T. Shishido, T. Tanaka, *ACS Catal.* 1 (2011) 187.

[75] S. Bonanni, K. Aït-Mansour, H. Brune, W. Harbich, *ACS Catal.* 1 (2011) 385.

[76] L. Calvillo, V. Celorrio, R. Moliner, M. J. Lázaro, *Mater. Chem. Phys.* 127 (2011) 335.

[77] K. Kwon, S. Jin, C. Pak, H. Chang, S. H. Joo, H. I. Lee, J. H. Kim, J. M. Kim, *Catal. Today.* 164 (2011) 186.

[78] N. Yamaguchi, N. Kamiuchi, H. Muroyama, T. Matsui, K. Eguchi, *Catal. Today.* 164 (2011) 169.

[79] A. S. Ivanova, E. M. Slavinskaya, R. V. Gulyaev, V. I. Zaikovskii, O. A. Stonkus, I. G. Danilova, L. M. Plyasova, A. I. Boronin, *Appl. Catal. B Environ.* 97 (2010) 57.

[80] D. Archonta, A. Frantzis, D. Tsiplakides, C. Vayenas, *Solid State Ionics.* 177 (2006) 2221.

[81] S. J. Tauster, S. C. Fung, R. T. K. Baker, J. A. Horsley, *Science.* 211 (1981) 1121.

[82] B. L. Mojet, M. J. Kappers, J. T. Miller, D. C. Koningsberger, *Surf. Sci. Catal.* 101 (1996). 1165.

[83] Q. Fu, T. Wagner, *Surf. Sci. Rep.* 62 (2007) 431.

[84] Q. Fu, T. Wagner, *Surf. Sci.* 574 (2005) L29.

[85] Q. Fu, T. Wagner, *J. Phys. Chem. B.* 109 (2005) 11697.

[86] Q. Fu, T. Wagner, S. Olliges, H. D. Carstanjen, *J. Phys. Chem. B.* 109 (2005) 944.

[87] P. Vernoux, L. Lizarraga, M. N. Tsampas, F. M. Sapountzi, A. De Lucas-Consuegra, J. -L. Valverde, S. Souentie, C. G. Vayenas, D. Tsiplakides, S. Balomenou, E. A. Baranova, *Chem. Rev.* 113 (2013) 8192.

[88] G. C. Bond, Heterogeneous Catalysis: Principles and Applications, Clarendon Press, 1974.

[89] C. Wagner, *Adv. Catal.* 21 (1970) 323.

[90] S. Stolen, T. Grande, Chemical Thermodynamics of Materials, West Sussex, England, 2004.

[91] Nano-Structured gamma alumina from amorophous precursors, Alcoa Lab.

[92] A. Bird, A. Stiles, Catalyst Supports and Supported Catalysts, Butterworth, Boston, USA, 1987.

[93] E. Auer, A. Freund, J. Pietsch, T. Tacke, *Appl. Catal. A Gen.* 173 (1998) 259.

[94] C. Corporation, Carbon Black, Vulcan XC72R.

[95] E. M. Slavinskaya, R. V. Gulyaev, O. A. Stonkus, A. V. Zadesenets, P. E. Plyusnin, Y. V. Shubin, S. V. Korenev, A. S. Ivanova, V. I. Zaikovskii, I. G. Danilova, A. I. Boronin, *Kinet. Catal.* 52 (2011) 282.

[96] H. Tanaka, M. Misono, Curr. Opin. *Solid State Mater. Sci.* 5 (2001) 381.

[97] F. Patel, S. Patel, *Procedia Eng.* 51 (2013) 324.

[98] T. Vaz, A. V. Salker, *Mater. Sci. Eng. B.* 143 (2007) 81.

[99] R. M. Horton, A. J. Haslam, A. Galindo, G. Jackson, M. W. Finnis, *J. Phys. Condens. Matter.* 25 (2013) 395001.

[100] R. Vassen, X. Cao, F. Tietz, D. Basu, D. Sto, *J. Am. Ceram. Soc.* 38 (2000) 2023.

[101] M. Kilo, C. Argirusis, G. Borchardt, R. A. Jackson, *Phys. Chem. Chem. Phys.* 5 (2003) 2219.

[102] M. Stoukides, C. G. Vayenas, *J. Catal.* 70 (1981) 137.

[103] A. Katsaounis, *J. Appl. Electrochem.* 40 (2010) 885.

[104] S. Bebelis, *J. Catal.* 118 (1989) 125.

[105] D. Tsiplakides, S. Balomenou, A. Katsaounis, D. Archonta, C. Koutsodontis, C. G. Vayenas, *Catal. Today.* 100 (2005) 133.

[106] T. Rebitzki, B. Delmon, J. H. Block, *AIChE J.* 41 (1995) 1543.

[107] E. Mutoro, C. Hellwig, B. Luerssen, S. Guenther, W. G. Bessler, J. Janek, *Phys. Chem. Chem. Phys.* 13 (2011) 12798.

[108] P. Vernoux, M. Guth, X. Li, *Electrochem. Solid-State Lett.* 12 (2009) E9.

[109] P. Vernoux, *J. Catal.* 208 (2002) 412.

[110] P. Vernoux, F. Gaillard, R. Karoum, A. Billard, *Appl. Catal. B Environ.* 73 (2007) 73.

[111] J. Nicole, D. Tsiplakides, C. Pliangos, X. E. Verykios, Ch. Comninellis, C. G. Vayenas, *J. Catal.* 204 (2001) 23.

[112] Y. Barron, D. Cornet, G. Maire, F. G. Gault, *J. Catal.* 2 (1963) 152.

[113] F. G. Gault, *Adv. Catal.* 30 (1981) 1.

[114] J. H. Sinfelt, *Rev. Mod. Phys.* 51 (1978) 569.

[115] V. Ponec, *Adv. Catal.* 32 (1983) 149.

[116] J. M. Muller, F. G. Gault, *Bull. Soc. Chim.* 2 (1970) 416.

[117] R. B. Levy, M. Boudart, *Science.* 181 (1973) 547.

[118] S. J. Tauster, *Acc. Chem. Res.* 20 (1987) 389.

[119] F. Garin, S. Aeiyach, P. Légaré, G. Maire, *J. Catal.* 77 (1982) 323.

[120] A. Dauscher, F. Garin, G. Maire, *J. Catal.* 105 (1987) 233.

3 Research Motivation and Objectives

The principal objective of this research was to develop a comprehensive understanding of the metal-support interaction or self-induced EPOC in heterogeneous catalysis using nanoparticles with low noble metal loadings, and then to use all this knowledge in developing catalytic systems for carbon monoxide and volatile organic compound (VOC) oxidation from automotive and power plant emissions which will have direct impact on the air quality, and consequently on health and environmental protection.

To achieve the main objective, the following approach with each point considered as a sub-objective was followed:

- To synthesize noble metal nanoparticles of specific size (1 - 7 nm) and shape and then to deposit them on different supports, basically on conventional non ionic conductive and on ionic and mixed ionic conductive supports with minimum loading (≤ 1 wt. %) of noble metal.

- To characterize the synthesized nanocatalysts in terms of actual metal loading, particle size, morphology, oxidation state, specific surface area and dispersion on the support surface.

- To study the catalytic activity of these nanoparticles for environmentally important reaction systems such as carbon monoxide oxidation and volatile organic compound oxidation with focus on the effect of particle size on metal-support interactions and investigate the structure-sensitivity of the reactions in interest.

- To compare the catalytic activity of the nanocatalyst when deposited on conventional non ionic conductive such as carbon and alumina vs. their activity when deposited on ionic and mixed ionic conductive supports for pollutant oxidation. Emphasis was made to utilize yttria-stabilized zirconia as a promising support for metals in heterogeneous catalysis.

- To investigate the effect of oxygen vacancy in the ionic and mixed ionic conductive supports and the backspillover of these ionic species from the supports to the catalyst surface as a result of metal-support interaction.

- To study the catalytic activity of new supports or new metal/support combinations that have not been used before for carbon monoxide and volatile organic compound oxidation and compare their activity with supports or catalysts of similar nature previously reported in literature for these specific reactions.

- To study the catalytic activity of the nanocatalysts for reactions other than oxidation such as carbon monoxide methanation for fuel cell operations at low temperatures $<100^{o}C$.

- To provide evidence of metal-support interaction between noble metal nanoparticles and the ionic and mixed ionic conductive supports. Several characterization and experimental analysis data were provided to serve this goal.

SECTION II: CATALYST SYNTHESIS AND EXPERIMENTAL SETUP

4 Nanoparticle Synthesis, Characterization and Experimental Setup

4.1 Synthesis of catalyst nanoparticles

Amongst the many methods reported to synthesize nanoparticles; wet impregnation might be the most conventional and widely used. In this method, the support (usually a powder) is soaked in a solution of the metal salt, followed by drying, and then by thermal treatment. The metal salt decomposes under high temperatures and converts to nanoparticles, which are finally dispersed on the support surface [1]. Although considered a straight forward method for nanoparticle synthesis, wet impregnation has some drawbacks such as poor control over the metal particle size and the size distribution [2]. Other synthesis methods were reported in literature including chemical synthesis of nanoparticles. The section below describes the modified polyol reduction method which was followed in this research for synthesis of all nanocatalysts.

4.1.1 Synthesis of nanoparticle colloids using modified polyol method

Platinum and ruthenium nanoparticles were synthesized using a polyol reduction method [3-5]. Table 4-1 shows a summary of the nanoparticles synthesized. In short, a metal salt of $PtCl_4$ (Alfa Aesar, 99.9% metals basis) or $RuCl_3$ (Alfa Aesar, 99.99% metals basis) was dissolved in 25-100 mL of ethylene glycol (Sigma Aldrich, anhydrous 99.8%) containing various amounts of NaOH (0.056, 0.06, 0.08, 0.15 and 0.20 M) (EM Science, ACS grade). The solution was stirred for 30 min at room temperature, and subsequently heated and refluxed for 3 h at 160^{o}C. A dark brown solution containing Pt or Ru nanoparticle colloids were formed.

Table 4-1: Summary of noble metal nanoparticles catalysts.

Catalyst metal	Final pH	Colloidal particle size (nm)[a]	Supported catalyst	Supported particle size (nm)[b]	Dispersion (%)[c]	Metal loading (wt%)[d]
Platinum (Pt)	4.0	7.4	Pt/C	6.3	5.3	0.38
			Pt/YSZ	6.7	9.5	1.0
	6.0	3.8	Pt/C	2.8	41.7	0.43
			Pt/YSZ	4.4	30.1	1.1
	7.5	2.8	Pt/C	1.9	52	0.37
			Pt/CeO_2	NA	19.9	1.0
			Pt/γ-Al_2O_3	2.5	45	0.7
			Pt/SDC	2.8	40	0.37
			Pt/YSZ	3.0	39.5	1.1
			Pt/SCF-0	NA	40.2	1.0
			Pt/SCF-1	NA	37.7	1.0
			Pt/SCF-5	2.5	45	1.0
	8.5	1.7	Pt/C	1.7	54	0.40
			Pt/YSZ	1.7	54	1.0
	9.0	1.0	Pt/C	1.5	68.3	0.44
			Pt/YSZ	1.9	51.8	0.9
Ruthenium (Ru)	7.0	1.9	Ru/YSZ	2.8	15	0.48
			Ru/C	2.6	22	0.19
			Ru/SDC	2.6	16	0.16
			Ru/γ-Al_2O_3	2.3	18	0.49

[a] from x-ray diffraction (XRD)
[b] from Transmission electron microscopy (TEM)
[c] from CO titration method
[d] from Inductively coupled plasma (ICP)

4.1.2 Deposition on ionic conductive and non ionic conductive supports

Pt or Ru colloids were deposited on the supports by taking appropriate amount of the colloidal nanoparticles and mixing them with 1.5 g of each support, namely YSZ (Tosoh, SSA = 13 m^2/g), carbon black (Vulcan XC-72R, Cabot Corp. SSA = 254 m^2/g), γ-Al_2O_3 (Alfa-Aesar, SSA = 120 m^2/g) and SDC (Fuel Cell Materials , 99.9% SSA = 35 m^2/g). The total Pt metal loading on YSZ was $\leq$1 wt%. The solution was left to mix over night. The resulting supported nanoparticles were then centrifuged and extensively washed with de-ionized water. The concentrate was then dried in air for 24 - 48 h at 40 - 80^oC. Fig. 4-1 shows a schematic diagram of nanoparticle synthesis.

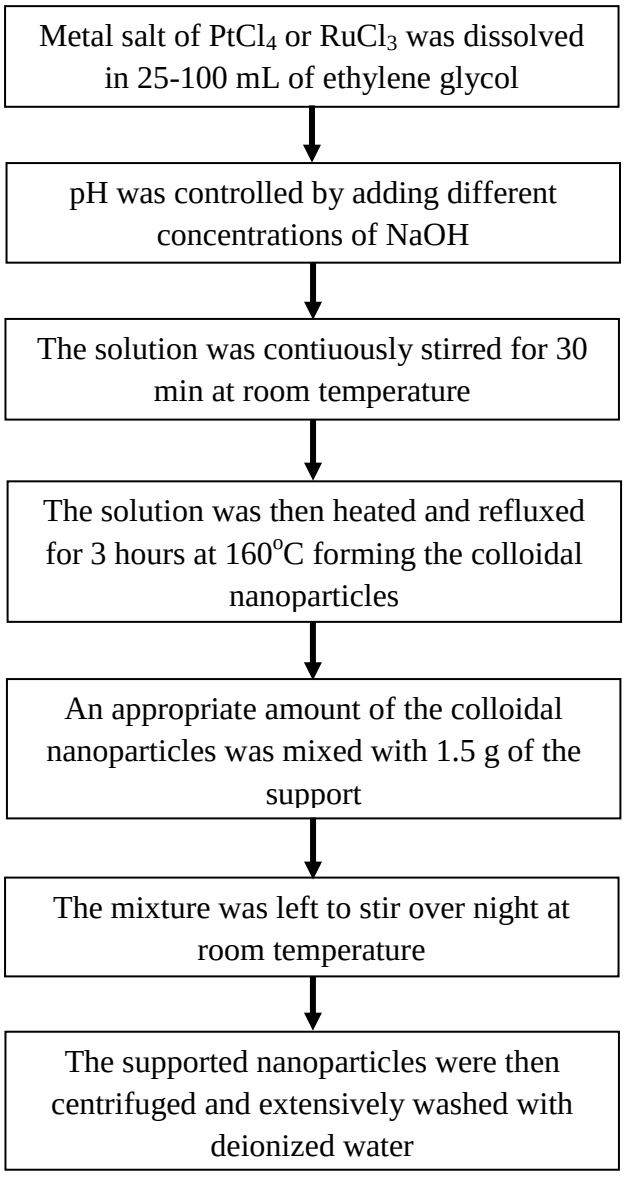

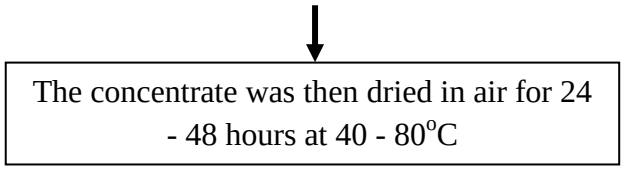

Figure 4-1: Scheme of Polyol reduction method for nanoparticle synthesis.

4.2 Characterization of nanoparticles

Physical "seeing" of nanoparticles was apparently not feasible prior to the invention of electron microscopy. During the first half of the 20th century, early studies of heterogeneous catalysis was rather called "black art" owing to the nature of catalysts being largely unknown. However, in the past two decades, significant developments in nanotechnology have enabled researchers not only to see nanoparticles clearly at atomic resolution and create well-defined nanoparticles, but also to look into the very fundamentals of catalytic processes [2]. The following sub-sections describe some of the characterization techniques used to study the synthesized nanocatalysts in this research.

4.2.1 Transmission electron microscopy of colloidal nanoparticles

The surface morphology and size distribution of the colloidal nanoparticles were characterized by TEM (JEOL JEM 2100F FETEM) operating at 200kV. For TEM measurements, a very small volume of Pt colloids was dispersed in ethanol at the ratio of 1:5. Then, the mixture was sonicated for 10 minutes. A drop of the solution was taken and deposited on a copper grid (Electron Microscopy sciences, CF- 300) and was left to dry for 30 min in air. The grids were then transferred to a grid holder and dried in an oven for 3 h. The size distribution and mean particle size were performed using the imaging software MeasureIt (Olympus Soft Imaging Solutions) or by using Image J software by measuring at least 200 nanoparticles from the TEM images.

Figure 4-2 shows the TEM micrograph and the corresponding histogram of Ru colloidal nanoparticles while Fig. 4-3 shows micrographs and the corresponding histograms of three colloidal Pt nanoparticles synthesized in different NaOH concentrations. The TEM

shows that well defined and almost spherical nanoparticles were prepared using ethylene glycol reduction method.

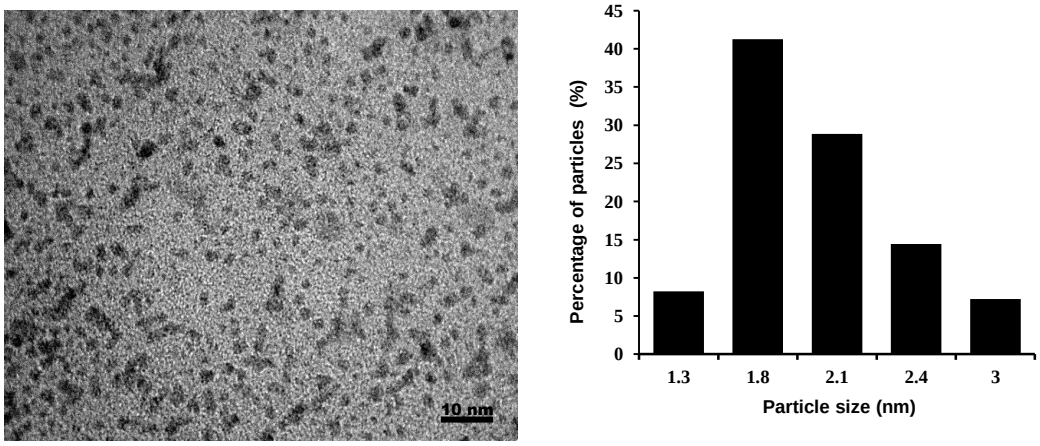

Figure 4-2: TEM image (left) and the corresponding histogram (right) of Ru colloids [6].

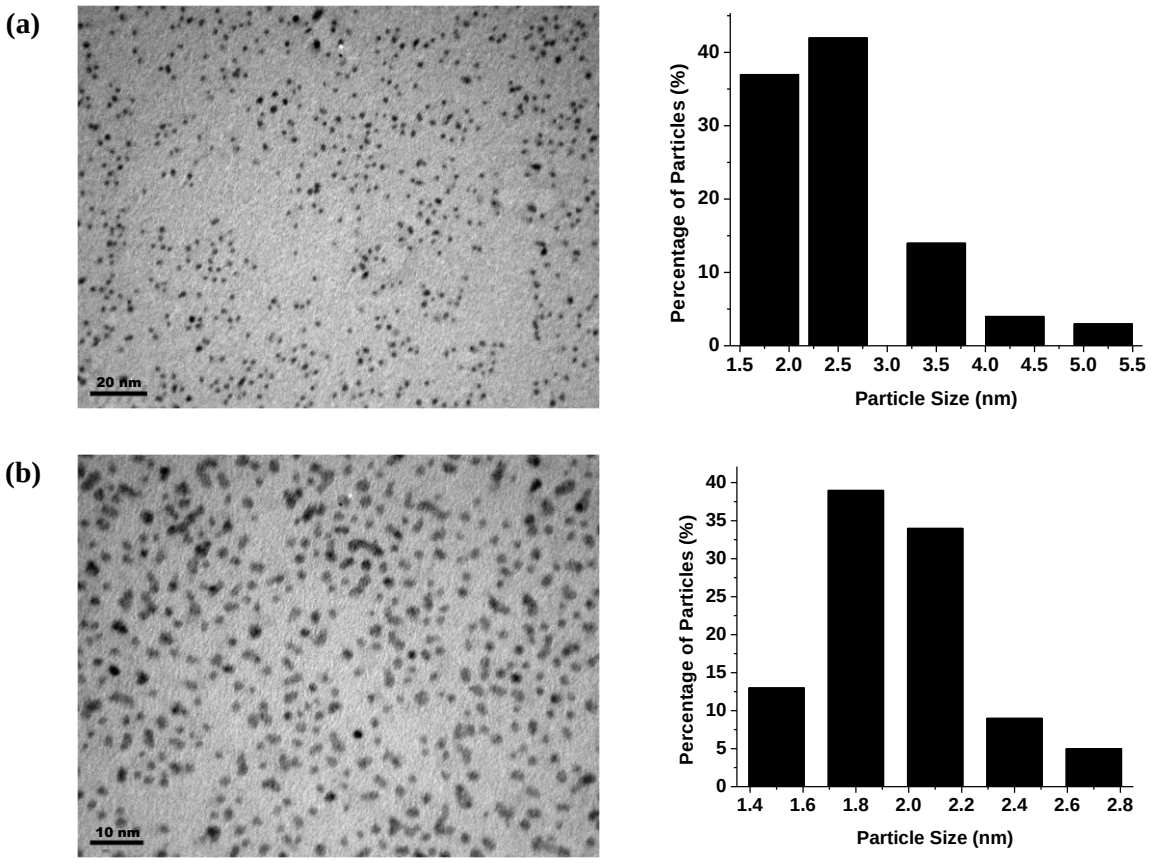

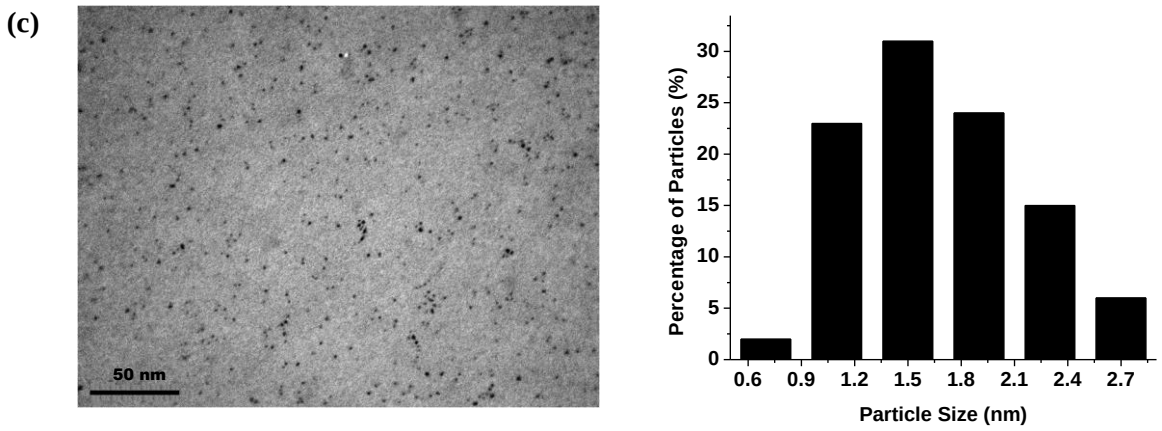

Figure 4-3: TEM images (left) and corresponding histograms (right) of Pt colloids, synthesized in ethylene glycol solutions using the following concentrations: (a) 0.06 M; (b) 0.08 M; (c) 0.15 M [7].

4.2.2 Transmission electron microscopy of supported nanoparticles

Transmission electron microscopy (TEM) were taken for Pt/YSZ, Pt/C, Pt/γ-Al_2O_3 and Ru/C as shown in Fig. 4-4 using (Transmission Electronic Microscopy, JEOL 2010 LaB6) for investigating the morphology and size of supported metal particles. An extraction-replica technique was used for YSZ and γ-Al_2O_3 sample preparation. The catalyst was dispersed in ethanol, deposited on a mica film and covered with a carbon layer. Then, the YSZ or γ-Al_2O_3 support and the film of mica were dissolved in hydrogen fluoride solution for 24 h whereas Pt particles remained fixed on the carbon film. Then, these particles were directly observed by TEM. For the preparation of carbon supported nanoparticles, the catalysts were dispersed in ethanol, deposited on a copper grid (Electron Microscopy sciences, CF-300), and were left to dry for 30 min in air. The grids were then transferred to a grid holder and dried in an oven for 3 h. Then, these particles were directly observed by TEM. The use of Image J software allowed for the determination of Pt particles size distribution.

(a)

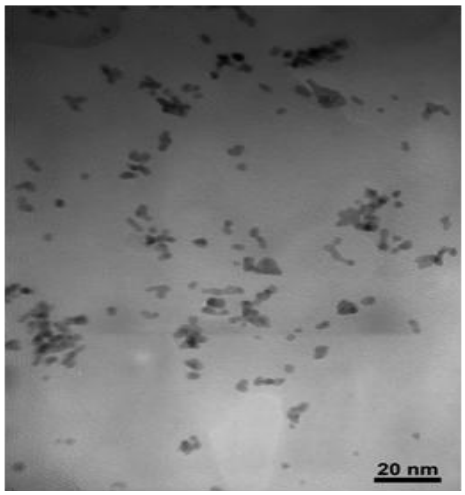
20 nm

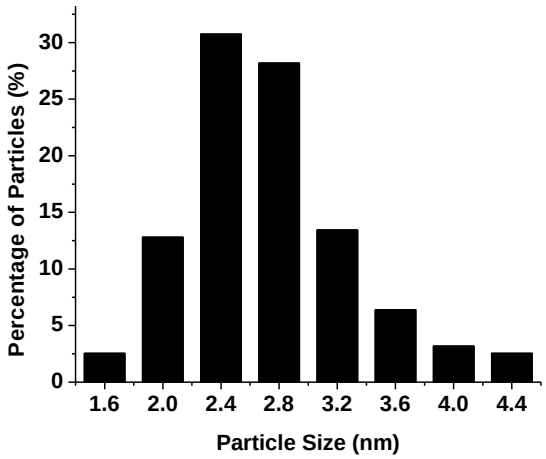
Percentage of Particles (%)
0
5
10
15
20
25
30
1.6
2.0
2.4
2.8
3.2
3.6
4.0
4.4
Particle Size (nm)

(b)

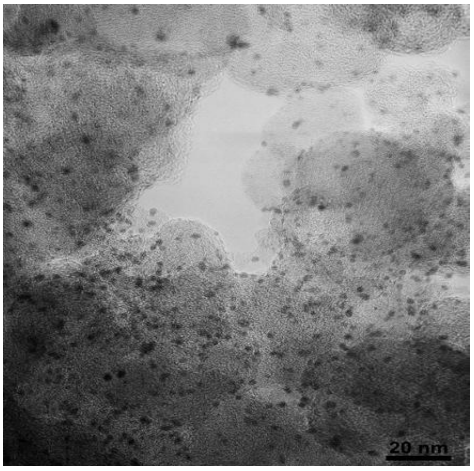
20 nm

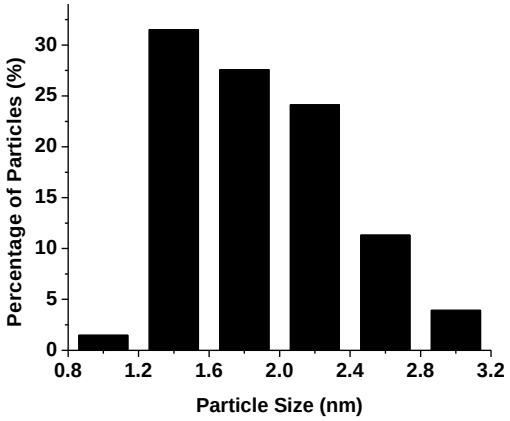
Percentage of Particles (%)
0
5
10
15
20
25
30
0.8
1.2
1.6
2.0
2.4
2.8
3.2
Particle Size (nm)

(c)

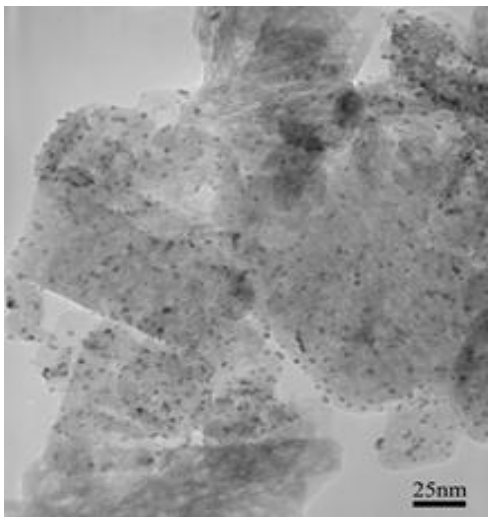
25nm

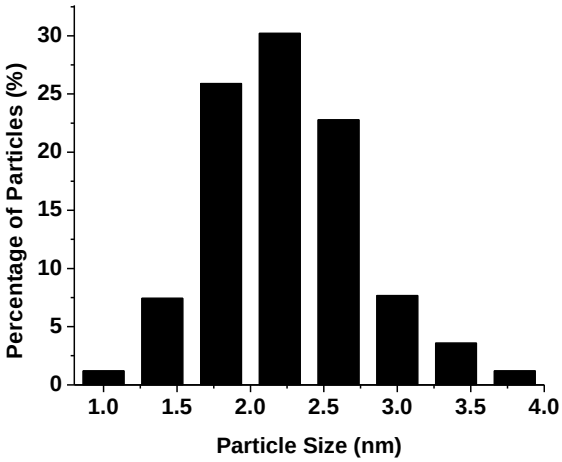
Percentage of Particles (%)
0
5
10
15
20
25
30
1.0
1.5
2.0
2.5
3.0
3.5
4.0
Particle Size (nm)

(d)

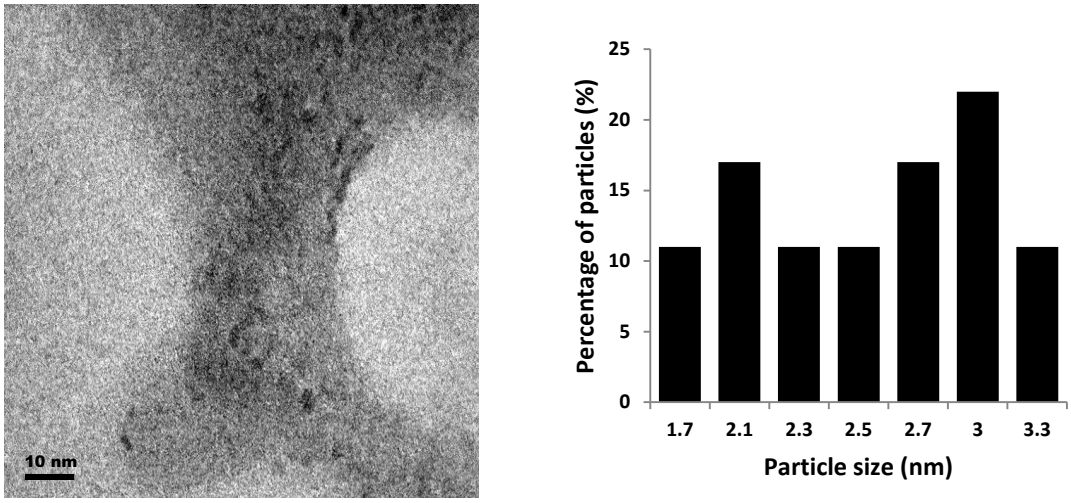

Figure 4-4: TEM images (left) and corresponding histograms (right) of Pt/YSZ catalysts prepared at 0.08M NaOH concentration: (a) Pt/YSZ, (b) Pt/C, (c) Pt/γ-Al_2O_3 and (d) Ru/C [8].

The TEM images show homogeneously dispersed nanoparticles on the supports. The supported nanoparticles are spherical in shape and have narrow size distribution with average particle sizes as summarized in Table 4-1.

4.2.3 Inductively coupled plasma measurements

Inductively coupled plasma (ICP) measurements were used to evaluate the metal loading on the supports using (ICP-OES Varian Vista-Pro CCD spectrometer). ICP results are summarized in Table 4-1.

4.2.4 X-ray diffraction measurements

X-ray diffraction patterns of all colloidal Pt nanoparticles were collected using Rigaku Ultima IV diffractometer using Cu Kα source. The experiments were run in the focused beam geometry with a divergence slit of 2/3 degree, a scan speed of 0.17 degree/min and a scan step of 0.06 degree for all experiments. The diffractograms were collected between 30^o and 50^o 2θ. X-ray diffraction patterns of the platinum nanoparticle colloids are shown in Fig. 4-5. Baranova et al. established a methodology for estimating the average size and composition of FCC Pt clusters. The average crystallite size was estimated using the full width at half maximum (FWHM) and full width at ¾ maximum (FW3/4M) of the FCC (111) peak as

described in [9]. The peak around 40° 2θ corresponds to Pt reflection (111), whereas sharp peaks at around 32 and 46° 2θ are attributed to NaCl phase, which is present in the sample as a result of the synthesis solution.

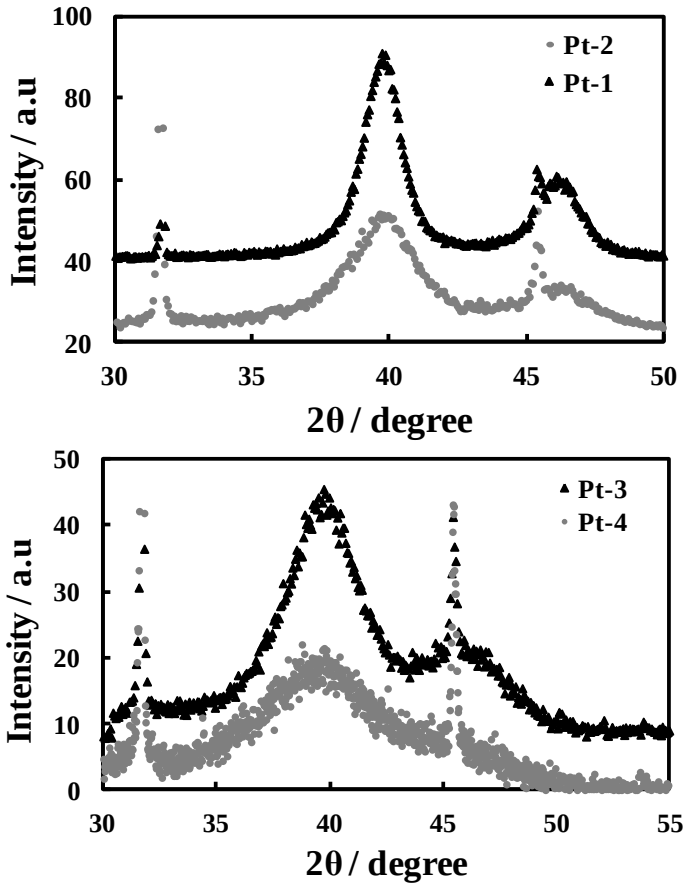

Figure 4-5: X-ray diffraction patterns of colloidal Pt nanoparticles showing Pt (111) peaks. Pt-1 (7.4 nm), Pt-2 (3.8 nm), Pt-3 (2.8 nm) and Pt-4 (1.0 nm) [10].

Table 4-1 shows a summary of XRD size distribution of the colloidal nanoparticles which indicates a broad agreement with size distribution deduced from TEM. It is worth mentioning that one of the limitations of TEM technique is that only relatively small amount of particles can be analyzed, while XRD is a bulk technique, which allows evaluation of the entire bulk sample.

4.2.5 Thermogravimetric analysis

The thermogravimetric profile of Pt/C (~ 1.5 nm) was measured to examine the catalyst stability using a thermogravimetric analyzer (Q500 TGA, TA Instruments). The powder sample was first treated in a flow of ultra high purity (UHP) nitrogen (N_2) at 150ºC for a period of 30 min to remove pre-adsorbed moisture. Then, it was decomposed by heating at 10ºC/min from room temperature to 800ºC under flowing N_2, the material was kept under isothermal conditions for 5 min. The amount of carbon was calculated from the weight loss that occurs typically above 150ºC.

Fig. 4-6 shows that Pt/C catalysts are very stable in the temperature range of interest. TGA was performed in nitrogen and air on Pt/C (~ 1.5 nm) catalyst. A first weight loss of about 1% occurred from room temperature to 150^{o}C due to evaporation of surface water adsorbed on carbon. The sample mass is almost stable between 150 - 400^{o}C in both air and N_2. The main weight loss of around 99% was after 500^{o}C in air due to the oxidation of carbon.

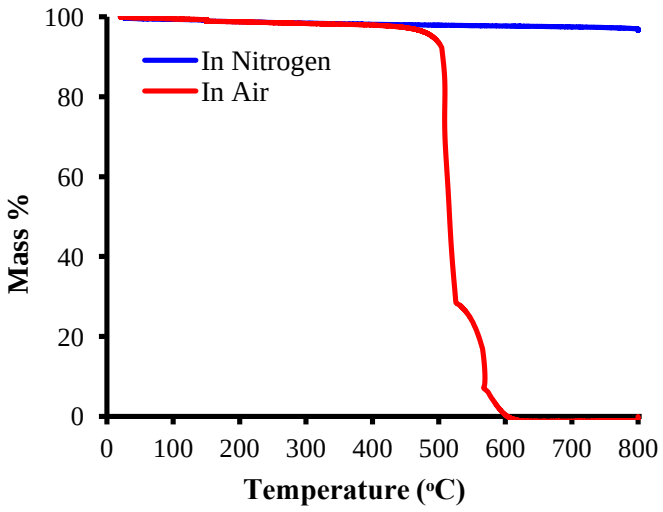

Figure 4-6: TGA analysis under air and nitrogen at 10^{o}C/min of Pt/C (1.5 nm).

4.2.6 X-ray photoelectron spectroscopy

X-ray photoelectron spectroscopy (XPS) measurements of four Pt/C and four Pt/YSZ catalysts each, of different particle size were performed using a KRATOS Axis Ultra DLD

with a Hybrid lens mode at 140 W and pass energy 20 eV using a monochromatic AlKα. The XPS core level spectra were analyzed with a fitting routine which decomposes each spectrum into individual mixed Gaussian-Lorentzian peaks using a Shirley background subtraction. In order to overcome charging effects, an electron gun was employed. The energy of the electrons was carefully selected so as to have a good signal to noise ratio while at the same time to eliminate charging effects. Details of the XPS spectra and analysis of Pt nanoparticles deposited on non ionic and ionic conductors are discussed in chapter 5 and 10, respectively.

4.3 Catalytic experimental setup

Catalytic activity measurements of CO and C_2H_4 oxidation as well as CO methanation experiments were carried out at atmospheric pressure in a continuous flow U-shaped quartz reactor. Approximately 50 mg of catalyst was placed into the reactor. The reactant mixture was composed of 909 ppm C_2H_4 (Linde, 5% in He) or 770 - 909 ppm CO (Linde, 1% in He) for oxidation experiments or 1000 ppm CO (Linde, 1% in He) with 10% H_2 for CO methanation experiments. The main gas flow was mixed with 3.5 - 4.4% O_2 (Linde, 100%) for C_2H_4 and CO experiments, and balance He (Linde, 100%). The total gas flow rate was 4.30 - 4.62 $L \cdot h^{-1}$ for C_2H_4 and CO oxidation experiments and 6.6 $L \cdot h^{-1}$ for CO methanation experiments, respectively. For the catalytic measurements in the absence of oxygen in the gas feed, the gas flowrate was 4.62 $L \cdot h^{-1}$ with 909 ppm CO or C_2H_4, balance He.

The samples were tested in the temperature range of 25 - 400^{o}C. The reactant and product gases were analyzed using an on-line gas chromatograph (GowMac 350) and non-dispersive infrared (NDIR) CO_2 gas analyzer (HORIBA VA-3001) to quantify concentrations of reactants and products. Each experiment was repeated for three cycles to test stability and reproducibility. Fig. 4-7 shows a schematic diagram for the experimental setup used for the catalytic activity measurements.

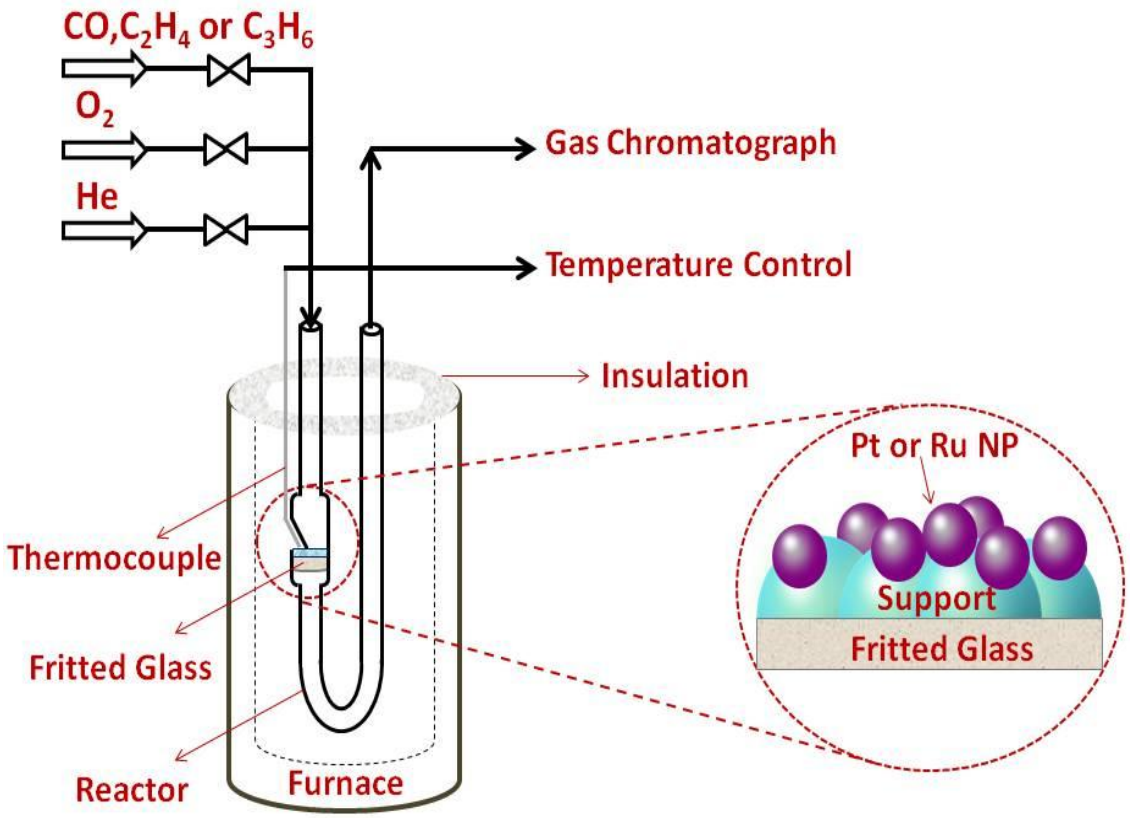

Figure 4-7: Schematic diagram of the catalytic activity setup.

4.4 Acknowledgement

In context of this, I would like to acknowledge Dr. Nimal de Silva (Dept. Earth Sciences) for running ICP measurements. Dr. Yun Liu (Centre for Catalysis Research and Innovation (CCRI)) at the University of Ottawa for taking TEM images of the colloidal catalysts. Microscopy services at Institut de Recherches sur la Catalyse et L'environnment de Lyon (IRCELYON) for TEM images of the supported catalysts. Dr. Tara Kell (Dept. Earth Sciences at UOttawa) for training me on using x-ray diffraction. Dr. Spyridon Ntais for running x-ray photoelectron spectroscopy (XPS) measurements and analyzing related data for chapters 5 and 10. Dr Martin Couillard for running annular dark field-scanning electron

microscopy (ADF-STEM) measurements for the catalysts in the manuscripts presented in chapter 10 and 11.

4.5 References

[1] G. C. Bond, Heterogeneous Catalysis: Principles and Applications, Clarendon Press, 1974.

[2] R. Jin, *Nanotechnol. Rev*. 1 (2012) 31.

[3] C. Bock, C. Paquet, M. Couillard, G. Botton, B. MacDougall, *J. Am. Chem. Soc.* 126 (2004) 8028.

[4] E. A. Baranova, N. Miles, P. H. J. Mercier, Y. Le Page, B. Patarachao, *Electrochim. Acta.* 55 (2010) 8182.

[5] E. A. Baranova, T. Amir, P. H. J. Mercier, B. Patarachao, D. Wang, Y. Page, *J. Appl. Electrochem.* 40 (2010) 1767.

[6] R. J. Isaifan, E. A. Baranova, *J. Catal. Today* (2014) CATTOD-D-14-00024R1 (in press).

[7] R. J. Isaifan, H. A. E. Dole, E. Obeid, L. Lizarraga, E. A. Baranova, P. Vernoux, *ECS Trans.* 35 (28) (2011) 43.

[8] R. J. Isaifan, H. A. E. Dole, E. Obeid, L. Lizarraga, P. Vernoux, E. A. Baranova, *Electrochem. Solid-State Lett.* 15(3) (2012) E14.

[9] E. A. Baranova, Y. Le Page, D. Ilin, C. Bock, B. MacDougall, P. H. J. Mercier, *J. Alloys Compd.* 471 (2009) 387.

[10] R. J. Isaifan, S. Ntais, E. A. Baranova, *Appl. Catal. A: Gen.* 464– 465 (2013) 87.

SECTION III: CONVENTIONAL SUPPORT — PARTICLE SIZE EFFECT

5 Particle size effect on catalytic activity of carbon-supported Pt nanoparticles for complete ethylene oxidation

Applied Catalysis A: General 464– 465 (2013) 87– 94

5.1 Abstract

Effect of Pt particle size on the catalytic activity of complete ethylene oxidation in the temperature range of 25 - 220^{o}C in fuel-lean conditions is investigated. Carbon black is used as a support for platinum nanoparticles of well-defined average sizes between 1.5 and 6.3 nm. The results demonstrate that ethylene oxidation on Pt/C is strongly size sensitive reaction. Thus, the smallest Pt/C-4 nanoparticles (1.5 ± 0.5 nm) exhibit much higher catalytic activity towards ethylene oxidation reaching 50% conversion at 88^{o}C compared to 164^{o}C for the largest Pt/C-1 (6.3 ± 0.5 nm) nanocatalysts. XPS shows that particle size decrease results in noticeable binding energy increase and Pt4f peak broadenings. This indicates that the electronic effect induced by small Pt nanoparticles might play a role in the observed increase in their activity towards C_2H_4 oxidation.

5.2 Introduction

Significant work has been done over the past few decades on nanostructured catalysts and in particular on understanding the effect of particle size on catalytic and electrocatalytic performance for various reactions. When the size of nanoparticles decreases, the ratio of surface to bulk atoms increases, meaning that more surface atoms become available for the reaction, however catalytic performance is not often in direct proportion with the increased surface area of smaller nanoparticles [1-3]. Size sensitive reactions may exhibit three distinct trends depending on the catalyst size. Thus, decrease in particle size may result in (i) an increase in catalytic activity; (ii) a decrease in catalytic performance; (iii) volcano type behavior. Depending on the catalytic system, these trends can be explained via electron structure effects, particle geometry effect and support structure effects. Over the last decades there have been several studies on effect of Pt nanoparticle size in heterogeneous catalysis and

electrocatalysis [4-6] and it was confirmed that observed catalytic activity largely depends on the reaction system under investigation and the reaction environment [7].

Ethylene is a low molecular weight volatile organic compound (VOC) and is considered as a harmful molecule that contributes to photochemical pollution. Partial ethylene oxidation has recently attracted significant interest due to its importance in industrial catalysis for ethylene oxide production as a raw material in ethylene glycol manufacturing processes, acrylonitrile and nonionic surfactants [8]. On the other hand, the complete ethylene oxidation is of specific interest due to the global need to decrease the hydrocarbon content of stationary and automotive emissions [9]. Ethylene is thermally stable and its oxidation at low temperatures (<100^{o}C) requires an active catalyst. It is well accepted that Pt is an excellent catalyst for complete hydrocarbon oxidation [7]. Various aspects of ethylene oxidation reaction have been studied on the single crystal Pt surfaces in ultra-high vacuum (UHV), as well as on supported Pt and other metals, such as Au and Ag [10-12]. Moreover, different studies have shown that ethylene oxidation follows Langmuir-Hinshelwood mechanism where ethylene adsorbs more strongly than oxygen over Pt active sites [13-15]. Smith et al. [16] and Morgan et al. [17] studied ethylene adsorption on clean surfaces of single (111) and (100) Pt crystals using low-energy electron diffraction and they found that ethylene is adsorbed irreversibly and dissociatively on four platinum atoms. Moreover, Van Strien et al. [18] used field emission probe-hole microscopy to study the structure sensitivity of ethylene adsorption on Pt in the temperature range of (-183 – 227^{o}C) and a detailed investigation of various transformations involving C-H and C-C bond breaking on Pt (111), (100), (110), (210) and (533) was presented. They concluded that ethylene molecule is markedly sensitive to the structure of the Pt surface and the decomposition of adsorbed ethylene is promoted on the stepped (533) surface compared to the close-packed (111) surface at lower temperature, while (110) and (210) surfaces are more active for the scission of C-H and C-C bonds. Somorjai [19,20] reported that surface irregularities on Pt atoms play a key role in hydrocarbon oxidation reactions, because step and kink surface sites of transition metals have high thermal stability and are characterized by low-coordinated atoms.

Previous studies on supported and single Pt catalysts revealed that ethylene oxidation is highly surface structure sensitive reaction. As shown in previous studies [20,21] in fuel lean

conditions it is improved when C_2H_4 adsorption energy is higher. The decrease in nanoparticle size may induce intrinsic effect due to very small size of Pt. Smaller Pt nanoparticles are characterized by a greater amount of very reactive low-coordinated atoms such as step-edge sites. Indeed, according to Schimpf et al. [22] for cubo-octahedron particle of 1.5 nm, almost 80 % are edge while the rest are corner sites. For 6.5 nm particle, 70 % are terrace sites, i.e., (111) while the rest is equally distributed between the edge and (100) sites [22]. There is no doubt that this noticeable variation in the surface site ratio may lead to a different structure-sensitive behavior of Pt nanoparticles. Though to the best of our knowledge, the effect of the Pt particle size (< 10 nm) for C_2H_4 oxidation at low temperatures (~100^{o}C) has not been studied so far. Therefore, in the present work a systematic study of the particle size effect on complete ethylene oxidation over carbon-supported Pt nanoparticles (Pt/C) is shown. XPS is used to analyze the surface composition of the as-prepared and spent Pt nanoparticles, as well as to evaluate the particle size effect.

5.3 Experimental

5.3.1 Synthesis of the carbon-supported Pt nanoparticles (Pt/C)

Platinum nanoparticles were synthesized using a modified polyol reduction method described in details elsewhere [23,24]. In short, Pt colloids were synthesized in ethylene glycol (anhydrous 99.8% Sigma Aldrich) at 160^{o}C, starting from 0.1227 g $PtCl_4$ (Alfa Aesar, 99.9% metals basis) precursor salt and using various sodium hydroxide (EM Science, ACS grade) concentrations of 0.056, 0.06, 0.08 and 0.20 M in order to adjust and control the particle size as shown in Table 5-1. The resulting dark brown Pt colloidal solution was deposited on carbon black (Vulcan XC-72R, Cabot Corp. specific surface area (a_s) of 254 $m^2 \cdot g^{-1}$) to give 0.37 - 0.44 wt.% of total Pt loading as confirmed by inductive coupled plasma measurements using (ICP-OES Varian Vista-Pro CCD spectrometer). Then, Pt/C catalysts were thoroughly washed with deionized water (18 MΩ.cm) in order to remove the residue formed during the synthesis and then it was finally dried at 80^{o}C for 3 h.

5.3.2 Characterization of Pt nanoparticles

5.3.2.1 X-ray diffraction (XRD)

X-ray diffraction (XRD) patterns of Pt colloids were obtained on a RigakuUltima IV diffractometer using a CuKa X-ray source (40 kV, 40 mA). The patterns were recorded in the focused beam geometry with a divergence slit of 2/3 degree, a scan speed of 0.17 deg min^{-1} and a scan step of 0.06 degrees between 30 and 60^{o}. The crystallite size of Pt clusters was determined using Debye formula for scattering by randomly oriented molecules and the methodology proposed earlier [23]. This approach allows for accurate interpretation of the diffraction patterns of Pt clusters smaller than 10 nm and calculation of the average crystallite sizes with high precision. The maximum-intensity peak position ($2\theta_{max}$) for the overlapping 111/200 peak was extracted from a third order polynomial fit to the top 10 – 20 % of the experimental intensities around 40° Bragg angle. The full-width at 3/4 (FW3/4M) and at half maximum (FWHM) of 111 peak height were determined assuming the minimum intensity measured around 2θ = 50 - 55^{o} as the zero height. Table 5-1 summarizes the XRD characteristics of four Pt colloids used for the determination of the average crystallite size.

5.3.2.2 Transmission electron microscopy (TEM)

TEM micrographs of colloidal and carbon-supported Pt nanoparticles were obtained using JEOL JEM 2100F FETEM operating at 200 kV. Image J software was used for the determination of Pt particles size distribution. The samples were prepared for TEM analysis by diluting about 4 μL of the colloidal solution or about 6 mg of the supported nanoparticles in ethanol. The diluted sample was then sonicated for 10 minutes, deposited on a copper grid and dried in air for 4 hours.

5.3.2.3 X-ray photoelectron spectroscopy (XPS)

XPS measurements were carried out using a KRATOS Axis Ultra DLD with a Hybrid lens mode at 140 W and pass energy 20 eV using a monochromatic AlKα. The XPS core level spectra were analyzed using the XPS Peak program with a fitting routine which decomposes each spectrum into individual mixed Gaussian-Lorentzian peaks using a Shirley background subtraction over the energy rate of the fit. The deconvolution of the Pt4f peaks was performed

using doublets with spin orbit splitting 3.35 eV and intensity ratio $Pt4f_{7/2}$: $Ptf_{5/2}$ = 4/3 while a peak asymmetry was used in the case of the Pt4f peaks attributed to the metallic based on the work of Hufner et al. [25]. For comparison reasons and in order to define the peak asymmetry of the metallic state, a Pt foil was also measured under the same experimental conditions. Before the measurement, the Pt foil was Ar^+-sputtered until only traces of oxygen could be detected. The Binding Energy (BE) scale was corrected using the C1s peak at 284.6 eV as an internal standard. The accuracy of measurement of the binding energy is ± 0.1 eV while that of FWHM is ± 0.05 eV.

5.3.2.4 Dispersion measurements

Dispersion was determined for the carbon-supported Pt nanoparticles using the CO titration technique [26-31]. The stoichiometric ratio of Pt/CO was assumed to be unity [27-30]. The catalyst was first reduced in H_2 (Linde, 99.99%) at 300^{o}C for 2 hours. Then, carbon monoxide (Linde, 1000 ppm CO in He) with a flow rate of 15 ml · min^{-1} was adsorbed on the Pt/C surface at 140^{o}C. The reactor was then purged with He (Linde, 100%) at the same temperature and flow rate of 100 ml · min^{-1}. An oxygen flow of 30 ml · min^{-1} (Linde, 99.997%) was then passed through the reactor and the amount of CO_2 formed was measured using an online non-dispersive infrared (NDIR) gas analyzer (HORIBA VA-3001) and gas chromatograph (GowMac 350). This procedure was repeated for different purging times ranging from 5 to 20 min, and the maximum reactive CO uptake was obtained by extrapolating to time equals zero.

5.3.2.5 Thermogravimetric analysis (TGA)

Thermogravimetric profile of Pt/C samples were recorded using a thermogravimetric analyzer (Q500 TGA, TA Instruments). The powder sample was initially out gassed under a flow of ultra high purity (UHP) N_2 at 150ºC for 30 min. Then, it was heated up to 800ºC under flowing air with a heating ramp of 10ºC · min^{-1} from room temperature. The amount of carbon was calculated from the weight loss that occurred above 150ºC.

5.3.3 Catalytic activity

The catalytic activity measurements of Pt/C for ethylene oxidation were carried out at atmospheric pressure in a continuous flow U-shaped quartz reactor using approximately 50 mg of catalyst. The reactive mixture consisted of 909 ppm C_2H_4 (Linde, 5% in He), 3.5% O_2 (Linde, 99.997%) while balance He (Linde, 100%) was used as carrier gas. The total gas flow rate was set at 4.62 $L \cdot h^{-1}$.

All the catalytic tests were performed in the temperature range of 25 - 220^{o}C. The temperature was measured using a thermocouple (Omega, k-type) placed in the close vicinity to the catalyst bed. Before each measurement, the system was maintained for at least 30 minutes in order to ensure that there is no temperature difference between the catalyst bed and the reactor. An on-line gas chromatograph (GowMac 350) and non-dispersive infrared (NDIR) gas analyzer (HORIBA VA-3001) was connected on line in order to quantify the concentrations of ethylene, O_2, and CO_2. Each experiment was repeated for three cycles to evaluate the catalyst stability and reproducibility of the measurements. In some cases, hysteresis between forward and backward ramp is observed, that is less than 1%. Due to the fact that this hysteresis is not observed in all samples, thermal effects are considered negligible in our experiments.

From the outlet concentrations of ethylene and CO_2, ethylene conversion was calculated with the following equation:

$$C_2H_4 \text{ Conversion } (\%) = [CO_2]_{OUT} / (2 \cdot [C_2H_4]_{OUT} + [CO_2]_{OUT}) \times 100\% \quad (5.1)$$

Turn over frequency (TOF) values were calculated using the following equation:

$$TOF = r / N_G \quad (5.2)$$

Where r is the ethylene oxidation rate ($mol \cdot s^{-1}$), and N_G is the moles of active Pt sites (mol).

The intrinsic activity (γ) was calculated as:

$$\gamma = F_{CO_2} / (w \,.\, a_s) \quad (5.3)$$

where F_{CO_2} stands for the molar flow rate of CO_2 exiting the reactor ($mol \cdot s^{-1}$), w is the mass of Pt in the reactor (g), and a_s is the specific surface area ($m^2 \cdot g^{-1}$) of Pt nanoparticles

5.4 Results and Discussion

5.4.1 XRD and TEM of Pt colloids and Pt/C

X-ray diffraction patterns of Pt colloids are shown in Fig. 5-1. The peak around 40^o 2θ corresponds to the Pt (111) reflection, whereas sharp peaks at around 32^o and 46^o are attributed to NaCl phase, which is present as a result of the synthesis procedure. It is worth noting that no NaCl phase was found in Pt/C catalyst. According to the analysis of the XRD data, the formation of Pt colloids with different crystallite sizes is confirmed. The calculated diameters of Pt colloids are summarized in Table 5-1.

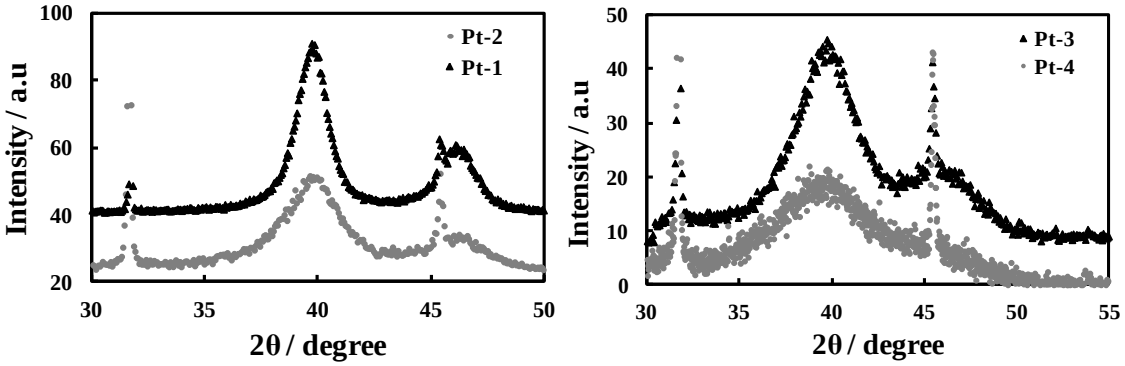

Figure 5-1: X-ray diffraction patterns of Pt colloids showing Pt(111) peak. Colloids numbers are according to Table 5-1.

Table 5-1: XRD characteristics of Pt colloids by polyol reduction method.

Pt Colloid	C_{NaOH} (M)	$2\theta_{max}$ (^{o})	FWHM (^{o})	$FW^3/_4M$ (^{o})	Diameter of Pt colloids (nm) ±5%
1	0.056	39.72	1.59	0.94	7.4
2	0.06	39.64	2.78	1.74	3.8
3	0.08	39.72	3.64	2.22	2.8
4	0.20	39.33	12.76	5.64	1.0

Figure 5-2 shows representative TEM micrographs of colloidal and carbon supported Pt nanoparticles Pt-2 and Pt/C-2 (numbers according to Tables 5-1 and 5-2) and the corresponding histograms.

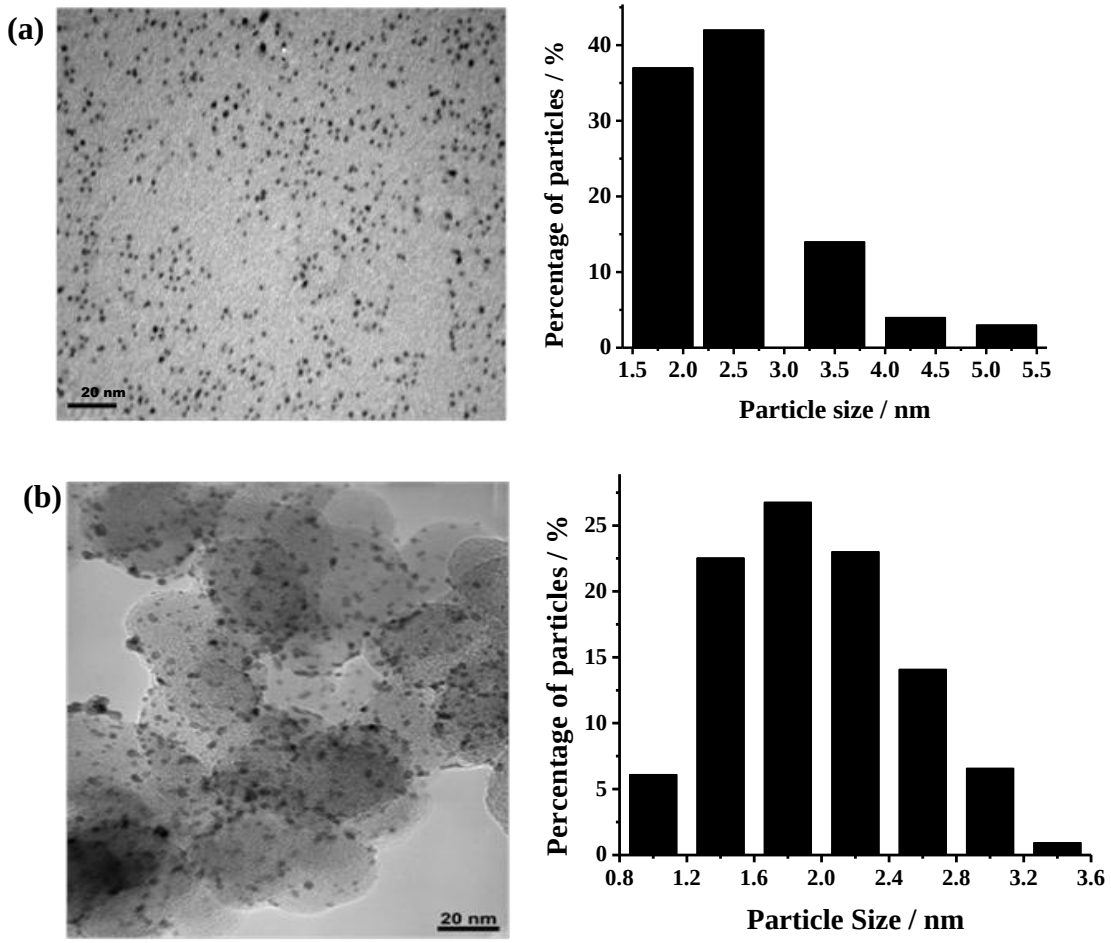

Figure 5-2: TEM image (left) and corresponding histogram (right) of (a) Pt colloids #2 and (b) carbon supported Pt/C-2 catalyst. Catalyst numbers correspond to those in Tables 5-1 and 5-2.

As it can be seen almost spherical Pt colloids were synthesized and they are characterized by a narrow size distribution. When supported on carbon black, the Pt nanoparticles are well dispersed without visible agglomeration. The mean particle sizes of the Pt/C-1, Pt/C-2, Pt/C-3 and Pt/C-4 estimated from TEM are 6.3 ± 0.5, 2.8 ± 0.8, 1.9 ± 1.0 and

1.5 ± 0.5 nm, respectively as shown in Table 5-2. Apparent limitations of TEM is that only small amount of nanoparticles can be evaluated (~300), whereas XRD is a bulk technique. However since carbon has a strong graphite reflections at ~30 and 40^{o} the XRD analysis of Pt/C crystallite sizes from 1 1 1/ 2 0 0 fcc reflections is rather complicated. Furthermore, the 220 reflection that is usually used for XRD analysis of the carbon supported nanoparticles, was not sufficiently intense to carry out the analysis due to the low Pt loading. Despite small discrepancies in the sizes found for colloidal Pt and carbon supported Pt/C, the range of sizes is comparable.

Table 5-2. Characteristics of Pt/C catalysts prepared by polyol reduction method.

Catalyst	Average size fromTEM (nm)	Pt loading[a]	Pt dispersion[b] (%)	E_a(kJ·mol^{-1})
Pt/C-1	6.3±0.5	0.38	5.30	66
Pt/C-2	2.8±0.8	0.43	41.7	40
Pt/C-3	1.9±1.0	0.37	52.0	31
Pt/C-4	1.5±0.5	0.44	68.3	16

[a] determined from ICP
[b] determined from CO titration

5.4.2 Ethylene oxidation on Pt/C

Oxidation of ethylene was carried out over all Pt/C catalysts for three successive heating ramps between 25 up to 220^{o}C. Figure 5-3a shows ethylene conversion as a function of temperature for the three successive heating ramps of Pt/C-4 catalysts of the smallest particle size (1.5 ± 0.5 nm). It was found that all four catalysts show very stable and reproducible performance in the temperature range of interest, indicating low degree of nanoparticle agglomeration and/or detachment from the carbon support, as well as a good stability of the support. As was confirmed by TGA analysis of Pt/C-4 catalyst that was carried

out in air (not shown here), carbon is very stable in the presence of O_2 to temperatures up to 500^{o}C.

To verify ethylene adsorption on carbon alone at low temperatures, 50 mg of carbon blank was tested for ethylene complete oxidation as shown in Fig. 5-3b. Carbon black alone does not show any catalytic activity up to 170^{o}C. At 170^{o}C, about 3.778 % of C_2H_4 conversion is found and complete conversion is noticed at 220^{o}C.

Moreover, carbon balance calculations were performed for all catalysts (not shown here). It is found that the amount of unidentified carbon is negligible in all catalyst and its maximum value is 3.8 % at 160^{o}C for the largest particle Pt/C-1.

The effect of Pt particle size on ethylene oxidation is presented in Figs. 5-3b and 3c, where the ethylene conversion and the intrinsic rate of ethylene oxidation as a function of temperature are depicted, respectively.

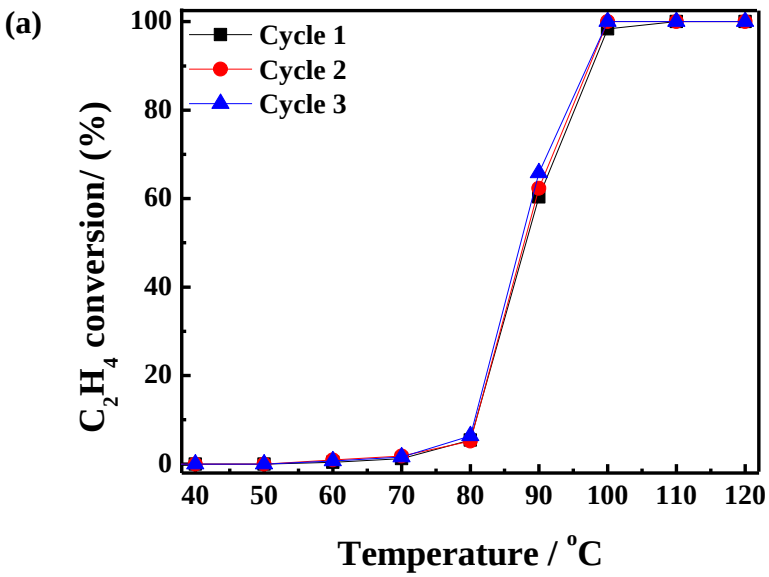

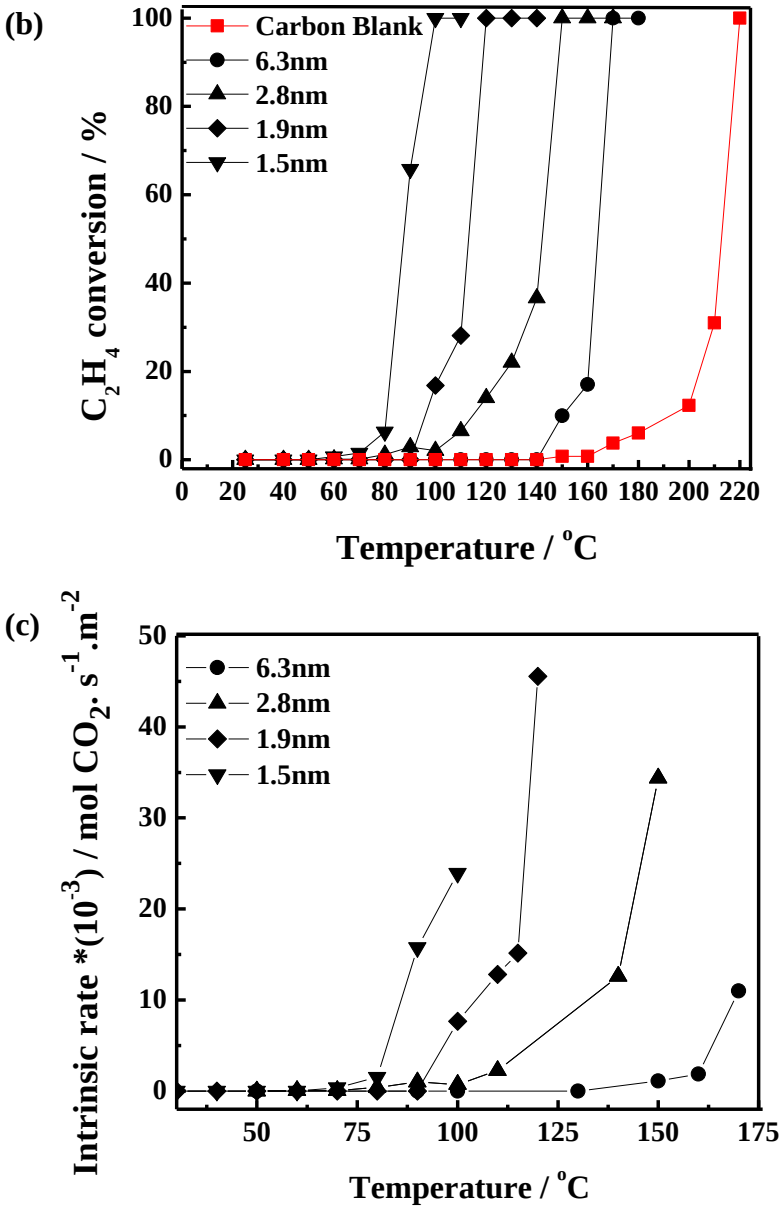

Figure 5-3: Ethylene oxidation over (a) Pt/C-4 nanoparticles repeated for three consecutive cycles, (b) ethylene conversion as a function of temperature over Pt/C catalysts, (c) Intrinsic rate of ethylene oxidation per specific surface area of Pt/C nanocatalysts of various average sizes as indicated in the figure. Space velocity= 14688 h^{-1}, gas composition is 909 ppm C_2H_4, 3.5 % O_2, balance He, total flowrate is 4.62 $L \cdot h^{-1}$.

As particle size decreases, the conversion curve shifts to the left and much lower temperatures are required to completely oxidize ethylene. The obtained results show that the smallest Pt/C-4 nanoparticles (1.5 ± 0.5 nm) exhibit a better catalytic performance than the larger ones. This observation might be assigned to the higher amount of Pt surface atoms that

are available for the reaction, because Pt/C-4 catalyst has the highest dispersion (Table 5-2). It should be mentioned here that Pt dispersion varies substantially among the prepared catalysts, thus the smallest Pt nanoparticles (1.5 ± 0.5 nm) exhibit the highest dispersion (68.3 %) while the largest Pt nanoparticles (Pt/C-1, 6.3 ± 0.5 nm) show a quite low dispersion of only 5.3 %.

In order to investigate the effect of particle size on the kinetics of ethylene oxidation over Pt supported nanoparticles, the largest Pt/C-1 and the smallest Pt/C-4 catalysts were tested for kinetics under different oxygen partial pressures and fixed ethylene partial pressure of 0.092 kPa. Both catalysts follow zero order in oxygen in our fuel-lean experimental conditions (figures not shown here). This is in accordance with order of reactions previously reported in literature for similar conditions [14,32,33].

Figure 5-4a shows the temperature corresponding to 50 % of ethylene conversion (T_{50}) and catalyst dispersion as a function of particle size for all four Pt/C catalysts.

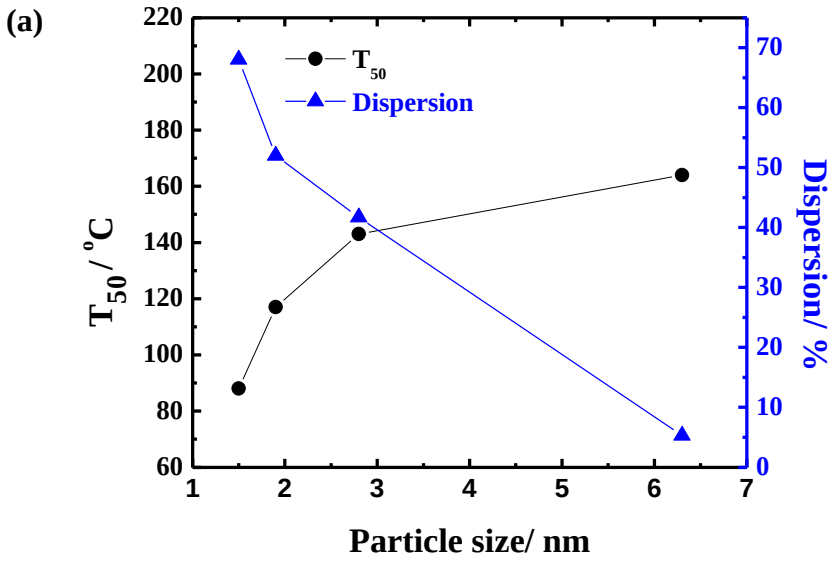

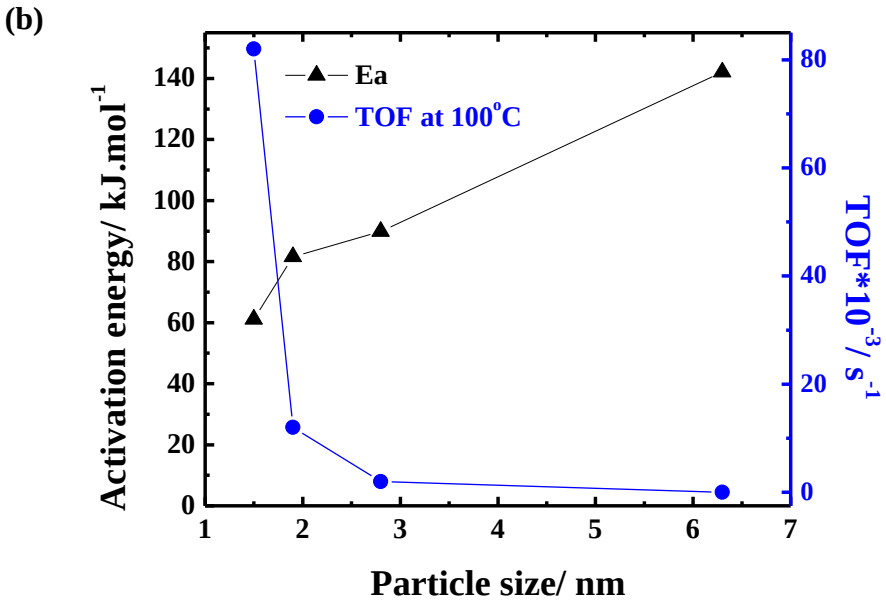

Figure 5-4: (a) Catalyst dispersion and T_{50} vs. Pt/C particle size, (b) Activation energy and TOFs at 100°C as a function of the Pt/C particle size.

In the case of Pt/C-4 catalyst, the 50 % of C_2H_4 conversion is achieved at about 88°C which is 2 times lower than in the case of the largest particle Pt/C-1 of the size (6.3 ± 0.5 nm). Pt/C-4 shows the highest catalytic performance and this is further confirmed by the activation energy for ethylene oxidation, which was determined using Arrhenius relationship calculated in the range below 20 % conversion according to:

$$\ln r = -E_a/(RT) + \ln k \qquad (5.4)$$

where r is ethylene oxidation rate ($mol \cdot s^{-1}$), E_a is the apparent activation energy ($J \cdot mol^{-1}$), R is the universal gas constant ($J \cdot mol^{-1} \cdot K^{-1}$), T is the reactor temperature (K), and k is the rate constant ($mol \cdot s^{-1}$). The activation energies were calculated for each catalyst from the slope of a linear fit in ln$r$ versus 1/T coordinates.

In figure 5-4b, TOFs at 100°C, as well as the calculated activation energies are plotted versus the particle size. As can be seen, the value of E_a increased from 61.1 to 142.1 kJ · mol^{-1} as the average Pt particle size increases from 1.5 to 6.3 nm. These results clearly indicate the strong size sensitivity of C_2H_4 oxidation over Pt/C.

5.4.3 XPS of as-prepared and "spent" Pt/C catalysts

X-ray photoelectron spectroscopy was used to acquire information about the oxidation state of Pt nanoparticles, as well as to shed light on the effect of particle size on the electronic properties of Pt/C catalyst. As we have mentioned in our previous work [34], the characterization of metal nanoparticles using surface sensitive techniques can be a rather complex task. It is well established in the literature that factors like structure, morphology, size and nature of the support can have significant impact on the electronic properties of the nanoparticles and consequently on the obtained data [4,5,11,12,35-39].

The decrease of the particle size is usually accompanied by increasingly positive binding energy shifts. Though, there is a controversy in the literature regarding the origin of these shifts. Some studies have assigned these shifts to changes of the electronic structure of nanoparticles (initial state effects) [36,38,40,41], while others to a positive charge that is produced on the surface of nanoparticles during the photoemission process, named as final state effect [37,42-44]. Moreover, the particle size has been shown [35-39] to influence the full width at half maximum (FWHM) of the recorded XPS spectra and this effect causes the increase of the inherent width of the recorded XPS peaks. This effect is more significant as the size of the nanoclusters decreases.

XPS measurements of Pt/C (supported on Carbon Vulcan) catalysts were carried out before and after the reaction of ethylene oxidation and the deconvoluted Pt4f peaks for all four samples before and after the reaction are shown in Figs. 5-5a and 5-5b, respectively. For comparison, the deconvoluted Pt4f peak of an Ar^+-sputtered platinum foil is also shown. Table 5-3 summarizes the binding energies (BE), FWHM and the relative intensities of each of the components and their assignment.

Table 5-3: Summary of XPS results.

Catalyst	As-prepared Pt/C samples			"Spent" Pt/C samples after reaction			Assignment
	Binding Energy (eV)	FWHM (eV)	% Relative intensities	Binding Energy (eV)	FWHM (eV)	% Relative intensities	
Pt/C-1	71.4	1.0	100	71.4	1.0	100	metallic Pt
Pt/C-2	71.8	1.2	61.1	71.8	1.2	100	metallic Pt
	72.8	1.4	24.5	-	-		Pt^{2+}
	74.6	1.5	14.4	-	-		Pt^{4+}
Pt/C-3	72	1.3	53.5	72	1.3	100	metallic Pt
	72.9	1.5	24.0	-	-		Pt^{2+}
	74.7	1.7	22.5	-	-		Pt^{4+}
Pt/C-4	72.5	1.8	100	72.4	1.8	100	metallic Pt
Sputtered foil	71.1	0.9	100	71.1	0.9	100	metallic Pt

For clarity reason, discussion of the "spent" samples (after reaction) is shown first. As it is seen in Fig. 5-5b, after the reaction, the deconvolution of Pt4f peak in all cases was performed with one asymmetric peak that has the same type of asymmetry as the corresponding Pt4f peak in the case of Pt foil and is attributed to platinum atoms in the metallic state. The comparison of the BE of the recorded peaks for all four samples with the position of the Pt4f peak of the platinum foil shows a gradual shift towards the higher BEs with the decrease of the particle size.

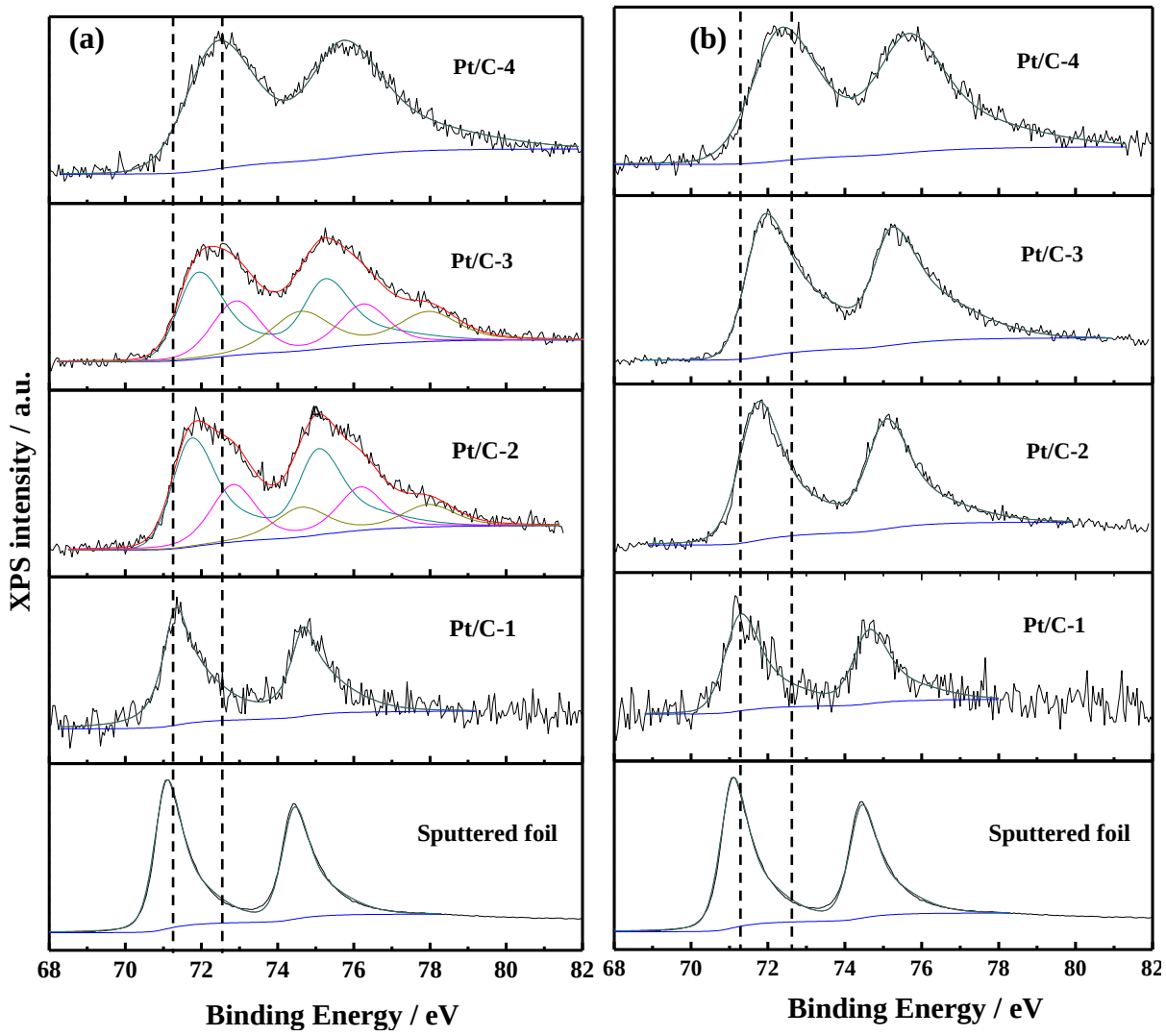

Figure 5-5: X-ray photoelectron spectra of Pt4f levels for (a) as-prepared Pt/C and (b) "spent" Pt/C nanocatalyst. Catalyst numbers correspond to those in Table 5-2.

More specifically, by comparing the position of the peak for the sample with the largest and the smallest particle size, a clear size effect is observed. The smallest particles Pt/C-4 (1.5 ± 0.5 nm) display higher BE shift (~1.3 eV) compared to the largest nanoparticle Pt/C-1 (6.3 ± 0.5 nm) that is about 0.3 eV. Moreover, the particle size has a significant impact on the FWHM of the recorded peaks. In the case of the platinum foil, the FWHM of the Pt4f peak is about 0.9 eV and it gradually increases to 1.8 eV for the catalyst of the smallest particle size (Pt/C-4). The observed changes of the position and of the FWHM of the Pt4f core level peaks with the increase of the particle size can be better depicted by calculating the

difference of the binding energy (ΔBE) and of the FWHM (ΔW) of all four "spent" samples and that of the platinum foil. Thus, in Fig. 5-6, the ΔBE and ΔW is plotted versus the particle diameter for the "spent" Pt/C catalysts.

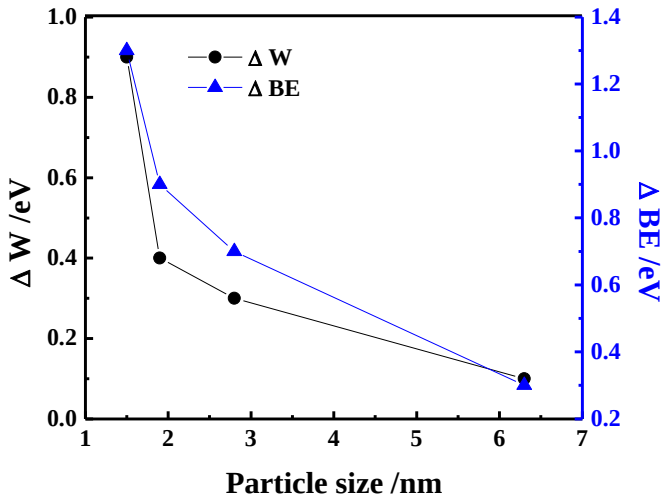

Figure 5-6: Variation of ΔBE and ΔW as a function of the particle size diameter for "spent" catalysts.

The calculated energy difference is rather small in the case of the largest particles but it becomes more pronounced as the particle size decreases. The difference of the width of the Pt4f peaks (ΔW) follows similar behavior and it increases significantly as the size of the platinum clusters decreases. The shift in Pt4f binding energies and the changes in the peak width as the size of Pt nanoparticle decreases are in good agreement with the experimental results reported elsewhere for Pt and other metal nanoparticles deposited on different supports [35-39]. In order to gain a better insight into the oxidation state of the as-prepared samples, XPS analysis of Pt/C samples was carried out before the reaction. The Pt4f peaks of samples Pt/C-1 and Pt/C-4 are detected at similar BEs and show the same FWHM as the corresponding catalysts after reaction indicating that under the corresponding synthesis condition the synthesized Pt nanoparticles are in the metallic state. On the other hand in the case of the samples Pt/C-2 and Pt/C-3, the XPS analysis shows the existence of platinum atoms in higher oxidation states as well. More specifically, the analysis shows the existence of two peaks at 72.8 - 72.9 eV and at 74.6 - 74.7 eV. These peaks are attributed to platinum atoms in the 2+

and 4+ oxidation states, respectively [34,45-47]. The fact that in all four samples the recorded peaks are detected at the same binding energy before and after the reaction strongly suggests that no agglomeration of the particles takes place, which would cause a shift of the binding energy of the recorded peaks. The existence of oxygen atoms attached to the carbon substrate makes it difficult to assign the higher oxidation states of platinum to a particular compound, i.e., PtO_2 or $Pt(OH)_4$. According to the XPS measurements of our samples, metallic platinum nanoparticles are synthesized in ethylene glycol in the presence of low (C_{NaOH} = 0.056 M) and high sodium hydroxide (C_{NaOH} = 0.2 M) concentrations, whereas intermediate NaOH concentrations (C_{NaOH} = 0.06 and 0.08 M) led to the formation of partially oxidized Pt colloids. From the above finding it is clear that the synthesis reaction conditions seem to influence the oxidation states of the as-synthesized platinum nanoparticles. Furthermore, during the ethylene oxidation reaction, the Pt nanoparticles are reduced to the metallic state independently of their size.

Therefore, for both sets of catalysts, i.e., before and after reaction, the clear shift to higher BEs and FWHM broadening of Pt4f peak is observed as particle size decreases. It is generally accepted that the physical and electronic properties of transition metal nanoparticles exhibit strong variations with their size. Bulk Pt metal exhibits a work function of ~5.3 eV while it increases to 9 eV for a single atom [48]. This indicates that by varying the nanoparticle size their activity could be strongly affected. The positive core level shift of XPS peaks, which is inversely proportional to the particle size, has been attributed to inefficient screening of the final state of the photoemission process, though initial state effects could play a role.

The decrease of the particle size causes reduction of the lattice strain that can lead to positive shifts of the obtained binding energies and consequently the rehybridization of the valence *d* and *sp* orbitals. Moreover, the metal - support or metal oxide- support charge transfer [49], and/or the particle geometry related to particle size [50] as well as the concentration of under coordinated atoms that increases as the particle size decreases can interpret the core level shifts. The XPS information by itself might not be enough to explain the origin of the binding energy shift and to distinguish between the initial and final state effects. Though it has been shown that the contribution of the initial state effect is generally

significantly smaller than that of final state effect at least in the case of metal particles supported on oxide substrates [51,52].

According to the observed catalytic performance of the Pt/C particles for ethylene complete oxidation, the smaller particles exhibit higher catalytic activity than the larger ones. It is known that the chemisorption strength between adsorbate and metal depends on the degree of filling of the antibonding states of coupling orbital. Thus, the change of the d-band center energy of Pt particles induced by the particle size decrease can affect the adsorption strength of ethylene. Furthermore, small particles comprise larger fraction of low-coordinate metal atoms. These metal atoms are characterized by high amount of edge and corner sites, thus binding reactants and intermediates differently and often more strongly. Combination of all above phenomena might be the reason for the better performance of the smaller Pt/C nanoparticles. Further studies are in progress so as to have deeper insight of the particles size effect and the role of the substrate on the obtained XPS data and the catalytic performance of the Pt/C nanoparticles.

5.5 Conclusions

Carbon supported Pt nanoparticles show high catalytic activity towards ethylene oxidation and this reaction is strongly size-dependent. XRD and TEM revealed that Pt/C nanoparticles of four well-defined sizes and face-centered structure are obtained. It was found that ethylene oxidation reaction remarkably depends on Pt particle size and catalyst dispersion. The smallest Pt/C-4 (1.5 ± 0.5 nm) nanoparticles show the highest catalytic activity of ethylene oxidation and some activity at ~50^{o}C. For the largest Pt/C-1 (6.3 ± 1nm) particles, much higher temperature ~160^{o}C is required to start ethylene oxidation. Smaller Pt/C nanoparticles are characterized by lower activation energy and earlier complete ethylene oxidation compared to larger nanoparticles. XPS measurements revealed that as-synthesized Pt/C catalysts contain surface atoms in Pt^{0}, Pt^{2+} and Pt^{4+}, while only the samples with the smallest and the largest particle size are in the metallic state. After ethylene oxidation though, Pt is in the metallic state in all cases, indicating that Pt undergoes reduction during the reaction of ethylene oxidation. As particle size decrease, the BEs of Pt4f shift to the higher values if compared with the bulk Pt, while the FWHM decreases considerably. These findings indicate the modification of the electronic properties of Pt as the size of clusters becomes

smaller. The modification of the electronic properties may be responsible for the enhancement of the catalytic properties of smaller Pt/C-4 (1.5 ± 0.5 nm) catalyst.

5.6 Acknowledgement

Financial support from Natural Science and Engineering Research Council (NSERC) and Ontario Graduate Scholarship (OGS) are acknowledged. In context of this, I would like to acknowledge Dr. Nimal de Silva (Dept. Earth Sciences at UOttawa) for running ICP measurements. Dr. Yun Liu (Centre for Catalysis Research and Innovation (CCRI)) at the University of Ottawa for taking TEM images of the colloidal catalysts. Microscopy services at Institut de Recherches sur la Catalyse et L'environnment de Lyon (IRCELYON) for TEM images of the supported catalysts. Dr. Spyridon Ntais for running x-ray photoelectron spectroscopy (XPS) measurements and analyzing related data for this chapter.

5.7 References

[1] G. C. Bond, *Chem. Soc. Rev*. 20 (1991) 441.

[2] B. Coq, F. Figueras, *Coord. Chem. Rev*. 180 (1998) 1753.

[3] R. J. Gilliam, D.W. Kirk, S. J. Thorpe, *Electrocatal*. 2 (2011) 1.

[4] J. R. Croy, S. Mostafa, J. Liu, Y. Sohn, B. R. Cyenua, *Catal. Lett*. 118 (2007) 1.

[5] J. R. Croy, S. Mostafa, J. Liu, Y. Sohn, H. Heinrich, B. R. Cyenua, *Catal. Lett.* 119 (2007) 209.

[6] I. E. Beck, V. I. Bukhtiyarov, I. Y. Pakharukov, V. I. Zaikovsky, V. V. Kriventsov, V. N. Parmon, *J. Catal*. 268 (2009) 60.

[7] F. Diehl, J. Barbier, D. Duprez, I. Guibard, G. Mabilon, *Appl. Catal*. B 95 (2010) 217.

[8] X. E. Verykios, F.P. Stein, R.W. Coughlin, *Catal. Rev*. 22 (1980) 197.

[9] U. Ackelid, L. R. Wallenberg, L. Petersson, *Catal. Lett*. 39 (1996) 129.

[10] D. -J. Ahn, C. Ho-Geun, L. Byoung-Min, *J. Nanosci. Nanotechno*. 6 (2006) 3599.

[11] S. Rojluechai, S. Chavadej, J. W. Schwank, V. Meeyoo, *Catal. Commun*. 8 (2007) 57.

[12] S. Chavadej, K. Saktrakool, P. Rangsunvigit, L. L. Lobban, and T. Sreethawong, *J. Chem. Eng*. 132 (2007) 345.

[13] G. M. Schwab, K. Gossner, *Annu. Rev. Phys. Chem*.14 (1963) 177.

[14] S. Bebelis , M. Makri , A. Buekenhoudt , J. Luyten , S. Brosda , P. Petrolekas ,C. Pliangos , C. G. Vayenas, *Solid State Ionics*. 129 (2000) 33.

[15] A. F. Carlsson, R. J. Madix, *J. Chem. Phys*. 115 (2001) 8074.

[16] D. L. Smith, R. Merrill, *J. Chem. Phys*. 52 (1970) 5861.

[17] A. E. Morgan, G. A. Somorjai, *J. Chem. Phys*. 51 (1969) 3309.

[18] A. Van Strien, B. E. Nieuwenhuys, *Surf. Sci*. 80 (1970) 226.

[19] G. A. Somorjai, *Science*. 227 (1985) 902.

[20] G. A. Somorjai, *Science*. 201 (1978) 489.

[21] R. A. Van Santen, H. P. Kuipers, Adv. Catal. 35 (1987) 265.

[22] S. Schimpf, M. Lucas, C. Mohr, U. Rodemerck, A. Brückner, J. Radnik, H. Hofmeister, P. Claus, *Catal. Today* 72 (2002) 63.

[23] E. A. Baranova, Y. Le Page, D. Ilin, C. Bock, B. MacDougall, P. H. J. Mercier, *J. Alloy Comp*. 471 (2009) 387.

[24] E. A. Baranova, C. Bock, D. Ilin, D. Wang, B. Macdougall, *Surf. Sci*. 600 (2006) 3502.

[25] S. Hufner, G. K. Wertheim, *Phys. Rev*. B 11(2) (1975) 678.

[26] C. G Vayenas, S. Bebelis, I. Yentekakis, H. Lintz, *Catal. Today*. 11 (1992) 303.

[27] M. Alves Fortunato, D. Aubert, C. Capdeillayre, C. Daniel, A. Hadjar, A. Princivalle , C. Guizarda, P. Vernoux, *Appl. Catal. A: General*. 403 (2011) 18.

[28] R. M. Rioux, J. D. Hoefelmeyer, M. Grass, H. Song, K. Niesz, P. Yang, G. A. Somorjai, *Langmuir*. 24 (2008) 198.

[29] S. -I. Kim, T. Yamamoto, A. Endo, T. Ohmori, M. Nakaiwa, *J. Ind. Eng. Chem*. 12 (2006) 769.

[30] M. Marwood, C. G. Vayenas, *J. Catal*. 178 (1998) 429.

[31] M. H. Kim, J. R. Ebner, R. M. Friedman, M. A. Vannice, *J. Catal*. 208 (2002) 381.

[32] C. G. Vayenas, S. Bebelis, I. V. Yentekakis, P. Tsiakaras, H. Karasali, *Platinum Met. Rev*. 34 (1990) 122.

[33] S. Bebelis, C.G. Vayenas, *J. Catal*. 118 (1989) 125.

[34] A. Allagui, M. Oudaha, X. Tuaev, S. Ntais, F. Almomani, E. A. Baranova, *Intl. J. Hydrogen Energ*. 38 (2013) 2455.

[35] P. Marcus, C. Hinnen, *Surf. Sci*. 392 (1997) 134.

[36] P. Zhang, T. K. Sham, *Phys. Rev. Lett*. 90 (2003) 245502/1.

[37] J. Radnik, C. Mohr, P. Claus, *Phys. Chem. Chem. Phys*. 5 (2003) 172.

[38] I. Lopez-Salido, D. C. Lim, R. Dietsche, N. Bertram, Y. D. Kim, *J. Phys. Chem. B* 110 (2006) 1128.

[39] S. Garbarino, A. Pereira, C. Hamel, E. Irissou, M. Chaker, D. Guay, *J. Phys. Chem. C* 114 (2010) 2980.

[40] M. G. Mason, *Phys. Rev. B* 27 (1983) 748.

[41] B. Richter, H. Kuhlenbeck, H.-J. Freund, P. S. Bagus, *Phys. Rev. Lett*. 93 (2004) 0268051.

[42] G. K. Wertheim, S. B. DiCenzo, S. E. Youngquist, *Phys. Rev. Lett*. 51 (1983) 2310.

[43] B. R. Cuenya, S. H. Baeck, T. F. Jaramillo, E. W. McFarland, *J. Am. Chem. Soc*. 125 (2003) 12928.

[44] A. Tanaka, Y. Takeda, M. Imamura, S. Sato, *Phys. Rev. B* 68 (2003) 1954151.

[45] S. Hu, L. Xiong, X. Ren, C. Wang, Y. Luo, *Int. J. Hydrogen Energ*. 43 (2009) 8723.

[46] Y. Liang, H. Zhang, H. Zhong, X. Zhu, Z. Tian, D. Xu, B. Yi, *J. Catal*. 238 (2006) 468.

[47] D. Briggs and M. P. Seah, Practical Surface Analysis, 2nd edition. New York, 1996.

[48] E. Roduner, *Chem. Soc. Rev*. 35 (2006) 583.

[49] D.W. Goodman, *Chem. Rev*. 95 (1995) 523.

[50] S. H. Overbury, L. Ortiz-Soto, H. Zhu, B. Lee, M. D. Amiridis, S. Dai, *Catal. Lett.* 95 (2004) 99.

[51] S. Zafeiratos, S. Kennou, *Surf. Sci*. 443 (1999) 238.

[52] K. Luo, X. Lai, C.-W. Yi, K. A. Davis, K. K. Gath, D. W. Goodman, *J. Phys. Chem. B* 109 (2005) 4064.

SECTION IV: IONIC VS. NON IONIC CONDUCTIVE SUPPORTS

6 Metal-Support Interaction of Pt Nanoparticles with Ionically and Non-Ionically Conductive Supports for CO Oxidation

Electrochemical and Solid State Letters 15(3) (2012) E14-E17.

6.1 Abstract

Platinum nanoparticles of narrow size distribution (~ 2.5 nm) were synthesized using a modified polyol method and deposited on yttria-stabilized zirconia (Pt/YSZ), carbon (Pt/C) and γ-alumina (Pt/γ-Al_2O_3) supports, resulting in 1 wt. % of Pt loading. It was found that Pt/YSZ catalysts have the highest catalytic activity towards CO oxidation among the studied catalysts. Decrease in the average particle size of Pt/YSZ led to an increase in CO conversion at low temperatures. Enhanced performances can be explained by the thermally-induced O^{2-} backspillover from YSZ over Pt nanoparticles in agreement with the electrochemical promotion mechanism. Observed effect becomes more pronounced with decreasing the particle size.

6.2 Introduction

Electrochemical promotion of catalysis (EPOC) is a phenomenon where the catalytic activity and selectivity of conductive catalysts deposited on solid electrolytes can be altered significantly and reversibly by applying small currents or potentials between the catalysts and a counter electrode [1-4]. Stoukides and Vayenas [1] were the first to show that the migration of ionic species from a solid electrolyte to the catalyst surface induced by electrical polarization can considerably improve the catalytic activity, and in some cases, selectivity. This phenomenon has been applied to numerous catalytic systems [2], including treatment of automotive exhaust and oxidation of volatile organic compounds (VOCs) [5-8]. Yttria-stabilized zirconia (YSZ) is one of the most studied solid electrolytes in EPOC catalytic systems and is known to be an O^{2-} conductor due to the presence of oxygen vacancies inside

its crystallographic structure. Recently, it was found that EPOC effect, e.g. backspillover of ionic species from the support to the gas-exposed catalyst surface, can be thermally induced without any electrical polarization by using metallic nanoparticles supported on ionically conducting ceramics, such as YSZ [9,10].

In the present work, Pt nanoparticles with the average particle size of 1.8 to 2.8 nm supported on YSZ, as well as on the larger surface area supports: γ-alumina and carbon black were tested in the model reaction of CO oxidation in the temperature range 25 - 250^{o}C. The effect of the support nature, as well as the Pt particle size on the rate of CO oxidation was investigated.

6.3 Experimental

6.3.1 Catalyst synthesis

Pt nanoparticles deposited on YSZ (Pt/YSZ), carbon (Pt/C) and γ-Al_2O_3 (Pt/ γ-Al_2O_3) were synthesized using a modified polyol reduction method [11-13]. In short, colloidal Pt nanoparticles were synthesized in ethylene glycol (anhydrous 99.8% Sigma Aldrich) at 160 ^{o}C, using $PtCl_4$ (Alfa Aesar, 99.9% metals basis) as a precursor salt [14]. Three Pt colloids were prepared using different sodium hydroxide concentrations (EM Science, ACS grade) (C_{NaOH} = 0.06, 0.08 and 0.15 M) and deposited on 8 mol % Y_2O_3-stabilized ZrO_2 (YSZ) (Tosoh, specific surface area (a_s) ~13 $m^2 \cdot g^{-1}$), carbon black (Vulcan XC-72R, Cabot Corp. a_s = 254 $m^2 \cdot g^{-1}$) and on γ-alumina (Alfa-Aesar, a_s = 120 $m^2 \cdot g^{-1}$) supports. Further details of the catalyst preparation are described in reference 14. The list of the prepared catalysts is summarized in Table 6-1. A reference catalyst of Pt/YSZ (reference catalyst) was prepared using a conventional wet impregnation method [10,15,16].

6.3.2 Transmission electron microscopy

Transmission electron micrographs of Pt nanoparticles deposited on YSZ and carbon were obtained using JEOL 2010 LaB6 [14]. An extraction replica technique was used for Pt/YSZ sample preparation [15,17]. The size distribution was carried out using the Image J software by measuring at least 200 nanoparticles from the TEM images.

6.3.3 Dispersion

Dispersion measurements of Pt/YSZ and Pt/C catalysts were performed using the CO titration method [18]. These results were compared to the dispersion estimated from TEM images using the following formula, considering spherical particles:

$$\text{dispersion } (\%) = \left(600 \cdot M_{Pt}\right) / \left(\rho \cdot d_{nm} \cdot a_{Pt} \cdot N_a\right) \quad (6.1)$$

where M_{Pt} is the molecular weight (195.08 g·mol^{-1}), a_{Pt} is the atomic surface area (8.06×10^{-20} m²/atom), ρ is the metal density (21.09 g·cm^{-3}), N_a is Avogadro's number, and d_{nm} is the average particle diameter estimated from TEM in nanometer [19].

6.3.4 Inductively Coupled Plasma (ICP)

ICP measurements were used to evaluate the Pt loading on the supports using (ICP-OES Varian Vista-Pro CCD spectrometer). ICP results are summarized in Table 6-1.

6.3.5 Catalytic Activity

Detailed description of the reaction set-up and conditions are presented in [14]. CO oxidation on the Pt catalysts was carried out at atmospheric pressure in a continuous flow quartz reactor [10]. Details of the reaction gas mixture composition are presented in [14]. The product gases were analyzed with an on-line micro-chromatograph (µGC-R3000 SRA instruments). CO_2 concentration in the outlet of the reactor was monitored by a non-dispersive infrared (NDIR) analyzer (HORIBA, VA-3000).

6.4 Results and Discussion

Figure 6-1a, and 6-1b shows representative TEM micrographs of Pt/YSZ2 and Pt/C2 catalysts synthesized in ethylene glycol at C_{NaOH} = 0.08M and the corresponding histograms. Average particle size is summarized in Table 6-1 for all catalysts. For both Pt/YSZ (YSZ1 – YSZ3) and Pt/C (C1 – C3) catalytic systems, the average particle size decreases with increasing C_{NaOH}. As was shown in a previous work [14], pH of the synthesis solution affects the resulting particle size and larger pH values lead to the formation of the smaller particles. Average sizes of Pt/YSZ catalyst were found to be 2.8, 2.6 and 2.1 nm for 0.06, 0.08 and 0.15

M of NaOH, respectively. The average size of Pt deposited on C is slightly smaller 2.0, 1.9 and 1.8 nm for 0.06, 0.08 and 0.15 M, respectively, however follows the trend, i.e., higher amount of NaOH in the synthesis solution results in the smaller Pt nanoparticles. It is worth to note that the same precursor colloids were used for the catalyst preparation, whereas smaller sizes are obtained for Pt/C systems than for Pt/YSZ for the nanoparticles synthesized at the same pH, e.g., 2.6 nm vs. 1.9 nm for YSZ1 and C1, respectively. Observed particle size difference can be attributed to the much higher specific surface area (254 $m^2 \cdot g^{-1}$) of carbon if compared to YSZ (13 $m^2 \cdot g^{-1}$), which prevents particle agglomeration.

Table 6-1: Characteristics of Pt nanoparticles supported on YSZ and carbon prepared by a modified polyol method.

Catalyst	C_{NaOH} (M)	Average particle size (nm)†	Pt Dispersion * (%)	Pt Dispersion # (%)	Pt loading (wt. %)‡	TOF (s^{-1})* ($\times 10^{-3}$) at 60°C	TOF (s^{-1})* ($\times 10^{-3}$) at 100°C
YSZ1	0.06	2.8	25	41	1.1	1.2	6.6
YSZ2	0.08	2.6	16	44	1.1	1.7	18.8
YSZ3	0.15	2.1	27	54	0.9	2.1	20.9
C1	0.06	2.0	22	57	1.0	-	0.3
C2	0.08	1.9	44	60	1.0	-	0.3
C3	0.15	1.8	77	63	1.0	-	0.1
GALMA2	0.08	2.2	-	52	0.7	-	5.6##

† determined from TEM
* determined from CO titration
# estimated from TEM (eqn. 6.1)
from calculated dispersion value
‡ estimated from ICP

As seen from Table 6-1, the Pt dispersion, estimated from CO titration, in Pt/YSZ catalysts does not vary significantly with NaOH concentration, whereas dispersion in Pt/C strongly increases from 22 to 77% with the NaOH concentration. Let us note that the Pt dispersions calculated from TEM observations are overestimated certainly because the statistic determination of the mean diameter is not accurate due to the heterogeneity of the samples.

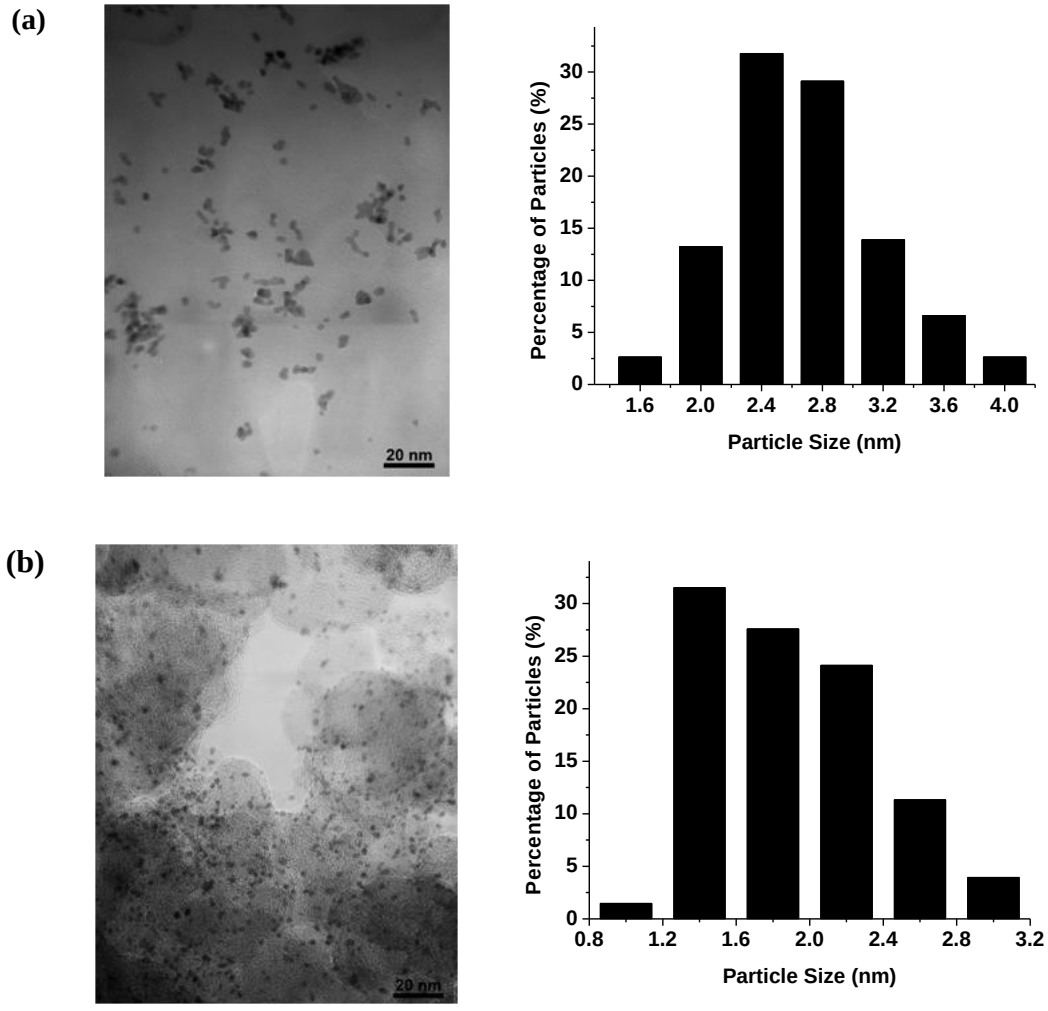

Figure 6-1: TEM image (left) and corresponding histogram (right) of (a) Pt/YSZ2 catalyst prepared at 0.08M of NaOH; (b) Pt/C2 catalysts prepared at 0.08M of NaOH.

Oxidation of CO was repeated at least for three successive heating ramps between 25 and 250^{o}C for each catalyst. It was found that Pt/YSZ and Pt/C systems show very stable and reproducible performance in the temperature range of interest. Figure 6-2 shows CO oxidation

on Pt nanoparticles prepared at C_{NaOH} = 0.08M deposited on YSZ (YSZ2), carbon (C2) and γ-alumina along with the activity of the reference catalyst (Pt/YSZ (ref)) synthesized by the wet impregnation technique on YSZ. The performance of the Pt/YSZ2 sample showed better activity than C2 and Pt/γ-Al_2O_3 sample. In spite of the specific surface area of Pt/γ-Al_2O_3 being 10 times larger than Pt/YSZ, as well as a higher Pt dispersion the γ-Al_2O_3-supported sample exhibits lower performances than YSZ2.

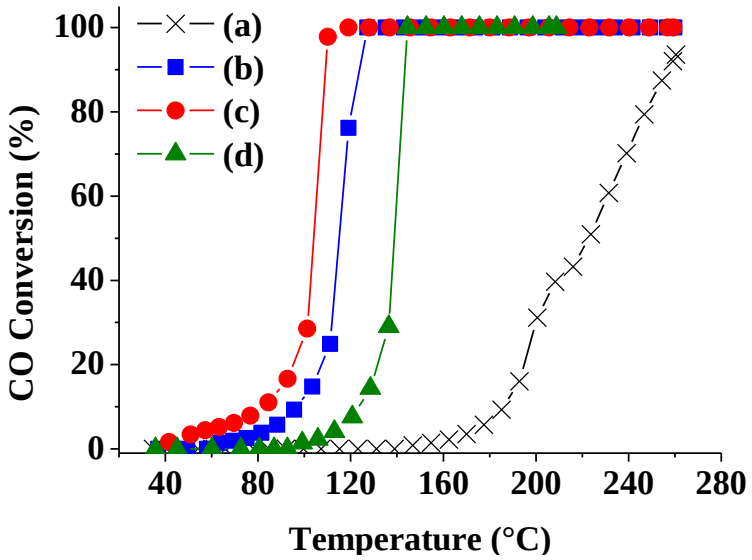

Figure 6-2: Comparison of catalytic performances for CO oxidation of Pt nanoparticles deposited on (a) Pt/YSZ (ref) by wet impregnation, (b) Pt/γ-Al_2O_3; (c) Pt/YSZ2; and (d) Pt/C2. Space velocity = 19000 h^{-1}, gas composition: total flowrate = 4.3 $L \cdot h^{-1}$, 770 ppm CO, 4.4% O_2, He balance.

In addition, the wet impregnation catalyst showed poor catalytic performance with a CO conversion starting from 160°C instead of 40°C for catalysts synthesized using the modified polyol method. This confirms that the modified polyol method produces smaller Pt nanoparticles with narrow size distribution than the conventional impregnation route, therefore improving the interactions between YSZ and Pt.

Effect of Pt particle size on the turnover frequency (TOF), which reflects the catalytic activity of the Pt/YSZ samples is shown in Figure 6-3 TOF values were calculated using the dispersion values found from CO titration The results demonstrate that the best performance is achieved by the smallest nanoparticles (2.1 nm), due to the higher amount of the surface active

sites. The smaller the size of the nanoparticle, the earlier the 100% conversion of CO is achieved.

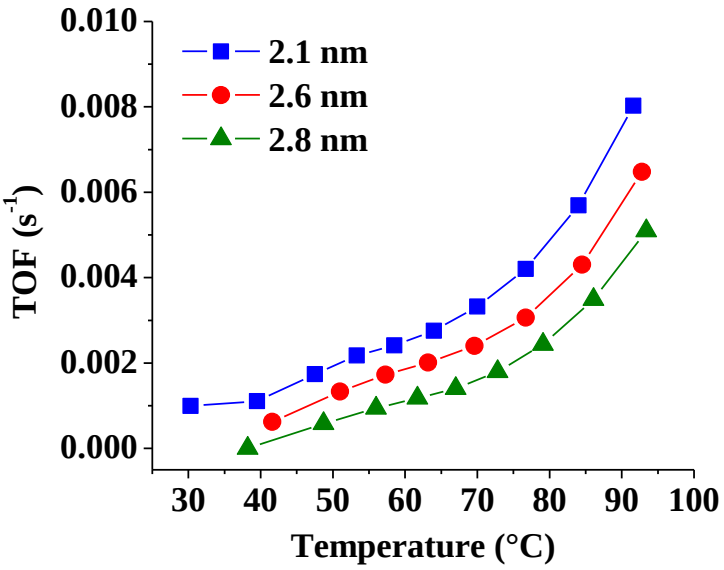

Figure 6-3: Particle size effect on turnover frequency, calculated using the dispersion values found from CO titration (Table 6-1) of Pt/YSZ catalysts. Space velocity = 19000 h^{-1}, gas composition: total flowrate = 4.3 $L \cdot h^{-1}$, 770 ppm CO, 4.4% O_2, He balance.

Table 6-1 summarizes the turnover frequency (TOF) for Pt catalysts at 60°C and 100°C, which was calculated using the following equation.

$$TOF(s^{-1}) = \frac{r}{n_{tot} \times \text{dispersion}(\%)} \qquad (6.2)$$

where r is the rate of CO oxidation ($mol \cdot s^{-1}$), n_{tot} is the total number of Pt moles in the catalytic reactor and dispersion estimated from the CO titration experiments. TOF is higher for Pt/YSZ catalysts of different average sizes if compared to three Pt/C materials. The highest TOF values were obtained for the smallest Pt nanoparticles (2.1 nm) supported on YSZ, which confirm their high catalytic activity for CO oxidation more than two times higher than for 2.8 nm Pt/YSZ particles. This can be attributed to the increase in the number of surface active sites for smaller Pt nanoparticles, because the ratio of the surface to bulk atoms increases with decreasing the size. Another explanation of the particle size effect might be related to the

improved interaction between Pt and YSZ for smaller particles. The TOF values recorded on Pt/C samples at 100^{o}C are much lower than those measured on YSZ supported catalysts despite the fact that the specific surface area of Pt/C is 20 times higher than Pt/YSZ catalysts. These results confirm that YSZ support strongly affects the catalytic activity of Pt. Among the three studied supports, only YSZ has an ionic conductivity and a presence of oxygen vacancies. This suggests the promoting role of O^{2-} ionic species containing in YSZ on the catalytic activity of Pt for CO oxidation. The promoting effect of O^{2-} for CO oxidation over Pt/YSZ film-catalyst was already demonstrated in the classical EPOC system, i.e., under applied polarization [21,22]. In the present case, similar backspillover mechanism of O^{2-} is presumed to occur in self-induced EPOC configuration without the application of an external current or potential. The driving force of O^{2-} backspillover is a difference in the work functions of YSZ and Pt nanoparticles, this interaction would plausibly increase as nanoparticles become smaller and diffusion distances for O^{2-} shorten. Detailed investigations of Pt/YSZ system will shed light on the mechanism of the self-induced EPOC.

6.5 Conclusions

Platinum nanoparticles of well controlled sizes and narrow size distribution were prepared by the modified polyol method and deposited on YSZ, carbon and γ-Al_2O_3 supports. Pt nanoparticles were found to be active and stable for CO oxidation at low temperatures (40 - 60^{o}C). Catalyst support plays an important role in the catalytic performance of Pt nanoparticles. Thus, Pt nanoparticles of 2.6 nm in size supported on YSZ show the highest catalytic activity followed by Pt supported on γ-alumina and then on carbon. High catalytic activity of Pt/YSZ is due to the thermally induced electrochemical promotion of Pt. Decreasing of the average particle size from 2.8 to 2.1 nm for Pt/YSZ catalyst further improved CO conversion at low temperatures, i.e., from 40^{o}C. Particle size effect was attributed to the higher active surface area of the smaller Pt nanoparticles and their improved contact with YSZ support.

6.6 Acknowledgement

Natural Science and Engineering Research Council (NSERC) for financial support. In context of this, I would like to acknowledge Dr. Nimal de Silva (Dept. Earth Sciences) for

running ICP measurements. Microscopy services at Institut de Recherches sur la Catalyse et L'environnment de Lyon (IRCELYON) for TEM images of the supported catalysts. Holly Dole for conducting the CO oxidation experiments. Dr. Phillipe Vernoux, Emil Obeid and Leonardo Lizarraga (IRCELYON) for their valuable comments for the manuscript in this chapter.

6.7 References

[1] M. Stoukides and C. G. Vayenas, *J. Catal.*, 70 (1981) 137.

[2] C. G.Vayenas, S. Bebelis, C. Plaingos, S. Brosda, D. Tsiplakides *Electrochemical Activation of Catalysis: Promotion, Electrochemical Promotion and Metal-Support Interaction*, Plenum Publishers, New York, (2011).

[3] S. Bebelis, C. G. Vayenas, *J. Catal.*, 118 (1989) 125.

[4] N. Anastasijevic, *Catal. Today*, 146 (2009) 308.

[5] A. Piram, X. Li , F. Gaillard , C. Lopez , A. Billard, P. Vernoux, *Ionics*, 11 (2005) 327.

[6] A. Katsaounis, *J. Appl. Electrochem.*,40 (2009) 885.

[7] C. Koutsodontis, A. Katsaounis, J. C. Figueroa, C. Cavalca, C. Pereira, and C. G. Vayenas, *Topics in Catal.*, 39 (2006) 97.

[8] S. Souentie, A. Hammad, S. Brosda, G. Foti, *J. Appl. Electrochem. 38 (2008) 1159.*

[9] J. Nicole, D. Tsiplakides, C. Pliangos, X. E. Verykios, Ch.Comninellis, C. G. Vayenas, *J.Catal*. 204 (2001) 23.

[10] P. Vernoux, M. Guth and X. Li, *Electrochem. Solid-State Lett.*, 12 (2009) E9.

[11] C. Bock, C. Paquet, M. Couillard, G. A. Botton, B. R. MacDougall, *J. Am. Chem. Soc.*,126 (2004) 8028.

[12] E. A. Baranova, T. Amir, P. H. J. Mercier, B. Patarachao, D. Wang, Y. Page, *J. Appl. Electrochem.*, 40 (2010) 1767.

[13] E. A. Baranova, C. Bock, D. Ilin, D. Wang B.R. MacDougall, *Surf. Scie.*, 600 (2006) 3502.

[14] R. Isaifan, H. Dole, E. Obeid, L. Lizarraga, E. A. Baranova, P. Vernoux, *ECS Trans., Electrocatalysis 5*, 35 (2011) 43.

[15] M. Alves Fortunato, D. Aubert, C. Capdeillayre, C. Daniel, A. Hadjar, A. Princivalle, C. Guizard, and P. Vernoux, *Appl. Catal. A: General*, 403 (2011) 18.

[16] M. Boudart and G. Djega-Mariadassou, Handbook of Heterogeneous Catalytic Reactions, NY: Princeton University Press 1984.

[17] J. Ayache, L. Beaunier, J. Boumendil, G. Ehret, and D. Laub, Sample Preparation Handbook for Transmission Electron Microscopy, Chapter 5 Replica Techniques, Springer (2010).

[18] C. G. Vayenas, S. Bebelis, I. V. Yentekakis, H. G. Lintz, *Catal. Today*, 11 (1992) 303.

[19] M. Boudart, *Adv. Catal*., 20 (1969) 153.

[20] P. Vernoux, F. Gaillard, L. Bultel, E. Siebert, M. Primet, *J.Catal.*, 208 (2002) 412.

[21] M. N. Tsampas, F. M. Sapountzi, and C. G. Vayenas, *Catal. Today*, 146 (2009) 351.

[22] L. Lizarraga, S. Souentie, L. Mazri, A. Billard, P. Vernoux, *Electrochem. Commun*. 12 (2010) 131.

7 Effect of ionically conductive supports on the catalytic activity of platinum and ruthenium nanoparticles for ethylene complete oxidation

Journal of Catalysis Today (2014) CATTOD-S-14-00030 (in press).

7.1 Abstract

The effect of the support nature on the catalytic activity of platinum and ruthenium nanoparticles is investigated for ethylene complete oxidation in the temperature range of 25 - 220^{o}C. The nanoparticles (NPs) were deposited on ionically conductive supports: yttria-stabilized zirconia (YSZ) and samarium-doped ceria (SDC), and on non-ionically conductive supports: carbon black (C) and gamma-alumina (γ-Al_2O_3) to give $\leq$ 0.7 wt. % loading and an average particle sizes of 1.9 – 2.9 nm depending on the support. The presence of O^{2-} ionic conductivity greatly enhanced Pt and Ru catalytic activity compared with the same metals deposited on non-ionically conductive supports for C_2H_4 complete oxidation. The light off temperatures of Pt/SDC and Ru/SDC were 60^{o}C and 70^{o}C, respectively, whereas for the same NPs deposited on the high surface area carbon, the higher temperatures of 90^{o}C for Pt/C and 130^{o}C for Ru/C were obtained. The same trend was observed with activation energies, which were 22 and 35.1 kJ/mol for Pt/SDC and Ru/SDC compared with 31 and 52.4 kJ/mol for Pt/C and Ru/C, respectively. It is proposed that metal-support interaction (MSI), in particular, the electronic effect between NPs and ionic conductors is responsible for the high catalytic activity. The electronic effect is manifested by the oxygen ion exchange in the vicinity of the three-phase boundary similar to the electrochemical promotion mechanism, which is thermally self-induced in the case of Pt and Ru NPs deposited on SDC and YSZ.

7.2 Introduction

Understanding the oxidation reactions of simple volatile organic compounds (VOCs), e.g., such as ethylene on supported metal or metal oxide nanoparticle catalysts, creates a

fundamental basis for the investigation of more complex hydrocarbon molecules and/or the oxidation of gas mixtures [1-3]. Elucidation of the effect of the nano-catalyst size, structure, morphology, shape and its interaction with the support on the performance of the supported catalyst represents a central topic in heterogeneous catalysis.

The general concept of catalytic oxidation of VOCs involves the use of two types of catalysts: metal oxides and noble metals [2]. Both were found to be active for many deep oxidation reactions. The mechanism of deep catalytic oxidation of VOCs involves lattice and surface oxygen for metal oxides and reduced metal sites for supported noble metals [2].

Metal-support interaction is a well-known phenomenon in heterogeneous catalysis, where the catalyst support enhances the catalytic activity and in some cases the selectivity of the catalyst via either the geometric or electronic effect. It was reported that supports with high surface area increase the dispersion of the catalyst and prevent nanoparticles from agglomeration, hence enhancing its catalytic activity [4]. Other effects were related to the presence of oxygen vacancies and reducibility of mixed ionic conductive supports such as TiO_2 and CeO_2 vs. non-ionic conductive supports such as Al_2O_3 [5].

Ionic conductive materials are found in many applications such as sensors, separators, solid oxide fuel cells (SOFC), heterogeneous catalysis [6,7] and in electrochemical promotion of catalysis (EPOC) [8-10]. Solid-state oxygen-ion conductors are solid solutions of oxides of divalent or trivalent cations (Y_2O_3, CaO, Yb_2O_3) in oxides of tetravalent metals (ZrO_2, ThO_2, CeO_2). Their O^{2-} conductivity is due to the oxygen ion vacancies created in the lattice of the tetravalent metal oxide after the doping [6].

Yttria-stabilized zirconia (YSZ) is one of the most studied solid electrolytes in SOFC and gas sensors and its good O^{2-} conductivity is due to the presence of oxygen vacancies inside its crystallographic structure. It found a particular interest as a solid-electrolyte in EPOC studies, where the catalytic activity and sometimes selectivity of metals or metal oxides interfaced with solid electrolyte is enhanced reversibly or in some cases irreversibly via potential or current application. The increase in the catalytic rate can be several orders of magnitude higher than that anticipated from Faraday's law due to the backspillover of ionic conductive species ($O^{\delta-}$ in case of YSZ) over the gas-exposed catalyst surface [8].

Recently, Vernoux et al. [11] proposed the functionally similar concept, termed "self-induced electrochemical promotion of catalysis", which is a MSI effect observed between NPs and purely ionic conductive support, e.g., YSZ. Vernoux and co-workers found that MSI in this case is manifested by the spontaneous backspillover of ionic species from the support to the gas-exposed catalyst surface. The backspillover is thermally induced without any electrical polarization, which is required in the conventional electrochemical promotion studies [8-10]. The "self-induced EPOC" was first demonstrated over Pt NPs of 10 nm average size deposited on YSZ for propane deep oxidation and more recently over the similar system but with Pt average size of 3 nm for CO and toluene oxidation [12-14]. It was found that for both CO and toluene oxidation, Pt/YSZ outperformed Pt deposited on carbon and γ-Al_2O_3 catalysts despite the much higher specific surface area of the two latter materials.

Ruthenium was extensively studied for carbon monoxide oxidation [15-17]. However, the application of Ru-based catalysts in the alkanes/alkenes combustion is limited. Toluene, propane and orthoxylene oxidation were studied over Ru/CeO_2 [18] and on Ru/γ-Al_2O_3 [19], propylene oxidation was studied over RuO_2/CeO_2 [20], low temperature oxidation of butane, ethyl acetate, acetaldehyde, and toluene oxidation were investigated over Ru supported on CeO_2, ZrO_2, SnO_2 and Al_2O_3 [21,22]. Furthermore, ethylene oxidation was investigated over a 1 mm thick film of RuO_2/YSZ electrochemically promoted catalysts and it was found that RuO_2 is a good catalyst for this reaction and the rate of ethylene oxidation can be further increased by a factor of ten via anodic polarization (supply of $O^{\delta-}$ promoters to the catalyst surface) and by a factor of three via cathodic polarization (removal of $O^{\delta-}$ from the catalyst surface) [23,24].

In this paper, Pt and Ru colloidal nanoparticles of 1.8 – 1.9 nm average size were synthesized using modified polyol process with ethylene glycol (EG) as a reducing agent. The colloidal nanoparticles were then deposited on yttria-stabilized zirconia (YSZ), samarium-doped ceria (SDC), gamma-alumina (γ-Al_2O_3) and carbon black (C) resulting in $\leq$ 0.7 wt. (weight) % of Pt and Ru on each support with a resulting nanoparticle average sizes ranging between 1.9 - 2.9 nm depending on the support. First, the kinetics of ethylene oxidation over Ru/YSZ NPs is investigated by varying C_2H_4 and O_2 partial pressures at 150^{o}C. Then the effect of the support for complete ethylene oxidation reaction at constant P_{O_2} and $P_{C_2H_4}$ was

carried out in the temperature range of 25 - 220^{o}C in fuel lean conditions. Furthermore, C_2H_4 oxidation over Pt/YSZ and Ru/YSZ in the absence of oxygen in the gas feed was performed.

7.3 Experimental

7.3.1 Synthesis and characterization of supported nanoparticles

Platinum and ruthenium nanoparticles were synthesized using a modified polyol reduction method, described in details elsewhere [25,26]. In short, first, Pt and Ru nanoparticles in the form of colloids were synthesized in ethylene glycol (Anhydrous 99.8% Sigma Aldrich) at 160^{o}C, starting from $PtCl_4$ (Alfa Aesar, 99.9% metals basis) and $RuCl_3$ (Alfa Aesar, 99.99% metals basis) precursor salts respectively using a sodium hydroxide (EM Science, ACS grade) concentration of 0.08 M as described previously [13]. An appropriate amount of the resulting dark brown solution of Pt and Ru nanoparticles in ethylene glycol were deposited on 1.5 g of 8 mol% Y_2O_3-stabilized ZrO_2 (Tosoh, specific surface area (a_s) = 13 $m^2 \cdot g^{-1}$), SDC (Fuel Cell Materials, a_s = 35 $m^2 \cdot g^{-1}$), carbon black (Vulcan XC-72R, Cabot Corp. a_s = 254 $m^2 \cdot g^{-1}$) and γ-Al_2O_3 (Alfa - Aesar, a_s = 120 $m^2 \cdot g^{-1}$). The mixture of the supported nanoparticles was left to stir over night at room temperature to achieve high dispersion of the metal nanoparticles on each support. The supported NPs were extensively washed with deionized water (18 MΩ · cm) and separated by centrifugation, then dried in air at 60^{o}C resulting in ≤ 0.7 wt. % of metal on the support as confirmed by inductive coupled plasma measurements using (ICP-OES Varian Vista-Pro CCD spectrometer).

As prepared, Ru is mostly present in the oxidized form, i.e., RuO_x ($x \leq 2$) while partial surface oxidation was found for Pt [4]. Therefore, before catalytic measurements, all supported Pt and Ru catalysts were reduced in H_2 (Linde, 99.99%) at 300^{o}C for 3 h then tested immediately.

The morphology and particle size of the resulting Pt and Ru colloids were characterized by TEM (JEOL JEM 2100F FETEM) operating at 200kV. A drop of the colloidal solution was deposited on a copper grid (Electron Microscopy sciences, CF-300). The size distribution and mean particle size were performed using the imaging software

MeasureIt (Olympus Soft Imaging Solutions) by measuring at least 200 nanoparticles from TEM images.

Dispersion of the supported Pt and Ru nanoparticles was determined using the CO titration technique [27-30]. In brief, carbon monoxide (Linde, 1000 ppm CO in He) with a flow rate of 15 ml·min^{-1} for Pt and 20 ml·min^{-1} for Ru was adsorbed on the catalyst surface at 140°C and 180°C for Pt and Ru, respectively. The reactor was then purged with He (Linde, 100%) at the same temperature and flow rate of 100 ml·min^{-1}. An oxygen flow of 30 ml·min^{-1} (Linde, 99.997%) was then passed through the reactor and the amount of CO_2 formed was measured using gas chromatograph and an online non-dispersive infrared (NDIR) CO_2 analyzer (HORIBA VA-3001). This procedure was repeated for different purging times ranging from 5 to 20 min, and the maximum reactive CO uptake was obtained by extrapolating to time equals zero. The CO/Pt ratio is assumed to be unity [10,30,31] but the CO/Ru ratio is taken as 2.3 for Ru nanoparticle of 2.5 nm size [16,32].

Calculation of the supported catalyst particle size was estimated using TEMs or using the following equation [33]:

$$d_{nm} = \frac{MW \times 600}{\rho \times dispersion\ \ (\%)\ \times a\ \times N_a} \qquad (7.1)$$

where *MW* is the molecular weight of Pt = 195.08 g·mole^{-1} or Ru = 101.07 g·mole^{-1}, *a* is the atomic surface area = 8.06 x10^{-20} m²·atom^{-1} for Pt and 1.96 x10^{-19} m²·atom^{-1} for Ru, ρ = 21.09 g·cm^{-3} for Pt and 12.2 g·cm^{-3} for Ru, N_a =Avogadro's number.

7.3.2 Catalytic activity

The catalytic activity measurements of the supported nanocatalysts for ethylene oxidation were carried out at atmospheric pressure in a continuous flow U-shaped quartz reactor. Approximately 50 mg of catalyst was placed into the reactor. The reactive mixture was composed of 909 ppm C_2H_4 (Linde, 5% in He), 3.5% O_2 (Linde, 99.997%) and balance He (Linde, 100%) as a carrier gas. The total gas flow rate was 4.62 L·h^{-1} unless otherwise stated. For the oxidation experimental part in absence of oxygen in the gas phase, the reactive

mixture composed of 909 ppm C_2H_4 (Linde, 5% in He) and balance He (Linde, 100%) as a carrier gas.

The catalyst samples were tested in the temperature range of 25 - 220^{o}C. The reactant and product gases were analyzed by an on-line gas chromatograph (GowMac 350) and on-line non-dispersive infrared (NDIR) CO_2 gas analyzer (HORIBA VA-3001) to quantify the concentrations of C_2H_4, O_2 and CO_2. Each experiment was repeated for three cycles to test stability and reproducibility. Experiments in the presence and absence of oxygen were carried out by stepping the temperature to the desired value. At each temperature, the catalyst was allowed to reach a steady state for 25 - 30 min and then three GC injections were performed. The average of three GC measurements at each temperature is reported, which is also confirmed by the on-line NDIR CO_2 gas analyzer. For experiments without O_2 in the gas feed using YSZ and SDC, due to the fast O^{2-} depletion from YSZ and SDC surfaces leading to catalyst deactivation [34], only one stable run from 25 to 220^{o}C was carried out per day, after which the catalyst was left in He overnight in order to re-equilibrate O^{2-} concentration between bulk and the surface in YSZ and SDC supports.

From the outlet concentrations of C_2H_4 and CO_2, ethylene conversion was calculated with the following equation:

$$C_2H_4 \text{ conversion } (\%) = ([CO_2]_{out} / (2 \cdot [C_2H_4]_{out} + [CO_2]_{out}))X100 \quad (7.2)$$

The turn over frequency (TOF) values were calculated using the following equation:

$$TOF = r / N_G \quad (7.3)$$

where r is the ethylene oxidation rate (mol·s^{-1}), and N_G is the moles of active Pt sites (mol).

The intrinsic activity (γ) was calculated as:

$$\gamma = F_{CO_2} / (w \cdot a_s) \quad (7.4)$$

where F_{CO_2} stands for the molar flow rate of CO_2 exiting the reactor (mol·s^{-1}), w is the mass of Ru or Pt in the reactor (g), and a_s is the specific surface area of Ru or Pt NP (m^2·g^{-1}).

The activation energy for C_2H_4 oxidation was determined using Arrhenius relationship calculated in the range below 20 % conversion according to:

$$\ln r = -E_a/(RT) + \ln k \tag{7.5}$$

where r is C_2H_4 oxidation rate ($mol \cdot s^{-1}$), E_a is the apparent activation energy ($J \cdot mol^{-1}$), R is the universal gas constant ($J \cdot mol^{-1} \cdot K^{-1}$), T is the reactor temperature (K), and k is the rate constant ($mol \cdot s^{-1}$).

7.4 Results and discussion

7.4.1 TEM of colloidal nanoparticles

Figure 7-1(a) and (b) shows the TEM micrographs and the corresponding histograms of the Ru and Pt colloids synthesized in ethylene glycol, respectively. The TEM shows that well defined and almost spherical Ru and Pt nanoparticles were prepared using modified polyol reduction method. The average size of Ru NPs is 1.8 nm and Pt NPs is 1.9 nm. Table 7-1 shows the average particle size of all catalysts estimated from TEM images and from equation (7.1) for supported catalysts using the dispersion values from CO titration measurements.

Table 7-1: List of catalysts and their characteristics.

Catalyst	Metal loading (wt%)*	Dispersion** (%)	Average size from eq. 7.1 / nm	Average size from TEM / nm	Ea (kJ/mol)
Ru colloids	-	-	-	1.8	-
Pt colloids	-	-	-	1.9	-
Ru/SDC	0.16	16	2.6	-	35.1
Ru/YSZ	0.48	15	2.8	-	50.7
Ru/C	0.19	22	1.9	2.6	52.4
Ru/γ-Al_2O_3	0.49	18	2.3	2.3	61.8

Pt/SDC	0.37	40	2.9	2.8	25.7
Pt/YSZ	0.48	39	2.9	2.6	22.0
Pt/C	0.38	52	2.2	1.9	31.0
Pt/γ-Al_2O_3	0.70	45	2.5	2.2	32.0

* from ICP-MS measurements
** from CO titration

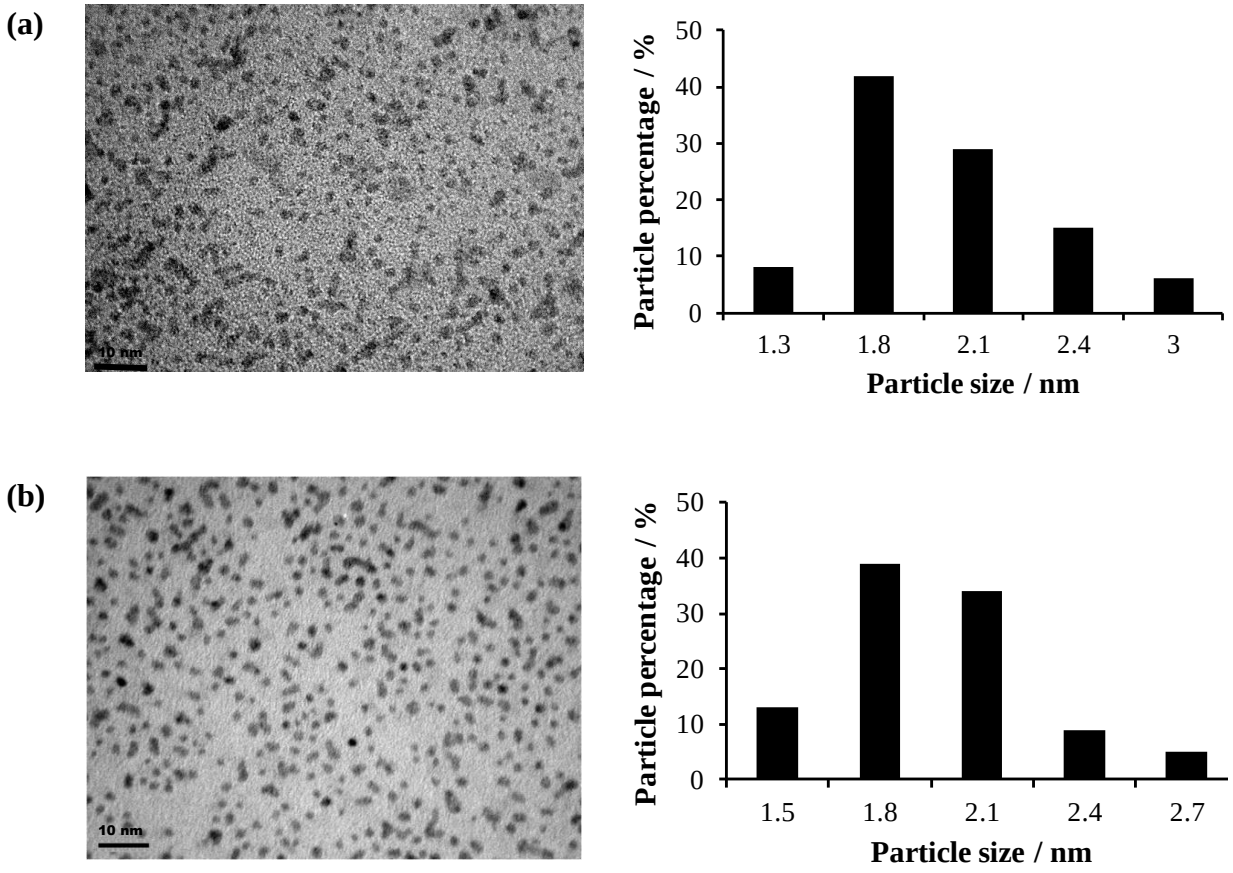

Figure 7-1: TEM images (left) and corresponding histograms (right) of nanoparticle colloids, (a) Ru and (b) Pt.

There is a good agreement between particle sizes estimated from TEM and eq. (7.1) showing that the average size ranges between 1.9 and 2.9 nm. The variation in dispersion values is larger resulting from the difference in the specific surface areas of supports. Higher dispersion values are observed for Ru and Pt when supported on C and γ-Al_2O_3, compared with dispersion values for metals deposited on YSZ or SDC. This is due to the larger surface area of C and γ-Al_2O_3, which are 250 and 120 $m^2 \cdot g^{-1}$ compared to 13 and 35 $m^2 \cdot g^{-1}$ for YSZ and SDC, respectively.

7.4.2 Kinetics of ethylene oxidation over Pt and Ru NPs supported on YSZ

Various aspects of ethylene oxidation reaction have been studied on single crystal Pt surfaces in ultra-high vacuum (UHV), as well as on supported Pt nanoparticles [35,36]. It was established that ethylene oxidation follows Langmuir-Hinshelwood mechanism where ethylene adsorbs more strongly than oxygen over Pt active sites [37-39]. Kinetics of ethylene oxidation over Pt NP deposited on different supports such as SiO_2, SBA-15, γ-Al_2O_3, TiO_2 and YSZ were extensively studied [30,35,40,41]. In fuel lean conditions, the reaction rate of ethylene over Pt/YSZ was found to be first order in C_2H_4 while it was independent of oxygen partial pressure (zero order in O_2) [41]. Similar results were found for the nanostructured Pt/YSZ in the present work (not shown here).

Kinetics of ethylene oxidation on Ru/YSZ was studied at 150^{o}C by varying the partial pressure of oxygen or ethylene. Figure 7-2 shows the dependence of C_2H_4 oxidation rate on the partial pressure of oxygen (P_{O2}) and the partial pressure of ethylene (P_{C2H4}) over Ru/YSZ nanoparticles. This temperature was chosen based on the temperature range reported earlier where the catalyst was found to oxidize ethylene into carbon dioxide and water at a rate of 10^{12} molecules$\cdot cm^{-2} \cdot sec^{-1}$ under fuel lean conditions [42].

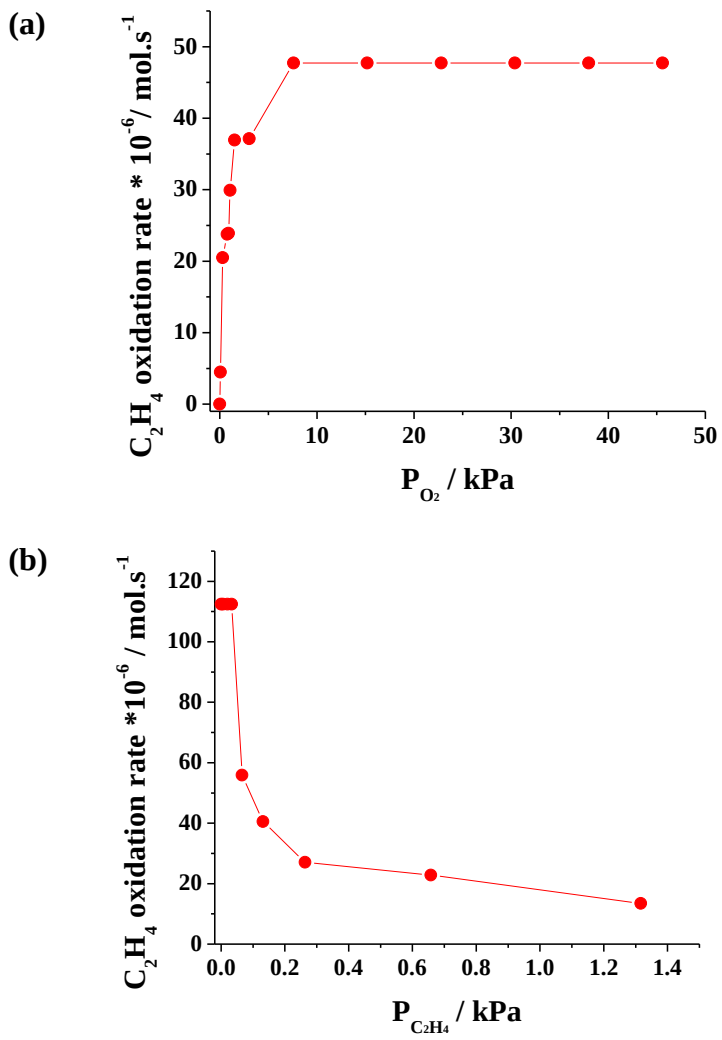

Figure 7-2: Kinetics of ethylene oxidation over Ru/YSZ nanoparticles at 150°C under (a) constant $P_{C_2H_4}$= 0.092 kPa and (b) constant P_{O_2}= 3.5 kPa.

The kinetics study shows that the order of reaction is positive and less than first order in oxygen for P_{O2} below 4 kPa. At high P_{O2} values (> 4 kPa), it gradually changes to zero-order reaction rate. Thus, when starting from low oxygen partial pressure at the pre-reduced catalyst surface, and gradually increasing the partial pressure of oxygen, the reaction rate follows the enhanced activity of almost first-order behavior, until a critical oxygen partial pressure value is reached over Ru/YSZ. At this state, the catalyst surface is oxidized and the reaction reaches a plateau. The same reaction order is observed in the reverse run by decreasing the partial pressure of oxygen back to zero. The rate of reaction is negative order in

ethylene in fuel lean gas composition, meaning that ethylene adsorbs more strongly on Ru surfaces than oxygen. Similar orders of reaction were observed for the effect of oxygen and ethylene partial pressures on Ru/SiO_2 and $Ru/\alpha\text{-}Al_2O_3$ for ethylene oxidation [1,35,41].

7.4.3 Effect of the support on C_2H_4 oxidation over Pt and Ru nanoparticles

The oxidation of 909 ppm ethylene was carried out over all catalysts for three successive heating ramps between 25 - 220°C. It was found that all catalysts show very stable and reproducible performance in the temperature range of interest.

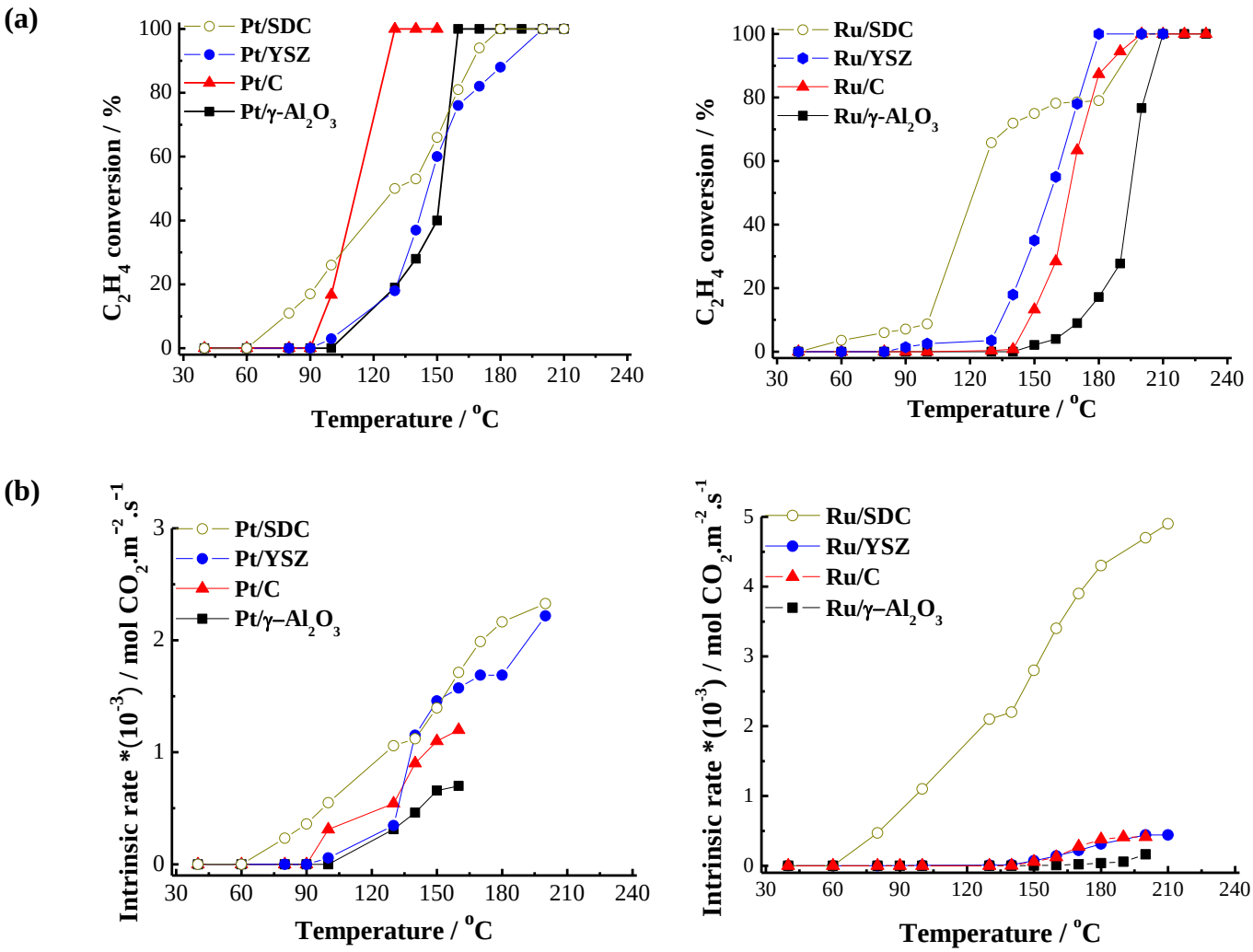

Figure 7-3: Ethylene oxidation on Pt and Ru NPs deposited on various supports, (a) C_2H_4 conversion and (b) intrinsic reaction rate. Space velocity = 14688 h^{-1}, gas composition: total flowrate = 4.62 $L \cdot h^{-1}$, 909 ppm C_2H_4, 3.5 % O_2, He balance.

Fig. 7-3a shows C_2H_4 conversion as a function of temperature over Pt and Ru supported catalysts, while Fig. 7-3b shows the intrinsic rate of all catalysts normalized by active metal surface area on each support. It is noted that Pt NPs supported on SDC show earlier catalytic activity compared with other supports (YSZ, C and γ-Al_2O_3). However the full conversion is reached at lower temperatures over Pt/C and Pt/γ-Al_2O_3. When the catalyst performance is compared in terms of the intrinsic rate, Pt/SDC shows the high rates in the whole range of temperatures followed by Pt/YSZ and Pt/C. For Ru NPs, both Ru/YSZ and Ru/SDC show higher conversions at lower temperatures than those deposited on non-ionically conductive supports. It is worth to note the shape of the light off curve for Ru/SDC (Fig. 7-3a) showing a plateau at intermediate conversion ~ 75%. Also the initial increase in conversion at 60^{o}C is quite low till 100^{o}C. This could be related to the oxidation state of Ru. The first plateau may correspond to C_2H_4 oxidation on Ru, while full conversion is reached over RuO_x at higher temperatures (> 150^{o}C). When the catalytic activity is represented in terms of intrinsic rate normalized to the metal active surface area as in Fig. 7-3b, the order of activity is shown to be the same for both Pt and Ru and the reaction rate decreases as SDC > YSZ > C > γ-Al_2O_3.

Figure 7-4 shows TOF values at 100 and 150^{o}C of Pt and Ru catalysts supported on various supports. It is noticed that for Pt catalysts at 100^{o}C, the catalytic activity based on the support is in the order of Pt/SDC > Pt/C > Pt/YSZ > Pt/γ-Al_2O_3 while at 150^{o}C, the order of activity becomes: Pt/C > Pt/SDC > Pt/YSZ > Pt/γ-Al_2O_3.

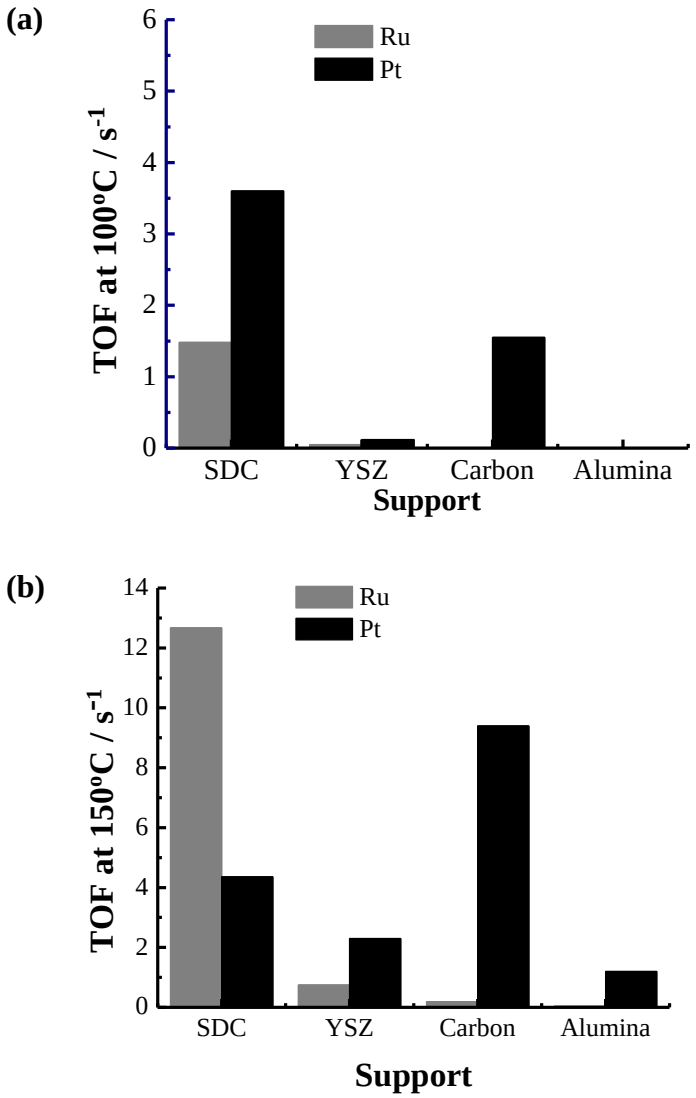

Figure 7-4: Turn over frequency (TOF) of Pt and Ru NPs deposited on various supports for ethylene oxidation at (a) 100°C and (b) 150°C.

The improved catalytic activity of Pt/C may be due to the higher dispersion of Pt on carbon, which is 52% in our study compared to 45, 40 and 39 % for γ-Al_2O_3, SDC and YSZ, respectively (Table 7-1). It is well known that ethylene oxidation is a structure sensitive reaction over Pt catalysts and the catalytic activity is significantly affected by dispersion and particle size [3,4,43]. Despite the low specific surface area of YSZ and SDC compared to γ-Al_2O_3, Pt/YSZ and Pt/SDC catalysts outperform Pt/ γ-Al_2O_3, indicating that ionic conductivity of the support affects the activity of Pt.

The catalytic activity of the Ru supported catalysts was found in the following order: Ru/SDC > Ru/YSZ > Ru/C > Ru/γ-Al_2O_3 over the whole range of temperature. This order indicates that the presence of O^{2-} conductivity has larger influence on C_2H_4 conversion than the degree of dispersion for Ru NPs when it is deposited on the high surface area C and γ-Al_2O_3 (Table 7-1). These oxygen anions from the support could enhance the formation of RuO_x which are believed to be active surface sites for C_2H_4 oxidation [23,24,44].

It is known that the ionic conductivity of SDC is higher than that of YSZ [7,34]. According to the manufacturers, SDC used in this work has bulk ionic conductivity value of $4.0 \cdot 10^{-2}$ Scm^{-1} at 700°C while YSZ has a value of $6.3 \cdot 10^{-3}$ Scm^{-1} at the same temperature. As estimated, in the temperature range of interest (~100°C), the bulk ionic conductivity of SDC decreases to $5.1 \cdot 10^{-3}$ Scm^{-1} however remains much higher than that of YSZ which is $8.42 \cdot 10^{-13}$ S cm^{-1}. This indicates that the bulk ionic conductivity at 100°C is quite low and bulk diffusion of O^{2-} at reasonable rates to the three phase boundary (tpb) is not probable. However, in this temperature range, the presence of the surface O^{2-} mobility and surface oxygen exchange in the vicinity of tpb cannot be ruled out and may contribute to the increase in the catalytic activity of Pt and Ru for C_2H_4 oxidation. Because the conductivity of SDC is higher, the surface O^{2-} diffusion is high as well, which is seen in the better performance of both Pt and Ru supported on SDC than YSZ.

Table 7-1 shows the activation energies of all catalysts. It is noticed that Pt supported on different supports always have lower activation energies compared with Ru supported on the same support indicating that Pt is a superior catalyst for this reaction, however the lower cost combined with a good stability of Ru may render it particularly attractive for ethylene oxidation. The same trend in activation energy was reported by Cant et al. [42] for ethylene oxidation under fuel lean conditions over 5 wt. % of Ru/SiO_2 (E_a = 25.8 kcal·mol^{-1}) vs Pt/SiO_2 (E_a = 18.5 kcal·mol^{-1}).

7.4.4 Ethylene oxidation on Ru/YSZ and Pt/YSZ in the absence of oxygen in the gas feed

To confirm the importance of the effect of ionic conductivity and the presence of O^{2-} exchange at the vicinity of tpb, the oxidation of C_2H_4 over Ru/YSZ and Pt/YSZ was carried

out in the absence of oxygen in the gas feed. It was shown recently [34], that when Pt nanoparticles (2.5 nm) are supported on ionically conductive (YSZ and SDC) and mixed ionic conductive (CeO_2) supports, the oxidation of CO and C_2H_4 could take place by O^{2-} from the ceramic at temperatures as low as 120°C. In this case, Pt NPs and the support form local galvanic cells, where electro-oxidation takes place in the vicinity of tpb and partial surface electro-reduction of ZrO_2 or CeO_2 occurs. Some carbon deposition may occur during the catalyst operation without O_2, which is as well removed via electrochemical reaction. The reaction continues as long as mobile O^{2-} exists on the surface, once all O^{2-} is consumed, the reaction rate falls to zero and the catalyst regeneration is required. As expected, when the same Pt NPs were deposited on non-ionic conductive supports such as carbon and alumina, there was no catalytic activity of Pt in the absence of oxygen in the gas feed [34].

In this work, the catalytic activity of Ru NPs deposited on YSZ is investigated in the absence of oxygen in the gas feed and compared with Pt NPs deposited on the same support. Figure 7-5 shows the catalytic activity of Pt and Ru NPs deposited on YSZ for the removal of 909 ppm C_2H_4 in absence and presence (P_{O2} = 3.5 kPa) of oxygen in the gas feed.

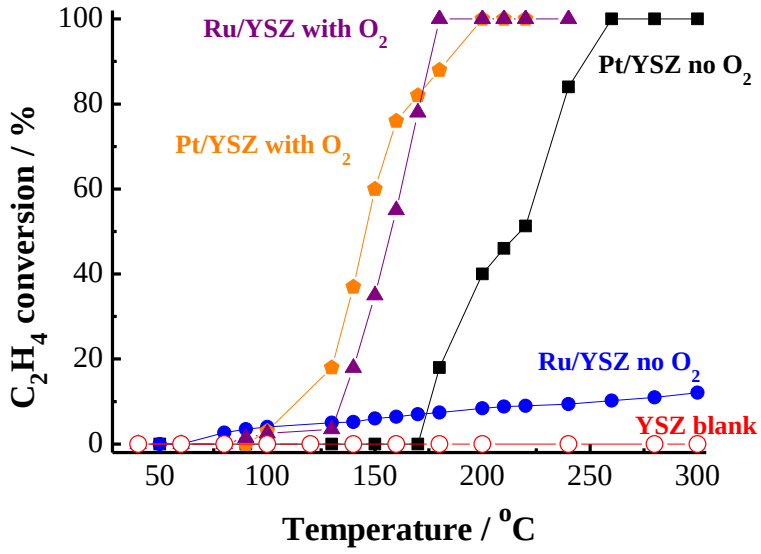

Figure 7-5: Ethylene oxidation in the absence (P_{O2} = 0 kPa) and presence (P_{O2} = 3.5 kPa) of oxygen in the gas feed. Space velocity = 14688 h^{-1}, gas composition: total flow rate is 4.62 $L \cdot h^{-1}$, ethylene concentration is 909 ppm, He balance.

Without O_2 in the gas phase, Ru/YSZ has earlier catalytic activity, however remains low at 10 %, even at 300^{o}C, whereas Pt/YSZ is inactive up to 170^{o}C. After this temperature, the conversion of ethylene increases and reaches full conversion at 260^{o}C. The low C_2H_4 conversion on Ru/YSZ could be explained by the lack of oxygen in the gas feed which slows and inhibits the formation of RuO_x, which is apparently a more efficient catalyst for C_2H_4 oxidation than Ru NPs. In the presence of oxygen, ethylene conversion starts at much lower temperatures of 110 and 135^{o}C for Pt and Ru, respectively.

7.4.5 Mechanism of the metal-support interaction over Pt and Ru NPs supported on ionically conductive supports

As was shown by Nicole et al. [12] more than a decade ago, MSI and EPOC are functionally similar phenomena linked through the mechanism of backspillover, which is spontaneous and thermally induced in the former, and *in-situ* controllable by current or potential application in the latter case. Therefore, EPOC was also termed "an electrically controlled metal-support interaction" [8,45], whereas MSI with ionically conductive supports was later called "self-induced EPOC" [7,11]. MSI is due to the electronic effect, where the charge is transferred from the solid with a lower work function (WF) to the solid with a high WF. The WF of metallic Pt and Ru is ~5.3 and 4.71 eV, respectively while WF of YSZ (~8 mol% Y_2O_3 doped ZrO_2) is 5.14 eV at P_{O2} = 1 atm [46]. Therefore the charge transfer will take place from the support to NPs. The mechanism of MSI or "self-induced EPOC" could be rationalized as follows: when small metal nanoparticles (< 5 nm) are deposited on ionically conductive supports, the generated charge transfer due to the difference in work function of support and metal, results in spontaneous $O^{\delta-}$ migration to the gas-exposed catalyst surface through the three-phase boundary. One would expect that the rate of backspillover will increase with temperature and as the catalyst particle size decreases. Recent work [34] and Fig. 7-5 confirms that there is an electrochemical reaction of C_2H_4 oxidation and O^{2-} oxidation over NPs/ionic conductor even at relatively low temperature ~175^{o}C. In the excess of oxygen, the rate of the electrochemical process is low and chemical reaction dominates. The low rate of the electrochemical reaction in NPs/solid electrolyte systems in the excess of oxygen is similar to the open circuit electrochemical reaction rate in classical electrochemistry described by the exchange current, I_o.

Figure 7-6 shows the equivalence between a conventional EPOC cell and MSI or "self-induced EPOC" over NPs/YSZ highly dispersed catalyst. Similar to EPOC, two processes take place simultaneously: the electrochemical reaction at the three-phase boundary represented by the electro-oxidation of C_2H_4 or O^{2-} and the backspillover of $O^{\delta-}$ from the ionic conductive support, which serves as a promoter for the reaction of ethylene oxidation. Electro-oxidation is accompanied by partial surface electro-reduction of ZrO_2 and/or gaseous O_2, depending on P_{O2}.

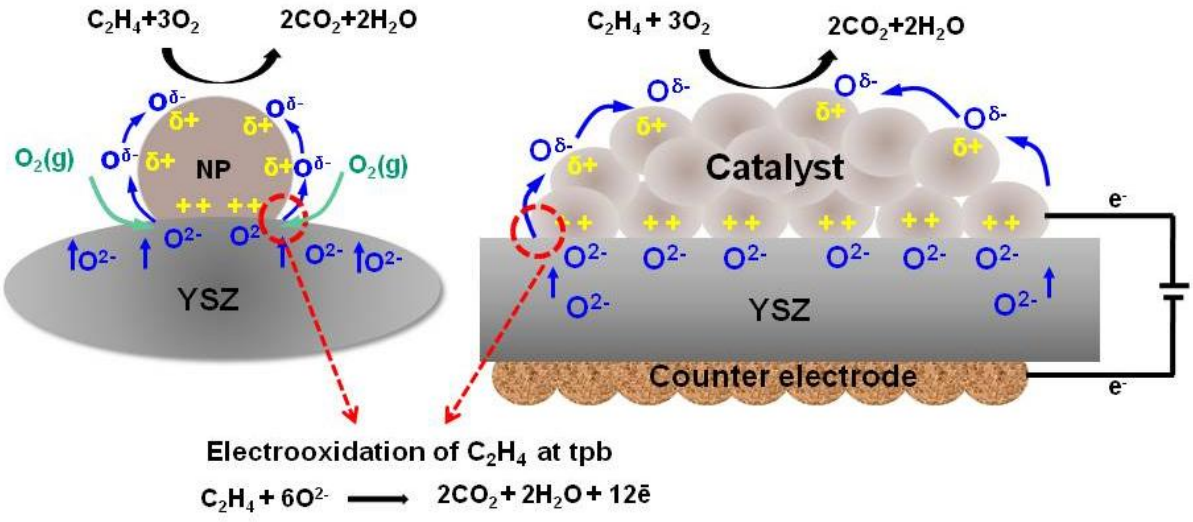

(a) **(b)**

Figure 7-6: Schematic diagram of the processes taking place over metal nanoparticle (< 5 nm) supported on YSZ in (a) Metal-support interaction or "self-induced EPOC" and (b) in the conventional electropromoted cell under EPOC conditions.

7.5 Conclusions

The present results show that the support nature plays a key role in the catalytic activity of Pt and Ru for ethylene oxidation. Pt and Ru nanoparticles deposited on SDC, YSZ, carbon and γ-Al_2O_3 were tested for complete C_2H_4 oxidation in the temperature range of 25 - 220^{o}C. Both metal nanoparticles were found to be active and stable towards C_2H_4 oxidation. The kinetics of C_2H_4 oxidation over Ru/YSZ in fuel lean conditions were found to be positive

and less than first order in oxygen for P_{O2} below 4 kPa and then it gradually changed to zero-order at higher P_{O2} values. Among Pt catalyst, Pt/C catalyst reached 100 % conversion at lower temperatures, because C_2H_4 oxidation is well known to be structure sensitive over Pt nanoparticles and highly affected by the catalyst dispersion. The dispersion of Pt/C was the highest in the present work (52 %), indicating that the large specific surface area of carbon stabilizes and prevents nanoparticles from agglomeration. At 100^{o}C the following order of activity was found for Pt: Pt/SDC > Pt/C > Pt/YSZ > Pt/γ-Al_2O_3. For Ru system, both ionically conducting supports SDC and YSZ outperformed carbon and alumina with the catalyst activity as follows: Ru/SDC > Ru/YSZ > Ru/C > Ru/γ-Al_2O_3 over the whole range of temperature. The measurements in the absence of oxygen in the gas feed showed that ethylene can be electrooxidized by Pt/YSZ and Ru/YSZ, however the conversion over the latter catalyst remained low (10 %) due to hindered RuO_x formation. Ionically conducting supports (YSZ and SDC) greatly enhanced the catalytic activity of NPs due to the metal-support interaction and the electronic effect, where the self-induced backspillover of $O^{\delta-}$ species to the catalyst surface promotes the reaction. It is proposed that in the case of Pt and Ru NPs supported on YSZ and SDC, two processes take place simultaneously: the electrochemical reactions at the three-phase boundary and the backspillover of $O^{\delta-}$ from the support to the catalyst surface similar to the classical EPOC mechanism.

7.6 Acknowledgement

Financial support from Natural Science and Engineering Research Council (NSERC) and Ontario Graduate Scholarship (OGS). In context of this, I would like to acknowledge Dr. Nimal de Silva (Dept. Earth Sciences at UOttawa) for running ICP measurements. Dr. Yun Liu (Centre for Catalysis Research and Innovation (CCRI)) at the University of Ottawa for taking TEM images of the colloidal catalysts.

7.7 References

[1] N. Cant, W. K. Hall, *J. Catal.* 16 (1970) 220.

[2] J. J. Spivey, *Ind. Eng. Chem. Res.* 26 (1987) 2165.

[3] A. Van Strien, B. E. Nieuwenhuys, *Surf. Sci.* 80 (1979) 226.

[4] R. J. Isaifan, S. Ntais, E. A. Baranova, *Appl. Catal. A Gen.* 27 (2013) 164.

[5] S. Rojluechai, S. Chavadej, J. W. Schwank, V. Meeyoo, *Catal. Commun.* 8 (2007) 57.

[6] I. Garagounis, V. Kyriakou, C. Anagnostou, V. Bourganis, I. Papachristou, M. Stoukides, *Ind. Eng. Chem. Res.* 50 (2011) 431.

[7] P. Vernoux, L. Lizarraga, A. De Lucas-Consuegra, D. Tsiplakides, M. N. Tsampas, J.-L. Valverde, S. Balomenou, F. M. Sapountzi, S. Souentie, E. A. Baranova, *Chem. Rev.* 113 (2013) 8192.

[8] C. G. Vayenas, S. Bebelis, C. Pliangos, S. Brosda, D. Tsiplakides, Electrochemical Activation of Catalysis, Promotion, Electrochemical promotion and Metal-support Interactions, Kluwer Academic/Plenum Publisher, New York, 2001.

[9] C. G. Vayenas, S. Bebelis, *Catal. Today.* 51 (1999) 581.

[10] M. Marwood, C. G. Vayenas, *J. Catal.* 178 (1998) 429.

[11] P. Vernoux, M. Guth, X. Li, *Electrochem. Solid-State Lett.* 12 (2009) E9.

[12] H. A. Dole, R. J. Isaifan, F. M. Sapountzi, L. Lizarraga, D. Aubert, A. Princivalle, P. Vernoux, E. A. Baranova, *Catal. Letters.* 143 (2013) 996.

[13] R. J. Isaifan, H. A. Dole, E. Obeid, L. Lizarraga, P. Vernoux, E. A. Baranova, *Electrochem. Solid-State Lett.* 15 (2012) E14.

[14] R. J. Isaifan, H. Dole, E. Obeid, L. Lizarraga, E. Baranova, P. Vernoux, *ECS Trans.* 35 (2011) 43.

[15] N. Cant, P. Hicks, B. Lennon, *J. Catal.* 54 (1978) 372.

[16] J. T. Kiss, R. D. Gonzalez, *J. Phys. Chem.* 88 (1984) 892.

[17] S. H. Joo, J. Y. Park, J. R. Renzas, D. R. Butcher, W. Huang, G. A. Somorjai, *Nano Lett.* 10 (2010) 2709.

[18] S. Aouad, E. Saab, E. Abi-Aad, A. Aboukaïs, *Catal. Today.* 119 (2007) 273.

[19] J. Okal, M. Zawadzki, *Catal. Letters.* 132 (2009) 225.

[20] S. Hosokawa, Y. Fujinami, H. Kanai, *J. Mol. Catal.* 240 (2005) 49.

[21] J. Okal, M. Zawadzki, *Appl. Catal. B Environ.* 89 (2009) 22.

[22] T. Mitsui, K. Tsutsui, T. Matsui, R. Kikuchi, K. Eguchi, *Appl. Catal. B Environ.* 81 (2008) 56.

[23] I. Constantinou, I. Bolzonella, C. Pliangos, C. Comninellis, C. G. Vayenas, *Catal. Letters.* 100 (2005) 125.

[24] S. Wodiunig, C. Comninellis, *J. Eur. Ceram. Soc.* 19 (1999) 931.

[25] E. A. Baranova, Y. Le Page, D. Ilin, C. Bock, B. MacDougall, P. H. J. Mercier, *J. Alloys Compd.* 471 (2009) 387.

[26] E. A. Baranova, C. Bock, D. Ilin, D. Wang, B. Macdougall, *Surf. Sci.* 600 (2006) 3502.

[27] M. A. Fortunato, D. Aubert, C. Capdeillayre, C. Daniel, A. Hadjar, A. Princivalle, C. Guizard, P. Vernoux, *Appl. Catal. A Gen.* 403 (2011) 18.

[28] C. G. Vayenas, S. Bebelis, I. Yentekakis, H. Lintz, *Catal. Today.* 11 (1992) 303.

[29] M. N. Seong-Ick Kim, T. Yamamoto, A. Endo, T. Ohmori, *J. Ind. Eng. Chem.* 12 (2006) 769.

[30] R. M. Rioux, J.D. Hoefelmeyer, M. Grass, H. Song, K. Niesz, P. Yang, G. A. Somorjai, *Langmuir.* 24 (2008) 198.

[31] S. Kim, T. Yamamoto, A. Endo, T. Ohmori, M. Nakaiwa, *J. Ind. Eng. Chem.* 12 (2006) 769.

[32] J. Chau-Hwa Yang, J. G. Goodwin, *React. Kinet. Catal. Lett.* 20 (1982) 13.

[33] M. Boudart, *Adv. Catal.* 20 (1969) 153.

[34] R. J. Isaifan, E. A. Baranova, *Electrochem. Commun.* 27 (2013) 164.

[35] C. Pliangos, I. V Yentekakis, V.G. Papadakis, C.G. Vayenas, X. E. Verykios, *Appl. Catal. B Environ.* 14 (1997) 161.

[36] S. Chavadej, K. Saktrakool, P. Rangsunvigit, L. Lobban, T. Sreethawong, *J. Chem. Eng.* 132 (2007) 345.

[37] G. M. Schwab, K. Gossner, *Annu. Rev. Phys. Chem.* 14 (1963) 177.

[38] S. Bebelis, M. Makri, A. Buekenhoudt, J. Luyten, S. Brosda, P. Petrolekas, C. Pliangos, C. G. Vayenas, *Solid State Ionics.* 129 (2000) 33.

[39] A. F. Carlsson, R. J. Madix, *J. Chem. Phys.* 115 (2001) 8074.

[40] R. Sant, D. J. Kaul, E. Wolf, *AIChE J.* 35 (1989) 267.

[41] S. Bebelis, *J. Catal.* 118 (1989) 125.

[42] N. W. Cant, W. K. Hall, *J. Catal.* 22 (1971) 310.

[43] G. H. Hatzikos, R. Masel, *Surf. Sci.* 185 (1987) 479.

[44] H. Over, *Chem. Rev*. 112 (2012) 3356.

[45] J. Nicole, D. Tsiplakides, C. Pliangos, X. E. Verykios, C. Comninellis, C.G, Vayenas, *J. Catal.* 204 (2001) 23.

[46] D. Tsiplakides, C. G. Vayenas, *J. Electrochem. Soc.* 148 (2001) E189.

8 Pt nanoparticles supported on $SmFeO_3$ perovskite group for carbon monoxide and ethylene oxidation

Submitted to the Journal of Applied Catalysis B: Environmental, APCATB-S-14-02169.

8.1 Abstract

Platinum-loaded $Sm_{1-x}Ce_xFeO_{3-\delta}$ (x = 0, 0.01, 0.05) perovskites, with an average Pt size of 2.5 nm, show high catalytic activity towards carbon monoxide and ethylene oxidation in the temperature range of 25 - 350^oC. The effect of relative Cerium doping in the perovskite and the ionic conductivity was studied for complete CO and C_2H_4 oxidation. It was found that the supports possess catalytic activity, but more significantly, the Pt-supported catalysts have 50 - 100^oC lower light-off temperatures than blank perovskites alone. The significant enhancement in the catalytic activity of this family is shown by the activation energies which are 25.7 kJ/mol over ($Pt/Sm_{0.95}Ce_{0.05}FeO_{3-\delta}$) and 18.3 kJ/mol over ($Pt/ Sm_{0.99}Ce_{0.01}FeO_{3-\delta}$) compared to the lowest values reported in the literature (37.6 and 26.4 kJ/mol) for CO and C_2H_4 oxidations, respectively. The increased activity is attributed to the high ionic conductivity of these catalysts at low temperatures.

8.2 Introduction

Perovskites are a particular class of mixed oxides typically containing rare-earth and transition metals. They are widely used in heterogeneous catalysis and solid-state electrochemistry both as electrodes and electrolytes [1,2] and have proved to be excellent catalysts in several oxygen involving reactions [3-5]. Catalytic oxidation using perovskites was first reported in the early 1950s [6], but the most interesting findings were from investigations conducted in the 1970s [7]. Meadowcroft [7] reported a perovskite-type catalyst ($La_{0.8}Sr_{0.2}CoO_3$), which showed high activity for the electrochemical reduction of oxygen. Subsequently, perovskites have been extensively studied due to their relative low cost, high thermal stability and good catalytic properties for their potential applications in electrocatalysis, auto-exhaust treatment and catalytic combustion [8-11].

Perovskites are generally less active for hydrocarbon oxidation reactions compared with noble metal catalysts [12,13]. The most important parameter controlling the oxide ion conductivity is the degree of distortion from the fully symmetric and stress-free lattice, in which the oxide vacancy has the highest mobility and the lowest activation energy for the vacancy hopping [87]. To improve their activity, the cations in the perovskite lattice can be partially substituted by dopants in the A-site or B-site, giving the general structural formulas as $A_{1-x}A'_xBO_3$ or $AB_{1-y}B'_yO_3$, without inducing large changes in the crystalline structure [98]. Proper introduction of such lattice defects cause modifications to the chemical or transport properties of the oxides which allows, directly or indirectly, for modification and enhancement in the catalytic properties [14-17].

Since Voorhoeve et al. [18] reported the high catalytic activity of $Ln_{1-x}Pb_xMnO_3$ and $LnCoO_3$ (Ln= La, Pr, Nd) for CO oxidation, a large number of research was conducted on the oxidation catalysis of perovskites. The impact of partial substitution has been shown to improve the catalytic activity of the perovskites for full oxidation of hydrocarbons (CO, C_2H_4 and C_3H_8) [15,19,20]. An alternative approach is to use the perovskite as a support for metal nanoparticles. The catalytic activity of perovskites for volatile organic compound (VOCs) oxidation has been shown to improve when low noble metal (Pt) loadings are deposited on the surface instead of substituting them in the perovskite structure [21,22]. The challenge is to maintain platinum in a reduced state with high dispersion under an oxidizing atmosphere. It was found that supporting Pt on perovskites allows the formation of stable metal catalyst particles with surface to volume ratios that differ from, and potentially exceed, those found on other poly-crystalline supports [21,23].

The catalytic oxidation of CO has been taken as a model reaction on a number of perovskite oxides with the aim of correlating the observed activity with the electronic state of the transition metal ions [14,16,17] or the defect chemistry of these compounds [24]. Patel et al. [97] reported that $La_{0.8}Sr_{0.2}CoO_3$ exhibited higher catalytic activity than the non-substituted perovskite $LaCoO_3$ reaching full conversion of 1% CO at 268^{o}C, while Vaz et al. [98] showed full conversion of 5% CO over $LaCoO_3$ at 200^{o}C.

On the other hand, few studies have demonstrated high catalytic activity of perovskite type electrodes for the oxidation of ethylene [19,25]. Yao et al. [19] tested many perovskite catalysts for the complete oxidation of 0.5% CO and 0.1% C_2H_4 in the temperature range of 150 - 500^oC and 350 - 500^oC for CO and C_2H_4 experiments, respectively. They found that the best catalyst for CO oxidation was $LaCoO_3$, while $La_{0.7}Pb_{0.3}MnO_3$ performed the best for C_2H_4 oxidation based on the activation energies obtained. Marnellos et al. [25] reported full conversion of ethylene under fuel lean conditions at 550^oC. However, the catalytic activities of different perovskite oxides were reported for the oxidation of other VOCs and light hydrocarbons such as toluene [26-28], propane [21], methane [22] and propylene [29].

In this work, Pt nanoparticles were synthesized using modified polyol method and then deposited on trimetallic perovskite oxides, $Sm_{1-x}Ce_xFeO_{3-\delta}$ (x =0.0, 0.01 and 0.05). The resulting highly dispersed catalysts contained ~ 1 wt. % of Pt loading. First, the properties of the supported Pt nanoparticles were characterized by transmission electron microscopy (TEM), BET for specific surface area and the 2-point contact method for conductivity measurements. Then the catalytic activity of the as-prepared perovskites and the supported Pt/perovskite systems were investigated for complete CO and C_2H_4 oxidation and were compared to the activity of Pt/YSZ and Pt/γ-Al_2O_3 in fuel lean conditions in the temperature range of 25 - 350^oC.

8.3 Experimental

8.3.1 Synthesis of the $SmFeO_3$ perovskite family

Perovskite powders with formulae $Sm_{1-x}Ce_xFeO_{3-\delta}$ (x = 0, 0.01, 0.05), abbreviated as SCF-0, SCF-1 and SCF-5 respectively, were prepared by decomposition of citrate precursors via sol-gel method. The basic preparation and characterization of these perovskites have been previously reported [30]. Starting materials included samarium nitrate ($Sm(NO_3)_3 \cdot 6H_2O$, Alfa Aesar, 99.9%), cerium nitrate hexahydrate ($Ce(NO_3)_3 \cdot 6H_2O$, Alfa Aesar, 99.5%), iron nitrate nonahydrate ($Fe(NO_3)_3 \cdot 9H_2O$, Alfa Aesar, > 98%), and citric acid monohydrate (Alfa Aesar, minimum 99%). The nitrates were weighed according to the desired stoichiometry and dissolved separately in de-ionized water. The metal nitrate solutions were combined and added to aqueous citric acid so that the ratio of citric acid to the total metal ion was 1:1. The

solution was dried at 120^{o}C for 24 h resulting in a citrate gel precursor that was subsequently ground and calcined at 850^{o}C for 24 h with ramp rates of 5^{o} C/min, yielding the dark orange perovskite powders. The doped materials exhibited a single perovskite phase in air up to 1350^{o}C and have specific surface areas typically in the range of 6.0 - 8.0 m^2/g [30].

8.3.2 Synthesis of the supported Pt nanoparticles

Synthesis of Pt nanoparticles was carried out using a modified polyol reduction method described earlier in [31,32]. In short, 0.2334 g of $PtCl_4$ metal salt (Alfa Aesar, 99.9% metals basis) was dissolved in 25 mL of ethylene glycol (anhydrous 99.8% Sigma Aldrich) containing 0.08M NaOH (EM Science, ACS grade). The solution was stirred for 30 min at room temperature, and subsequently heated and refluxed for 3 h at 160^{o}C. A dark brown solution containing Pt nanoparticle colloids was formed. Pt colloids were deposited on the supports by taking an appropriate amount of the colloidal nanoparticles and mixing them with 1.5 g of each support, namely YSZ (Tosoh, a_s ~ 13 m^2/g), γ-Al_2O_3 (Alfa Aesar, a_s ~ 120 m^2/g), $SmFeO_3$ (a_s ~ 6 m^2/g), $Sm_{0.99}Ce_{0.01}FeO_{3-\delta}$ (a_s ~ 8 m^2/g) and $Sm_{0.95}Ce_{0.05}FeO_{3-\delta}$ (a_s ~ 8 m^2/g). The colloidal solution and supports were stirred for 24 h at room temperature. The total Pt metal loading in all cases was ~1 wt. % as confirmed by ICP-OES measurements. The resulting supported catalysts were washed and centrifuged extensively with de-ionized water and washed and dried in air for 48 h at 60^{o}C.

8.3.3 Characterization

8.3.3.1 Transmission Electron Microscopy of supported nanoparticles

Transmission electron microscopy (JEOL JEM-2100F Field Emission-TEM) with an energy dispersive x-ray spectroscopy (EDS X-Sight) attachment was used to image the morphology of the supported nanoparticles.

Furthermore, the particle sizes were also calculated using the dispersion values from CO titration using the following equation to compare it with particle size values from TEM images:

$$d_{nm} = \frac{M \times 600}{\rho \times dispersion(\%) \times a_s \times N_a} \quad (8.1)$$

where M is the molecular weight of Pt = 195.08 ($g \cdot mole^{-1}$), ρ is the catalyst density which is 21.09 ($g \cdot cm^{-3}$) for Pt, d_{nm} is the average particle size (nm), a_s is the atomic surface area = 8.06 $x10^{-20}$ ($m^2 \cdot atom^{-1}$), N_a =Avogadro's number.

8.3.3.2 Conductivity measurements of perovskite supports.

The total bulk conductivity of the materials was measured on circular pellets using the 2 point contact method. Pellets (diameter = 6 mm, thickness = 2 mm) of $Sm_{1-x}Ce_xFeO_{3-\delta}$ (x = 0, 0.01 and 0.05) were made by pressing 2 g of powder to 15000 lbs and sintering in air at 1200°C for 4 h with ramp rates of 2°C/min. Platinum mesh (Alfa Aesar, 99.9%) was added as a current collector on each face of the circular pellet by adhesion with platinum paste followed by removal of the organic binder at 800°C for 1 h. The pellet was contained in a quartz tube inside a tube furnace controlled by a Barber-Colman temperature controller. Measurements were recorded at temperatures between 100 - 1000°C in air, at a constant air flow rate of 50 sccm.

To determine the contributions of ionic and electronic conductivity to the total conductivity, an aluminum (Al) blocking electrode was used. The Al electrode blocks the flow of O^{2-} species, therefore $\sigma = \sigma_E$. The ionic conductivity was inferred from the difference between σ_T and σ_E. To measure σ_E, two pellets of $Sm_{1-x}Ce_xFeO_{3-\delta}$ (x = 0, 0.01 and 0.05) were made as previously described and a thin film of Al was added between the pellets. The "sandwiched" pellets were heated to 660°C for 4 h with ramp rates of 2°C/min to soften the Al and minimize contact resistance. Platinum mesh was added as a current collector on each side of the combined pellets and electronic conductivity measurements were recorded at temperatures 100 - 1000°C in air.

8.3.3.3 Specific surface area measurements (BET).

Specific surface areas of $Sm_{1-x}Ce_xFeO_{3-\delta}$ (x = 0, 0.01 and 0.05) perovskite powders pre and post Pt loading were measured using a Quantachrome-1 surface area analyzer. All powder samples were de-gassed for 24 hours at 200°C before measurement. The programmed

measurement involved a 40-point physisorption experiment using N_2 vector gas and surface areas were calculated from the resulting BET plot.

8.3.3.4 Dispersion of the supported catalysts

Dispersion was determined for the supported Pt nanoparticles using the CO titration technique [33-36]. Initially, the catalyst was purged with carbon monoxide (Linde, 1000 ppm CO in He) with a flow rate of 15 ml·min^{-1} at 140^{o}C followed by 100 ml·min^{-1} He (Linde, 100%) at the same temperature. Finally, an oxygen flow of 30 ml·min^{-1} (Linde, 99.997% O_2) was passed through the reactor and the amount of CO_2 formed was measured using an online CO_2 analyzer and gas chromatograph. This procedure was repeated for different purging times ranging from 5 to 20 min, and the maximum reactive CO uptake was obtained by extrapolating to time equals zero. The CO/Pt ratio is assumed to be unity [35-37].

8.3.4 Catalytic activity

Catalytic activity measurements were carried out at atmospheric pressure in a continuous flow U-shaped quartz reactor. Approximately 50 mg of the as prepared catalyst was placed into the reactor. The reactant mixture was composed of 909 ppm C_2H_4 (Linde, 5% in He) or CO (Linde, 1% in He), 3.5% O_2 (Linde, 99.997%) and balance He (Linde, 100%). The total gas flow rate was 4.62 L·h^{-1} for CO and C_2H_4 experiments. The samples were tested in the temperature range of 25-350^{o}C. The reactant and product gases were analyzed using an on-line gas chromatograph (GowMac 350) and non-dispersive infrared (NDIR) CO_2 gas analyzer (HORIBA VA-3001) to quantify concentrations of reactants and products.

The activation energy for CO and C_2H_4 oxidation was determined using Arrhenius relationship calculated in the range below 20 % conversion of carbon monoxide or ethylene according to:

$$\ln r = -E_a/(RT) + \ln k \qquad (8.2)$$

Where r is CO or C_2H_4 oxidation rate (mol·s^{-1}), E_a is the apparent activation energy (J·mol^{-1}), R is the universal gas constant (J·mol^{-1}·K^{-1}), T is the reactor temperature (K), and k is the reaction rate constant (mol·s^{-1}).

External mass and heat transfer limitations were evaluated for the highest catalytic reaction rate of each experiment (see supplementary information) using Weisz - Prater criterion for internal mass diffusion [38,39]:

$$C_{WP} = \frac{-r'_{A(obs)}\,\rho_c R^2}{D_e C_{As}} < 1 \qquad (8.3)$$

where,

$-r'_{A(obs)}$ = observed reaction rate (kmol · kg-cat^{-1}·s^{-1}) preferably at the highest temperature, ρ_c = solid catalyst density (kg·m^{-3}), R = catalyst particle radius (m), D_e = effective gas-phase diffusivity (m^2·s^{-1}) and C_{As} is the gas concentration of CO or C_2H_4 (kmol · m^{-3}).

The mass and heat interphase and intraparticle transport limitations were calculated using Weisz-Hicks criterion [40-42]:

$$\varphi = \frac{-r'_A\,\rho_c R^2}{C_A D_e}\exp\frac{\gamma\beta}{(1+\beta)} = C_{WP}\exp\frac{\gamma\beta}{(1+\beta)} \quad <1 \qquad (8.4)$$

so that,

$$\gamma = \frac{E_a}{R_g T};\ \text{and}\ \beta = \frac{(-\Delta H_r) D_e C_A}{kT}$$

where;

E_a: activation energy (J·mol^{-1}), R_g: gas constant = 8.314 (J·m^{-1}·K^{-1}), T is preferably the maximum temperature at which high reaction rates are observed (K), ΔH_r: heat of reaction = -283×10^3 (J·mol^{-1}) for CO combustion and -1411 ×10^3 (J·mol^{-1}) for ethylene combustion, k: catalyst thermal conductivity = 70 (w ·m^{-1}·K^{-1}) for platinum.

8.4 Results and Discussion

8.4.1 Characterization

8.4.1.1 TEMs

Figure 8-1 shows a representative TEM of Pt/$Sm_{0.95}Ce_{0.05}FeO_{3-\delta}$ (SCF-5).

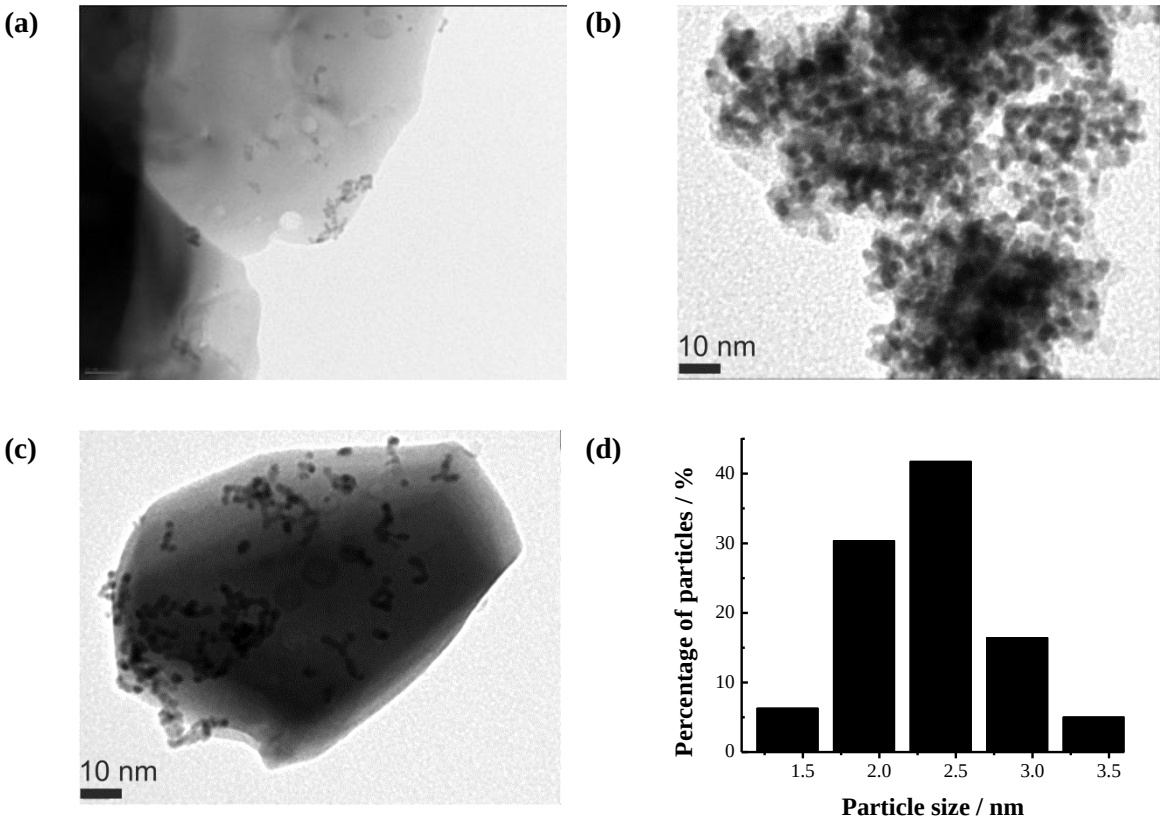

Figure 8-1: TEM of Pt/SCF-5 and the corresponding histogram.

The TEM shows homogeneous dispersion of Pt nanoparticles with little agglomeration. The average Pt particle size of Pt/SCF-5 is 2.5 nm. TEMs of other supported nanoparticles (not shown here) show relatively uniform and spherical nanoparticles in shape. The average dispersion of nanoparticles over the perovskites is in the range of 45 - 40% as shown in Table 8-1 from CO titration. These values are also close to the dispersion of Pt/YSZ (44%) as reported earlier [31]. It is worth mentioning that dispersion over perovskites and

YSZ are both less than that of Pt/γ-Al_2O_3 (52%) since alumina has much higher specific surface area [31].

Table 8-1: List of catalysts and their characteristics.

Catalyst	Metal loading (wt%)	Dispersion** (%)	Average size from eq. 8.1 / nm	Average size from TEM / nm
Pt colloids	-	-	-	1.9
Pt/SCF-0	1.0	40.2	2.8	-
Pt/SCF-1	1.0	35.6	3.2	-
Pt/SCF-5	1.0	37.7	3.0	2.5
Pt/YSZ	1.1*	44.3	2.9	2.6
Pt/γ-Al_2O_3	0.70*	52.0	2.5	2.2

* from ICP-MS measurements
** from CO titration

Moreover, the nanoparticle average particle size was calculated from (eq. 8.1) using dispersion of catalysts from CO titration method as shown in Table 8-1. In general, the values are in reasonable agreement with slightly larger average particle sizes compared with TEM values. This is because as a general point of view, the average particle size from TEM counts for 250 - 300 nanoparticles and might not count for the larger ones which might deviate the values to lower figures comparatively.

8.4.1.2 Bulk and ionic conductivity measurements

The total conductivities of $Sm_{1-x}Ce_xFeO_{3-\delta}$ (x = 0, 0.01 and 0.05) perovskite materials were measured on dense sintered pellets from 100-1000^oC in air. The contributions of electronic and ionic to total conductivity were determined by using aluminum (Al) blocking electrodes. Here, the Al blocks the flow of ionic species through the material; therefore the measured conductivity is electronic. The ionic conductivity was then inferred from the difference according to $\sigma_T = \sigma_{ionic} + \sigma_{electronic}$. A comparison between ionic and electronic

conductivities of the $Sm_{1-x}Ce_xFeO_{3-\delta}$ (x = 0, 0.01 and 0.05) perovskites is shown in Figure 8-2.a.

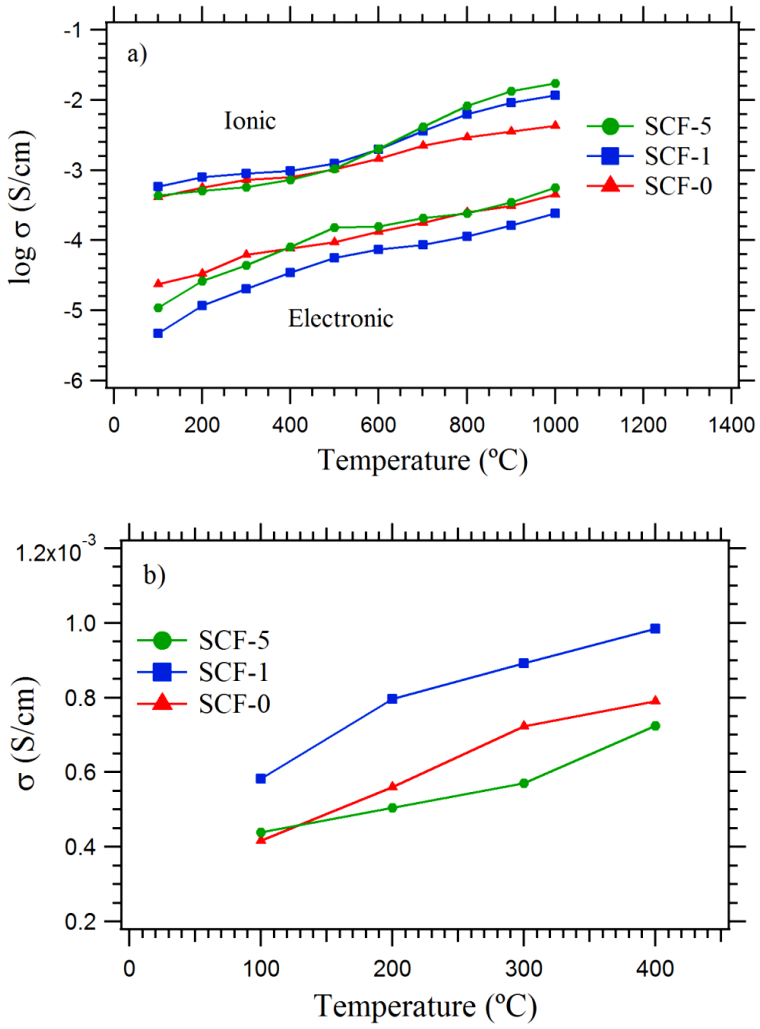

Figure 8-2: (a) Log of ionic and electronic conductivities vs. temperature for $Sm_{1-x}Ce_xFeO_{3-\delta}$ (x=0, 0.01, and 0.05) perovskites between 100-1000°C, (b) Ionic conductivities for $Sm_{1-x}Ce_xFeO_{3-\delta}$ (x=0, 0.01, and 0.05) perovskites at low temperature.

All materials are predominantly ionic conductors, with ionic conductivities 2 orders of magnitude larger than the electronic contribution. Furthermore, Ce doping increases the ionic conductivity of these materials at high temperatures. For example, the parent ($SmFeO_3$) and 5% doped ($Sm_{0.95}Ce_{0.05}FeO_{3-\delta}$) perovskites have ionic conductivities of $2.96 \cdot 10^{-3}$ Scm^{-1} and $8.18 \cdot 10^{-3}$ Scm^{-1} at 800°C, respectively. Figure 8-2(b) shows the ionic conductivities of the SCF perovskites at temperatures of 100 - 400°C, directly relevant to the catalytic experiments.

The 1% doped $Sm_{0.99}Ce_{0.01}FeO_{3-\delta}$ material exhibits the highest value for ionic conductivity at low temperature, with a σ value of $5.83 \cdot 10^{-4}$ Scm^{-1} at 100°C.

8.4.1.3 Surface area measurements

The specific surface areas of $Sm_{1-x}Ce_xFeO_{3-\delta}$ (x=0, 0.01, and 0.05) perovskites before and after Pt loading are listed in Table 8-2.

Table 8-2: Specific surface areas ($m^2 g^{-1}$) of $Sm_{1-x}Ce_xFeO_{3-\delta}$ (x=0, 0.01, and 0.05) perovskite powders before and after Pt-loading.

	SCF-0	SCF-1	SCF-5
a_s (as prepared) $m^2 \cdot g^{-1}$	5.88	7.85	8.45
a_s (Pt-loaded) $m^2 \cdot g^{-1}$	11.78	8.65	9.75

The as-prepared perovskite samples have relatively low specific surface areas, with values in the order of 6-8 m^2 g^{-1}. Loading of the perovskites with Pt has an impact on the specific surface area, increasing it with ratios ranging from 10%, 15% to 100%, for SCF-1, SCF-5 and SCF-0, respectively. Nevertheless, the observed differences in catalytic activity for Pt loaded vs. the as prepared perovskites are not associated solely to surface area effect. In other words, as will be shown below, the enhancement in catalytic activity is a function of Pt content, either through direct catalysis or metal-support interaction and not solely due to an increase in the overall surface area.

8.4.2 Carbon monoxide and Ethylene oxidation

8.4.2.1 Activity of blank supports for carbon monoxide and ethylene oxidation

Figure 8-3a shows the rate of CO oxidation as a function of temperature over $Sm_{1-x}Ce_xFeO_{3-\delta}$ (x = 0 (SCF-0), 0.01 (SCF-1) and 0.05 (SCF-5)) as well as on YSZ powder.

(a)

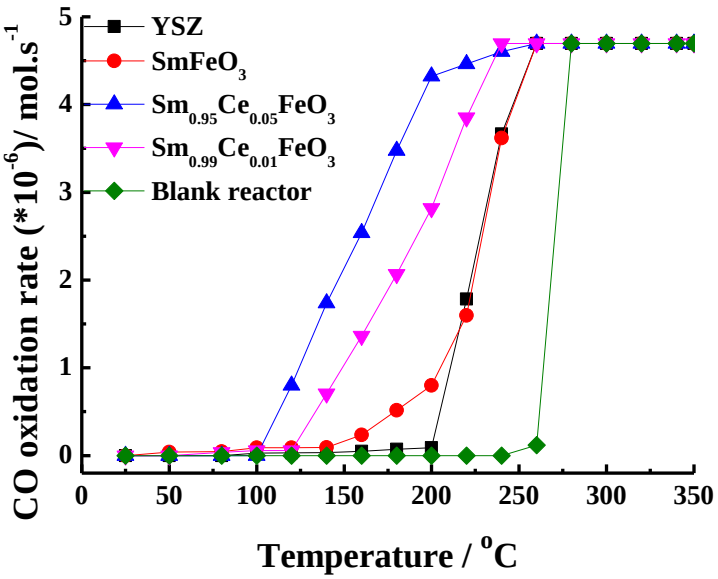

(b)

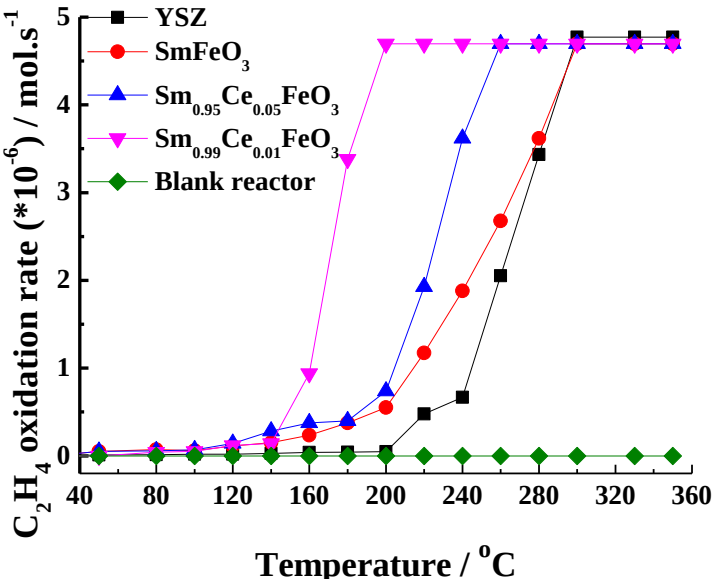

Figure 8-3: catalytic activity of blank supports for complete oxidation of 909ppm (a) CO, (b) C_2H_4. Space velocity = 14688 h^{-1}, gas composition: total flowrate= 4.62 $L \cdot h^{-1}$, [CO or C_2H_4] = 909 ppm, 3.5 kPa O_2 and He balance.

CO oxidation was investigated in the temperature range of 25 - 240°C. Blank experiments with an empty reactor show that no homogeneous gas phase oxidation takes place up to 270°C. All experiments were run starting from the lower temperature (25°C) and maintaining each temperature for 20 - 30 min until steady-state conversion was reached. The

results show that as cerium dopant concentration increases, the catalytic activity towards CO oxidation increases in the following order SCF-5 > SCF-1 > SCF-0 > YSZ. It was reported that the catalytic reaction ($CO + 1/2\ O_2 \rightarrow CO_2$) presumably occurs by the activation of gas-phase oxygen on the perovskite surface [43], the participation of the surface oxygen vacancies as activation centers for the O_2 reactant cannot be excluded. The superior activity of SCF-5 may hence be due to the presence of additional surface oxygen as observed during the analysis of O1s peak using detailed XPS characterization of SCF-0, SCF-1 and SCF-5 as was previously reported [30].

Cerium is usually reported as a good promoter in perovskites up to 10% partial substitution since it enhances reducibility and oxygen desorption [44]. Above this percentage, segregation in the perovskite structure is typically observed which decreases their catalytic activity [44]. According to several studies, partial substitution of perovskites with Ce led to an increase in catalytic oxidation activity for propane [45], CO [46], CH_4 [47] and ethanol [38]. Levasseur et al. [44] studied the effect of Ce doping in $La_{1-x}Ce_xCoO_3$ on the catalytic activity for VOCs oxidation (carbon monoxide, methane and methanol). They reported that doping this perovskite with 10% Ce enhanced its reactivity towards the oxidation of the mentioned VOCs. For instance, the T_{50} and T_{100} for 5% CO oxidation decreased from 162 and 229 to 85 and 104^oC, for the undoped and 10% Ce-doped perovskites, respectively. The same trend was observed for the catalytic oxidation activity of 0.5% methanol and 0.25% methane. The temperature-programmed reduction experiments (TPR-H_2) clearly indicated that the insertion of Ce in the perovskite lattice facilitates reduction of Co^{3+} to Co^{2+}.

Moreover, Falcon et al. [43] investigated the effect of Sr doping on the catalytic activity of $Ln_xNi_{1-x}O_3$ where (Ln = Pr, Sm, Eu) with (x = 0.01, 0.05 and 0.10) as compared to non-doped $LnNiO_3$ for complete CO oxidation. They found that the effect of Sr substitution is much more marked in $Pr_{0.95}Sr_{0.05}NiO_3$, in which the activity drastically increases for CO oxidation. The effect of Sr doping was more pronounced in Pr > Sm > Eu based-perovskites. They conducted thermogravimetric analysis (TG) and temperature-programmed reduction (TPR) experiments to explain this trend. Both analysis methods showed that the thermal decomposition of the Sr-doped samples under reduction conditions takes place at a significantly lower temperature, which suggests that the activity is also related to the ease of

oxygen removal, as has been observed in the $LaCoO_{3-\delta}$ series [49]. The reduction temperatures decrease as the size of the rare-earth cation becomes larger, which may be evidence that the lattice oxygen is participating in this reaction in such a way that the trend observed for reducibility is closely related with that observed in CO oxidation. They also reported that the reduction temperature decreases when Ni valence increases using a suitable partner in the crystal lattice. This means that the electronic density is shifted towards Ni–O, giving shorter Ni–O bonds, still richer in electrons; therefore they are reduced at lower temperatures. In other words, the lattice oxygen (or some of it) is more mobile and can participate more easily in external redox processes. Applying this explanation to our case, higher percentage of Ce doping would be expected to shorten Fe-O bond further and hence the lattice oxygen would participate more readily in oxidizing CO. This reasoning is supported by our observations, SCF-5 which contains higher percentage of Ce shows superior catalytic activity compared to SCF-1 and SCF-0 as shown in Fig. 8-3a.

Figure 8-3b shows the catalytic activity of all blank supports for complete ethylene oxidation in the temperature range of 25 - 350^{o}C. It is noticed that the order of catalytic activity of the supports is not the same as in the case of CO. In this case, ethylene oxidation is highly affected by the ionic conductivity of the supports. It is shown that the catalytic activity of these supports are found to be in the following order SCF-1 > SCF-5 > SCF-0 > YSZ which is in agreement with the ionic conductivity of these materials in the temperature range of 100-300^{o}C. Figure 8-2b shows that the ionic conductivity at 100^{o}C of SCF-1 ($5.83 \cdot 10^{-4}$ S·cm^{-1}) > SCF-5 ($4.38 \cdot 10^{-4}$ S·cm^{-1}) > SCF-0 ($4.16 \cdot 10^{-4}$ S·cm^{-1}) compared with the ionic conductivity of YSZ ($8.42 \cdot 10^{-13}$ S·cm^{-1}) in the same temperature range. This is in accordance with the results reported earlier by Teraokoa et al. [50] who showed that the catalytic activity of $La_{1-x}Sr_xCo_{0.8}Fe_{0.2}O_3$ increases as the ionic conductivity increases for ethylene oxidation. They compared the ionic conductivity of these perovskites with that of YSZ and found it to largely exceed that of YSZ which indicates that these perovskites have highly mobile oxide ions that provide a base for their enhanced catalytic activity [50]. The amount of oxygen desorbed which increases as fraction of substitution in A-site increases was extensively studied using temperature-programmed desorption (TPD) [20,45].

The catalytic performance of perovskites as mixed ionic conductive supports was evaluated for volatile organic compound oxidation reactions [21,25,27,29]. It was found that the A-site substitution in Co- and Fe- perovskite systems increases steeply with the A-site substitution for hydrocarbon oxidation. In $La_{1-x}Sr_xCoO_3$ for example, the optimum x value is 0.2 for propane oxidation but it takes the range of 0.1 - 0.6 for CO oxidation [51]. Co- and Fe-perovskites tend to be optimized at smaller x values than Mn-perovskites which over all depends on the calcination temperature used during preparation [52] which is observed in the present work for the $SmFeO_3$ perovskite family. The optimum value of x is found to be 0.05 for CO and 0.01 for C_2H_4 oxidations.

Marnellos et al. [25] investigated the catalytic and electrocatalytic oxidation of ethylene on a perovskite electrode $La_{0.6}Sr_{0.4}Co_{0.8}Fe_{0.2}O_{3-\delta}$ in the temperature range of 350-550^{o}C. Complete conversion of 10,000 ppm C_2H_4 was achieved at 550^{o}C under fuel lean conditions, which showed that perovskites act as active catalysts for this type of reactions. Moreover, Pereniguez et al. [28] compared the reactivity of $LaNi_{1-y}Co_yO_{3-\delta}$ with the unsubstituted perovskite $LaCoO_3$ and $LaNiO_3$ for the total oxidation of 500 ppm toluene. They confirmed that the partial substitution of A and/or B sites confers to this type of oxides great anionic mobility due to the presence of oxide vacancies, which results in an increased reactivity for the oxidation reactions [53] of VOCs and of soots [8,54]. In all types of perovskites investigated, the total oxidation is achieved at temperatures well below 500^{o}C. Especially remarkable is the catalytic behavior shown by the cobalt-containing perovskites, where a 100% conversion is reached at 250^{o}C. The cobalt containing perovskites present higher catalytic activity coinciding with the release of oxygen at lower temperatures in the range of 200-300^{o}C. They also showed that the availability of these oxygen species could also be favored by the high mobility of inner network oxygen, as detected by x-ray absorption spectra (XAS) during hydrogen reduction of the $LaCoO_3$ perovskite.

Fortunato et al. [55] studied the catalytic activity of perovskites supported on YSZ and TiO_2 for complete oxidation of 1000 ppm toluene. The results showed clear improvement in catalytic activity in the presence of ionic or mixed conductive supports such as YSZ and TiO_2. These results could be attributed to perovskite-support interactions. Using YSZ as a catalytic support induces interactions between oxygen vacancies and perovskite particles on the

surface. Also, the presence of oxygen vacancies is responsible for facilitating the mobility of oxygen ions from the YSZ bulk toward the surface of the support. These surface oxygen ions are highly reactive, as has been shown in systems such as Pt/YSZ [26,31,34]. In the case of TiO_2, the interaction can change the reducibility properties of TiO_2, as already demonstrated with noble metal-supported TiO_2 [56].

8.4.2.2 Ethylene and CO oxidation over supported Pt nanoparticles

Figure 8-4 shows the catalytic activity of Pt supported on SCF-0, SCF-1, SCF-5, YSZ and γ-Al_2O_3 for CO and C_2H_4 oxidation. The rate of reaction is normalized per catalyst active surface area. It is noticed that there is a pronounced shift in the light-off curves to lower temperatures compared to the catalytic activity of the supports alone (Fig. 8-3). Complete CO conversion is achieved at least 100°C lower than the most active perovskite alone (SCF-5), (also see Fig. A-2 in the supplementary information in Appendix A).

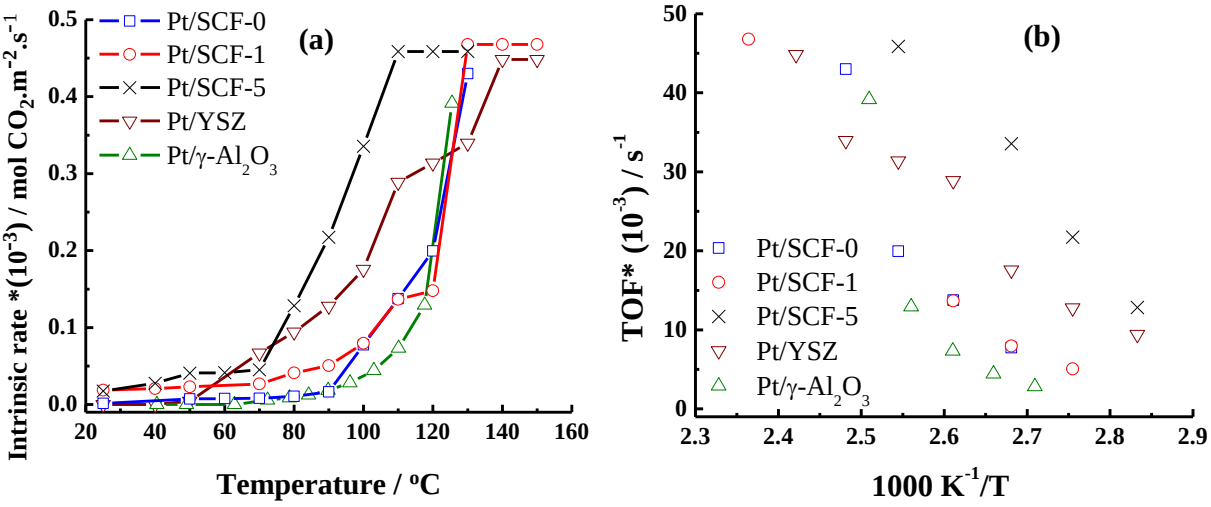

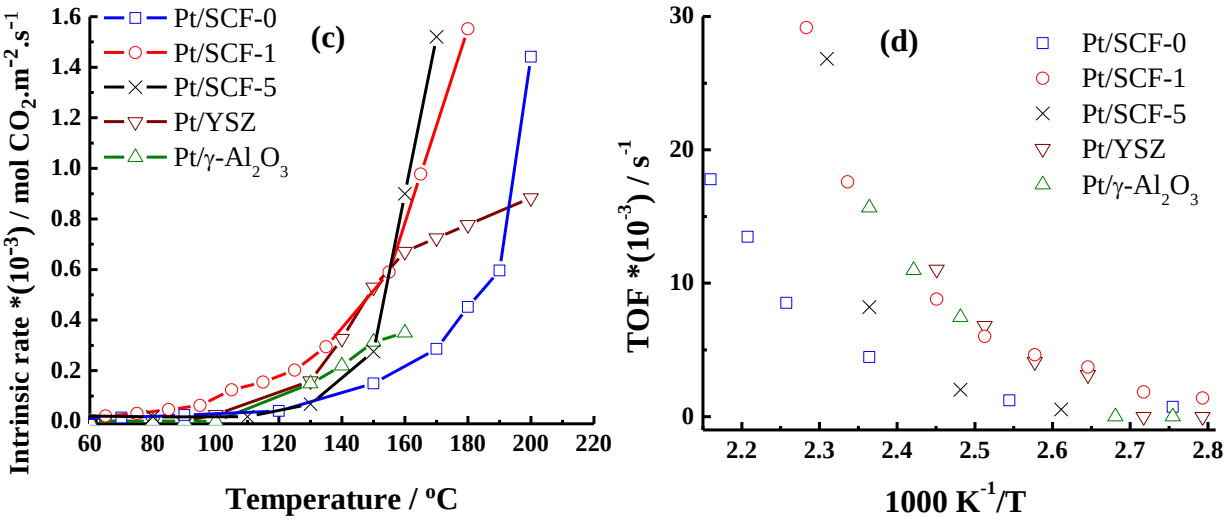

Figure 8-4: The catalytic activity of Pt/YSZ, Pt/SCF-0, Pt/SCF-1, Pt/SCF-5 and Pt/ γ-Al_2O_3: (a) intrinsic rate per catalyst active surface area and (b) turn over frequency for CO oxidation, and (c) intrinsic rate per catalyst active surface area and (d) turn over frequency for C_2H_4 oxidation. Space velocity = 14688 h^{-1}, gas composition: total flowrate= 4.62 L·h^{-1}, [CO or C_2H_4] = 909 ppm, 3.5 kPa O_2 and He balance.

Similarly, for C_2H_4, complete oxidation was achieved at least 50°C lower when compared to the best perovskite alone (SCF-1). The higher catalytic activity is contributed to two effects when depositing Pt on each support. First, there is synergetic effect between Pt and the ionic or mixed ionic conductive supports induced thermally due to the strong metal-support interaction with YSZ and the perovskites, respectively. Secondly, it has been noticed that the specific surface area increased when Pt is deposited on the perovskites compared with the as-prepared perovskites alone as per Table 8-1. The highest increase in surface area is for SCF-0 at 100%, followed by SCF-5 (15%) and last by SCF-1 at (10%). Increased specific surface area would goes hand in hand with dispersion of Pt nanoparticles on the support, hence improving the catalytic activity towards C_2H_4 oxidation which is a structure-sensitive reaction [57,58].

The effect of Pt has been investigated particularly for $La_{0.7}Pb_{0.3}MnO_3$ and $La_{1-x}Sr_xCoO_{3-\delta}$ for CO oxidation reaction [59]. Gallagher et al. [59] studied the catalytic activity of $La_{0.7}Pb_{0.3}MnO_3$ and $La_{0.7}Sr_{0.3}MnO_3$ with and without supported Pt for the oxidation of CO. They found out that adding 60-1600 ppm Pt on $La_{0.7}Pb_{0.3}MnO_3$ were of slight better activity towards CO oxidation compared with $La_{0.7}Pb_{0.3}MnO_3$ alone. Adding further Pt in the range of

2200-5500 ppm showed appreciably better activity than perovskites alone. The higher activity and lower activation energy of the supported samples were attributed to the presence of Pt. Moreover, Wu et al. [22] investigated the effect of Pt-containing perovskites for catalytic methane combustion. They reported that the catalytic activity of $Pt/La_{0.95}Ce_{0.05}CoO_3$ > $La_{0.95}Ce_{0.05}$ $Pt_{0.05}Co_{0.95}$ O_3 > $La_{0.95}Ce_{0.05}CoO_3$ catalysts which may be attributed to that in the case of $Pt/La_{0.95}Ce_{0.0}{}_5CoO_3$, most of platinum is being dispersed on the surface of the catalyst, while it is within the crystalline structure in the case of the platinum-substituted perovskite, i.e., $La_{0.95}Ce_{0.05}$ $Pt_{0.05}Co_{0.95}O_3$.

The mixed ionic conductive supports (perovskites) and ionic conductive support (YSZ) have been reported to show metal-support (MSI) interaction when noble metals are deposited on them. It was shown that Pt/YSZ has higher catalytic activity for volatile organic compounds oxidation compared with $Pt/\gamma\text{-}Al_2O_3$ [26,31,60]. This is due to the metal-support interaction between Pt nanoparticles and the ionic or mixed ionic conductive supports where charge transfer is induced between the conducting ceramic and the nanoparticles. This charge transfer modifies the work function of the catalyst surface and hence improves its catalytic properties. In the case of perovskites, three explanations have been proposed to explain the variation in activity when A-site is partially substituted with another cation. The first one assumes that as x increases, the amount of active oxygen increases while its specific reactivity decreases. The catalytic activity as determined by balancing these two factors becomes maximum eventually at an intermediate value of x [15,61]. In the second explanation, the assumption is made that an increase in x brings about an increase in reducibility or oxidizing power but a decrease in reoxidation ability [15]. The third explanation proposed by Yamazoe et al. [15] indicates that an increase in oxide ion mobility with increasing x facilitates the supply of oxygen from the bulk to the surface catalytic sites, thus increasing the availability of oxygen for the catalytic oxidation of hydrocarbons.

Moreover, it has been reported that when Pt nanoparticles are deposited on perovskites, the catalytic activity is favored towards VOC catalytic oxidation. Enterkin et al. [21] reported that $Pt/SrTiO_3$ shows promising catalytic activity for low temperature hydrocarbon combustion for automotive applications. These materials have more than 50^oC lower light-off temperature for propane oxidation than a conventional Pt/Al_2O_3 catalyst, turn

over frequencies up to 3 orders of magnitude higher, and show improved resistance to deactivation. They tested the effect of depositing 1, 3 and 5 atomic layers of Pt on $SrTiO_3$ and compared it with $SrTiO_3$ blank. Without Pt, $SrTiO_3$ was found to be inactive for propane oxidation, where only 5% propane conversion was achieved at the highest temperature of 450^oC. Propane T_{50} decreased from 198 to 168^oC and TOFs increased from 493 to 21162 h^{-1} with increased Pt loadings. The increased activity is attributed to the stabilization of a Pt/PtO core/shell structure during operating conditions by the strong epitaxy between the Pt and the $SrTiO_3$ support. Platinum on the $SrTiO_3$ nanocuboid supports has been seen to be less oxidized than platinum on either alumina or titania supports under similar conditions. Furthermore, supporting the presence of metallic platinum and epitaxy between $SrTiO_3$ and Pt, BET surface area measurement yielded a value of 31 m^2 g^{-1}, indicating an increase of about 55% in surface area upon deposition of platinum.

The estimation of the mass and heat transfer limitations was carried out for the highest reaction rate in each experimental run for the five catalysts (see supplementary information for detailed calculations and results in Table A1-A3 in Appendix A). The Weisz- Prater (eq. 8.3) and Weisz-Hicks (eq. 8.4) results show very negligible mass and heat resistances for CO and C_2H_4 electrooxidations over the catalysts in the order of 10^{-6} to 10^{-5}. These values are far less than unity, as required by both criteria, indicating negligible mass and heat transfer limitations. This is in accordance with previous results presented for other studies on nanoparticles for heterogeneous catalytic systems, where mass and heat transfer limitations were found negligible [39, 42].

Figure 8-5 shows the activation energy of all the supported Pt catalysts for CO and C_2H_4 oxidation. It is noted that the trend of decreasing activation energy is consistent with increasing the catalytic activity of the catalysts.

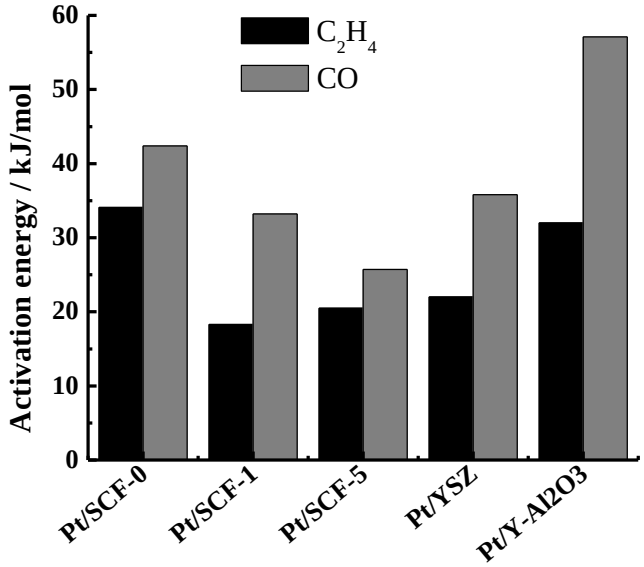

Figure 8-5: The activation energy of CO and C_2H_4 oxidation over Pt supported on perovskites catalysts.

The lowest activation energy for CO was achieved over Pt/SCF-5 catalyst which has the earliest catalytic activity for CO oxidation. The activation energy of Pt/SCF-5 is 25.7 kJ/ mol which is the lowest compared with the reported values in literature; 37.6 kJ/mol reported by Vaz et al. over $LaNi_{0.3}Co_{0.7}O_3$ [14] and 46.4 kJ/mol reported by Yao et al. over $LaCoO_3$ [19]. These figures indicate that not only is Pt a better catalyst than perovskites alone, but the addition of SCF-5 as a support for the Pt catalyst produces the most active Pt-supported catalyst for this reaction. The same is observed for C_2H_4, where the lowest activation energy of 18.3 kJ/mol was achieved over Pt/SCF-1, which is the most active for ethylene oxidation. Due to the scarcity of work reported on perovskite activity for ethylene oxidation, our value is compared with the one reported by Yao et al. [19] over $La_{0.7}Pb_{0.3}MnO_3$ in the temperature range of 200-500^{o}C which is 26.4 kJ/mol.

8.5 Conclusions

Different sets of samarium-perovskites prepared via sol-gel method have been tested for complete oxidation of CO and C_2H_4 showing excellent catalytic activity at temperatures below 300^{o}C for all the samples evaluated. The effect of doping cerium in the A-sites in the $Sm_{1-x}Ce_xFeO_{3-\delta}$ series was found to further improve the total conversion yields. It is found that when testing blank supports alone, $Sm_{0.95}Ce_{0.05}FeO_{3-\delta}$ (SCF-5) is the best in activity towards

CO oxidation while $Sm_{0.99}Ce_{0.01}FeO_{3-\delta}$ is the best for C_2H_4 oxidation. When supporting Pt on the supports, the mixed ionic conductive supports represented by perovskite groups as well as the ionic conductive support (YSZ) have the earliest catalytic activity which is further enhanced with the addition of Pt. Loading Pt over those active supports is believed to cause the enhancement in activity through stabilization of the catalyst, increase in specific surface area and improvement of the ionic conductivity for the total oxidation of the volatile organic compounds under study. Moreover, the higher ionic conductivity of the perovskites compared to YSZ at low temperatures further enhanced their activity towards the VOC oxidation before and after Pt loading.

8.6 Acknowledgement

Financial support from the Natural Science and Engineering Research Council (NSERC) and Ontario Graduate Scholarship (OGS) are acknowledged. In context of this, I would like to acknowledge Dr. Nimal de Silva (Dept. Earth Sciences) for running ICP measurements. Dr. Javier Georgi (Chemistry Dept., UOttawa) for providing the novel perovskite materials and his valuable comments for the manuscript in this chapter. Will Penwell (Chemistry Dept., UOttawa) for running conductivity, surface area and TEM characterization measurements and providing discussion part related to the perovskites characterization in the manuscript presented in this chapter. Joao O. C. Filizzolla who was an undergraduate student under my supervision for his help in the experiments related to the use of blank supports as a catalyst for the oxidation of VOCs.

8.7 Supporting information statement

Detailed mass and heat resistance calculations for all the catalysts are available in Appendix A.

8.8 References

[1] P. Vernoux, L. Lizarraga, A. De Lucas-Consuegra, D. Tsiplakides, M. N. Tsampas, J. -L. Valverde, S. Balomenou, F. M. Sapountzi, S. Souentie, E. A. Baranova, *Chem. Rev.* 113 (2013) 8192.

[2] H. Tanaka, M. Misono, Curr. Opin. *Solid State Mater. Sci.* 5 (2001) 381.

[3] S. Cimino, L. Lisi, S. Rossi, M. Faticanti, P. Porta, *Appl. Catal. B Environ.* 43 (2003) 397.

[4] M. Federica, B. Arstad, B. Egil, *J. Catal.* 275 (2010) 25.

[5] A. Kaddouri, P. Gelin, N. Dupont, *Catal. Commun.* 10 (2009) 1085.

[6] G. Parravano, *J. Chem. Phys.* 20 (1952) 342.

[7] D. B. Meadowcroft, *Nature.* 226 (1970) 847.

[8] J. L. Hueso, A. Caballero, M. Ocana, A. R. Gonzalez-Elipe, J. Catal. 257 (2008) 334.

[9] R. Pereniguez, J. L. Hueso, J.P. Holgado, F. Gaillard, A. Caballero, *Catal. Letters.* 131 (2009) 347.

[10] M. A. Pena, J. L. Fierro, *Chem. Rev.* 101 (2001) 1981.

[11] T. Nakamura. M. Misono, Y. Yoneda, *Chem. Lett.* 10 (1981) 1589.

[12] M. Alifanti, J. Kirchnerova, B. Delmon, D. Klvana, *Appl. Catal.* 262 (2004) 167.

[13] A. Musialik-Piotrowska, H. Landmesser, *Catal. Today*. (2008) 357.

[14] T. Vaz, V. Salker, *Mater. Sci. Eng. B.* 143 (2007) 81.

[15] N. Yamazoe, Y. Teraoka, *Catal. Today.* 8 (1990) 175.

[16] F. Patel, S. Patel, *Procedia Eng*. 51 (2013) 324.

[17] Y. Zhang-Steenwinkel, J. Beckers, A. Bliek, *Appl. Catal. A Gen.* 235 (2002) 79.

[18] R. J. H. Voorhoeve, J. P. Remeika, P. E. Freeland, B.T. Matthais, *Science.* 177 (1972) 353.

[19] Y. F. Yu Yao, *J. Catal.* 36 (1975) 266.

[20] T. Nitadori, S. Kurihara, M. Misono, *J. Catal.* 98 (1986) 221.

[21] J.A. Enterkin, W. Setthapun, W. Elam, S. T. Christensen, F. A. Rabu, L. D. Marks, P. C. Stair, K. R. Poeppelmeier, C. L. Marshall, *ACS Catal.* 1 (2011) 629.

[22] Y. Wu, L. Luo, Russ. *J. Phys. Chem. A.* 85 (2011) 2429.

[23] J.A. Enterkin, K. R. Poeppelmeier, L. D. Mark, *Nano Lett.* 11 (2011) 993.

[24] E. Vrieland, *J. Catal.* 415 (1974) 32.

[25] G. Marnellos, C. Athanasiou, T. Angelidis, M. Stoukides, *Ionics*. 3 (1997) 96.

[26] H. A. E. Dole, R. J. Isaifan, F. M. Sapountzi, L. Lizarraga, D. Aubert, A. Princivalle, P. Vernoux, E. A. Baranova, *Catal. Letters.* 143 (2013) 996.

[27] R. Pereñíguez, J. L. Hueso, F. Gaillard, J. P. Holgado, A. Caballero, *Catal. Letters.* 142 (2012) 408.

[28] R. Pereñíguez, J. L. Hueso, J. P. Holgado, F. Gaillard, A. Caballero, *Catal. Letters.* 131 (2009) 164.

[29] K. Rida, A. Benabbas, F. Bouremmad, M. A. Peña, A. Martínez-Arias, *Catal. Commun.* 7 (2006) 963.

[30] S. M. Bukhari, J. B. Giorgi, *Solid State Ionics.* 180 (2009) 198.

[31] R. J. Isaifan, H. A. E. Dole, E. Obeid, L. Lizarraga, P. Vernoux, E. A. Baranova, *Electrochem. Solid-State Lett.* 15 (2012) E14.

[32] E. A. Baranova, C. Bock, D. Ilin, D. Wang, B. Macdougall, *Surf. Sci.* 600 (2006) 3502.

[33] C. G. Vayenas, S. Bebelis, I. Yentekakis, H. Lintz, *Catal. Today.* 11 (1992) 303.

[34] M. A. Fortunato, D. Aubert, C. Capdeillayre, C. Daniel, A. Hadjar, A. Princivalle, C. Guizard, P. Vernoux, *Appl. Catal. A Gen.* 403 (2011) 18.

[35] R. M. Rioux, J. D. Hoefelmeyer, M. Grass, H. Song, K. Niesz, P. Yang, G. A. Gabor, *Langmuir.* 24 (2008) 198.

[36] S. -I. Kim, T. Yamamoto, A. Endo, T. Ohmori, M. Nakaiwa, *J. Ind. Eng. Chem.* 12 (2006) 769.

[37] M. Marwood, C. G. Vayenas, *J. Catal.* 178 (1998) 429.

[38] H. S. Fogler, Elements of Chemical Reaction Engineerin, fourth edition, Pearsons Education Inc., New Jersy, 2006.

[39] S. T. Oyama, X. Zhang, J. Lu, Y. Gu, T. Fujitani, *J. Catal.* 257 (2008) 1.

[40] P. B. Weisz, J. S. Hicks, *Chem. Eng. Sci.* 17 (1962) 265.

[41] D. E. Mears, *Ind. Eng. Chem. Process. Des. Dev.* 10 (1971) 541.

[42] M. H. Chahbani, J. Labidi, J. Paris, *Appl. Therm. Eng.* 22 (2002) 23.

[43] H. Falcon, J. A. Alonso, *Solid State Ionics.* 131 (2000) 237.

[44] B. Levasseur, S. Kaliaguine, *Appl. Catal. B Environ.* 88 (2009) 305.

[45] T. Nitadori, M. Misono, *J. Catal.* 93 (1985) 459.

[46] L. Forni, C. Oliva, F. P. Vatti, M. A. Kandala, A. M. Ezerets, A.V. Vishniakov, *Appl. Catal. B Environ.* 7 (1996) 269.

[47] M. Alifanti, R. Auer, J. Kirchnerova, F. Thyrion, P. Grange, B. Delmon, *Appl. Catal. B Environ.* 41 (2003) 71.

[48] B. Bialobok, J. Trawczynski, W. Mista, M. Zawadzki, *Appl. Catal. B Environ.* 72 (2007) 395.

[49] T. Nakamaru, M. Misono, Y. Yoneda, *Bull Chem Soc Jpn.* 55 (1982) 394.

[50] Y. Teraoka, H. M. Zhang, K. Okamoto, N. Yamazoe, *Mater. Res. Bull.* 23 (1988) 51.

[51] T. Nakamura, M. Misono, Y. Yoneda, *J. Catal.* 83 (1983) 151.

[52] K. Tabata, I. Matsumoto, S. Kohiki, M. Misono, *J. Mater. Sci.* 22 (1987) 4031.

[53] L. G. Tejuca, J. L.G. Fierro, Properties and applications of perovskite-type oxides, Marcel Dekker Inc., New York, 1993.

[54] N. Russo, D. Fino, G. Saracco, V. Specchia, *J. Catal.* 229 (2005) 459.

[55] M. A. Fortunato, M. Richard, J. A. Diaz, S. Gil, N. Bion, F. Can, A. Giroir-Fendler,

6th Int. Annu. Meet. GDRI. (2013) 1.

[56] M. Ousmane, L. F. Liotta, G. Pantaleo, A. M. Venezia, G. Di Carlo, M. Aouine, L. Retailleau, A. Giroir-Fendler, *Catal. Today.* 176 (2011) 7.

[57] A. Van Strien, B. E. Nieuwenhuys, *Surf. Sci.* 80 (1979) 226.

[58] R. J. Isaifan, S. Ntais, E. A. Baranova, *Appl. Catal. A Gen.* 464-465 (2013) 87.

[59] P. K. Ghallagher, D. W. Johnson, J. J. P. Remeika, F. Schrey, L. E. Trimble, E. M. Vogel, R. J. H. Voorhoeve, *Mat. Res. Bull.* 10 (1975) 529.

[60] R. J. Isaifan, H. Dole, E. Obeid, L. Lizarraga, E. A.Baranova, *ECS Trans.* 35 (2011) 43.

[61] T. Seiyama, N. Yamazoe, K. Eguchi, *Ind. Eng. Chem. Prod. Res. Dev.* 24 (1985) 19.

SECTION V: INSIGHT INTO THE EFFECT OF OXYGEN VACANCY (O^{2-}) IN THE SUPPORTS

9 Catalytic electrooxidation of volatile organic compounds by oxygen-ion conducting ceramics in oxygen-free gas environment

Electrochemistry Communications, 27 (2013) 164-167.

9.1 Abstract

Pt nanoparticles (2.5 ± 0.5 nm) deposited on yttria-stabilized zirconia (YSZ), ceria (CeO_2) and samarium doped-ceria (SDC) show a strong metal-support interaction (SMSI) resulting in O^{2-} transfer towards Pt through the triple phase boundary (tpb) and electron transfer from Pt to the ceramic. This charge transfer leads to a remarkable catalytic activity of Pt nanoparticles interfaced with ionically and mixed conductive supports for carbon monoxide and ethylene oxidation in the absence of O_2 in the gas feed. It is proposed, that Pt nanoparticles and the conducting ceramic form local galvanic cells, where anodic reaction is VOCs oxidation by O^{2-} at the tpb and the cathodic reaction is the partial reduction of zirconia or ceria. The complete electrooxidation of 909 ppm of CO and C_2H_4 by O^{2-} from the conductive ceramic support was achieved in the temperature range of 120 – 240^{o}C depending on the support. The total oxygen fraction consumed from each support per catalytic run was 1.9– 2.4 and 16.9 – 25.9 % for oxidation of 909 ppm of CO and C_2H_4, respectively. The catalytic activity of Pt/solid electrolytes was compared with YSZ, CeO_2 and SDC blank supports and also with Pt nanoparticles deposited on non-ionically conductive carbon black (Pt/C) and γ-alumina (Pt/γ -Al_2O_3) supports, which all showed no catalytic activity in the absence of oxygen in the gas feed.

9.2 Introduction

Solid ionic conductors such as yttria stabilized zirconia (YSZ) and doped-ceria (Sm-CeO_2 or Gd-CeO_2) are widely used in the fuel cell and sensor technologies as well as in heterogeneous catalysis, in particular in electrochemical promotion of catalysis (EPOC) [1-3]

and their operation at low temperatures is of great importance [4-6]. The bulk ionic O^{2-} conductivity of YSZ is caused by the presence of oxygen vacancies and is not significant below 600^{o}C. In conventional solid oxide fuel cells, operating temperatures as high as 800^{o}C are required to generate sufficient bulk ionic conductivity in the solid electrolytes [7, 8]. Ceria (CeO_2) is a n-type semiconductor with a fluorite structure. Under a redox environment, Ce^{3+} / Ce^{4+} interchange may take place leading to a shift between CeO_2 and Ce_2O_3. The interesting catalytic properties of ceria were attributed to its ability to release or store oxygen in its cubic structure and due to high oxygen mobility at its surface [9,10]. It has been reported recently that ionic conductivity of ionically conductive YSZ [5, 11-13] and mixed conductive CeO_2 [14, 15] can be enhanced up to 6 orders of magnitude at temperatures as low as 70^{o}C. These works have related superionic conductivity of YSZ and CeO_2 to the creation of lattice strains and misfit locations that alter migration barriers of ionic species in the supports. Kushima et al. [5,12] used the density functional theory (DFT) and nudged elastic band (NEB) methods to assess the oxygen vacancy migration paths in YSZ as a function of lattice strain. Sallissen et al. [11] reported an enhancement of lateral ionic conductivity in YSZ up to 3.5 orders of magnitude due to interfacial effects. Moreover, Vayssilov et al. [14] recently reported that the interaction of Pt nanoparticles deposited on CeO_2 favored the electron transfer from Pt nanoparticles to the support and oxygen transfer from CeO_2 to Pt leading to strongly enhanced catalytic activity of nano-structured ceria-supported noble metal catalysts.

In this study the catalytic activity of Pt nanoparticles (2.5 ± 0.5 nm) deposited on ionically conductive YSZ (ZrO_2, 8%Y_2O_3) and SDC ($Sm_{0.2}Ce_{0.8}O_{1.9}$), as well as mixed CeO_2 supports was compared with the same Pt nanoparticles deposited on non-ionically conductive supports, such as carbon black (C) and γ-alumina (γ-Al_2O_3) as well as with the blank conductive supports. The supported catalysts were used for carbon monoxide (CO) and ethylene (C_2H_4) oxidation at 40 – 240^{o}C under the absence of oxygen in the gas feed.

9.3 Experimental

Pt nanoparticles were synthesized by a modified polyol reduction method using ethylene glycol in the presence of NaOH (C_{NaOH} = 0.08M) [16,17]. Resulting Pt nanoparticles have 2.5 ± 0.5 nm average particle size as confirmed by TEM (not shown) and are deposited

on YSZ, CeO_2, SDC, γ-Al_2O_3 and carbon. The loading of Pt nanoparticles on each catalyst was 1 wt. % [17]. Catalytic activity measurements were carried out at atmospheric pressure in a continuous flow U-shaped quartz reactor. Approximately 50 mg of catalyst was placed into the reactor. The reactant mixture was composed of 909 ppm C_2H_4 (Linde, 5% in He) or CO (Linde, 1% in He) and balance He (Linde, 100%). The total gas flow rate was 4.62 $L \cdot h^{-1}$ for C_2H_4 and CO experiments. The samples were tested in the temperature range of 25 – 400^oC. The reactant and product gases were analyzed by an on-line gas chromatograph (GowMac 350) and non-dispersive infrared (NDIR) gas analyzer (HORIBA VA-3001). Each experiment was repeated for at least three consecutive cycles and the third catalytic run is shown unless otherwise stated.

9.4 Results and Discussion

9.4.1 Catalytic activity

Figure 9-1 shows the conversion of CO and C_2H_4 as function of temperature over Pt nanoparticles deposited on various supports. Pt supported on YSZ, CeO_2 and SDC shows high catalytic activity for CO and C_2H_4 oxidation and complete oxidation is achieved at T < 220^oC. Pt/C and Pt/γ-Al_2O_3 systems show no catalytic activity in the absence of oxygen as well as the ionically conductive ceramics by themselves are not active. Full conversion of CO is reached at lower temperatures (130 – 150^oC) compared to ethylene (175 – 210^oC) and it seems that CO oxidation is less sensitive to the type of the conductive support. The earlier catalytic activity of Pt/SDC for C_2H_4 oxidation compared to Pt/YSZ and Pt/CeO_2 is attributed to the higher bulk ionic conductivity of SDC and plausibly easier release of O^{2-} from CeO_2 surface compared to YSZ.

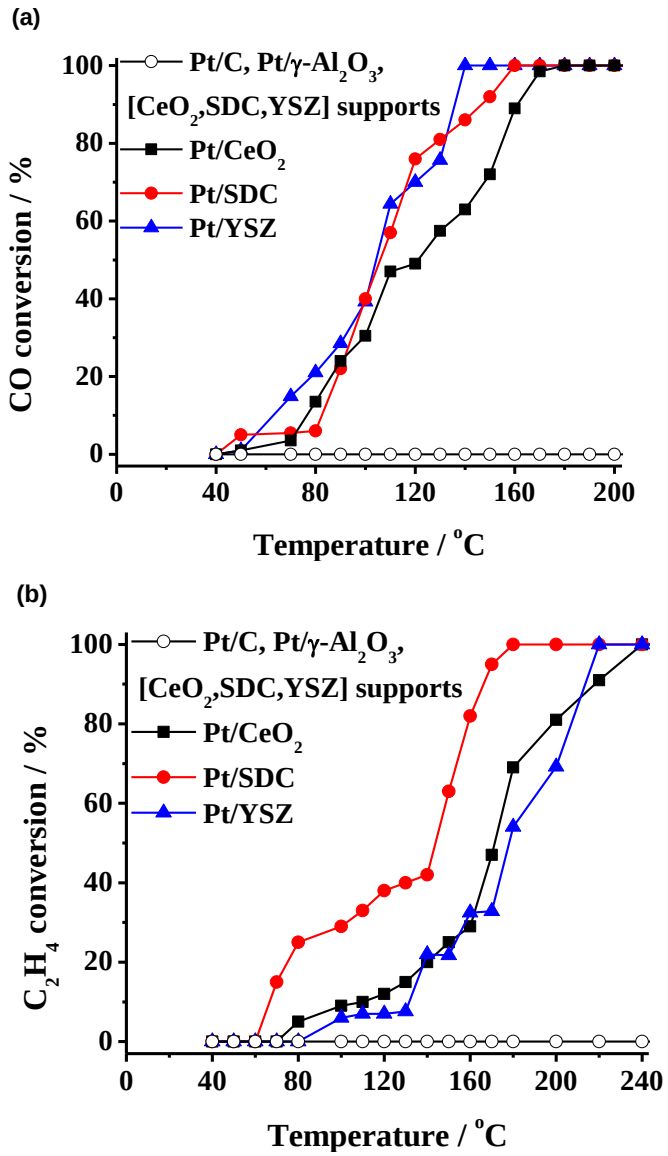

Figure 9-1: Conversion of (a) CO and (b) C_2H_4 over Pt supported on YSZ, SDC and CeO_2 and non-ionically conductive C, γ-Al_2O_3 supports. Conversion over blank YSZ, SDC and CeO_2 is also shown. Space velocity = 14688 h^{-1}, gas composition: total flowrate= 4.62 L·h^{-1}, [CO or C_2H_4] = 909 ppm, He balance. No O_2 in the gas feed.

Absence of O_2 in the gas feed implies that O^{2-} from the support reacts with CO and C_2H_4 in the electrochemical reaction. This reaction occurs at temperatures as low as ~ 70°C indicating that very high localized surface O^{2-} mobility already exists in these conductive ceramics.

It is proposed that Pt nanoparticles and the solid electrolyte form local micro-galvanic cells where the following reactions are taking place for Pt/YSZ system for both CO and ethylene oxidation:

Anodic reaction at tpb:

Electrooxidation of CO:

$$CO + O^{2-} - 2\bar{e} \rightarrow CO_2 \quad (9.1)$$

or

Electrooxidation of C_2H_4:

$$C_2H_4 + 6O^{2-} - 12\bar{e} \rightarrow 2CO_2 + 2H_2O \quad (9.2)$$

Cathodic reaction at tpb:

Partial electroreduction of ZrO_2 [18]:

$$ZrO_2 + 2\delta e^- + \delta V_O^{\cdot\cdot} \rightarrow ZrO_{2-\delta} + \delta O_o^x \quad (9.3)$$

Overall reactions are:

$$\delta CO + 2ZrO_2 + 2\delta V_O^{\cdot\cdot} \rightarrow \delta CO_2 + 2ZrO_{2-\delta} + \delta O_o^x \quad (9.4)$$

$$\delta C_2H_4 + 12ZrO_2 + 12\delta V_O^{\cdot\cdot} \rightarrow 2\delta CO_2 + 12ZrO_{2-\delta} + 2\delta H_2O + 6\delta O_o^x \quad (9.5)$$

Similar reactions showing electrooxidation of VOCs and electroreduction of the support can be written for Pt/CeO_2-based ceramics, where Ce^{4+} is reduced to Ce^{3+} [9, 10, 14]. According to the literature, deposition of carbon on Pt/solid electrolyte systems could take place at relatively low temperatures (< 600K), e.g., ethylene cracking [19] leading to the deposition of carbon and H_2 production, as well as Boudouard reaction, resulting in formation of CO_2 and carbon [20]. It is worth noting that during the former reaction, no H_2 production was observed. Furthermore, the performed carbon balance (not shown here) confirmed that CO_2 was the main product for both CO and C_2H_4 oxidation reactions on Pt/CeO_2 and Pt/SDC, while small quantities (<14 %) of unidentified carbon were found for Pt/YSZ system.

To confirm the possible carbon deposition of Pt/YSZ, the catalyst was left to deactivate by VOC and then it was subject to reaction with molecular oxygen. If carbon was deposited, one would observe CO_2 formation, which was not the case in the present study.

However, deposition of small amounts of carbon on Pt/conducting ceramic systems cannot be completely ruled out. Deposited carbon could be electrochemically oxidized via eq. (9.6):

$$C + 2O^{2-} \rightarrow CO_2 \quad (9.6)$$

Table 9-1 summarizes the total fraction of oxygen ions consumed after one catalytic run of CO and C_2H_4 electrooxidation (Fig. 9-1) over Pt/YSZ, Pt/SDC and Pt/CeO_2. As expected from eqs. (9.1) and (9.2), C_2H_4 electrooxidation requires higher quantities (17 - 26 %) of O^{2-} from the support per run. After the three successive catalytic runs, O^{2-} consumption can reach up to 77.7% for C_2H_4 oxidation on CeO_2, therefore for the efficient catalyst operation, the re-introduction of oxygen to the support is needed.

Table 9-1: Total amount of CO_2 formation and O^{2-} consumption during CO and C_2H_4 electrooxidation in the absence of molecular oxygen in the feed.

		CO_2 formation (μmol/g support) in oxidation of		**Fraction (%) of O^{2-} in support consumed during VOCs oxidation****		
Catalyst/support	**Total amount of O (μmol/g support)***	**CO**	**C_2H_4**	**CO**	**C_2H_4**	**T (^oC)**
Pt/YSZ	15,825	373.7	446	2.4	16.9	40 - 220
Pt/SDC	11,010	222.3	436	1.9	23.7	40 - 220
Pt/CeO_2	11,620	224.0	502	2.0	25.9	60 - 240

* According to manufacturer
**Based on 50 mg of catalyst for 1 catalytic cycle.

9.4.2 Effect of volatile organic compound concentration

In order to investigate the effect of VOC concentration on the catalytic activity of the catalyst, the gas feed composition was varied up to 8,000 ppm of CO and C_2H_4 (Fig. 9-2).

Different temperatures were chosen based on Fig. 9-1 where CO and C_2H_4 conversion of 100 % is achieved on Pt/YSZ.

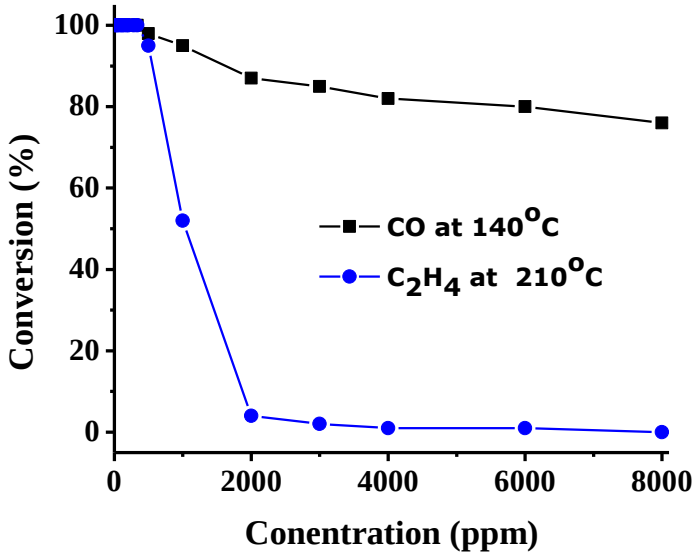

Figure 9-2: Effect of CO and C_2H_4 concentration on the catalytic activity of Pt/YSZ towards CO and C_2H_4 electrooxidation. Space velocity = 19000 h^{-1}, gas composition: total flowrate= 4.62 $L \cdot h^{-1}$, no O_2 in the gas feed.

The results show that Pt/YSZ is more active towards CO oxidation compared to C_2H_4, which can be explained in accordance with the proposed reactions (eqs. (9.1) – (9.3)). The reactions show that each C_2H_4 molecule needs six O^{2-} from the ionic conductor (eq. 9.2), while CO oxidation requires only one anion (eq. 9.1). This leads to a rapid catalyst deactivation, because available surface oxygen ions are consumed in the oxidation reaction. Catalyst can be easily reactivated by swiping O_2 through the reactor or just by leaving the catalyst in He overnight allowing O^{2-} concentration to reach an equilibrium between the bulk and the surface.

9.4.3 Catalytic activity in presence of oxygen

Figure 9-3 compares the catalytic activity of Pt/YSZ for CO and C_2H_4 oxidation in the presence and absence of oxygen in the gas feed. It can be seen that light-off curve shifts to the lower temperatures when 3.5 kPa of O_2 is added, resulting in 100 % CO conversion at 105°C compared to 135°C without oxygen.

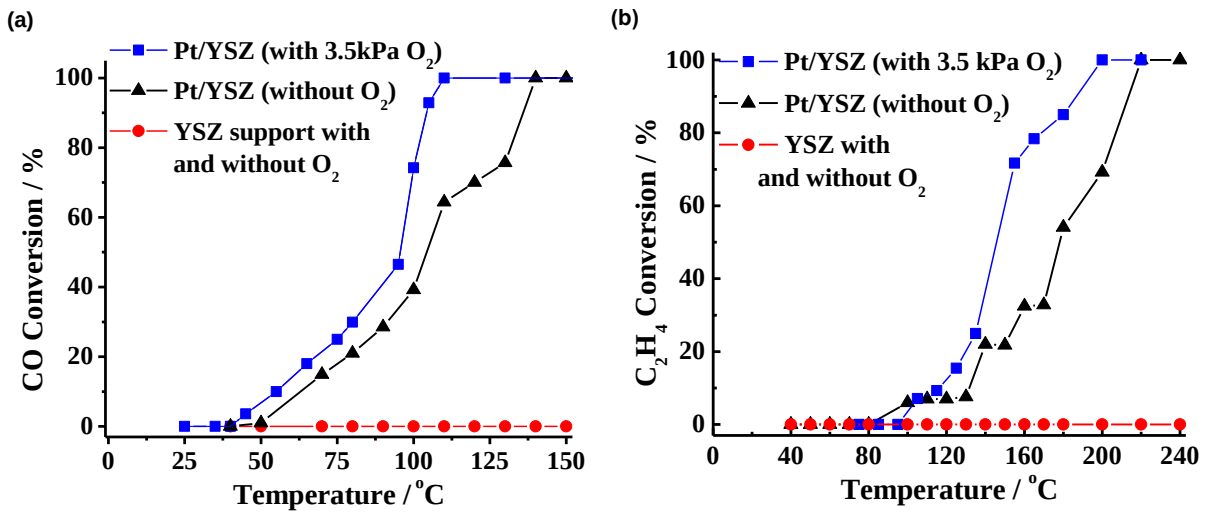

Figure 9-3: Conversion of CO (a) and C_2H_4 (b) as function of temperature on Pt/YSZ catalysts in the presence (Po_2 = 3.5 kPa) and absence of oxygen in the gas feed. Space velocity = 14688 h^{-1}, gas composition: total flowrate= 4.62 $L \cdot h^{-1}$, [CO or C_2H_4] = 909 ppm.

Similar trend is observed for C_2H_4 oxidation, indicating that both electrochemical and chemical oxidation of VOCs are taking place simultaneously when Pt nanoparticles are interfaced with the ionically conductive supports and oxygen is present in the reaction mixture. Corresponding chemical reactions are given as:

$$CO + 1/2O_2 \rightarrow CO_2 \qquad (9.7)$$

or

$$C_2H_4 + 3O_2 \rightarrow 2CO_2 + 2H_2O \qquad (9.8)$$

It is worth to note that Pt supported on γ-Al_2O_3 and carbon shows high catalytic activity for CO and C_2H_4 oxidation in the presence of oxygen [17], while without oxygen in the feed, the activity is zero (Fig. 9-1), confirming that only reactions (eq. 9.7) and (eq. 9.8) can take place on these catalytic systems.

The enhanced ionic conductivity observed for Pt/YSZ, Pt/SDC and Pt/CeO_2 catalytic systems when can be related to the strong metal support interaction generated between the metal and the ionic conductive support [21-25]. Recently, Vayssilov et al. [14] investigated at the microscopic level, the enhanced performance of the supported Pt/CeO_2. They

demonstrated that after supporting Pt on CeO_2, the support showed characteristic defect structure, which boosted oxygen back spillover from ceria to Pt surface. Moreover, recently it was demonstrated that when YSZ is used as a catalyst support for Pt nanoparticles for CO and propene oxidation reactions, the thermally induced backspillover of O^{2-} plays an important role in modification of the catalytic activity of the metal catalysts [17,26].

9.5 Conclusions

It is shown that strong metal support interaction between Pt nanoparticles and ionic and mixed ionic conductive supports leads to the great enhancement in the catalytic activity of Pt nanoparticles towards CO and C_2H_4 oxidation in the absence of oxygen in the feed. The high ionic surface-localized O^{2-} mobility is observed at relatively low temperatures and allows efficient electrochemical oxidation of VOCs at Pt/solid electrolyte interface, which makes ionically conductive supports very attractive for oxidation reactions. Moreover, this finding clearly confirms that localized surface ionic conductivity or oxygen vacancy mobility exist in ionically conductive ceramics even at ~70^{o}C. Systems consisted of nanostructured metal or metal oxide catalyst interfaced with O^{2-} conducting ceramics might be of great potential interest for applications where poor oxygen environment exists and for the treatment of gaseous streams from VOCs traces.

9.6 Acknowledgement

The financial support from Natural Sciences and Engineering Research Council (NSERC) and Ontario Graduate Scholarship (OGS) are acknowledged.

9.7 References

[1] C. Xu, R. Zeng, P. K. Shen, Z. Wei, *Electrochim. Acta.* 51 (2005) 1031.

[2] J. H. Shim, C. Chao, H. Huang, F. B. Prinz, *Chem. Mater.* 19 (2007) 3850.

[3] V. Baglio, A. D. Blasi, A. S. Aricò, V. Antonucci, P. L. Antonucci, *J. New Mater. Electrochem.* Sys. 280 (2004) 275.

[4] A. Saigal, *Electrochem. Soc.* 2007, 72.

[5] A. Kushima, B. Yildiz, *Electrochem. Soc.* 159 (2012) 599.

[6] S. D. Souza, S. J. Visco, L. C. D. Jonghe, *Electrochem. Soc.* 144 (1997) 243.

[7] H. Huang, M. Rottmayer, R. Singh, P. Directorate, M. Engineering, *Electrochem. Soc.* 45 (2012) 515.

[8] E. Lee, F. Prinz, W. Cai, *Phys. Rev. B.* 83 (2011) 1.

[9] F. Esch, S. Fabris, L .Zhou, L. Montini, C. Africh, P. Fornasiero, G. Comelli, R. Rosie, *Science.* 309 (2005) 752.

[10] P. Dutta, S. Pal, M. S. Seehra, Y. Shi, E. M. Eyring, R. D. Ernst, *Chem. Mater.* 18 (2006) 5144.

[11] M. Sillassen, P. Eklund, N. Pryds, E. Johnson, U. Helmersson, J. Bøttiger, *J. Adv. Funct. Mater.* 20 (2010) 2071.

[12] A. Kushima, B. Yildiz, *J. Mater. Chem.* 20 (2010) 4809.

[13] N. Schichtel, C. Korte, D. Hesse, N. Zakharov, B. Butz, D. Gerthsen, J. Janek, *Phys. Chem. Chem. Phys.* 12 (2010) 14596.

[14] G. N. Vayssilov, Y. Lykhach, A. Migani, T. Staudt, G. Petrova, N. Tsud, T. Skála, A. Bruix, F. Illas, K. Prince, V. Matolín, K. Neyman, J. Libuda, *Nat. Mater.* 10 (2011) 310.

[15] A. Migani, G.N. Vayssilov, S. T. Bromley, F. Illas, K.M. Neyman, U.D. Barcelona, *Chem. Commun.* 46 (2010) 5936.

[16] E. A. Baranova, C. Bock, D. Ilin, D. Wang, B. Macdougall, *Surf. Sci.* 600 (2006) 3502.

[17] R. J. Isaifan, H. A. E. Dole, E. Obeid, L. Lizarraga, P. Vernoux, E. A. Baranova, *Electrochem. Solid-State Lett.* 15 (2012) E14.

[18] J. Janek, C. Korte, *Solid State Ionics* 116 (1999) 181.

[19] S. M. Davis, F. Zaera, B. E. Avis, B. E. Gordon, G. A. Somorjai, J. Catal. 92 (1985) 240.

[20] E. P. J. Mallens, J. H. B. J. Hoebink, G. B. Marin, *Catal. Lett.* 33 (1995) 291.

[21] C. Harding, V. Habibpour, S. Kunz, A. Farnbacher, U. Heiz, B. Yoon, U. Landman, *J. Am. Chem. Soc.* 131 (2009) 538.

[22] S. Tauster, *Acc. Chem. Res.* 20 (1987) 389.

[23] W. C. Conner, J. L. Falconer, *Chem. Rev.* 95 (1995) 759.

[24] G. Thornton, *Science.* 300 (2003) 1378.

[25] I. S. Metcalfe, S. Sundaresan, *AIChE J.* 34(1988) 195.

[26] P. Vernoux, M. Guth, X. Li, *Electrochem. Solid-State Lett.* 12 (2009) E9.

10 Size-dependent activity of Pt/yttria-stabilized zirconia catalyst for wireless electrooxidation of ethylene and carbon monoxide in oxygen free environment

Submitted to the Journal of Catalysis, JCAT-14-609.

10.1 Abstract

The effect of Pt average particle size (1.9 - 6.7 nm) on the catalytic activity of 909 ppm carbon monoxide and ethylene oxidation by O^{2-} from yttria-stabilized zirconia (YSZ) was studied at 25 - 400^{o}C. The results show that CO and C_2H_4 oxidation in the absence of oxygen in the gas feed is strongly size dependent in analogy to their catalytic oxidation in oxygen-rich environment. The local nano-galvanic cell mechanism is proposed, where CO and C_2H_4 electrooxidation is accompanied by partial surface electroreduction of YSZ. The smallest Pt nanoparticles (NPs) (1.9 ± 0.4 nm) have higher TOF, higher intrinsic rates at lower temperatures and have lower activation energies compared with the larger Pt NPs (4.4 ± 0.3 nm): 30.3 vs. 64.8 kJ mol^{-1} for CO and 12.5 vs. 38.4 kJ mol^{-1} for C_2H_4 oxidation. XPS measurements show a charge transfer from YSZ to Pt NPs as a result of metal-support interaction (MSI), which can explain the observed high catalytic activity of Pt/YSZ system for CO and C_2H_4 oxidation by O^{2-} from YSZ.

10.2 Introduction

Yttria-stabilized zirconia (YSZ) has attracted significant attention in the last decades due to its interesting chemical and physical properties. Pure zirconia (ZrO_2) has a monoclinic structure at temperatures up to 1170^{o}C, where it changes to the tetragonal modification. It is possible to stabilize the high temperature phase by doping ZrO_2 with oxides such as yttria (Y_2O_3), calcia (CaO) or magnesia (MgO) [1,2]. When these dopants are added to zirconia, oxygen vacancies are created to compensate the charge balance. Among the above mentioned oxides, yttria is the most common dopant that stabilizes the cubic polymorph of zirconia,

giving yttria-stabilized zirconia. YSZ has O^{2-} ionic conductivity in the temperature range of 300 - 1000^{o}C [3] and this relatively high ionic conductivity is due to the presence of oxygen vacancies in its crystallographic structure. YSZ is a common solid electrolyte in solid oxide fuel cells (SOFCs) and has been extensively investigated in the electrochemical promotion of catalysis (EPOC) studies in the past 30 years. In this phenomenon, the application of small current or potential to the catalyst-electrode in contact with a solid electrolyte support leads to the backspillover of promoting ionic species between the support and the gas-exposed catalyst surface. This backspillover through the three-phase-boundary (tpb) results in modification of the catalyst work function and thus, enhances its catalytic activity, and in some cases, selectivity [4-6]. In 2009, Vernoux et al. [7] reported that the backspillover of ionic species from the support to the gas-exposed catalyst surface, can be thermally induced without any electrical polarization by using metallic nanoparticles supported on YSZ [5,8,9]. Several studies demonstrated that YSZ can finely disperse and stabilize nanoparticles and strongly enhance the catalytic activity of metal or metal oxide nanostructured catalysts via metal-support interaction (MSI) [10] or strong metal-support interaction (SMSI) [11], which make it very promising support material in heterogeneous catalysis [12-15]. Despite, the recent interest in using YSZ as a catalyst support material, its effect on the catalytic activity of nanosized catalysts is not fully understood and the role of oxygen ion conductivity on oxidation of VOCs still remains to be elucidated.

When the gas phase oxidation reaction occurs over nanoparticles supported on mixed ionic electronic conductors (MIEC), e.g., CeO_2 and TiO_2 [16,17] or metal oxide catalysts, e.g. iron, vanadium, manganese, copper oxides, etc., the reaction pathway may involve lattice oxide ions either from the catalyst support in the former case of MIEC, or the catalyst itself in the latter case. This mechanism is known as Mars-van Krevelen (MvK) mechanism [18], but other names, redox or regenerative mechanism can be also found in the literature [19]. For instance, depending on the gas phase composition, CO oxidation on Au nanorodes supported on CeO_2 can proceed through MvK mechanism that could be rationalized as follows:

$$CO_{(g)} + \sigma \rightarrow CO_{(ads)} \quad (10.1)$$

$$CO_{(ads)} + 2CeO_2 \rightarrow CO_2 + Ce_2O_3 + \sigma \quad (10.2)$$

$Ce_2O_3 + 1/2O_2 \rightarrow 2CeO_2$ (10.3)

where σ is metal site (Au, Pt, etc). First CO adsorbs on the metal site close to the ceria surface. Then reaction of CO with the neighboring oxygen ion from ceria takes place, resulting in CO_2 formation (step 2), the removal of oxygen ion from CeO_2 leads to Ce_2O_3 formation. In step 3, molecular oxygen from the gas phase re-oxidizes Ce(III) to Ce(IV). The steps (1) and (2) are similar to the redox mechanism of the water gas shift reaction (WGS) proposed by Flytzani-Stephanopoulos and co-workers [20]. Therefore, CO is being oxidized by lattice oxide ions at the catalyst surface and the function of gas-phase oxygen is to replenish the reduced sites by adsorption and solid-state diffusion.

Recently [21], we reported oxidation of CO and ethylene over Pt nanoparticles (2.5 ± 0.5 nm) deposited on ionic and MIEC supports: YSZ, ceria (CeO_2) and samarium doped-ceria (SDC). The full conversion of 909 ppm of CO and C_2H_4 by reaction with lattice O^{2-} from the conductive ceramic supports was achieved in the temperature range of 120 - 240^oC depending on the support. The conversion was observed already at temperature as low as 70^oC indicating that surface O^{2-} is an active reactant, because bulk ionic conductivity of YSZ, ceria and doped-ceria is quite low below 300 ^oC. We showed that once available surface oxygen ions were consumed from the surface of the support, the reaction rate fell to zero and catalyst regeneration was required. Catalyst was reactivated by sweeping O_2 through the reactor or just by leaving the catalyst in helium overnight allowing O^{2-} concentration to reach equilibrium between the bulk and the surface [21]. The proposed redox mechanism of CO and C_2H_4 oxidation involves formation of local nano-galvanic cells at the three-phase boundary, i.e., Pt NPs / conducting ceramic support / gas phase, where anodic and cathodic processes occur simultaneously but separated in space. The anodic reaction is the volatile organic compounds oxidation by O^{2-} (eqs. 10.4, 10.5) and / or carbon oxidation (eq. 10.6), whereas the cathodic reaction is the partial surface reduction of zirconia or ceria at the tpb (eq.10. 7) [21]:

Anodic reactions:

Electrooxidation of CO:

$CO + O^{2-} \rightarrow CO_2 + 2\bar{e}$ (10.4)

or

Electrooxidation of C_2H_4:

$C_2H_4 + 6O^{2-} \rightarrow 2CO_2 + 2H_2O + 12\bar{e}$ (10.5)

In addition, chemically formed carbon on Pt/YSZ can be removed via:

$C + 2O^{2-} \rightarrow CO_2 + 4\bar{e}$ (10.6)

Cathodic reaction is the surface partial electroreduction of YSZ [21,22]:

$ZrO_2 + 2\delta\bar{e} + \delta V_o^{\cdot\cdot} \rightarrow ZrO_{2-\delta} + \delta O^{2-}$ (10.7)

The proposed nano-galvanic cell mechanism is essentially the same as the well-known MvK or redox mechanism, however for the first time, complete oxidation of CO and C_2H_4 is carried out without gaseous phase O_2 thus confirming the paramount role of surface lattice oxygen ions from the conductive support. Furthermore, in [21] the nano-galvanic cell mechanism was extended to Sm doped-ceria and purely ionic conductor YSZ, the latter being known to be unreducible support unlike ceria or titania [21]. The oxidation of CO and C_2H_4 was only observed when Pt NPs were deposited on conductive ceramics, while YSZ, ceria and doped-ceria did not show any activity alone, indicating that metal catalyst sites and their interaction with the support are essential for the reaction.

In the present work, we synthesized Pt NPs with four average particle sizes: 1.9, 3.0, 4.4 and 6.7 nm using the modified polyol method in order to gain better understanding of the earlier proposed nano-galvanic cell mechanism, the role of O^{2-} and metal-support interaction (MSI) in Pt NPs deposited on YSZ support. Scanning transmission electron microscopy (STEM) coupled with energy dispersed x-ray spectroscopy (EDX) and X-ray photoelectron spectroscopy (XPS) were used to explore morphology, size and surface composition of Pt/YSZ catalysts. The particle size effect on the oxidation of 909 ppm CO and C_2H_4 over Pt/YSZ at 25 – 400^{o}C under the absence of oxygen in the gas feed is studied and compared to the catalytic activity in the presence of 3.5 kPa oxygen.

10.3 Experimental

10.3.1 Synthesis of the supported Pt nanoparticles

Synthesis of Pt nanoparticles was carried out in 25 mL of ethylene glycol and the particle size was adjusted by varying the pH of the synthesis solution. The mechanism of synthesis that shows the effect of pH on the resulting particle size is described in details

elsewhere [13,23]. First, $PtCl_4$ precursor salt was mixed with ethylene glycol (Anhydrous 99.8%, Sigma Aldrich) containing between 0.056 and 0.2 M NaOH (EM Science, ACS grade) for 30 min and then refluxed at 160^{o}C for 3h. Then, the supported catalysts were prepared by mixing an appropriate amount of the colloidal nanoparticles with 1.5 g of YSZ (Tosoh, as = 13 $m^2 \cdot g^{-1}$). The Pt colloidal solution and YSZ powder were vigorously stirred for 24 h at room temperature and then separated by centrifugation. The resulting supported catalyst was extensively washed with deionized water (18 MΩ cm) and air dried for 48 h at 60^{o}C. The total Pt metal loading in all cases was ~1 wt. % as confirmed by inductively coupled plasma (ICP) measurements.

10.3.2 Characterization

10.3.2.1 STEM of Pt/YSZ

The scanning transmission electron microscopy (STEM) analysis was carried out on a FEI Titan^3 80-300 TEM operated at 300 keV, and equipped with a CEOS aberration corrector for the probe forming lens and an energy dispersive X-ray (EDX) spectrometer (EDAX Analyzer, DPP-II). Annular dark-field (ADF) images, which provide a contrast related mainly to the atomic number (Z) and the thickness of the region analyzed, were acquired with a Fishione detector. The convergence and collection angle were 17 and 60 mrad, respectively. The TEM specimens were prepared by sonicating the as-prepared catalyst powders in ethanol. One drop of the solution was then placed onto a 200 mesh TEM copper grid coated with a lacey carbon support film (Ted Pella) and dried in air. The bright features observed in the ADF-STEM images were identified as the Pt catalyst. The elemental composition of both the catalyst and the support was also confirmed by spatially-resolved EDX (Fig. B-1 in the supporting information in Appendix B). The use of Image J software allowed for the determination of Pt particles size distribution.

10.3.2.2 XPS characterization

The X-ray photoelectron spectroscopy (XPS) analysis was conducted using a KRATOS Axis Ultra DLD with a Hybrid lens mode at 140 W and pass energy 20 eV using monochromatic radiation AlKα (E=1486.6 eV). In all cases, the operating pressure in the

analysis chamber was less than 1 x 10^{-9} mbar. Due to the insulating nature of the samples under study, a charge neutralizing flood gun was employed. The Pt4f peak was analyzed using a doublet with spin orbit splitting 3.35 eV and intensity ratio 4/3 [24] while a peak asymmetry was used in the case of the Pt4f peak attributed to the metallic state [25,26].

10.3.2.3 Dispersion of the supported catalysts

Dispersion was determined for the supported Pt nanoparticles using the CO titration technique [6,27-29]. Initially, the catalyst was purged with carbon monoxide (Linde, 1000 ppm CO in He) with a flow rate of 15 ml·min^{-1} at 140^{o}C followed by 100 mL · min^{-1} He (Linde, 100%) at the same temperature. Finally, an oxygen flow of 30 mL · min^{-1} (Linde, 99.997% O_2) was passed through the reactor and the amount of CO_2 formed was measured using an online CO_2 analyzer and gas chromatograph. This procedure was repeated for different purging times ranging from 5 to 20 min, and the maximum reactive CO uptake was obtained by extrapolating to time equals zero. The CO/Pt ratio is assumed to be unity [28-30].

Furthermore, the dispersion was also calculated using the average nanoparticle sizes from ADF-STEM images using the following equation to compare it with CO titration results:

$$dispersion(\%) = \frac{MW \times 600}{\rho \times d_{nm} \times a \times N_a} \qquad (10.8)$$

where MW is the molecular weight of Pt = 195.08 (g·$mole^{-1}$), ρ is the catalyst density which is 21.09 (g·cm^{-3}) for Pt, d_{nm} is the average particle size (nm), a is the atomic surface area = 8.06 x10^{-20} (m^2·$atom^{-1}$), N_a =Avogadro's number.

The activation energy for CO and C_2H_4 oxidation and electrooxidation was determined using Arrhenius relationship calculated in the range below 20 % conversion of carbon monoxide or ethylene according to:

$$\ln r = -E_a/(RT) + \ln k \qquad (10.9)$$

where r is CO or C_2H_4 oxidation or electrooxidation rate (mol·s^{-1}), E_a is the apparent activation energy (J·mol^{-1}), R is the universal gas constant (J·mol^{-1}·K^{-1}), T is the reactor temperature (K), and k is the reaction rate constant (mol·s^{-1}).

External mass and heat transfer limitations were evaluated for the highest catalytic reaction rate of each experiment (see supplementary information) using Weisz - Prater criterion for internal mass diffusion [31,32]:

$$C_{WP} = \frac{-r'_{A(obs)}\,\rho_c R^2}{D_e C_{As}} < 1 \qquad (10.10)$$

where, $-r'_{A(obs)}$ = observed reaction rate (kmol · kg-cat^{-1}·s^{-1}) preferrably at the highest temperature, ρ_c = solid catalyst density (kg · m^{-3}), R = catalyst particle radius (m), D_e = effective gas-phase diffusivity (m^2·s^{-1}) and C_{As} is the gas concentration of CO or C_2H_4 (kmol · m^{-3}).

The mass and heat interphase and intraparticle transport limitations were calculated using Weisz-Hicks criterion [33-35]:

$$\varphi = \frac{-r'_A\,\rho_c R^2}{C_A D_e}\exp\frac{\gamma\beta}{(1+\beta)} = C_{WP}\exp\frac{\gamma\beta}{(1+\beta)} \quad <1 \qquad (10.11)$$

so that,

$$\gamma = \frac{E_a}{R_g T};\ \text{and}\ \beta = \frac{(-\Delta H_r) D_e C_A}{kT}$$

where, E_a: activation energy (J·mol^{-1}), R_g: gas constant = 8.314 (J·m^{-1}·K^{-1}), T is preferably the maximum temperature at which high reaction rates are observed (K), ΔH_r : heat of reaction = -283×10^3 (J·mol^{-1}) for CO combustion and -1411×10^3 (J·mol^{-1}) for ethylene combustion, k: catalyst thermal conductivity = 70 (w·m^{-1}·K^{-1}) for platinum.

10.3.3 Catalytic activity

Catalytic activity measurements were carried out at atmospheric pressure in a continuous flow U-shaped quartz reactor into which 50 mg of catalyst was placed. The reactant mixture was composed of 909 ppm C_2H_4 (Linde, 5% in He) or CO (Linde, 1% in He) and balance He (Linde, 100%). The total gas flow rate was 4.62 L·h^{-1} for CO and C_2H_4 experiments. The samples were tested in the temperature range of 25 - 400^{o}C. The reactant

and product gases were analyzed using an on-line gas chromatograph (GowMac 350) and non-dispersive infrared (NDIR) CO_2 gas analyzer (HORIBA VA-3001) to quantify concentrations of reactants and products.

10.3.4 Calculation of O^{2-} fraction consumed from YSZ

An approximate calculation of the fraction of O^{2-} consumed from YSZ surface to electrooxidize CO and C_2H_4 from the gas phase was based on the total concentration of CO_2 produced in each experimental run from the reactions in (eqs. 10.4 and 10.5) as obtained using an on-line gas chromatograph (GowMac 350) and non-dispersive infrared (NDIR) CO_2 gas analyzer (HORIBA VA-3001) and on the total amount of O^{2-} in the support according to YSZ manufacturer:

Fraction of O^{2-} consumed in CO electrooxidation

$$= \frac{\text{moles of } O^{2-} \text{ consumed to completely electrooxidize 909 ppm CO to } CO_2}{\text{total moles of } O^{2-} \text{in YSZ}}$$

$$= \frac{\text{total moles of CO converted to } CO_2}{\text{total moles of } O^{2-} \text{in YSZ}} \qquad (10.12)$$

Fraction of O^{2-} consumed in C_2H_4 electrooxidation

$$= \frac{\text{moles of } O^{2-} \text{ consumed to completely electrooxidize 909 ppm } C_2H_4 \text{ to } CO_2}{\text{total moles of } O^{2-} \text{in YSZ}}$$

$$= \frac{6 \text{ x total moles of } C_2H_4 \text{ converted to } CO_2}{\text{total moles of } O^{2-} \text{in YSZ}} \qquad (10.13)$$

Where, moles of CO or C_2H_4 converted to CO_2 are in (μmol $O^{2-} \cdot g^{-1}$ YSZ) and the moles of O^{2-} in 50 mg catalyst are = 15825 (μmol $O^{2-} \cdot g^{-1}$ YSZ) as per the composition of YSZ $(Y_2O_3)_{0.08}$ $(ZrO_2)_{0.92}$ provided by the manufacturer.

10.4 Results and Discussion

10.4.1 ADF-STEM of the supported nanoparticles

Figure 10-1 shows ADF-STEM images of the four Pt/YSZ catalysts where the bright localized features correspond to the Pt nanoparticles (also see Figure B-1 for EDX spectra of the catalysts in the supplementary information in Appendix B).

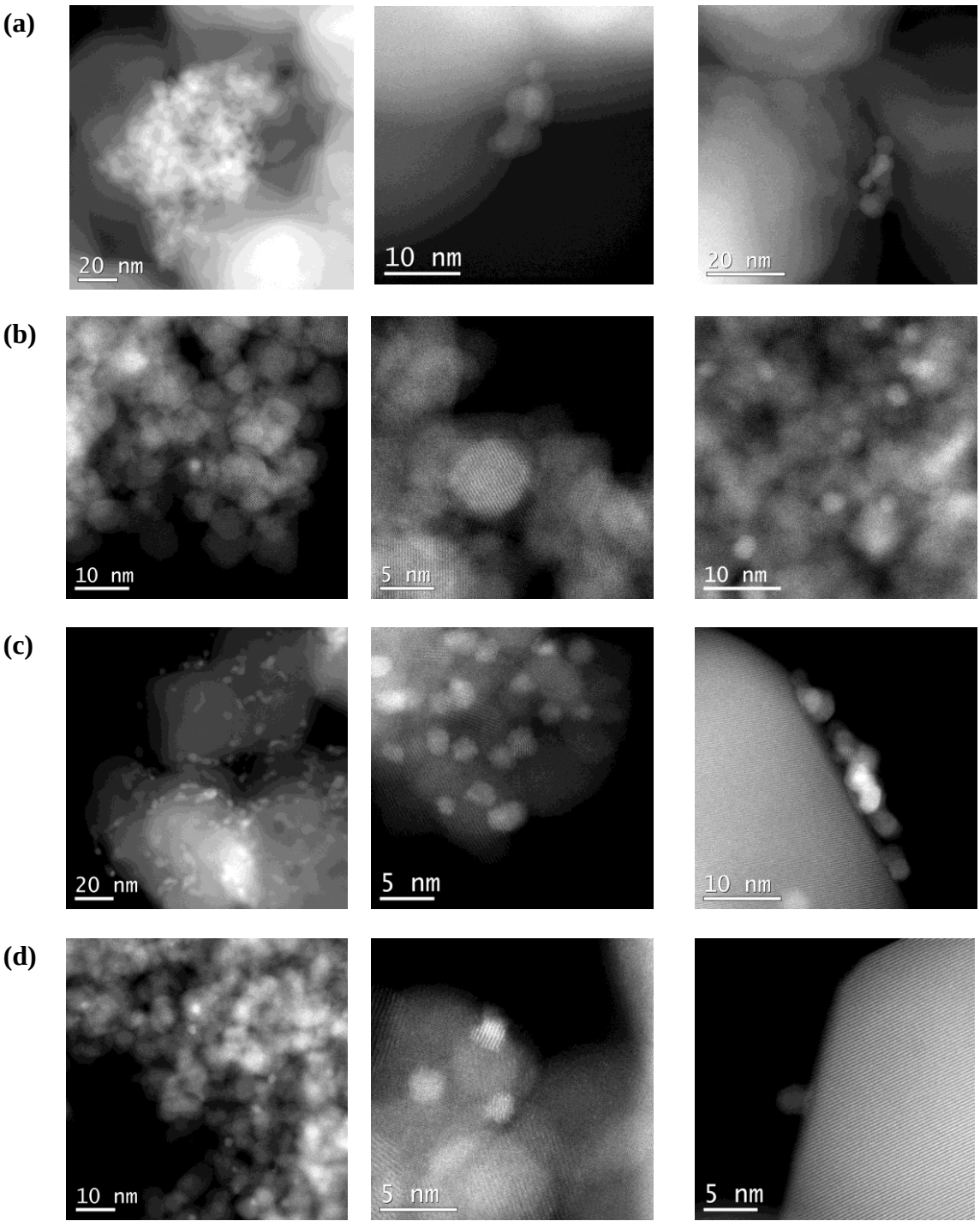

Figure 10-1: ADF-STEM images of (a) Pt/YSZ-1; (b) Pt/YSZ-2, (c) Pt/YSZ-3 and (d) Pt/YSZ-4. Catalyst numbers correspond to those in Table 10-1.

The average Pt particle sizes for the four samples were obtained from a series of images and are summarized in Table 10-1. In general, the Pt NPs are uniform and spherical in

shape, with the presence of non-uniform particles resulting from agglomeration. The STEM images of the catalyst prepared using the largest Pt NPs (Pt/YSZ-1) reveal poor dispersion of the particles; a fact that is further supported by the dispersion value (9.5%) obtained from the CO titration (Table 10-1). Also, it is noticed that both Pt/YSZ-2 (Fig. 10-1b) and Pt/YSZ-3 (Fig. 10-1c) show some degree of agglomeration as well, whereas the smallest particles Pt/YSZ-4 (Fig. 10-1d) have a more uniform distribution. The low specific surface area of YSZ may be responsible for the agglomeration of Pt NPs on YSZ support.

Table 10-1: List of Pt/YSZ catalysts, catalyst dispersion, and catalyst loading.

Catalyst	Final pH	Pt size from ADF-STEM (nm)	Pt Loading (wt. %)[a]	Pt Dispersion (%)[b]	Pt Dispersion (%)[c]	Δr_{CO} at 120°C[d]	Δr_{C2H4} at 200°C[d]
Pt/YSZ-1	4	6.7 ± 1.0	1.0	9.5	17.0 + 78%	1.44×10^{-7}	1.05×10^{-6}
Pt/YSZ-2	6	4.4 ± 0.3	1.1	30.1	25.9 + 14%	4.67×10^{-6}	2.86×10^{-7}
Pt/YSZ-3	7.5	3.0 ± 0.8	1.1	39.5	38.0 + 4%	2.85×10^{-6}	1.90×10^{-6}
Pt/YSZ-4	9	1.9 ± 0.4	0.9	51.8	60.0 + 17%	0.94×10^{-6}	4.34×10^{-6}

[a] determined from ICP
[b] from CO titration
[c] from ADF-STEM using eq. (10.8)
[d] from eq. (10.16)

10.4.2 XPS measurements of Pt/YSZ catalyst

The as-prepared catalysts were characterized using X-ray photoelectron spectroscopy to gain a better insight of their surface properties. Table 10-2 summarizes the peak positions of Zr3d, Y3d and O1s for all samples under study.

Table 10-2: XPS binding energy peak position of $Zr3d_{5/2}$, $Y3d_{5/2}$ and O1s components for all Pt/YSZ samples.

	YSZ blank	Pt/YSZ-4	Pt/YSZ-3	Pt/YSZ-2	Pt/YSZ-1
$Zr3d_{5/2}$	181.8 eV	181.8 eV	181.8eV	181.9 eV	181.8 eV
$Y3d_{5/2}$	156.9 eV	156.8 eV	156.8 eV	156.9 eV	156.8 eV
O1s	529.7 eV	529.7 eV	529.6 eV	529.7 eV	529.7 eV
	531.3 eV	531.5 eV	531.4 eV	531.3 eV	531.4 eV
	532.6 eV	532.7 eV	532.6 eV	532.7 eV	525.8 eV

The $Zr3d_{5/2}$ and $Y3d_{5/2}$ peaks for the YSZ powder are detected at 181.9 and 156.8 eV which are characteristic of yttrium and zirconium atoms in yttria-stabilized zirconia [36]. The analysis of the O1s spectra for the YSZ (not shown here) revealed the existence of three components at about 529.7, 531.4 and 532.6 eV. The peak at lower BE is attributed to the lattice oxygen atoms in the mixed YSZ oxide [36], while the one at 531.3 eV is attributed to hydroxyl groups and/or chemisorbed oxygen as it has been shown before in the case of oxides [36-38]. The component at the highest BE (O^{III}) is due to oxygen species related to atmospheric carbon contamination (C-O bonding) [39]. The relative intensity of the O1s components in the case of YSZ powder is 75:20:5.

After Pt NPs deposition, small changes in the position and the FWHM of the Zr3d and Y3d are detected. The analysis of the O1s reveals the existence of three peaks but with relative intensity ratio of 65:25:10, showing a small increase of the abundance of the oxygen containing species to which the O^{II} and O^{III} peaks are attributed. The relative intensities of the O1s components do not vary significantly in the case of the other samples. These changes can be related to the presence of Pt NPs that induce an increase of the chemisorbed oxygen species $O^{\delta-}$ and/or the increase of the OH groups present on the surface after the deposition procedure.

In all cases, the recorded Pt4f spectra show poor signal to noise ratio (not shown here). A possible explanation for this is either the low content of platinum (~ 1 wt. % loading) or Pt agglomeration as evident on the corresponding ADF-STEM images and also from dispersion

measurements. This agglomeration causes a decrease in the Pt surface available and consequently measured. Figure 10-2 compares the Pt4f peak of Pt/YSZ-3, which has the best signal to noise ratio among the measured samples, to Pt4f peak of an oxygen-free platinum foil.

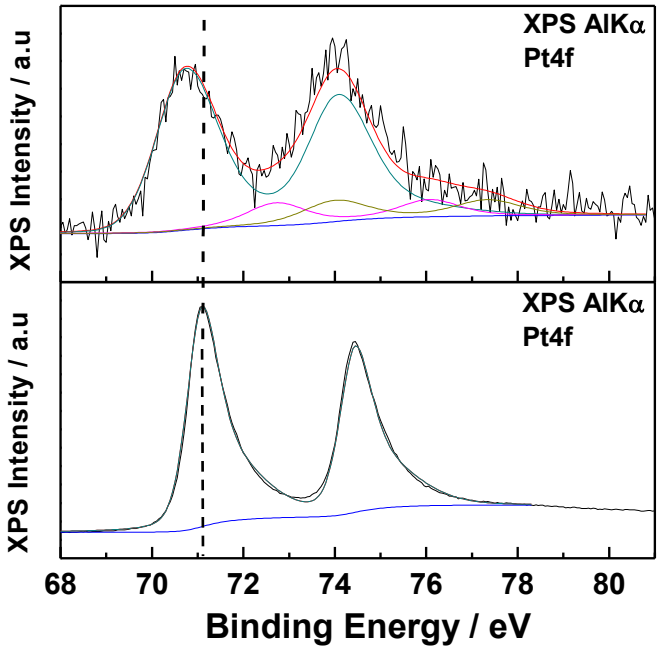

Figure 10-2: Representative Pt4f peak of Pt/YSZ-3 (upper spectra), and an oxygen-free platinum foil (lower spectra).

The analysis of the Pt4f peak in the Pt/YSZ-3 sample reveals the existence of three components at 70.6, 72.9 and 74.2 eV, which are attributed to Pt^{0}, Pt^{+2} and Pt^{4+} oxidation states, respectively. The characteristic Pt4f components for 2+ and 4+ oxidation states are detected at similar position for both Pt/YSZ and Pt/C samples [26]. It is worth to note that the Pt4f component attributed to the metallic state is detected at 0.5 eV lower than in Pt foil. Similar shift towards lower BEs for the Pt4f peak was observed in the case of Pt supported on TiO_2 [40] and on mixed CeO_2/TiO_2 [41] and was assigned to the strong metal-support interaction effect, where the charge is transferred from the support to the metal. Therefore, the observed BE downshift of the Pt4f component that corresponds to the metallic state compared to the peak in the case of Pt foil indicates MSI effect induced between Pt NPs and YSZ, which

is responsible for the observed electrochemical and catalytic activity of Pt/YSZ catalyst. A detailed XPS study of the Pt/YSZ system as a function of Pt particle size is a subject of another publication [42].

10.4.3 Ethylene and carbon monoxide electrooxidation on Pt/YSZ catalysts in the absence of O_2 in the gas feed

10.4.3.1 Stability, activation and deactivation of Pt/YSZ catalysts

Each experimental run was repeated for three cycles to confirm reproducibility of the results. To test the effect of heat transfer limitations experimentally, the temperature was increased and held for 30 minutes at each value to reach the steady-state in a forward scan (second run in Figure B-2 in the supplementary information in Appendix B), then the temperature was lowered and held for 30 min to reach the steady-state in a reverse scan (third run in Figure B-2 in the supplementary information in Appendix B). All light-off curves show high stability and reproducibility of the catalytic measurements. Fig. B-2 (supplementary information in Appendix B) shows representative light-off curves for the smallest nanocatalyst (Pt/YSZ-4) for the oxidation of CO and C_2H_4 in the absence of oxygen in the gas phase, respectively. Similar results were obtained for the other three catalysts (not shown) and all three light-off curves for each catalyst show good stability and reproducibility. CO and C_2H_4 conversion is already observed at 30 and 80^oC, respectively. It is worth mentioning that after each cycle, the catalyst was kept in He overnight for regeneration. This procedure allows O^{2-} concentration to reach equilibrium between the bulk and the surface, hence reactivating the catalyst [21]. Figure 10-3 shows the activation-deactivation curve of (Pt/YSZ-3) for the oxidation of 909 ppm of C_2H_4 at 260^oC in the absence of oxygen.

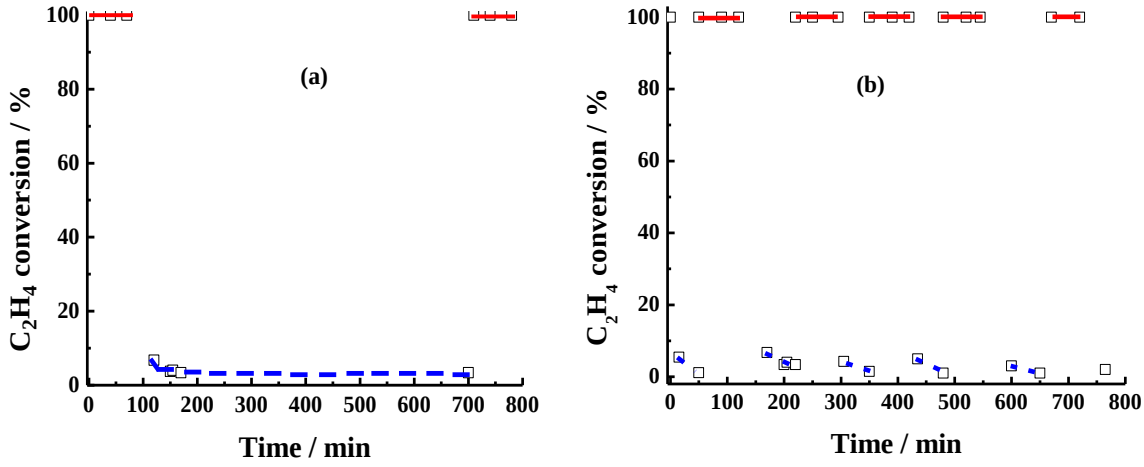

Figure 10-3: Activation-deactivation curve for the electrooxidation of 909 ppm of C_2H_4 on Pt/YSZ-3 catalyst, T=260^{o}C in the absence of O_2 in the gas phase, (a) red dashed-line segments: catalyst was left in 909 ppm C_2H_4, blue dashed-line segment: catalyst was left in He over night, (b) red dashed-line segments: catalyst was left in 909 ppm C_2H_4, blue dashed-line segments: catalyst was left 10 min in He, then 20 min in 3.5 kPa O_2 and then 10 min in He for regeneration.

The results show that the freshly prepared catalyst deactivates completely after 75 min, whereas the "spent" catalyst after the first run shows deactivation after about 50 min under reaction conditions. The deactivation is a result of the depletion of all available surface oxygen ions from YSZ by the electrooxidation reaction (eq. 10.5). The reactivation of the catalyst is required because the bulk ionic conductivity of YSZ is quite low in this temperature range. Two reactivation procedures were proposed: (i) the catalyst was reactivated under He stream (overnight) as mentioned earlier and as shown in Fig (10-3a); (ii) another way to activate Pt/YSZ can be done by purging the catalyst with He for 10 min, then keep it in O_2 for 20 min and then remove O_2 with He for 10 min at 220 - 260^{o}C as shown in Fig (10-3b). First, leaving the catalyst under He for 10 min sweeps away the reaction and product gases, then adding oxygen for 20 minutes replenishes O^{2-} concentration on YSZ surface compensating those consumed during the electrooxidation of VOC. This equilibrium reaction is given by eqs. (10.14) and (10.15) [30,31]:

$$\tfrac{1}{2}\, O_{2\,(g)} + 2\bar{e}_{\,(Pt)} + V_o^{\cdot\cdot}{}_{(ysz)} \leftrightarrow O^x_{(ysz)} \qquad (10.14)$$

Or simply:

$$O_{2\,(g)} + 4\bar{e}_{\,(Pt)} \leftrightarrow 2O^{2-}_{(YSZ)} \qquad (10.15)$$

Finally, sweeping the catalyst with He for 10 min removes away the extra oxygen gas over the catalyst to avoid driving reaction (10.15) to the left side and prepares the catalyst for the next catalytic cycle. As can be seen in (Fig. 10-3b) the catalyst was regenerated for 5 times, however this procedure could be repeated as long as Pt nanoparticles remain active.

10.4.3.2 Effect of the particle size

Figure 10-4 shows the catalytic activity for CO (a and b) and C_2H_4 (c and d) electrooxidation as a function of temperature for four Pt/YSZ catalysts in the absence of oxygen in the gas feed.

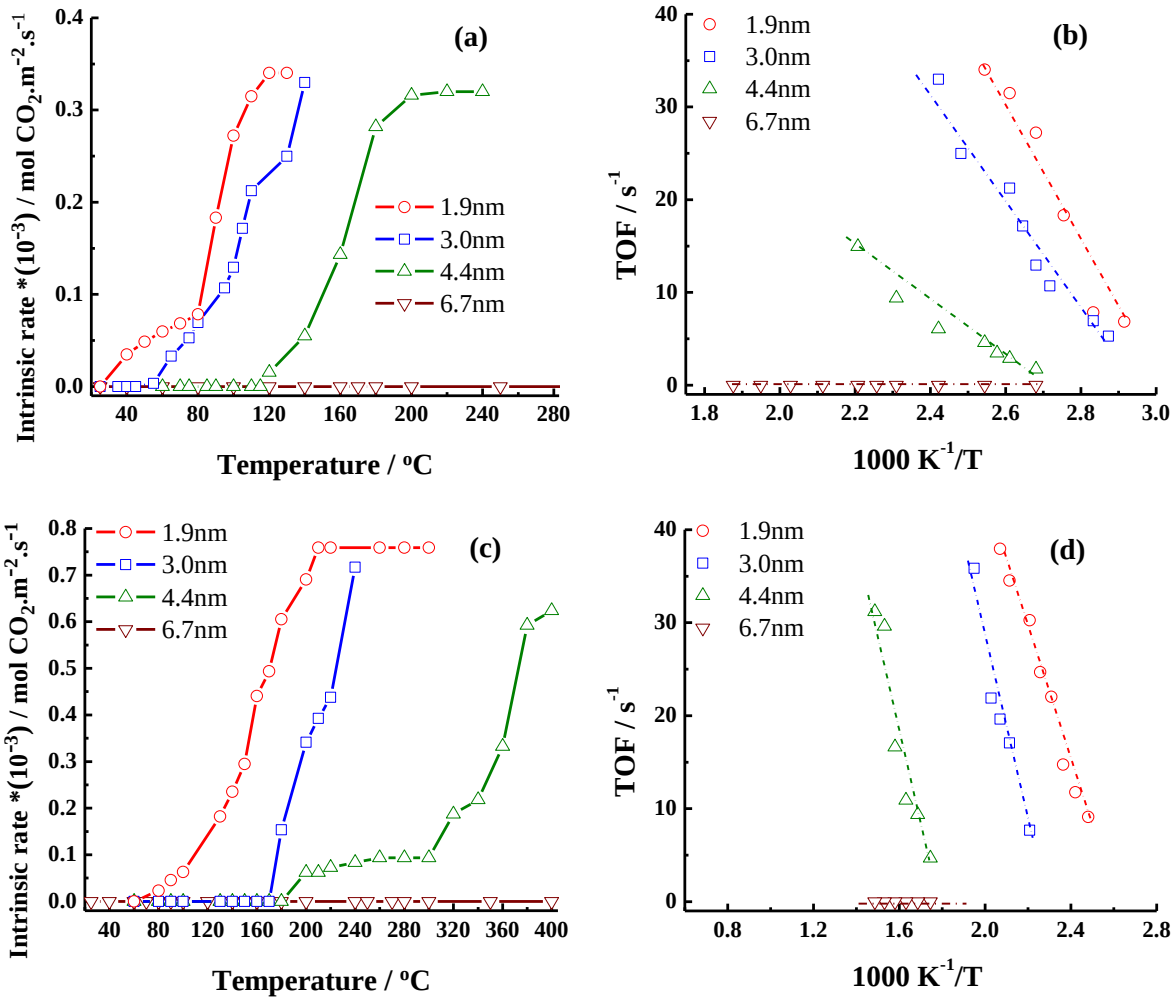

Figure 10-4: Effect of Pt/YSZ particle size on CO electrooxidation expressed in (a) intrinsic rate per catalyst active surface area and (b) turn over frequency, and on C_2H_4

electrooxidation expressed in (c) intrinsic rate per catalyst active surface area and (d) turn over frequency, both reactions in the absence of O_2 in the gas phase. Space velocity = 14688 h^{-1}, gas composition: total flowrate= 4.62 $L \cdot h^{-1}$, [CO or C_2H_4] = 909 ppm, He balance, no O_2 in the gas feed.

The reaction rates are normalized per metal active surface area and the data reveals a strong dependence of CO and C_2H_4 conversion on the mean Pt particle sizes. The highest intrinsic rates and turn over frequency per unit of time are observed for the nanoparticles having the smallest size (Pt/YSZ-4) at the lowest temperature, which are also characterized by the lowest activation energy (Table 10-3).

Table 10-3: List of activation energies (E_a) for the oxidation and electrooxidation of CO and C_2H_4 reactions and total length of three-phase boundary.

Catalyst	E_a, oxidation of CO ($kJ \cdot mol^{-1}$)	E_a, oxidation of C_2H_4 ($kJ \cdot mol^{-1}$)	E_a, electrooxidation of CO ($kJ \cdot mol^{-1}$)	E_a, electrooxidation of C_2H_4 ($kJ \cdot mol^{-1}$)	Three-phase boundary (m)
Pt/YSZ-1	52.9	45.7	N.A.	N.A.	0.38×10^6
Pt/YSZ-2	47.4	42.5	64.8	38.4	2.53×10^6
Pt/YSZ-3	48.2	22.0	55.5	30.7	6.02×10^6
Pt/YSZ-4	31.3	9.1	30.3	12.5	19.30×10^6

The largest Pt NPs (6.7 nm) do not show any catalytic activity up to 400^oC for both CO and C_2H_4 electrooxidation. It is worth mentioning that YSZ blank support was found inactive towards CO or C_2H_4 oxidation in the absence of oxygen in the gas phase (Fig. B-3 and Fig. B-4 in the supplementary information in Appendix B).

The estimation of the mass and heat transfer limitations was carried out for the highest reaction rate in each experimental run for all four catalysts (see supplementary information for detailed calculations and results in Table B-1-Table B-6 in Appendix B). The Weisz-Prater (eq. 10.10) and Weisz-Hicks (eq. 10.11) results show very negligible mass and heat resistances for CO and C_2H_4 electrooxidations over the four catalysts in the order of 10^{-4} to 10^{-6}. These values are far less than unity, as required by both criteria, indicating negligible mass and heat transfer

limitations. This is in accordance with previous results presented for other studies on nanoparticles for heterogeneous catalytic systems, where mass and heat transfer limitations were found negligible [35]. It is worth mentioning that as the particle size increases, mass and heat transfer limitations effect increases from the order of 10^{-6} for the smallest nanoparticle (Pt/YSZ-4) to 10^{-4} for the largest nanoparticle (Pt/YSZ-1) in our study, which can be compared with the 10^{-2} order of magnitude for the micro-size particles in other studies [32]. These findings are consistent with the reported trend stating that intraparticle transport resistance can be eliminated as catalyst particle size decreases [45]. This in general shows that nanoparticles are effective catalysts for hydrocarbon oxidations in terms of negligible mass and heat resistances compared with larger particles in the micro-meter range.

As it was proposed earlier [21], Pt nanoparticles and the solid electrolyte form local nano-galvanic cells, where CO or C_2H_4 are electrooxidized by O^{2-} at the tpb and the surface of YSZ is partially reduced. On one hand, it is expected that the smaller the particle size, the more nano-galvanic cells would be available for the electrochemical reaction, i.e., larger tpb where reactions are taking place as shown by the total length of tpb for each particle size in Table 10-3 (also see supplementary information for detailed calculations of tpb lengths in Appendix B). On the other hand, it is reasonable to expect that as particle size decreases, the electronic interaction between Pt and YSZ increases resulting in a larger charge transfer between YSZ and Pt. Similar trend of catalyst particle size effect was observed for methanol and CO oxidation over Pt/TiO_2 and Au/TiO_2 systems [46,47]. Yoo et al. [46] reported that as Pt NPs size decreases from 6 to 1 nm, there is stronger metal-support interaction depicted from greater change in the electronic factors which causes the modification of the work function of the catalyst surface. Authors used the potential of zero total charge (PZTC) and *in-situ* x-ray absorption near-edge structure (XANES) to analyze the electronic states and show that small noble metal NPs in the range of 1.5 nm exhibit much higher changes in the electronic properties which explains their high activity towards organic molecules oxidation [46-48]. Smallest NPs were also found to have higher surface coverage by oxygenated species promoted by TiO_2 than larger NPs [46].

10.4.3.3 Fraction of oxygen consumed during C_2H_4 and CO electrooxidation and carbon balance

Table 10-4 shows the approximate values of the fraction of oxygen consumed from YSZ for CO and C_2H_4 electrooxidation per complete catalytic reaction run (i.e. each light-off curves for the electrooxidation in absence of oxygen in Fig. 10-4) as they were determined based on the total amount of O^{2-} in the support.

Table 10-4: Estimated percentage of O^{2-} consumption during CO and C_2H_4 electrooxidation in the absence of molecular oxygen in the feed. Total amount of O in YSZ is 15825 µmol / g YSZ.

Catalyst	% of O in YSZ consumed during CO oxidation	% of O in YSZ consumed during C_2H_4 oxidation	Temperature range (^oC)
Pt/YSZ-1	0.00	0.00	40 - 400
Pt/YSZ-2	0.65	2.74	40 - 400
Pt/YSZ-3	1.03	6.19	40 - 250
Pt/YSZ-4	1.39	18.61	25 - 200

As can be seen, the O^{2-} consumption is always higher for C_2H_4 electrooxidation compared to CO electrooxidation for the same catalyst. This is because each C_2H_4 molecule consumes $6O^{2-}$ compared to one O^{2-} in the case of CO electrooxidation based on the electrochemical reactions (10.4) and (10.5).

As the Pt particle size decreases from 4.4 to 1.9 nm, the oxygen consumption increases from 0.65 and 2.74 to 1.39 and 18.61% for CO and C_2H_4 electrooxidation, respectively. This confirms that the smallest nanocatalysts are inherently more active for these reactions, leading to higher O^{2-} consumption from YSZ to oxidize CO and C_2H_4. The largest nanoparticles (6.7 nm) had zero oxygen consumption due to its inactivity towards CO and C_2H_4 electrooxidation under the reaction conditions.

The carbon balance calculations were performed for all catalysts (not shown here). It is found that the amount of unidentified carbon is negligible in all catalysts. According to the literature [49], the formation of carbon on Pt/solid electrolyte systems could take place at

relatively low temperatures (< 327°C), e.g., ethylene cracking leading to the deposition of carbon and H_2 production, as well as Boudouard reaction, resulting in the formation of CO_2 and carbon [50]. The maximum values for the unidentified carbon in our system are 0.6%, 0.7% and 1.0% for Pt/YSZ-2, Pt/YSZ-3 and Pt/YSZ-4, respectively. It is worth mentioning that during the former reaction, no H_2 formation was observed. However, any traces of carbon deposited on YSZ can be removed by O^{2-} via an electrochemical reaction (eq. 10.6).

10.4.4 CO and C_2H_4 oxidation in the excess of O_2 in the gas feed

To investigate further the particle size effect of Pt/YSZ catalysts, the reactions of CO and C_2H_4 oxidation in the presence of O_2 in the gas feed (P_{O_2}= 3.5 kPa) were carried out. Figure 10-5 shows the catalytic activity of all four Pt/YSZ catalysts for CO and C_2H_4 oxidation in the presence of oxygen in the gas feed.

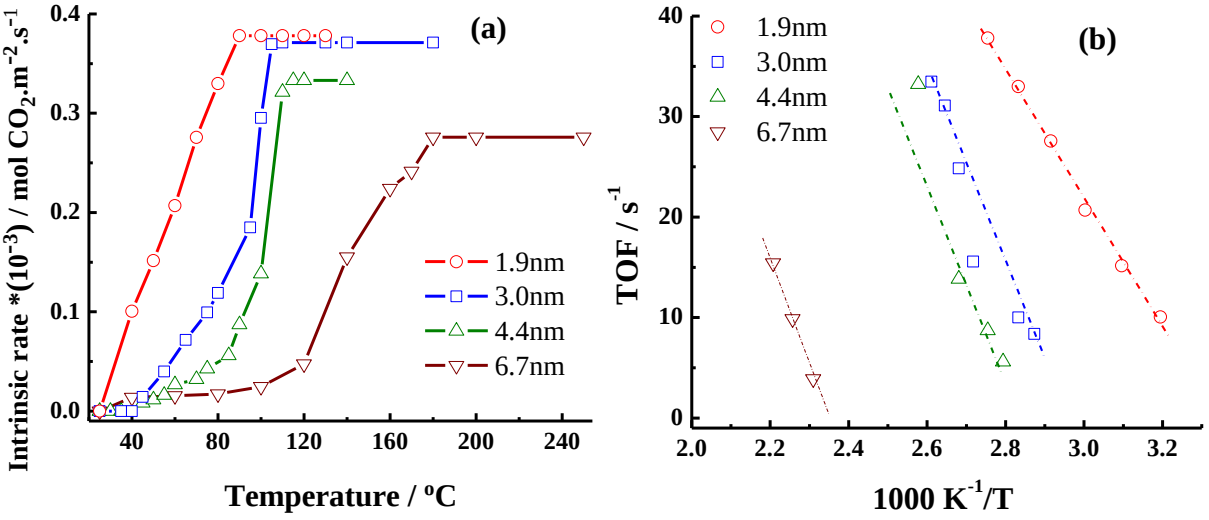

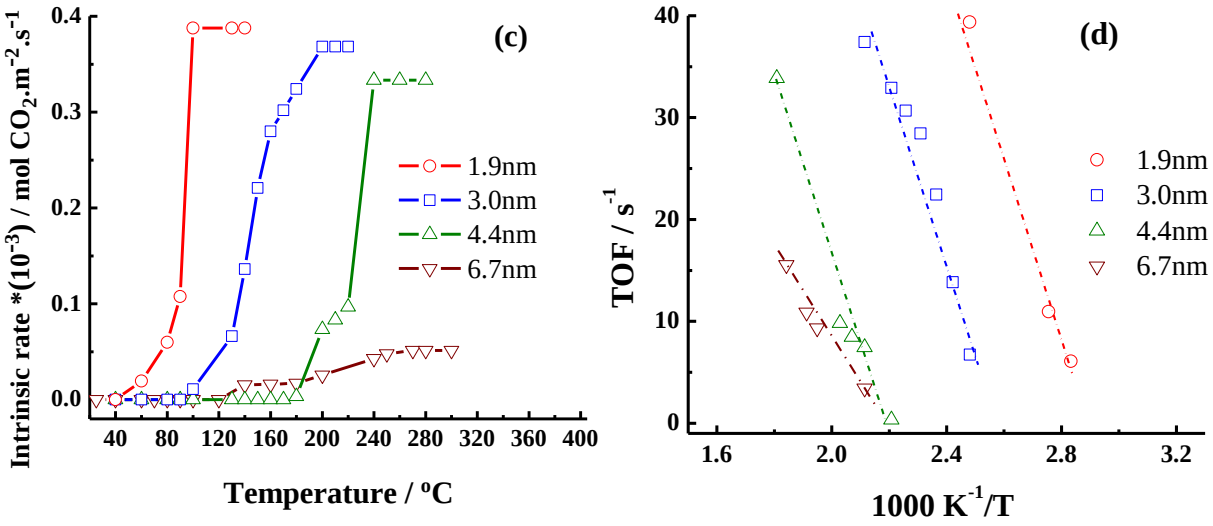

Figure 10-5: Effect of Pt/YSZ particle size on CO oxidation expressed in (a) intrinsic rate per catalyst active surface area and (b) turn over frequency, and on C_2H_4 oxidation expressed in (c) intrinsic rate per catalyst active surface area and (d) turn over frequency. Space velocity = 14688 h^{-1}, gas composition: total flowrate= 4.62 $L \cdot h^{-1}$, [CO or C_2H_4] = 909 ppm, 3.5 kPa O_2 and He balance.

It can be seen that the light-off curves shift to lower temperatures for both reactions, when 3.5 kPa of O_2 is added. More specifically, over the full range of catalyst mean particle sizes, the temperatures, where oxidation takes place, are about 30 - 160^oC and 30 - 120^oC lower for CO and C_2H_4 oxidation, respectively than corresponding temperatures for electrooxidation reactions. The activity of YSZ support alone towards CO and C_2H_4 oxidation was zero up to T > 225^oC (Fig. B-4 in the supplementary information in Appendix B). However, YSZ has been shown to be an effective catalyst for VOC and soot oxidation at temperatures > 270^oC in the presence of oxygen gas phase as indicated earlier [13, 15]. Similar to electrooxidation by O^{2-}, the oxidation of both CO and C_2H_4 by gas phase oxygen is particle-size dependent. The smaller the Pt particles the higher the reaction rates at lower temperatures. This is in agreement with our previous work on CO oxidation over Pt/YSZ [13] and on ethylene oxidation over Pt/C catalysts [26] confirming that the smallest particles have the highest catalytic activity for these reactions. The effect of the particle size can be attributed to the enhanced metal-support interaction between the smallest Pt nanoparticles and YSZ support. Moreover, it is noticed that as the particle size decreased, higher dispersion of the catalyst was achieved (Table 10-1). The smallest nanocatalyst (Pt/YSZ-4) has the highest

dispersion of 51.8% compared to the largest nanoparticle (Pt/YSZ-1) which has only 9.5% (Table 10-1). It is worth mentioning that the dispersion values estimated using (eq. 10.8) which depends on the average particle size from ADF-STEM images slightly over estimates those deduced from CO titration method. A general point of view in this regards, is that the dispersion values from (eq. 10.8) deals with TEM images that counts about 200 - 300 nanoparticles and might not count all the larger ones in each image. Nevertheless, smaller nanoparticles has much higher dispersion in both cases than the larger ones which indicates that there are more catalytic sites available for the reaction compared to the available sites for the largest catalyst. To this point we should mention that the relatively low dispersion is also reflected in the low signal of the XPS Pt4f peak in all cases.

In the presence of oxygen, both oxidation over the gas exposed active surface area of Pt NPs and electrooxidation at tpb are taking place simultaneously, however it is expected that the rate of the latter reaction is slow in the excess of molecular oxygen, because of the high Po_2, thus decreasing the driving force for O^{2-} interfacial exchange. In Figs. 10-4 and 10-5 the intrinsic rates of CO and C_2H_4 electro- / oxidation are evaluated per the number of active surface Pt sites found from CO titration experiments. By using intrinsic rates in the presence of oxygen and no oxygen, one can calculate the difference in the reaction rate, Δr, as:

$$\Delta r = r_{\text{oxidation}} - r_{\text{electrooxidation}} \qquad (10.16)$$

Table 10-1 shows the difference in reaction rates between CO and C_2H_4 oxidation and electrooxidation at 120^{o}C and 140^{o}C, respectively. The found Δr may roughly correspond to the reaction rate of CO and C_2H_4 oxidation on Pt supported on inert supports, i.e., silica, alumina, carbon, etc., giving that NPs have the same dispersion. The rate difference (Table 10-1) reflects the particle size effect and emphasizes the role of the lattice oxygen ions in promoting oxidation reaction.

10.5 Conclusions

Pt/YSZ catalysts with four average particle sizes (1.9 - 6.7 nm) show high catalytic activity towards carbon monoxide and ethylene oxidation in the absence and excess of molecular gas phase O_2. These reactions are strongly size-dependent, thus the smallest

Pt/YSZ-4 (1.9 ± 0.4 nm) nanoparticles show the highest catalytic activity for CO and C_2H_4 oxidation and electrooxidation. The largest Pt/YSZ-1 (6.7 ± 1nm) particles showed late catalytic activity towards CO and C_2H_4 oxidation at 100 and 120^oC, respectively but showed no catalytic activity towards CO or C_2H_4 electrooxidation up to 300^oC.

XPS measurements revealed that the deposition of platinum NPs causes a change of the chemical environment of Y and Zr atoms with a change in the relative intensities of the O1s components attributed to the "active" oxygen related species (chemisorbed oxygen, OH-groups). In addition, the Pt4f peak shows a BEs downshift if compared to the platinum foil indicating an electron transfer from the YSZ support to the Pt nanoparticles as a result of the metal-support interaction. It is proposed that the increase in the activity of both oxidation and electrooxidation reactions as particle size of Pt NPs decreases is due to the larger electronic interaction between Pt and YSZ and the higher active surface area of the smaller particles, hence larger amount of the local nano-galvanic cells available for the electrochemical oxidation of the volatile organic compound.

10.6 Acknowledgement

Financial support from the Natural Science and Engineering Research Council (NSERC) and Ontario Graduate Scholarship (OGS) are acknowledged. In context of this, I would like to acknowledge Dr. Nimal de Silva (Dept. Earth Sciences) for running ICP measurements. Dr. Spyridon Ntais for running x-ray photoelectron spectroscopy (XPS) measurements and analyzing related data for the manuscript presented in this chapter. Dr. Martin Couillard (National Research Council Canada) for running annular dark field-scanning electron microscopy (ADF-STEM) measurements and the related discussion for the catalysts in the manuscript presented in this chapter.

10.7 Supporting information statement

Detailed mass and heat resistance calculations for all the catalysts are available in Appendix B.

10.8 References

[1] E. C. Subbarao, H. S. Maiti, *Solid State Ionics.* 11(1984) 317.

[2] V. V. Kharton, F. M. Marques, A. Atkinson, *Solid State Ionics.* 174 (2004) 135.

[3] C. Zhang, C. -J. Li, G. Zhang, X. -J. Ning, C. -X. Li, H. Liao, C. Coddet, *Mater. Sci. Eng. B.* 137 (2007) 24.

[4] S. Bebelis, M. Makri, A. Buekenhoudt, J. Luyten, S. Brosda, P. Petrolekas, C. Pliangos, C. G.Vayenas, *Solid State Ionics.* 129 (2000) 33.

[5] C. G. Vayenas, S. Bebelis, C. Pliangos, S. Brosda, D. Tsiplakides, Electrochemical Activation of Catalysis, Promotion, Electrochemical promotion and Metal-support Interactions, Kluwer Academic/Plenum Publisher, New York, 2001.

[6] C. G. Vayenas, S. Bebelis, I. Yentekakis, H. Lintz, *Catal. Today.* 11 (1992) 303.

[7] P. Vernoux, M. Guth, X. Li, *Electrochem. Solid-State Lett.* 12 (2009) E9.

[8] P. Vernoux, L. Lizarraga, M. N. Tsampas, F. M. Sapountzi, A. De Lucas-Consuegra, J.-L. Valverde, S. Souentie, C.G. Vayenas, D. Tsiplakides, S. Balomenou, E. A. Baranova, *Chem. Rev.* 113 (2013) 8192.

[9] J. Nicole, D. Tsiplakides, C. Pliangos, X. E. Verykios, Ch. Comninellis, C. G. Vayenas, *J. Catal.* 204 (2001) 23.

[10] G. M. Schwab, K. Koller, *J. Am. Chem. Soc.* 90 (1968) 3078.

[11] S. J. Tauster, *Acc. Chem. Res.* 20 (1987) 389.

[12] R. J. Isaifan, E. A. Baranova, *Catal. Today*, CATTOD-9011 (in press).

[13] R. J. Isaifan, H. A. E. Dole, E. Obeid, L. Lizarraga, P. Vernoux, E. A. Baranova, *Electrochem. Solid-State Lett.* 15 (2012) E14.

[14] H. A. E. Dole, R. J. Isaifan, F. M. Sapountzi, L. Lizarraga, D. Aubert, A. Princivalle, P. Vernoux, E. A. Baranova, *Catal. Letters.* 143 (2013) 996.

[15] L. Lizarraga, E. Obeid, M. N. Tsampas, A. Boréave, M. C. Steil, P. Vernoux, *ECS Trans.* 45 (2012) 225.

[16] W. Song, E. Hensen, *Catal. Sci. Technol.* 3 (2013) 3020.

[17] D. Widmann, B. R. Behm, *Accounts Chem. Res.* 47 (2014) 740.

[18] P. Mars, D. W. Van Krevelen, *Chem. Eng. Sci. Spec. Suppl.* 3 (1954) 41.

[19] C. Doornkamp, V. Ponec, *J. Mol. Catal. A-Chem.* 162 (2000) 19.

[20] Y. Li, Q. Fu, M. Flytzani-Stephanopoulos, *Appl. Catal. B* 27 (2000) 179.

[21] R. J. Isaifan, E. A. Baranova, *Electrochem. Commun.* 27 (2013) 164.

[22] J. Janek, C. Korte, *Solid State Ionics.* 116 (1999) 181.

[23] E. A. Baranova, C. Bock, D. Ilin, D. Wang, B. Macdougall, *Surf. Sci.* 600 (2006) 3502.

[24] D. Briggs, M. P. Seah, Practical Surface Analysis, 2nd edition, volume 1, Wiley, New York, 1996.

[25] S. Hufner, G. K. Wertheim, *Phys. Rev. B.* 11 (1975) 687.

[26] R. J. Isaifan, S. Ntais, E. A. Baranova, *Appl. Catal. A Gen.* 464-465 (2013) 87.

[27] M. A. Fortunato, D. Aubert, C. Capdeillayre, C. Daniel, A. Hadjar, A. Princivalle, C. Guizard, P. Vernoux, *Appl. Catal. A Gen.* 403 (2011) 18.

[28] R. M. Rioux, J. D. Hoefelmeyer, M. Grass, H. Song, K. Niesz, P. Yang, G. A. Gabor, *Langmuir.* 24 (2008) 198.

[29] S. -I. Kim, T. Yamamoto, A. Endo, T. Ohmori, M. Nakaiwa, *J. Ind. Eng. Chem.* 12 (2006) 769.

[30] M. Marwood, C. G. Vayenas, *J. Catal.* 178 (1998) 429.

[31] H. S. Fogler, Elements of Chemical Reaction Engineering, Forth edition, Pearsons Education Inc., New Jersy, 2006.

[32] S. T. Oyama, X. Zhang, J. Lu, Y. Gu, T. Fujitani, *J. Catal.* 257 (2008) 1.

[33] P. B. Weisz, J. S. Hicks, *Chem. Eng. Sci.* 17 (1962) 265.

[34] D. E. Mears, *Ind. Eng. Chem. Process. Des. Dev.* 10 (1971) 541.

[35] M. A. Al-Saleh, M. S. Al- Ahmadi, M. A. Shalabi, *Chem. Eng.* 37 (1988) 35.

[36] D. Majumdar, D. Chatterjee, *J. Appl. Phys.* 70 (1991) 988.

[37] S. Ardizzone, M. G. Cattania, P. Lugo, *Electrochim. Acta.* 39 (1994) 1509.

[38] H. B. Wang, C. R. Xia, G. Y. Meng, D. K. Peng, 44 (2000) 23–28, *Mater. Lett.* 44 (2000) 23.

[39] S. Ntais, V. Dracopoulos, A. Siokou, *J. Mol. Catal. A Chem.* 220 (2004) 199.

[40] M. Spichiger-Ulmann, A. Monnier, M. Koudelka, J. Augustynski in "Spectroscopic and electrochemical study of the state of Pt in Pt-TiO_2 catalysts". ACS symposium series "Strong Metal-Support Interactions", ed. by R. T. K. Baker, S. J. Tauster, and J. A. Dumesic, ACS, Washington, 298 (1986) 212.

[41] A. Dauscher, L. Hilaire, F. LeNormand, W. Muller, G. Maire, A. Vasquez, *Surf. Interface Anal.* 16 (1990) 341.

[42] S. Ntais, R. Isaifan, E. A. Baranova, accepted at *J. Mat. Chem. Phys.* matchemphys-s-14-01541.

[43] R. Ramamoorthy, P. K. Dutta, S. A. Akbar, *J. Mater. Sci.* 38 (2003) 4271.

[44] C. G. Vayenas, S. Bebelis, *Catal. Today.* 51 (1999) 581.

[45] M. H. Chahbani, J. Labidi, J. Paris, *Appl. Therm. Eng.* 22 (2002) 23.

[46] S. J. Yoo, T. -Y. Jeon, K. -S. Lee, K. -W. Park, Y. -E. Sung, *Chem. Commun.* 46 (2010) 794.

[47] B. R. Cuenya, S. -H. Baeck, T. F. Jaramillo, E. W. McFarland, *J. Am. Chem. Soc.* 125 (2003) 12928.

[48] C. Linsmeier, E. Taglauer, *Appl. Catal. A Gen.* 391 (2011) 175.

[49] S. Davis, F. Zaera, B. E. Gordon, G. A. Somorjai, *J. Catal.* 92 (1985) 240.

[50] E. P. J. Mallens, J. H. B. J. Hoebink, G. B. Marin, *Catal. Letters.* 33 (1995) 291.

11 Particle size effect of Pt/yttria-stabilized zirconia on carbon monoxide methanation and preferential electrooxidation for hydrogen gas purification at low temperatures

To be submitted to the Journal of Power Sources.

11.1 Abstract

The effect of (1 wt. %) Pt/YSZ particle size (1.9 – 6.7 nm) on the catalytic activity of CO methanation and preferential electrooxidation in hydrogen-rich stream is investigated in the temperature range of 25 - 120^{o}C. The results demonstrate that CO methanation and electrooxidation are strongly size sensitive reactions over Pt/YSZ with higher activity of smaller nanoparticles. The turnover frequency at 60^{o}C of CO methanation reaction rate per surface metal atom increases by a factor of 9.7 with decreasing Pt/YSZ mean particle size from 6.7 to 1.9 nm. The maximum H_2 consumption was ≤ 3% for any of the four catalysts in the study. The effect of CO concentration showed 20% decrease in CO conversion as the concentration increases from 1000 to 9000 ppm, while good stability over time was achieved at 100^{o}C over the smallest catalyst Pt/YSZ (1.9 ± 0.4 nm) for 70 h.

11.2 Introduction

Fuel cells (FCs) are electrochemical devices that convert chemical energy of fuels into electrical energy directly. FCs are considered as promising power generation devices due to their high efficiency and low environmental impact [1,2]. A proton exchange membrane fuel cell (PEMFC) is based on an anode and a cathode separated by a catalyst and a proton-conducting electrolyte layer. The ideal fuel for PEMFCs is hydrogen which can be efficiently produced through steam reforming, or partial oxidation of natural gas in combination with water gas shift reaction [1,3,4]. Hydrogen could be produced on board of a fuel cell powered vehicle using a reformer, however it will likely contain carbon monoxide impurities between

0.1 - 1.0% CO in H_2 feed [2,5]. This can easily poison the anode catalyst of PEMFC, which usually consists of Pt or PtRu nano-catalysts supported on carbon and operates at relatively low temperatures (80 – 120^{o}C) [1,6]. Therefore it is necessary to eliminate the traces of CO in the hydrogen stream with minimum hydrogen loss at low temperatures.

Several different methods were proposed for CO removal: (i) purification with hydrogen selective membranes, (ii) CO methanation, (iii) pressure swing adsorption and (iv) preferential oxidation (PROX) of CO [1,7]. All the above mentioned methods have their advantages and disadvantages, though among them, CO methanation is one of the most promising processes to remove small amounts of CO with minimum H_2 conversion and it has been widely used in industry to remove CO in hydrogen or ammonia plants [8]. CO methanation is more advantageous compared to preferential oxidation PROX of CO because it does not require addition of oxygen (air) in the hydrogen-rich gas stream, which may give rise to various problems related to reduced hydrogen yield, dilution, safety issues and restrictions in the operating parameters [9,10]. In addition, methane produced is inert to the PEMFC electrodes and can be utilized in the afterburner [8]. However, depending on the operating conditions and the catalyst employed, CO methanation may run in parallel with the undesired methanation of CO_2, which consumes significant quantities of valuable hydrogen [2,7,8].

The selective CO methanation is presented by (Eq.11.1) and can accompany the following reactions [1,2]:

$$CO + 3H_2 \rightarrow CH_4 + H_2O \qquad \Delta H^o_{298} = -206.2\ kJ\cdot mol^{-1} \qquad (11.1)$$

$$CO_2 + 4H_2 \rightarrow CH_4 + 2H_2O \qquad \Delta H^o_{298} = -164.9\ kJ\cdot mol^{-1} \qquad (11.2)$$

$$CO + 1/2O_2 \rightarrow CO_2 \qquad \Delta H^o_{298} = -283.6\ kJ\cdot mol^{-1} \qquad (11.3)$$

$$H_2 + 1/2O_2 \rightarrow H_2O \qquad \Delta H^o_{298} = -243.5\ kJ\cdot mol^{-1} \qquad (11.4)$$

$$CO_2 + H_2 \rightarrow CO + H_2O \quad (RWGS) \qquad \Delta H^o_{298} = 41.1\ kJ\cdot mol^{-1} \qquad (11.5)$$

However, current PROX systems operate at high temperatures (150 – 250^{o}C) and require the use of oxygen in order to oxidize CO to CO_2; this results in undesirable reaction of oxygen with hydrogen (Eq. 11.4) and increase in reactor volume [4,11]. Therefore the development of

an efficient and highly selective CO methanation catalytic systems with minimum O_2 concentration in the H_2 + CO mixture is imperative [3,11-13].

Baker et al. [14] were among the first to utilize a selective CO methanation process, by using ruthenium or rhodium supported on alumina to selectively hydrogenate carbon monoxide in the presence of carbon dioxide. Platinum [15-17] and ruthenium-based catalysts [4-7] dispersed on metal oxide carriers have been found to exhibit high activity for CO and CO_2 methanation. Galletti et al. [2] investigated selective CO methanation over different Ru loadings (3, 4 and 5 wt. %) supported on γ-Al_2O_3. Complete removal of 500 ppm CO in the temperature range of 180 - 420^{o}C with acceptable low level of CO_2 methanation and negligible reverse water gas shift reaction was achieved over the 4 wt. % Ru/ γ-Al_2O_3. Another study about the effect of Ru loading (1 - 7 wt. %) over γ-Al_2O_3 for the same reaction was reported by Dagle et al. [7]. It was found that Ru loading has a tremendous effect on hydrogen consumption. The CO methanation activity increases with metal loading while hydrogen consumption increases in parallel due to increased CO_2 methanation. Therefore the catalyst with (3 wt. %) of Ru loading was found to have the optimum catalytic activity for this system.

A number of studies have shown that the nature of the support may play a crucial role in the mechanism of CO/CO_2 hydrogenation reactions, since metal–support interactions can modify the catalytic properties of the metallic phase [4,13,18,19]. Kim et al. [4] prepared Ru catalysts deposited on different supports such as yttria-stabilized zirconia (YSZ), ZrO_2, TiO_2, SiO_2 and γ-Al_2O_3 with a wet impregnation method. Among them, Ru/YSZ showed the highest CO conversion especially at low temperatures (~ 150^{o}C) and it reduced the high inlet CO concentration from 10,000 ppm to less than 10 ppm at the exit of the reactor. Another study was conducted by Panagiotopoulou et al. [8] on the effect of different supports for CO methanation over Ru nanocatalysts in the temperature range of 170 - 470^{o}C. Results of kinetic measurements showed that the specific reaction rate of CO conversion depends strongly on the nature of the support. In particular, activity decreases in the order of TiO_2 > Al_2O_3, CeO_2 > YSZ > SiO_2 based on the turn over frequency values at 200^{o}C.

In addition, catalytic performance of dispersed metal catalysts for CO methanation reactions is often affected by crystallite size since CO hydrogenation is well known to be a

structure sensitive reaction and is highly affected by metal size and surface area [8,13,20-23]. Ojeda et al. [21] prepared several alumina-supported Rh nanoparticles with narrow size distribution to investigate the catalyst size effect on CO hydrogenation. They conducted XPS measurements to show that the electronic metal–support interaction increases as the particle size decreases, leading to partially oxidized Rh atoms with increased selectivity as rhodium particle size decreases. Takenaka et al. [24] found that larger Ni crystallites supported on ZrO_2 and smaller Ru crystallites supported on TiO_2 are more effective for CO methanation.

Recently [25], we have shown that there is a strong metal-support interaction between Pt nanoparticles (2.5 ± 0.5 nm) and the ionic conductive supports or mixed-ionic conductive supports when deposited on yttria-stabilized zirconia (YSZ), ceria (CeO_2) and samarium doped-ceria (SDC). This strong metal-support interaction (SMSI) enhances O^{2-} transfer towards Pt and electron transfer from Pt to the ceramic support at the vicinity of the triple phase boundary (tpb) [25]. This charge transfer leads to a remarkable catalytic activity of Pt nanoparticles interfaced with ionically and mixed ionic conductive supports for 909 ppm carbon monoxide and ethylene oxidation in the absence of oxygen in the gas feed. It is proposed that Pt nanoparticles and the conducting ceramic form local nano-galvanic cells, where the anodic reaction is volatile organic compounds oxidation by O^{2-} and the cathodic reaction is the surface partial reduction of zirconia or ceria at the tpb.

In the present work, the particle size effect of Pt/YSZ nanocatalysts on the methanation and preferential electrooxidation of CO in hydrogen-rich gas stream is investigated in the absence of oxygen in the gas feed. Minimum load of noble metal catalyst on support is used (≤1 wt. %). Conversion of reactants and selectivity of the desired products are calculated and compared with values reported in literature. Long time stability of the catalyst is conducted under different operating conditions and various CO concentrations up to 9000 ppm.

11.3 Experimental

11.3.1 Synthesis of the YSZ-supported Pt nanoparticles (Pt/YSZ)

Platinum nanoparticles were synthesized using a modified polyol reduction method described in details elsewhere [26,27]. In short, Pt colloids were synthesized in ethylene

glycol (anhydrous 99.8% Sigma Aldrich) at 160^{o}C, starting from 0.1227 g $PtCl_4$ (Alfa Aesar, 99.9% metals basis) precursor salt and using various sodium hydroxide (EM Science, ACS grade) concentrations of 0.056, 0.06, 0.08 and 0.20 M in order to adjust and control the particle size as shown in Table 11-1. The resulting dark brown Pt colloidal solution was deposited on 1.5 g YSZ (Aldrich, specific surface area specific surface area (a_s) of 13 $m^2 \cdot g^{-1}$) to give ~1 wt. % of total Pt loading as confirmed by inductive coupled plasma measurements using (ICP-OES Varian Vista-Pro CCD spectrometer). The resulting supported catalysts were washed and centrifuged extensively with de-ionized water and washed and dried in air for 48 h at 60^{o}C.

Table 11-1: List of Pt/YSZ catalysts, catalyst dispersion, catalyst loading, activation energies (E_a) and TOF for CO methanation reactions.

Catalyst	Pt size from ADF-STEM (nm)	Pt Loading (wt. %)[a]	Pt Dispersion (%)[b]	T_{50} (^{o}C)	Ea (kJ/mol)	TOF (s^{-1}) at 60^{o}C
Pt/YSZ-1	6.7 ± 1.0	-	9.5	N.A.	16.6	0.3
Pt/YSZ-2	4.4 ± 0.3	1.1	30.1	120	13.0	1.5
Pt/YSZ-3	3.0 ± 0.8	1.1	39.5	104	11.6	2.6
Pt/YSZ-4	1.9 ± 0.4	0.9	51.8	26	11.2	2.9

[a] determined from ICP
[b] from CO titration

11.3.2 Characterization of Pt nanoparticles

11.3.2.1 ADF-STEM of Pt/YSZ

The scanning transmission electron microscopy (STEM) analysis was carried out on a FEI Titan^3 80-300 TEM operated at 300 keV, and equipped with a CEOS aberration corrector for the probe forming lens and an energy dispersive X-ray (EDX) spectrometer (EDAX Analyzer, DPP-II). Annular dark-field (ADF) images, which provide a contrast related mainly

to the atomic number (Z) and the thickness of the region analyzed, were acquired with a Fishione detector. The convergence and collection angle were 17 and 60 mrad, respectively. The TEM specimens were prepared by sonicating the as-prepared catalyst powders in ethanol. One drop of the solution was then placed onto a 200 mesh TEM copper grid coated with a lacey carbon support film (Ted Pella) and dried in air. The bright features observed in the ADF-STEM images were identified as the Pt catalyst. The elemental composition of both the catalyst and the support was also confirmed by spatially-resolved EDX. The use of Image J software allowed for the determination of Pt particles size distribution.

11.3.2.2 Dispersion measurements

Dispersion was determined for the Pt/YSZ nanoparticles using the CO titration technique [28-33]. The stoichiometric ratio of Pt/CO was assumed to be unity [29-32]. In brief, carbon monoxide (Linde, 1000 ppm CO in He) with a flow rate of 15 $ml \cdot min^{-1}$ was adsorbed on the Pt/C surface at 140°C. The reactor was then purged with He (Linde, 100%) at the same temperature and flow rate of 100 $ml \cdot min^{-1}$. An oxygen flow of 30 $ml \cdot min^{-1}$ (Linde, 99.997%) was then passed through the reactor and the amount of CO_2 formed was measured using an online gas chromatograph. This procedure was repeated for different purging times of He ranging from 5 to 20 min, and the maximum reactive CO uptake was obtained by extrapolating to time equals zero.

11.3.3 Catalytic Activity

The catalytic activity measurements of Pt/YSZ for CO methantion and electrooxidation were carried out at atmospheric pressure in a continuous flow U-shaped quartz reactor using approximately 50 mg of catalyst. The reactive mixture consisted of 1000 ppm CO (Linde, 1% in He), 10 % H_2 (Linde, 99.99 %), balance He (Linde, 100%). The total gas flow rate was set at 6.60 $L \cdot h^{-1}$.

All the catalytic tests were performed in the temperature range of 25 - 120^{o}C. The temperature was measured using a thermocouple (Omega, k-type) placed in the close vicinity to the catalyst bed. Before each measurement, the system was maintained for at least 30 minutes in order to ensure that there is no temperature difference between the catalyst bed and

the reactor. An on-line gas chromatograph (GowMac 350) was connected on line in order to quantify the concentrations of CO, H_2, CH_4 and CO_2. Qualitative analysis of the reaction products were performed with an online mass spectrometer (Proline DM 100). Each experiment was repeated for three cycles to evaluate the catalyst stability and reproducibility of the measurements.

From the outlet concentrations of CO, H_2, CH_4 and CO_2, the following experimental values were calculated:

$$\text{CO Conversion (\%)} = ([CO]_{IN} - [CO]_{OUT}) / [CO]_{IN} \times 100\% \quad (11.6)$$

$$H_2 \text{ conversion (\%)} = [H_2]_{IN} - ([H_2]_{OUT} / [H_2]_{IN}) \times 100\% \quad (11.7)$$

$$CH_4 \text{ selectivity} = [CH_4]_{out} / ([CO]_{IN} - [CO]_{OUT}) \times 100\% \quad (11.8)$$

$$CH_4 \text{ yield} = [CH_4]_{out} / [CO]_{IN} \times 100\% \quad (11.9)$$

Turn over frequency (TOF) values were calculated using the following equation:

$$TOF = r / N_G \quad (11.10)$$

Where r is the CO methanation rate ($mol \cdot s^{-1}$), and N_G is the moles of active Pt sites (mol).

11.4 Results and Discussion

11.4.1 ADF-STEM of supported nanoparticles

Figure 11-1 shows ADF-STEM micrographs of the four Pt/YSZ catalysts where Pt particles are the bright localized features. In general the Pt NPs are uniform and spherical in shape with some agglomeration of the largest nanoparticles.

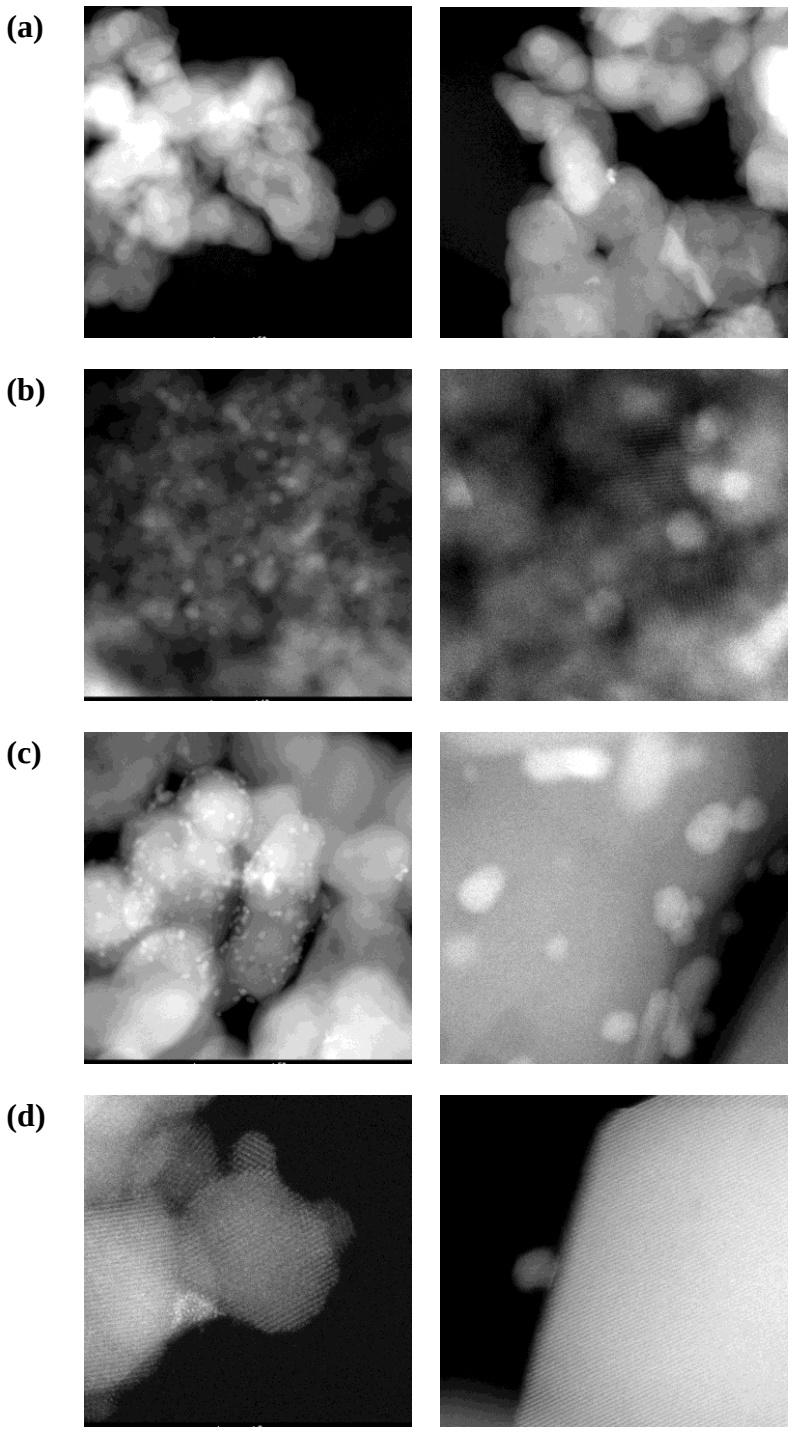

Figure 11-1: ADF-STEMs of (a) Pt/YSZ-1,(b) Pt/YSZ-2,(c) Pt/YSZ-4 and (d) Pt/YSZ-4

The average particle sizes obtained from a series of STEMs are shown in Table 11-1 ranging from 1.9 to 6.7 nm.

The dispersion shows high values for the smaller nanoparticles compared with the larger ones. The low dispersion values in general are due to the small specific surface area of YSZ compared with other conventional catalyst supports such as carbon and alumina. However, the smallest nanoparticles Pt/YSZ-4 (1.9 ± 0.4 nm) are well dispersed with 51.9 % dispersion as per the CO titration method. STEM imaging also provides evidence to an interaction between the catalyst and the support especially in the case of the smallest nanoparticles where a change in the shape and morphology of the nanoparticle at the interface with YSZ is apparent in Fig. 11-1d. The shape of the catalyst is modified near the surface having a more ellipsoid than circular shape due to the interaction with the support.

11.4.2 Effect of Particle Size on CO methanation and preferential electrooxidation

Figure 11-2 shows representative light-off curves for all nanocatalysts under investigation in terms of CO conversion.

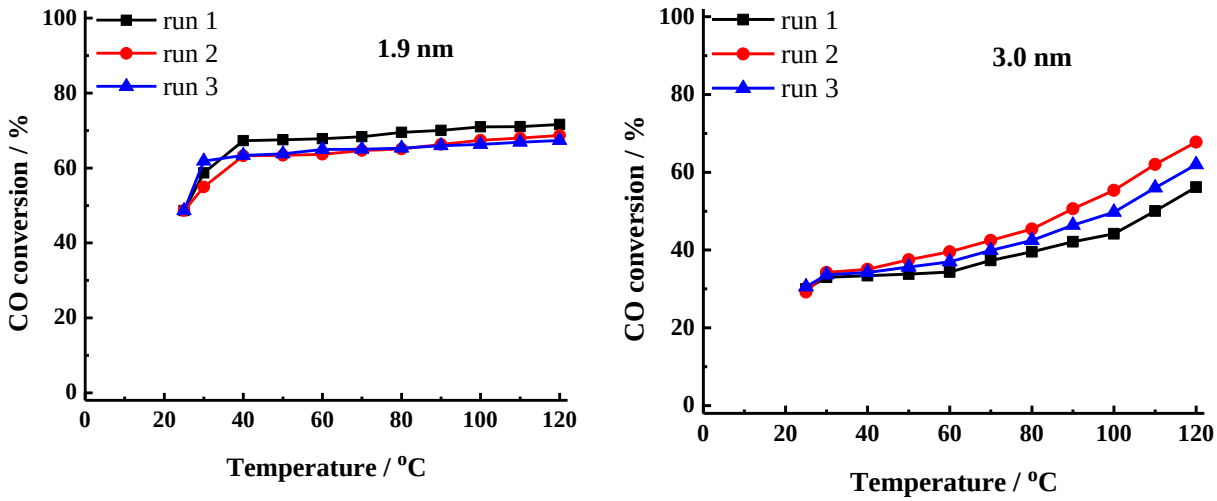

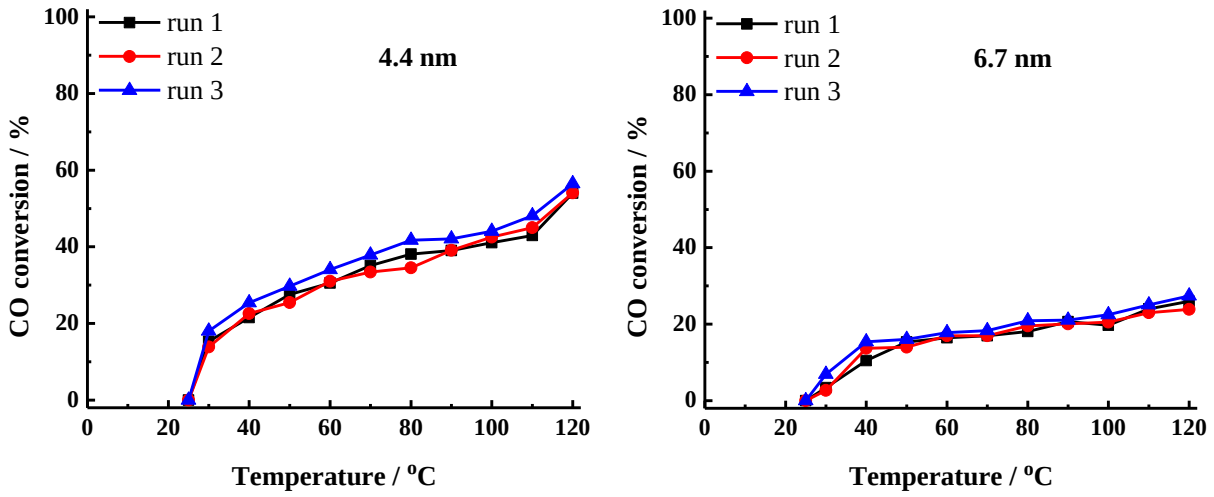

Figure 11-2: Stability of Pt/YSZ-1, Pt/YSZ-2. Pt/YSZ-3 and Pt/YSZ-4 catalysts. Space velocity = 19000 h^{-1}, gas composition: total flowrate= 6.6 $L \cdot h^{-1}$, [CO] = 1000 ppm, 10% H_2 and He balance, no O_2 in the gas feed.

All light-off curves show good stability and reproducibility for three runs per experiment. The catalyst Pt/YSZ-3 (3.0 nm) shows relatively less stability compared to the other three catalysts between run 2 and run 3 which can be due to the agglomeration of this catalyst as was shown in Fig. 11-1c. It is worth mentioning that after each cycle, the catalyst was kept in He overnight for regeneration. This procedure allows O_{2-} concentration to reach an equilibrium between the bulk and the surface, hence reactivating the catalyst [25].

Fig. 11-3 shows the effect of the particle size on the catalytic activity for CO methanation and oxidation from hydrogen rich stream in the absence of oxygen in the gas phase in terms of CO conversion Fig. 11-3a and intrinsic rate per catalyst surface area based on CH_4 formation as per Fig. 11-3b.

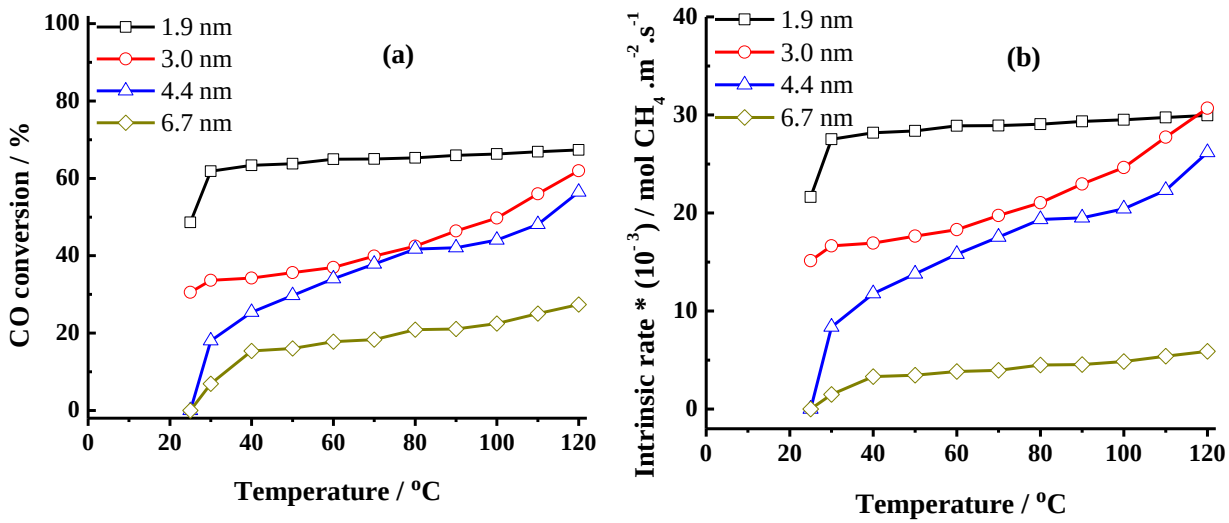

Figure 11-3: Effect of particle size on (a) CO conversion and (b) Intrinsic rate per metal surface area. Space velocity = 19000 h^{-1}, gas composition: total flowrate= 6.6 $L \cdot h^{-1}$, [CO] = 1000 ppm, 10% H_2 and He balance, no O_2 in the gas feed.

It is clearly shown that as the particle size increases, the catalytic activity decreases. The two smaller nanoparticles Pt/YSZ-3 (3.0± 0.8 nm) and Pt/YSZ-4 (1.9± 0.4 nm) show high catalytic activity at room temperature already with CO conversion of about 30 and 50%, respectively. On the other hand, the two larger nanoparticles Pt/YSZ-1 (6.7± 1.0 nm) and Pt/YSZ-2 (4.4± 0.3 nm) show CO conversion starting at slightly higher temperature of about 30°C. It is clear that there is a direct relation between the catalyst size, the catalyst dispersion and its activity towards CO methanation reaction. Smaller Pt nanoparticles have much higher catalytic activity per surface are than larger nanoparticles. The smallest catalyst Pt/YSZ-4 has an intrinsic rate of 28.89 x 10^{-3} mol CH_4 per active surface area compared to 3.94 x 10^{-3} for the largest nanocatalyst at 60°C. This trend is in agreement with other studies reported on the effect of catalyst size and dispersion on CO methanation over ruthenium, cobalt and nickle catalysts [34-36]. Abdel-Mageed et al. [34] investigated the impact of calcination procedure in preparing different particle sizes of 2.2 wt. % Ru/zeolite catalysts for CO selective methanation. They showed that the increase in calcination temperature resulted in a decrease in Ru particle size from 1.51 to 1.05 nm with better dispersion. The dispersion of the nanocatalysts increased from 47 % to 68 % when the particle size decreased from 1.51 to 1.05 nm. This higher dispersion of the smaller nanoparticles was related to the distinct increase in

the activity and selectivity of Ru/zeolites for CO methantion reaction. Another study reported by Kok et al. [35] showed that the catalyst active site density for CO methanation depends on the catalyst particle size, dispersion and degree of catalyst reduction. They also emphasized the importance of synthesizing highly dispersed catalyst for stronger interaction with the supports to obtain better activity for CO methanation. They compared different cobalt (Co) catalyst deposited on γ-Al_2O_3 for CO methanation using 200 mg of each powder. Smaller Co nanoparticles (5.6 nm) have 30% more dispersion than the largest ones in the study (8.6 nm). The highest CO conversion obtained by the smallest nanocatalyst was about 45% compared with the conversion obtained by the largest one (34 %). It is worth mentioning that hydrogen consumption that associates CO methanation and electrooxidation in our study does not exceed 3.0 % for the largest nanoparticle. This is a better advantage of performing such experiments in the absence of oxygen in the gas feed where reaction (eq. 11.4) is suppressed, hence least H_2 is consumed. Another factor that eliminates higher consumption of H_2 is operating at low temperatures to avoid the RWGS reaction (eq. 11.5) which is highly endothermic and requires higher operating temperatures [37]. In previous studies to investigate the activity of other metals for CO preferential oxidation and methanation, three factors were found to control the activity and selectivity of the catalysts in these reactions: (a) size of the catalyst particles, (b) strong contact between the particles and the support (metal-support interaction), and (c) suitable selection of the support [12,21,22,38].

Takenaka et al. [24] investigated the effect of supports and Ru particle size for the complete removal of 0.5 % CO from hydrogen-rich gas stream. They supported Ru over MgO, Al_2O_3, SiO_2, TiO_2 and ZrO_2. Among these catalysts, Ru/TiO_2 performed the best for CO methanation with least H_2 consumption. The order of catalytic activity was found to be Ru/TiO_2> Ru/Al_2O_3> Ru/ZrO_2> Ru/MgO = Ru/SiO_2. To further explain this activity, the authors performed Extended x-ray Absorption Fine Structure (EXAFS) analysis for the catalysts to investigate the different structures on each support. They found that the coordination number of Ru-Ru and the particle size were greatly influenced by the type of the support with the smallest particle size in the case of Ru/TiO_2. TEMs of Ru/TiO_2 showed that most Ru metal particles observed were smaller than 5 nm with narrow size distribution, while the range of Ru/MgO for example ranged from 2-30 nm. The authors concluded that catalytic activity of Ru nanoparticle increased as the particle size decreased due to the higher dispersion

of smaller nanoparticles compared to larger ones which indicates the availability of more number of active sites for CO methanation [24]. The same trend is observed for our catalysts as per the dispersion values reported in Table 11-1. The smallest nanoparticle Pt/YSZ-4 has a dispersion value of 51.8 % compared with the dispersion of 9.5 % for the larger catalyst Pt/YSZ-1, which can be directly related to the enhanced catalytic activity of the smallest nanoparticles even at ambient temperatures. Moreover, the enhanced activity of the smaller nanoparticles is further confirmed by lower activation energies as shown in Table 11-1. The activation energy for CO methanation was determined using Arrhenius relationship calculated in the range below 20% conversion according to:

$$\ln r = -E_a/(RT) + \ln k \tag{11.11}$$

where r is CO methanation rate ($mol \cdot s^{-1}$), E_a is the apparent activation energy ($J \cdot mol^{-1}$), R is the universal gas constant ($J \cdot mol^{-1} \cdot K^{-1}$), T is the reactor temperature (K), and k is the rate constant ($mol \cdot s^{-1}$). The activation energies were calculated for each catalyst from the slope of a linear fit in ln$r$ versus 1/T coordinates. The activation energy of the smallest nanoparticle (1.9 nm) is 11.2 kJ/mol compared to 16.6 kJ/mol for the largest one (6.7nm). This trend is further supported by a recent study conducted by Hu et al. [9] on the catalytic activity of series of Ni/Al_2O_3 catalysts of different mean particle sizes for CO methanation for the production of synthesized natural gas. They reported that smaller Ni particles had higher activity, stronger resistance to carbon deposition and longer thermal stability. Similar results were reported recently by Zhu et al. [39] on the effect of particle size on the catalytic activity of Co_3O_4 nanocatalysts for CO methanation. They compared the activity of 20, 40 and 80 nm catalysts and found that smallest nanoparticles have much higher catalytic activity than the larger ones reaching complete CO conversion at 177^{o}C compared with 300^{o}C for the 80 nm catalyst. This pronounced enhancement in activity is related to the increased active surface area of smaller nanoparticle (50 m^2/g) with comparison with that of the largest ones (10 m^2/g) and the availability of more Co^{3+} active sites on the larger surface area catalyst as observed by TPR-H_2 spectra, hence enhancing CO methanation.

Moreover, Fig. 11-4 shows methane yield and selectivity produced over the smallest catalyst PtYSZ-4 (1.9 ± 0.4 nm).

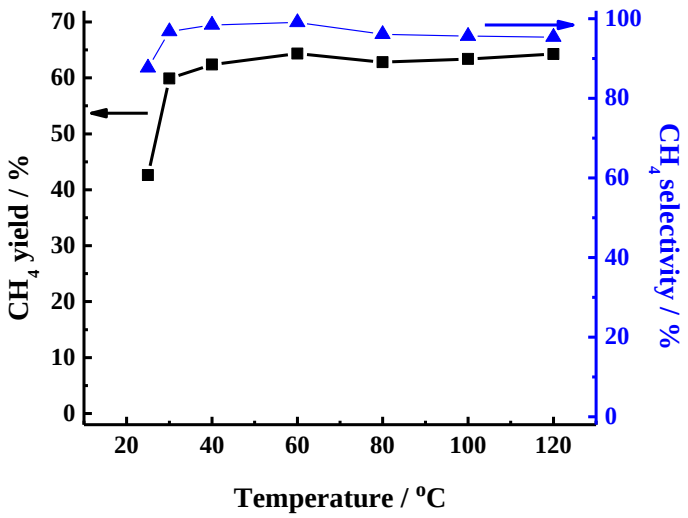

Figure 11-4: Methane yield and selectivity over Pt/YSZ 4 (1.9 nm± 0.4 nm). Space velocity = 19000 h^{-1}, gas composition: total flowrate= 6.6 $L \cdot h^{-1}$, [CO] = 1000 ppm, 10% H_2 and He balance, no O_2 in the gas feed.

The results show that methane selectivity starts at about 85% at room temperature and increases to an average value of 97 % for the rest of experimental range of temperature. This trend is well reported where the selectivity reaches a value and stays almost constant even with further increase in temperature [8]. In a study by Darensbourg et al. [40] and by Kikuchi et al. [41] to explain the observed rate enhancement of supported Pt for CO methanation, a decrease in the bond strength of adsorbed CO was due to the decrease in Pt size to around 2 nm. They reported that the turnover number (TOF) decreased by 20% as the particle size grew from 2 nm to 6 nm. Similarly, based on the TOF values reported for our catalysts at 60°C in Table 11-1, TOF value drops from 2.9 s^{-1} for the smallest nanoparticle to 0.3 s^{-1} for the largest catalyst. Hu et al. [9] studied more factors that enhanced CH_4 selectivity over Ni/Al_2O_3 catalysts such as running the reaction at relatively low gas space velocity of about 30 000 mL/g·h and a molar ratio of $H_2/CO > 3$: 1 which applies well to the conditions of our experiments. The high selectivity for methane production over noble metals supported on ionic or mixed ionic conductive supports was shown to be favored over methanol and dimethyl ether production. Shen et al. [42] demonstrated that the higher methane selectivity of Pd/TiO_2 was assigned to SMSI due to the decoration effect of the reduced TiO_x species on Pd surface, which aids the dissociation of CO. In a detailed study about the effect of the support on the catalytic activity of noble metals for CO removal from H_2 gas stream, Shubert el al.

[43] investigated the catalytic activity of highly dispersed gold nanoparticles on metal oxides which has been attributed to their ability to provide reactive oxygen. They grouped various oxide supports into two categories: inert supports (SiO_2, Al_2O_3, and MgO) and active supports (reducible transitional metal oxides such as TiO_2, CoO_x, CeO_2, and Fe_2O_3). Gold was shown to exhibit higher catalytic activity when it is deposited as nanoparticles on the metal oxide supports. The gold catalysts supported on reducible oxides were more active than on non-reducible oxides mainly due to the ability of reducible oxides to supply reactive oxygen for CO oxidation at low temperature [12,43]. Similar results were reported to show that oxygen species provided by YSZ surface are much more reactive than oxygen gas species for several reaction systems at low temperatures [25,44-46]. Generally, there are two main reactions that might run in parallel during CO methanation process: the undesirable CO_2 methanation given by (eq. 11.2) and the reverse water-gas shift reaction given by (eq. 11.5). The later reaction is negligible in the temperature range under investigation (25 – 120^oC), which absence in this case is further supported by no evidence of an increase in CO outlet concentration monitored by the gas chromatograph. Moreover, based on the heats of formation listed above, the RWGS in (eq. 11.5) is endothermic which encounters the need of high temperatures for significant conversion of CO_2 to CO. On the other hand, CO conversion to CO_2 as per (eq. 11.3) does not exceed 1% as per the outlet concentration of CO_2 in the GC due to the absence of oxygen in the gas stream and the dependence of conversion CO to CO_2 solely on consuming oxygen anions supplied from YSZ surface. More specifically, (eq. 11.3) and (eq. 11.4) can be re-written in the form of electrooxidation instead of oxidation due to the absence of oxygen in the gas feed:

$$CO + O^{2-} \rightarrow CO_2 + 2\bar{e} \qquad (11.3)'$$

and

$$H_2 + O^{2-} \rightarrow H_2O + 2\bar{e} \qquad (11.4)'$$

which can be accompanied by surface partial electroreduction of ZrO_2 [47]:

$$ZrO_2 + 2\delta e^- + \delta V_O^{\cdot\cdot} \rightarrow ZrO_{2-\delta} + \delta O_o^x \qquad (11.12)$$

The overall electrochemical reactions are [25]:

$$\delta CO + 2ZrO_2 + 2\delta V_O^{\cdot\cdot} \rightarrow \delta CO_2 + 2ZrO_{2-\delta} + \delta O_o^x \quad (11.13)$$

or

$$\delta H_2 + 2ZrO_2 + 2\delta V_O^{\cdot\cdot} \rightarrow \delta H_2O + 2ZrO_{2-\delta} + \delta O_o^x \quad (11.14)$$

It is worth noting that reaction (11.3)' and (11.4)' are more favorable to take place as eq. 11.3 and eq. 11.4 if excess of oxygen is supplied by factor of 2 and 4, respectively [1]. This condition is not valid in our experimental system since no oxygen is available in the gas phase.

Figure 11-5 shows the effect of CO concentration on the stability of the smallest nanoparticle Pt/YSZ-4 (1.9 ± 0.4 nm).

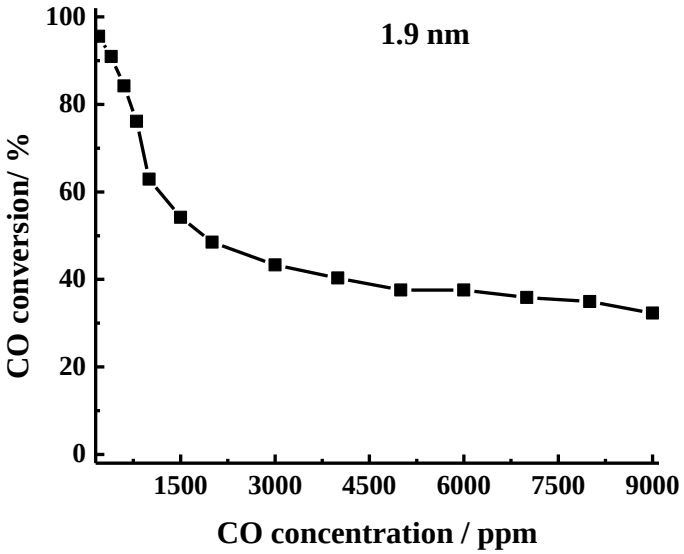

Figure 11-5: Effect of CO concentration on conversion over Pt/YSZ-4 (1.9± 0.4 nm). Space velocity = 19000 h^{-1}, gas composition: total flowrate= 6.6 $L \cdot h^{-1}$, no O_2 in the gas feed.

The results shows an average of 20% decrease in CO conversion when CO concentration increases from 1000 to 9000 ppm. It is reported that catalyst activity for CO methanation decreases at high CO concentration. In a recent study by Sehested et al. [48] to study the effect of CO and H_2 inlet concentration on the catalytic activity of nickel for CO methanation, faster catalyst deactivation was observed at high CO concentration and high temperatures. Further

explanation was provided by Panagiotopoulou et al. [13] who investigated selective methanation of CO over noble metals (Ru, Rh, Pt and Pd) supported on Al_2O_3. The enhanced catalytic activity of Ru compared with Pt was attributed to the lower affinity of Ru for CO compared to that of Pt surfaces which are known to strongly chemisorb CO and displaces hydrogen from the adsorbed layer. Deactivation of Pt/YSZ under CO without oxygen in the gas feed is plausibly related to the lack of O^{2-} for the reaction when high concentrations CO are introduced over the catalyst [25]. High VOCs concentrations require large amounts of O^{2-} from the surface of the support, because bulk O^{2-} diffusion in YSZ is slow at these relatively low temperatures (25 – 120^{o}C), hence concentration gradient of O^{2-} in YSZ will exist between the bulk and the surface. Diffusion of O^{2-} to the triple phase boundary is a reaction limiting step. When available at the surface, O^{2-} ions are consumed in the electrochemical reactions and the catalyst slightly deactivates. As mentioned earlier [25], the catalyst can be easily reactivated not only by sweeping O_2 through the reactor, but also by leaving the catalyst in He overnight allowing O^{2-} concentration to reach an equilibrium between the bulk and the surface. The heat of reaction for Eq. (11.1) is higher than that of Eq. (11.2), which could be another reason that CO oxidation is favored and negligible H_2 conversion is observed in the range of 1 - 3% (not shown here). From past studies [49], it has been found that the methanation reaction over Pt metal group in particular is frequently close to zero order in CO concentration and near first order in H_2 concentration [49,50]. From this data, it has been assumed that the catalyst surface is nearly completely covered with strongly adsorbed CO while the more weakly bound hydrogen competes for adsorption on the small number of available metal sites remaining.

Figure 11-6 shows the stability over time of the smallest nanoparticle Pt/YSZ-4 at 100^{o}C.

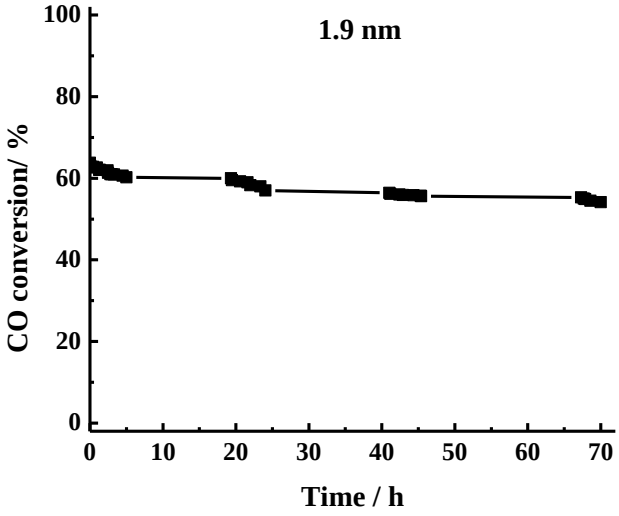

Figure 11-6: Stability of Pt/YSZ-4 (1.9± 0.4 nm) over time at 100^{o}C. Space velocity = 19000 h^{-1}, gas composition: total flowrate= 6.6 L·h^{-1}, [CO] = 1000 ppm, 10% H_2 and He balance, no O_2 in the gas feed.

Catalyst lifetime is a key consideration in the economical production of synthesized natural gas from coal-derived gases and for fuel cell applications [9]. CO methanation catalysts can deactivate over time due to two main factors: carbon deposition which is often an intermediate product during the methanation reaction that leads to catalyst deactivation [51,52], and/or the catalyst sintering at very high temperatures which deteriorates the catalyst activity as reported earlier [9]. The later factor is excluded under the reaction conditions of our experiments where the maximum temperature investigated is 120^{o}C. Therefore, the effect of carbon deposition and carbon balance calculations will be discussed. Carbon balance calculation performed for the four catalysts shows negligible amounts of unidentified carbon which does not exceed 1.23% as expected in our experimental conditions. Several studies were devoted for the investigation of carbon fouling or deposition on CO methanation catalysts [35,48,51,52]. They concluded that increasing H_2 content in the gas feed stream shifts the thermodynamic equilibrium to be unfavorable towards carbon deposition. The ratio H_2/CO is 100 in our experiments. Another factor that affected the rate of carbon deposition was operating conditions at higher pressures and temperatures. In a similar study conducted by Sehested et al. [48] about the mechanism and kinetics of CO methanation over Ni catalysts under high H_2/CO ratio, they have reported that catalyst deactivation was observed at temperatures > 350^{o}C probably related to carbon deposition and physical blockage of catalyst

active sites. It was reported that at low temperature and pressure, very little carbon accumulation and catalyst deactivation occurred. This would explain the relatively high stability of our catalysts over time.

11.5 Conclusions

The removal of CO contained in hydrogen-rich stream gas was conducted over four Pt/YSZ nanocatalysts with size range of (1.9 - 6.7 nm) in the absence of oxygen in the gas feed in the temperature range of 25 - 120^{o}C. The reaction was found to be strongly size dependent in analogy to its nature when oxygen gas is available. The smallest nanoparticles have the highest activity per atom surface area, 60% of CO conversion was achieved at room temperature over the smallest nanocatalyst. The high dispersion of the smaller nanoparticles enhanced its catalytic activity for CO methanation with minimum hydrogen consumption of about 1.5 %. The absence of oxygen in the gas feed and the low temperature conditions as well as the high H_2/CO ratio contributed efficiently to the stability of catalysts for long period of time. The effect of CO concentration shows deactivation as CO concentration increases probably due to strong adsorption of CO on Pt surfaces which competes with hydrogen and displaces the later from the adsorbed layer.

11.6 Acknowledgement

Financial support from Natural Science and Engineering Research Council (NSERC) and Ontario Graduate Scholarship (OGS) are acknowledged. In context of this, I would like to acknowledge Dr. Nimal de Silva (Dept. Earth Sciences at UOttawa) for running ICP measurements. Dr. Martin Couillard (National Research Council Canada) for running annular dark field-scanning electron microscopy (ADF-STEM) measurements and the related discussion for the catalysts in the manuscripts presented in this chapter.

11.7 References

[1] A. Mishra, R. Prasad, *Bull. Chem. Eng. Catal.* 6 (2011) 1.

[2] C. Galletti, S. Specchia, G. Saracco, V. Specchia, *Chem. Eng. Sci.* 65 (2010) 590.

[3] I. H. Son, A.M. Lane, *Catal. Lett.* 76 (2001) 151.

[4] Y. H. Kim, E. D. Park, H. C. Lee, D. Lee, *Appl. Catal. A Gen.* 366 (2009) 363.

[5] S. Alayoglu, A. U. Nileka, M. Marvrikakis, B. Eichhom, *Nat. Mater.* 7 (2008) 333.

[6] A. F. Ghenciu, *Curr. Opin. Solid State Mater. Sci.* 6 (2002) 389.

[7] R. A. Dagle, Y. Wang, G. -G. Xia, J. J. Strohm, J. Holladay, D. R. Palo, *Appl. Catal. A Gen.* 326 (2007) 213.

[8] P. Panagiotopoulou, D. I. Kondarides, X. E. Verykios, *Appl. Catal. B Environ*. 88 (2009) 470.

[9] D. Hu, J. Gao, Y. Ping, L. Jia, P. Gunawan, Z. Zhong, *Ind. Eng. Chem. Res.* 51 (2012) 4875.

[10] M. Kramer, M. Duisberg, K. Stowe, W. Maier, *J. Catal.* 251 (2007) 410.

[11] L. Chang, N. Sasirekha, Y. Chen, W. Wang, *Ind. Eng. Chem. Res.* 45 (2006) 4927.

[12] Y. -W. Chen, D. -S. Lee, H. -J. Chen, *Int. J. Hydrogen Energy.* 37 (2012) 15140.

[13] P. Panagiotopoulou, D. I. Kondarides, *Appl. Catal. A Gen.* 344 (2008) 45.

[14] B. Baker, J. Huebler, H. Linden, J. Meek, United States Patent No. 3, 615, 164, 1971.

[15] J. L. Ayastuy, M. P. Gonzalez-Marcos, J. R. Gonzalez Velasco, M. A. Gutierrez-Ortiz, *Appl. Catal. B Environ.* 70 (2007) 532.

[16] L. Huanling, M. Lei, S. Saibing, L. Zenghe, W. Aiqin, H. Yanqiang, Z. Ta, *J. Catal.* 28 (2007) 1077.

[17] B. Atalik, D. Uner, *J. Catal.* 241 (2006) 268.

[18] S. -Y. Wang, S. H. Moon, M. Albert Vannice, *J. Catal.* 71 (1981) 167.

[19] J. D. Bracey, R. Burch, *J. Catal.* 86 (1984) 384.

[20] M. Ojeda, S. Rojas, F. J. García-García, M. L. Granados, P. Terreros, J. L. G. Fierro, *Catal. Commun.* 5 (2004) 703.

[21] M. Ojeda, S. Rojas, M. Boutonnet, F. J. Pérez-Alonso, F. Javier García-García, J. L. G. Fierro, , *Appl. Catal. A Gen.* 274 (2004) 33.

[22] T. Hanaoka, H. Arakawa, T. Matsuzaki, Y. Sugi, K. Kanno, Y. Abe, *Catal. Today.* 58 (2000) 271.

[23] K. Otsuka, A. Kuwabara, A. Nakamura, T. Yamamoto, K. Matsunaga, Y. Ikuhara, *Appl. Phys. Lett.* 82 (2003) 877.

[24] S. Takenaka, *Int. J. Hydrogen Energy.* 29 (2004) 1065.

[25] R. J. Isaifan, E. A. Baranova, *Electrochem. Commun.* 27 (2013) 164.

[26] E. A. Baranova, Y. Le Page, D. Ilin, C. Bock, B. MacDougall, P. H. J. Mercier, *J. Alloys Compd.* 471 (2009) 387.

[27] E. A. Baranova, C. Bock, D. Ilin, D. Wang, B. Macdougall, *Surf. Sci.* 600 (2006) 3502.

[28] C. Vayenas, S. Bebelis, I. Yentekakis, H. Lintz, *Catal. Today.* 11 (1992) 303.

[29] M. Alves Fortunato, D. Aubert, C. Capdeillayre, C. Daniel, A. Hadjar, C. Guizard, P. Vernoux, *Appl. Catal. A Gen.* 403 (2011) 18.

[30] R. M. Rioux, J. D. Hoefelmeyer, M. Grass, H. Song, K. Niesz, P. Yang, *Langmuir*, 104 (2008) 198.

[31] S. Kim, T. Yamamoto, A. Endo, T. Ohmori, M. Nakaiwa, *J. Ind. Eng. Chem.* 12 (2006) 769.

[32] M. Marwood, C. G. Vayenas, *J. Catal.* 178 (1998) 429.

[33] J. Lee, H. Moon, H. Lee, J. Kim, K. Yoon, *Solid State Ionics.* 148 (2002) 15.

[34] A. M. Abdel-Mageed, S. Eckle, H. G. Anfang, R. J. Behm, *J. Catal.* 298 (2013) 148.

[35] E. Kok, N. Cant, D. Trimm, J. Scott, *Catal. Today.* 178 (2011) 79.

[36] K. Urasaki, Y. Tanpo, Y. Nagashima, R. Kikuchi, S. Satokawa, *Appl. Catal. A Gen.* 452 (2013) 174.

[37] Q. Liu, X. Dong, X. Mo, W. Lin, *J. Nat. Gas Chem.* 17 (2008) 268.

[38] M. A. Vannice, *J. Catal*. 37 (1975) 462.

[39] H. Zhu, R. Razzaq, L. Jiang, C. Li, *Catal. Commun.* 23 (2012) 43.

[40] D. J. Darensbourg, R. P. Eischens, *Proc. Int. Congr. Catal.* 1 (1973) 321.

[41] E. Kikuchi, P. C. Flynn, S. E. Wanke, *J. Catal.* 34 (1974) 132.

[42] W. -J. Shen, M. Okumura, Y. Matsumura, M. Haruta, *J. Appl. Catal. A* 213 (2001) 225.

[43] M. M. Schubert, S. Hackenberg, A. C. Veen, M. Muhler, V. Plzak, R. J. Behm, *J. Catal.* 197 (2001) 113.

[44] R. J. Isaifan, H. A. Dole, E. Obeid, L. Lizarraga, P. Vernoux, E. A. Baranova, *Electrochem. Solid-State Lett*. 15 (2012) E14.

[45] L. Lizarraga, E. Obeid, M. N. Tsampas, A. Boreave, M.C. Steil, P. Vernoux, *ECS Trans.* 45 (2012) 225.

[46] H. A. Dole, R. J. Isaifan, F. M. Sapountzi, L. Lizarraga, D. Aubert, A. Princivalle, P. Vernoux, E. A. Baranova, *Catal. Letters.* 143 (2013) 996.

[47] J. Janek, C. Korte, *Solid State Ionics.* 116 (1999) 181.

[48] J. Sehested, S. Dahl, J. Jacobsen, *J. Phys. Chem. B.* 109 (2005) 2432.

[49] M. A. Vannice, *J. Catal.* 37 (1975) 462.

[50] M. E. Dry, T. Shingles, L. J. Boshoff, *J. Catal.* 25 (1972) 99.

[51] C. H. Bartholomew, *Appl. Catal. A Gen.* 212 (2001) 17.

[52] J. A. Moulijn, A. Van Diepen, F. Kapteijn, *Appl. Catal. A Gen*. 212 (2001) 3.

SECTION VI: CONCLUSIONS

12 General conclusions and recommendations

12.1 Introduction

The rapid industrial development in the 20th century caused major pollution problems affecting air, water and natural resources. Clean air was ranked by experts to be the first main item essential for life on Earth, and it is not the responsibility of individual nations anymore. Sources of air pollution include vehicle emissions, power plants, industrial factories and natural sources such as volcanoes and forest fires. Contrary to water pollution which might take the form of local effects, air pollution can extend to places far away from the source of pollution and where no people or other people live. For example, pesticides and harmful chemicals have been found in the Antarctic ice sheet [1]. Therefore, global concerns towards air pollution control have been the subject of interest for many researchers.

Recent progress in catalysis science explored the chemistry of catalyst systems for air pollution control from mobile and stationary sources. As vehicle population is projected to grow up to 1300 million by the year 2030 [2], emission standards and advanced control strategies are tightened to reduce pollutants due to incomplete combustion in engines. Despite that development in nanotechnology over the past two decades has provided some great opportunities to the catalysis research community in this field, there still some key issues in nanocatalyst synthesis, application and commercialization for air pollution control to be resolved [3].

Noble metals, although high in cost, have been extensively applied in catalytic converters for automobile emission control. Amongst these precious metals, platinum has several advantages including resistance to poisons such as sulfur oxides, efficient recycling, high melting point and more importantly, its capability to oxidize carbon monoxide and hydrocarbons and reduce nitrogen oxides. The main issues in catalytic converters are how to improve the catalyst efficiency at low temperature, to reduce the amount of platinum used and at the same time enhance its dispersion and to avoid catalyst deactivation due to ageing at high temperatures.

As a small contribution from our lab in solving air pollution problems, we explored some of the factors affecting metal-support interaction between noble nanoparticles and ionic vs. non ionic conductive supports for automotive and power plant emission control to which this thesis is devoted. To achieve better understanding of these factors and develop catalysts with high efficiency, a set of requirements must be met including: (i) synthesis of well-defined size and shape nanoparticles, (ii) use of least noble metal content, yet achieving maximum efficiency at lower temperatures, (iii) simple synthesis procedure that is easy to scale up (iv) low cost synthesis materials, equipment and conditions, (v) accessible catalytic sites through high dispersion of the catalyst, (vi) catalyst reactivation ability and (vii) long stability over time and under high pollutant concentrations.

12.2 General discussions

The ultimate goal of this research was to apply the knowledge we get in the field of metal-support interaction or self-induced electrochemical promotion to develope a catalyst with enhanced performance to replace the commercial catalyst used in vehicle catalytic converters. The flow of our research investigation was to serve (i) minimizing the amount of noble metals in the commercial catalyst while (ii) trying to find the metal-support combination that has high catalytic activity at low temperatures for the removal of two of the main automotive pollutants.

The amount of platinum currently used in the commercial catalyst depends on three factors: size of the vehicle, kind of fuel being used and the local air regulations. In general, Pt mass in commercial catalytic converters ranges between 1-2 g for a small car in lightly regulated environment to 12-15 g for big trucks. The reason why this large amount of noble metals is employed in vehicles is due to poor dispersion of the large-sized catalyst particles in the range of 0.5-8 μm. The low dispersion (~ 10 %) of the metal on the supports reduces the catalyst activity at low temperatures since only small portion of the active phase is exposed to the gases and hence available for the reaction to take place. Therefore, the compartment of the catalytic converter is placed in the vicinity near the engine to get enough heat to activate the catalyst at high temperature. On the other hand, this high temperature causes platinum particles to agglomerate forming large clumps that cannot carry the reactions out as

effectively; consequently converters must contain more mass of noble metals to compensate for the loss of efficiency.

In this thesis, only nanomaterials were considered in the investigation of metal-support interaction effect on their catalytic activity towards pollutant removal to serve the objective of lowering the amount of noble metal in catalytic converters which as well has a pronounced economic effect on the cost of vehicles. More than twenty nanocatalysts with noble metal content ($\leq$ 1 wt. % on each support) were synthesized, characterized and studied for carbon monoxide and ethylene oxidation as well as hydrogen stream purification in oxygen-rich and oxygen-free environment.

To begin with, the catalysts under investigation can be divided into two main groups, noble metals deposited on ionic or mixed ionic conductive and noble metals deposited on non ionic conductive supports. Carbon black of high specific surface area was used as a support for Pt which enhanced the nanoparticle dispersion on the surface which is a vital factor for ethylene oxidation. The effect of four particle sizes of Pt/C ranging between 1.5 - 6.3 nm with increasing activity as the nanoparticle size decreases proved that ethylene oxidation over Pt surfaces is highly structure sensitive which is in agreement with previous studies over other Pt/support catalysts as shown in chapter 5. On the other hand, when noble metals were deposited on ionic and mixed ionic conductive supports, further enhancement in catalytic activity depicted by early light-off curves, complete conversion of pollutants at low temperatures and low activation energy were observed as discussed in chapters 6-8. For instance, the light off temperature of Pt and Ru deposited on samarium-dopes ceria for ethylene oxidation were at 60^{o}C and 70^{o}C, respectively compared with higher temperatures of 90^{o}C and 130^{o}C for Pt and Ru deposited on carbon black, respectively. The same trend of pronounced enhanced activity was observed further when Pt was deposited on a novel perovskite mixed oxide group for carbon monoxide and ethylene oxidation. The novel perovskite $SmFeO_3$ group has high ionic conductivity at low temperatures which further increased when 1-5 % cerium was doped in their structure. This improved activity of nanoparticles deposited on ionic or mixed ionic conductors is of great importance since catalytic converters are mainly composed of Pt and Rh deposited on ionic or mixed ionic

conductive supports that serve as an oxygen storage component enabling the oxidation of carbon monoxide and hydrocarbons when the engine exhaust is fuel-rich.

To emphasize the importance of the presence of promoting ionic species (O^{2-}), complete oxidation of ~ 1000 ppm CO and C_2H_4 were achieved for the first time over Pt/ ionic or mixed ionic conductive supports using only O^{2-} from these supports as presented in chapters 9 and 10. The strong metal-support interaction induced an electronic effect through the exchange of O^{2-} at the vicinity of the three phase boundary (metal nanoparticles / conducting ceramic support / gas phase) which is responsible for the high activity of these catalysts. It was proposed that local nano-galvanic cells are formed where the anodic reaction is the pollutant electrooxidation by O^{2-} from the support and the cathodic reaction is the surface partial electroreduction of the ionic or mixed ionic support at the tpb. The nanoparticle size effect (1.9 - 6.7 nm) was investigated, and it was found that complete electrooxidation of 909 ppm CO and C_2H_4 was achieved over the smallest nanoparticle (1.9 nm) at ~ 120 and 200^{o}C, respectively. It is worths noting that the largest nanoparticles (6.7 nm) showed no catalytic activity at all in the absence of oxygen in the gas phase. The effect of particle size was attributed to stronger electronic interaction between Pt and YSZ and the higher surface area of the smallest nanoparticles, hence more nano-galvanic cells are available for the electrochemical reactions to take place.

However, the pronounced catalytic activity of nanoparticles deposited on ionic or mixed ionic conductive supports, due to strong metal-support interaction in the absence of oxygen in the gas feed, is of great interest especially for applications where minimum or no presence of oxygen is favoured. Therefore, further investigation was carried out on the activity of these Pt/YSZ nanoparticles for hydrogen fuel purification for fuel cell operations as presented in chapter 11. Hydrogen, being the ideal fuel for almost all fuel cell types except for direct methanol fuel cells, contains carbon monoxide impurities that should be removed at low temperatures. Carbon monoxide methanantion is one of the successful methods for CO removal, but it has always been studied in the presence of oxygen. Adding oxygen causes reduced hydrogen yields, dilution, safety issues and restrictions in operating conditions. The detailed study of the catalytic activity of four particle size Pt/YSZ catalysts revealed that the

smallest nanoparticle (1.9 nm) had high catalytic activity giving ~ 70% CO conversion at 40^{o}C and 85% selectivity for methane production at room temperature.

12.3 Summary of the main findings in this thesis

The following specific outcomes were obtained with respect to the defined project objectives:

- **Novel application of noble metal nanocatalyst supported on ionic and mixed ionic conductive supports for complete pollutant oxidation in the absence of oxygen in the gas phase.** Before this work, some ionic and mixed ionic conductors were used as catalysts in presence of oxygen gas in the reactant feed. This research showed that the ionic conductive species in the ionic conductors are highly active when there is metal-support interaction between the support and noble metal nanoparticles. Strong metal-support interaction was achieved by depositing noble metals in the size range of (1 - 7 nm) on ionic and mixed ionic conductors which was studied for the complete oxidation of ~ 0.1% CO and C_2H_4 at low temperatures (140 - 240^{o}C) over different nanocatalysts using the oxygen anions from the supports only for the first time.

- **Mechanism of electrooxidation of carbon monoxide and organic compounds over noble metal nanoparticles in oxygen-free environment is proposed.** This mechanism is based on the concept of formation of nano-galvanic cells, where the anodic reaction is the electrooxidation of the pollutant and the cathodic reaction is the surface partial reduction of the ionic conductive support. Both reactions take place simultaneously but separate in space at the three phase boundary (metal nanoparticles / ionic conductive ceramic / gas phase) with detailed mechanism presented in Chapter 9 and 10. This mechanism also suggests that as nanoparticle size decreases, more active sites are available for the reaction to take place, with longer three phase boundary and stronger induced electronic interaction, hence all explaining the enhanced catalytic activity as metal particle size decreases.

- **Comparison between the well known Electrochemical promotion of catalysis (EPOC) and self-induced EPOC phenomena is presented.** Since the commercial

application of EPOC at its present configuration is not feasible due to specifications of catalyst electrodes, sensitivity of electrical connections and need of special reactor design, self-induced EPOC can be utilized in commercial, industrial and environmental applications because it eliminates the need of the above mentioned requirements. Chapter 7 discusses this similarity and shows a schematic comparison between the two phenomena.

- **Rapid catalyst regeneration procedure is proposed after deactivation in the oxygen-free environment experiments.** Since the novel application of using metal-support interaction phenomenon to completely oxidize pollutants in oxygen-free environment consumes oxygen from the support solely, hence deactivates the catalyst when all available surface promoting species are consumed, it is essential to propose a feasible catalyst regeneration process. To the best of our knowledge, the new rapid deactivation scheme is presented for the first time in this work. Chapter 10 presents detailed steps for catalyst reactivation.

- **Carbon black was used for the first time as a support for platinum nanoparticles for ethylene catalytic oxidation.** Carbon black as a support of high specific surface area greatly enhanced platinum nanoparticle dispersion and hence their activity towards ethylene oxidation was improved. These results are in agreement with results reported earlier in literature about the structure sensitivity of ethylene oxidation over noble metal catalyst which is affected by catalyst dispersion and particle size.

- **The effect of the Pt particle size (< 10 nm) for C_2H_4 oxidation at low temperatures (~ 100^oC) has not been studied before**. In this work (Chapter 5), a systematic study of the particle size effect on complete ethylene oxidation over carbon-supported Pt nanoparticles (Pt/C) is shown by analyzing the surface composition of the as-prepared and spent Pt nanoparticles using x-ray photoelectron spectroscopy. XPS analysis showed that there is a noticeable increase in binding energy as nanoparticle size decreases which explained the improved catalytic activity of smaller particles compared with the larger ones.

- **Ruthenium, as a noble metal ten times cheaper than platinum, was supported on ionic conductive supports and compared with platinum activity towards volatile organic compound oxidation and electrooxidation.** More specifically, Ru deposited on yttria stabilized zirconia (Ru/YSZ) was used for the first time as a catalyst for complete ethylene oxidation in the presence and absence of oxygen in the gas feed. Kinetics of C_2H_4 oxidation over Ru/YSZ nanoparticles was investigated under fuel lean conditions with different partial pressures of ethylene and oxygen. Catalytic activity results in Chapter 7 showed that Ru and Pt were highly active for C_2H_4 oxidation emphasizing strong metal-support interaction when they were both deposited on ionic and mixed ionic conductive supports.

- **Novel perovskite group was studied as catalysts and as supports for platinum for carbon monoxide and ethylene oxidation.** The results shows strong metal-support interaction resulted in the lowest activation energies reported in literature for both reactions. This perovskite group has higher ionic conductivity at low temperatures compared to other ionic conductors as presented in Chapter 8. The effect of cerium doping on the ionic conductivity and the catalytic activity was discussed. Moreover, the addition of 1 wt. % platinum as a metal supported on these perovskites further enhanced their catalytic activity towards pollutants oxidation.

- **Effect of platinum particle size deposited on YSZ was studied for hydrogen gas purification for fuel cells application.** The removal of 60 % of 1000 ppm carbon monoxide from hydrogen stream was achieved at temperatures below 100^{o}C in the absence of oxygen in the gas feed which was not investigated before. The impact of this study is of great interest for 2 reasons: first, it is highly recommended that oxygen concentration is reduced and preferably eliminated to avoid the side reaction of hydrogen oxidation and loss in fuel cell applications. Secondly, the operation of fuel cells at low temperatures is of great importance to avoid the water reverse gas shift reaction from taking place at elevated temperatures. Moreover, the effect of Pt/YSZ particle sizes was investigates and the results showed that CO methanation is a strongly-size sensitive reaction.

- **Evidence of strong-metal support interaction as nanoparticle size decreases.** The effect of particle size is clear in the work presented in Chapter 5, 10 and 11. It is concluded that as the particle size decreases, stronger metal-support interaction is induced. The conclusions were supported by several characterization and catalytic activity measurements and are in agreement with previous studies on other catalysts.

12.4 Publications and contributions

The work performed in this thesis resulted in the publication of 4 articles in peer-reviewed journals whose manuscripts are included here as Chapters 5, 6, 7 and 9, one conference transaction paper, two submitted manuscripts (Chapter 8 and 10), a lab manual for nanoparticle synthesis and several conference presentations as detailed in Appendix C. Two other manuscripts (Chapters 11 and one related to propylene oxidation, not shown here) will be submitted soon for publication.

12.5 Recommendations and future work

- Further investigation is required to understand metal-support interaction such as the effect of creating defects on the catalyst surface for better interaction with the support and hence, to improve its activity and stability. Mechanical stability and adhesion of the nanoparticles onto the support surface can be another topic to investigate. It is expected that surface modification of the supports can provide sufficient binding sites to anchor precursor metal ions or metal nanoparticles (during the catalyst preparation process) and hence, enhance the catalyst dispersion and prevents agglomeration or particle loss. Steam itching of support surfaces to modify surface morphology and active sites is one of the methods that could be used for this purpose [1].

- The novel application of self-induced EPOC in oxygen-free environment can be further investigated over other ionic conductive or mixed ionic conductive supports not studied in this research. Moreover, this phenomenon can be utilized to electrooxidize other compounds. Meanwhile, propylene oxidation and electrooxidation is being investigated in our lab as one of the main exhaust emission pollutants and as a larger VOC molecule to compare our catalysts

activity with the results obtained for carbon monoxide and ethylene oxidation and electrooxidation.

- It would be interesting to study the effect of further lowering the noble metal content by adding a non precious metal in different proportions and investigate their activity under similar conditions. Other structural configurations can be suggested to investigate the effect of adding another metal to the main active one such as the use of core/shell configuration [2].

- One of the main applications in which these active catalysts can be utilized is for nitrogen oxide reduction. Nitrogen oxides being one of the main pollutants in diesel automotive exhaust emissions should be reduced over the nanocatalysts and studied under different metal combinations [3].

- To investigate the possibility of commercialization, we should be able to obtain nanocatalysts with desired morphology as well as desired properties, such as high activity and high selectivity, in large-volume production and in a low-cost manner, therefore, computer-aided programs to simulate the nanocatalyst synthesis and predicted activity can be utilized.

12.6 References

[1] M. Wang, F. Xu, Q. Liu, H. Sun, R. Cheng, H. He, E. A. Stach, J. Xie, *Carbon.* 49 (2011) 256.

[2] Q. Zhang, Y. Yin, *Pure Appl. Chem.* 86 (2014) 53.

[3] B. Patel, K. Patel, *Int. J. Appl. Eng. Res.* 7 (2012) 1.

SECTION VII: APPENDICES

Appendix A: Supplementary information for Chapter 8

Platinum nanoparticles supported on $SmFeO_3$ perovskite group for carbon monoxide and ethylene oxidation

Figure A-1 shows CO and ethylene conversion as a function of temperature of blank supports for complete oxidation of 909 ppm (a) CO, (b) C_2H_4, 3.5% O_2, balance He in terms of conversion vs. temperature.

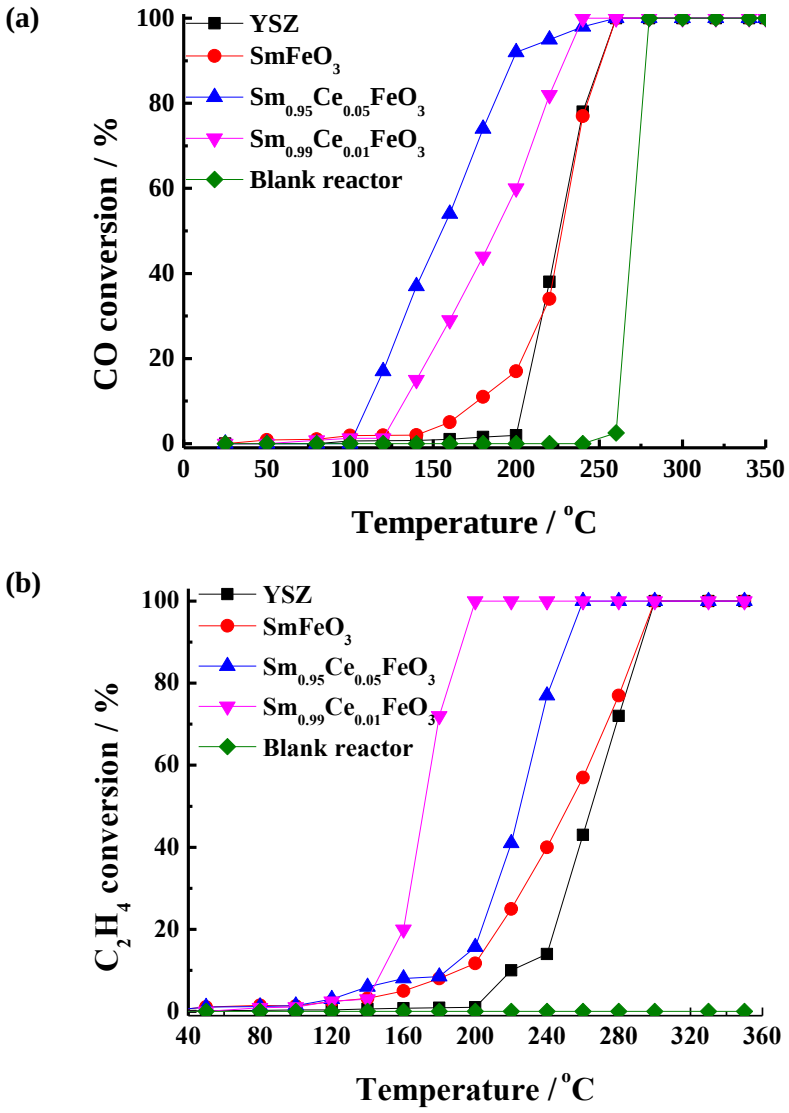

Figure A-1: Conversion of CO (a) and C_2H_4 (b) as a function of temperature on various materials as indicated in the figure.

Figure A-2 shows the conversion as a function of temperature of supported Pt nanoparticles for complete oxidation of 909ppm (a) CO, (b) C_2H_4, 3.5% O_2, balance He in terms of conversion vs. temperature.

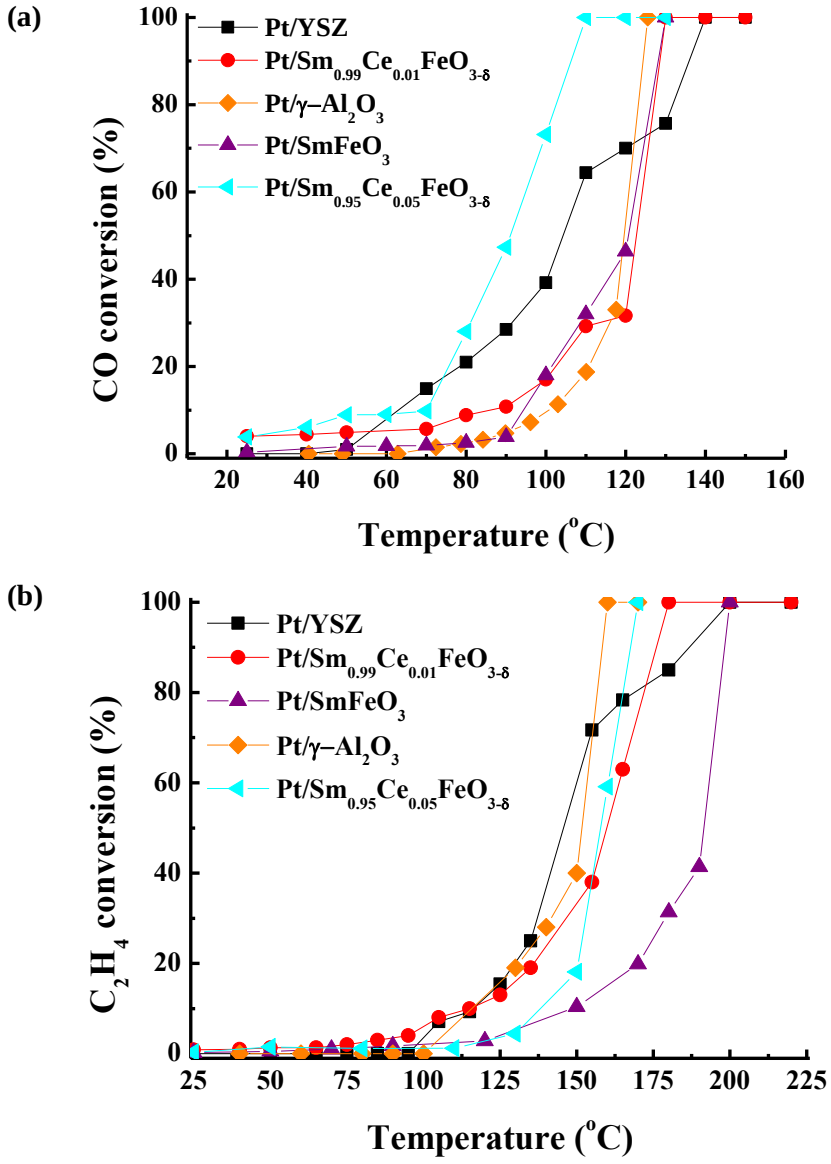

Figure A-2: Conversion of CO (a) and C_2H_4 (b) as a function of temperature over Pt nanoparticles supported on various materials as indicated in the figure.

Mass and Heat Transfer limitation calculations for Carbon Monoxide and ethylene oxidation over Pt/YSZ, Pt/SCF-0, Pt/SCF-1, Pt/SCF-5 and Pt/γ-Al_2O_3

Assume all nanoparticles are spherical, non porous and uniform in shape with the average particle sizes deducted from ADF-STEMs as per Table 8-1 page 133.

All reaction rates are calculated based on the maximum rate at the highest temperature in each run at which high conversions are achieved within the temperature range of experiments

1- Weiss-Prater Criterion for Internal Mass Diffusion (Fouler, p839)

If $C_{WP} = \frac{-r'_{A(obs)} \rho_c R^2}{D_e C_{As}} < 1$, then internal mass transfer effects can be neglected.

$-r'_{A(obs)}$ = observed reaction rate, kmol/kg-cat · s

R = catalyst particle radius, m

ρ_c = solid catalyst density, kg/m^3; [ρ_c, for Pt = 21090 kg/m^3]

D_e = effective gas-phase diffusivity, m^2/s **[Fogler, p815]**

$= \frac{D_{AB}\phi_p\sigma_c}{\tau}$ where

D_{AB} = gas-phase diffusivity m^2/s; D_{AB}= 2.03×10^{-9} m^2/s for CO and 1.87×10^{-9} m^2/s for C_2H_4 **[Cussler, E. L. (1997). Diffusion: Mass Transfer in Fluid Systems (2nd ed.). New York: Cambridge University Press]**

ϕ_p = pellet porosity; σ_c =constriction factor; τ =tortuosity, all assumed to be unity for nonporous, uniform spherical nanoparticles.

C_{As} = gas concentration of A at the catalyst surface, = 0.00003 kmol CO/m^3 and 0.00003 kmol C_2H_4/m^3

Pt/YSZ, R =(2.9/2) nm =1.45nm for CO oxidation

$C_{WP} = \frac{-r'_{A(obs)} \rho_c R^2}{D_e C_{As}}$=[9.03 × 10^{-5} kmol-CO/kg-cat . s] × [2.109×10^4 kg-cat/m^3] × [1.45 × 10^{-9} m]^2 / ([2.03 × 10^{-9} m^2/s] × [0.00003 kmol-CO/m^3]) = **6.58× 10^{-5} << 1**

Pt/YSZ, R =(2.9/2) nm =1.45 nm for C_2H_4 oxidation

$$C_{WP} = \frac{-r'_{A(obs)}\rho_c R^2}{D_e C_{As}} = [9.17 \times 10^{-5} \text{ kmol-}C_2H_4\text{/kg-cat . s}] \times [2.109\times10^4 \text{ kg-cat/m}^3] \times [1.45 \times 10^{-9} \text{ m}]^2 / ([1.87 \times 10^{-9} \text{ m}^2\text{/s}] \times [0.00003 \text{ kmol-}C_2H_4\text{/m}^3]) = \mathbf{7.25\times 10^{-5} << 1}$$

Similar calculations were performed to the rest of the catalysts and summary of results are in the following tables:

Table A-1: Weisz-Prater criterion for internal mass diffusion for CO and C_2H_4 oxidation.

Catalyst	R (nm)	C_{WP} for CO oxidation	C_{WP} for C_2H_4 oxidation
Pt/YSZ	1.45	6.58×10^{-5}	7.25×10^{-5}
Pt/Y-AL_2O_3	1.25	4.89×10^{-5}	5.39×10^{-5}
Pt/SCF-0	1.40	6.02×10^{-5}	6.63×10^{-5}
Pt/SCF-1	1.60	7.57×10^{-5}	8.35×10^{-5}
Pt/SCF-5	1.50	6.91×10^{-5}	7.61×10^{-5}

2- Weisz-Hicks Criterion for Intraparticle mass and heat transfer Diffusion [Weisz-Hicks 1962 and Mears 1971]

$$\varphi = \frac{-r'_A \rho_c R^2}{C_A D_e} \exp\frac{\gamma\beta}{(1+\beta)} = C_{WP} \exp\frac{\gamma\beta}{(1+\beta)} \quad <1$$

$$\gamma = \frac{E_a}{R_g T}; \quad \beta = \frac{(-\Delta H_r) D_e C_A}{kT};$$

Ea: activation energy , J/mol

R_g: gas constant= 8.314 J/mol·K

T: preferably maximum temperature at which high reaction rates are observed, K

ΔH_r: heat of reaction= -283×10^3 J/mol for CO combustion and -1411 kJ/mol for ethylene combustion

k: catalyst thermal conductivity

Pt/YSZ for CO oxidation

Ea = 35.8 kJ/mol

$T_{max} = T_{100} = 140^{o}C = 413K$

$\gamma = 35.8\times10^{3}$ J/mol /[8.314 J/mol.K × 413 K] =10.4

$\beta = [-283\times10^{3}$ J/mol × 2.03 $x10^{-9}$ $m^2/s \times 0.03$ mol/m^3]/[70 J/m.s.K × 413K] = -6.0×10^{-10}

$\varphi = 6.58\times 10^{-5} \times (0.99) = 6.56\times10^{-5} << 1$

Table A-2: Weisz-Hicks Criterion for intraparticle mass and heat transfer Diffusion for CO oxidation.

Catalyst	**R (nm)**	**C_{WP}**	**T_{max} (K)**	**Ea kJ/mol**	**γ**	**β**	**φ**
Pt/YSZ	1.45	6.58×10^{-5}	413	35.8	10.4	-6.0×10^{-10}	6.56×10^{-5}
Pt/Y-AL_2O_3	1.25	4.89×10^{-5}	398	57.1	17.3	-6.2×10^{-10}	4.87×10^{-5}
Pt/SCF-0	1.40	6.02×10^{-5}	403	42.4	12.7	-6.1×10^{-10}	6.01×10^{-5}
Pt/SCF-1	1.60	7.57×10^{-5}	403	33.2	9.9	-6.1×10^{-10}	7.56×10^{-5}
Pt/SCF-5	1.50	6.91×10^{-5}	383	25.7	8.1	-6.4×10^{-10}	6.90×10^{-5}

Pt/YSZ for C_2H_4 oxidation

Ea = 22 kJ/mol

$T_{max} = T_{100} = 200^{o}C = 473K$

$\gamma = 22\times10^{3}$ J/mol /[8.314 J/mol.K × 473 K] =5.59

$\beta = [-1411\times10^{3}$ J/mol × 1.87 $\times10^{-9}$ $m^2/s \times 0.03$ mol/m^3]/[70 J/m.s.K × 473K] = -2.39×10^{-9}

$\varphi = 7.25\times 10^{-5} \times (0.99) = 7.24\times10^{-5} << 1.$

Table A-3: Weisz-Hicks Criterion for intraparticle mass and heat transfer Diffusion for C_2H_4 oxidation.

Catalyst	R (nm)	C_{WP}	T_{max} (K)	Ea kJ/mol	γ	B	φ
Pt/YSZ	1.45	7.25×10^{-5}	473	22.0	5.59	-2.4×10^{-9}	7.24×10^{-5}
Pt/Y-AL_2O_3	1.25	5.39×10^{-5}	433	32.0	8.88	-2.6×10^{-9}	5.38×10^{-5}
Pt/SCF-0	1.40	6.63×10^{-5}	473	34.1	8.67	-2.4×10^{-9}	6.62×10^{-5}
Pt/SCF-1	1.60	8.35×10^{-5}	453	18.3	4.85	-2.5×10^{-9}	8.34×10^{-6}
Pt/SCF-5	1.50	7.61×10^{-5}	443	20.5	5.56	-2.6×10^{-10}	7.60×10^{-5}

All values obtained in Table A1- Table A3 are far less than unity which indicates the absence of internal mass and heat-transfer resistances.

Appendix B: Supplementary information for Chapter 10

Size-dependent activity of Pt/yttria-stabilized zirconia catalyst for wireless electrooxidation of ethylene and carbon monoxide in oxygen free environment

Figure B-1 presents the spatially-resolved energy dispersive X-ray spectroscopy (EDX) analysis for Pt/YSZ-2. The EDX spectra 1 and 2 were acquired at the locations labeled on the ADF-STEM image. Peaks for Y, Zr and O are present on both spectra. The Cu peak is an artifact corresponding to spurious X-rays originating from the TEM grid. Around 2 keV, the peaks associated with Zr, Y and Pt overlaps, and the elemental analysis is less straight forward. However, the Pt L_α and L_β peaks at around 9.5 and 11 keV appear clearly on spectrum 1, whereas they are absent on spectrum 2. This observation confirms that the nanometer-sized bright features observed on the ADF-STEM image correspond to Pt catalyst supported on the YSZ substrate.

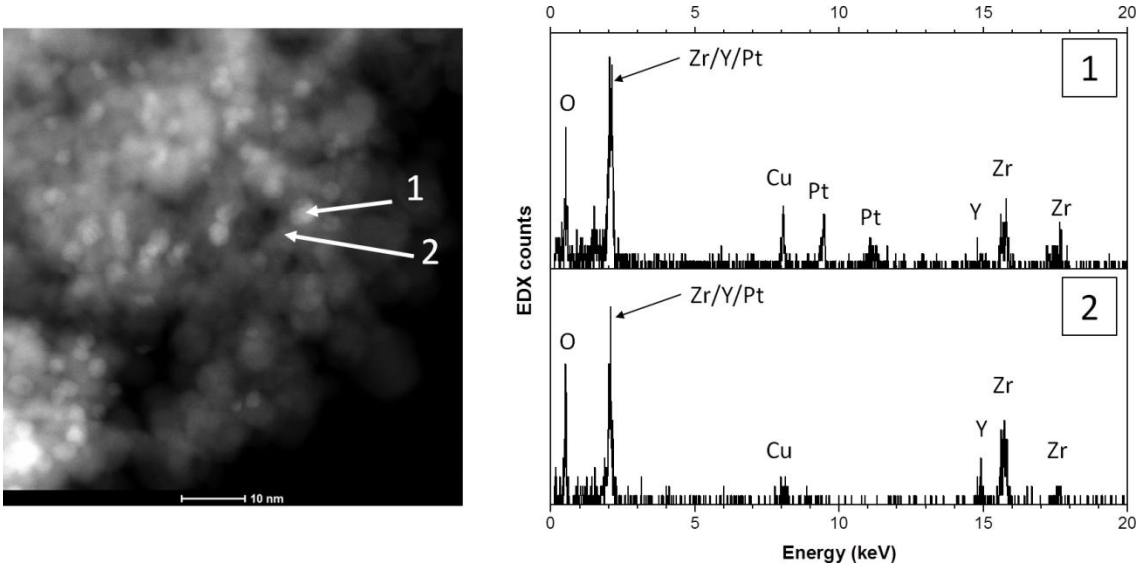

Figure B-1: EDX spectra of Pt/YSZ-2 (4.4 nm).

Figure B-2 is a representative light-off curve of the smallest nanoparticles Pt/YSZ-4. To insure the reproducibility of the experimental results, each run was repeated for three

times. The second cycle is the forward scan with increasing temperature; the third cycle is the backward or reverse scan with decreasing temperature.

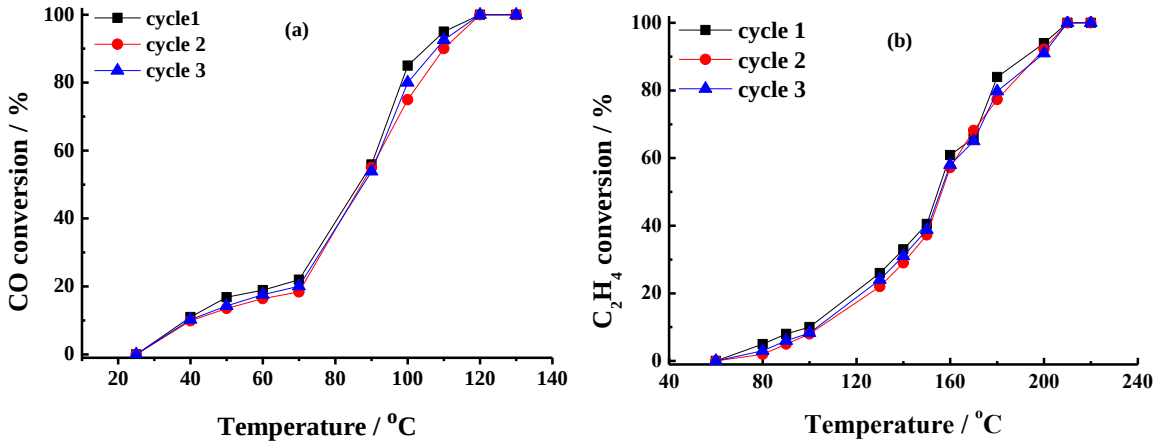

Figure B-2: Conversion vs. temperature of Pt/YSZ-4 for the electrochemical oxidation of (a) CO and (b) C_2H_4. Space velocity = 14688 h^{-1}, total flowrate = 4.62 $L \cdot h^{-1}$, [CO or C_2H_4] = 909 ppm, He balance, no O_2 in the gas feed.

Figure B-3 shows the effect of the particle size of the four catalysts for CO and C_2H_4 electrooxidation in terms of conversion as function of temperature.

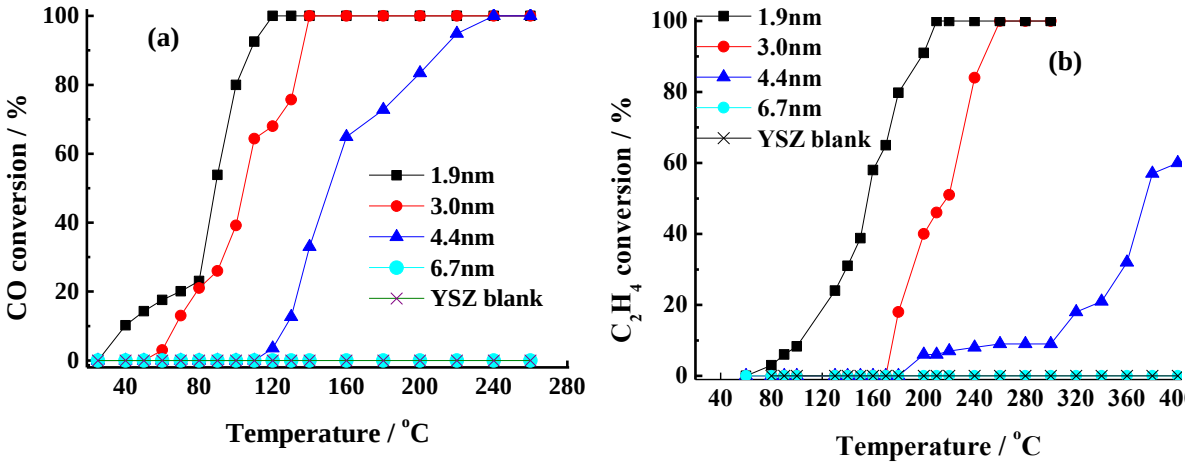

Figure B-3: Light-off curves of the effect of Pt/YSZ particle size on (a) CO and (b) C_2H_4 oxidation in the absence of O_2 in the gas phase. Space velocity = 14688 h^{-1}, total flowrate = 4.62 $L \cdot h^{-1}$, [CO or C_2H_4] = 909 ppm, He balance, no O_2 in the gas feed.

Figure B-4 shows the light-off curves for YSZ blank with oxygen (closed blue circles) and without oxygen (open blue circles) for CO and C_2H_4 oxidation and electrooxidation,

respectively. YSZ shows catalytic activity for CO and C_2H_4 oxidation at temperatures higher than 200°C in the presence of 3.5 kPa oxygen in the gas feed, while it shows no catalytic activity for CO and C_2H_4 oxidation in the absence of oxygen in the gas feed.

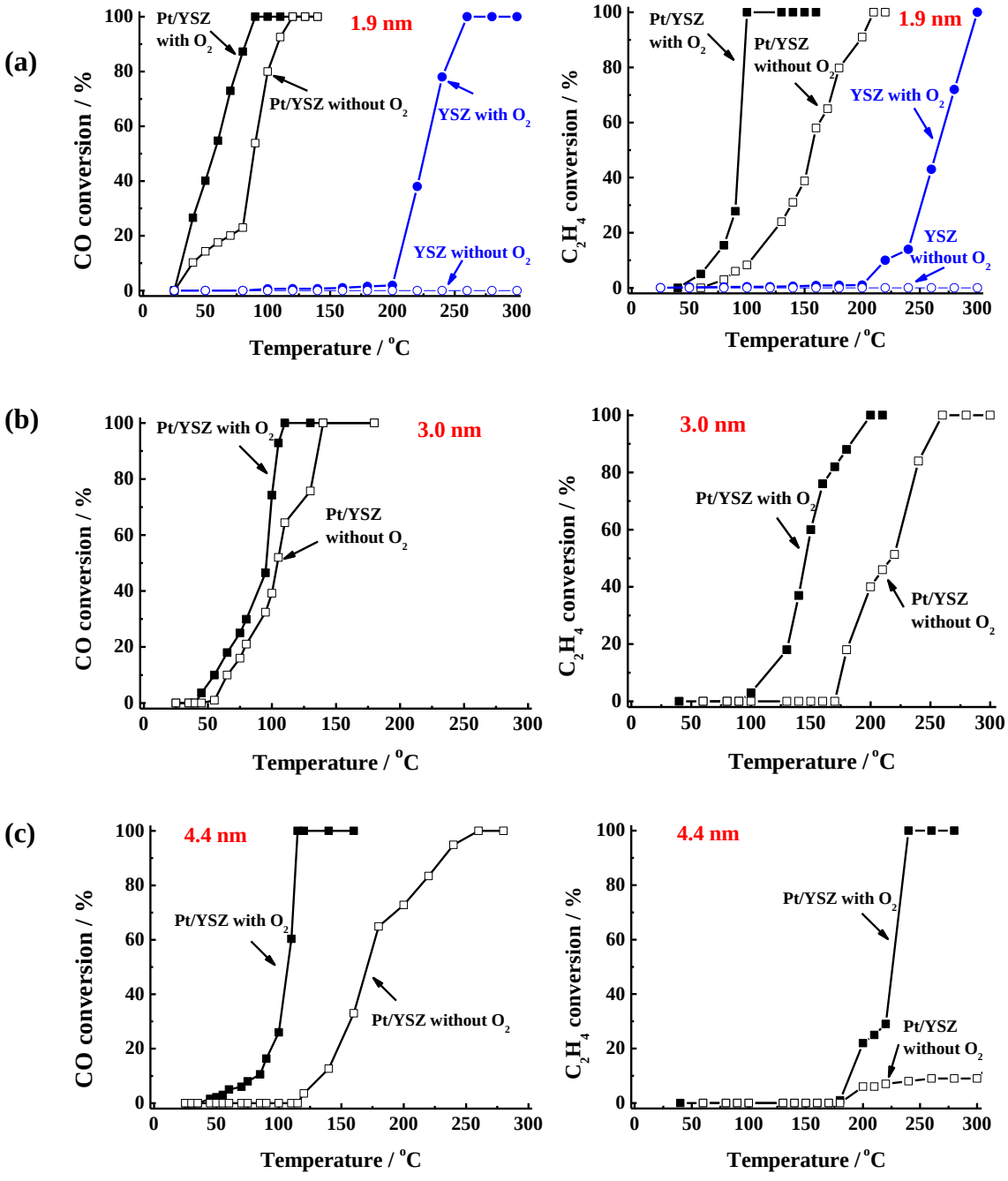

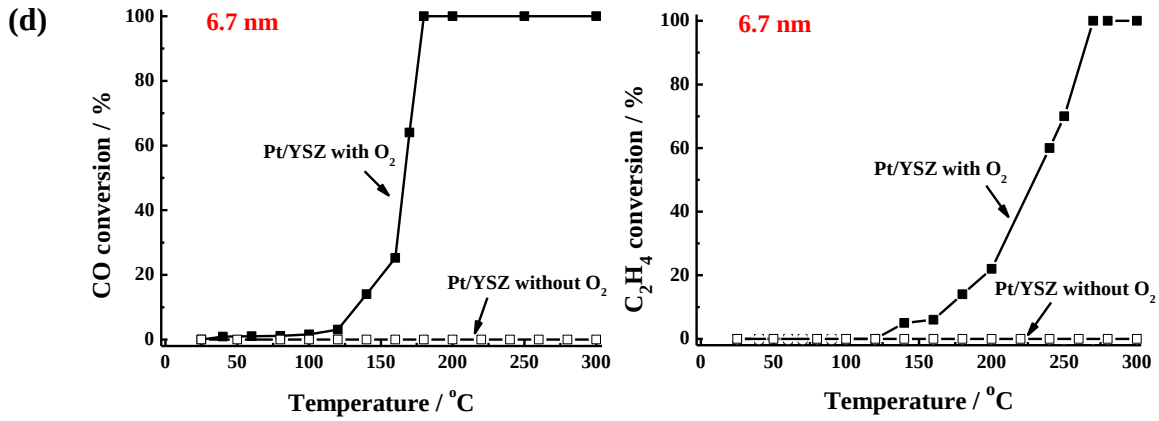

Figure B-4: Conversion of CO (left) and C_2H_4 (right) as a function of temperature on Pt/YSZ catalysts of various average sizes: (a) 1.9 nm (b) 3.0 nm, (c) 4.4 nm and (d) 6.7 nm. Curves labeling: (—●—) YSZ with 3.5 kPa O_2; (—○—) YSZ without O_2; (—■—) Pt/YSZ with 3.5 kPa O_2 and (—□—) Pt/YSZ without O_2.

Mass and Heat Transfer limitation calculations for Carbon Monoxide and ethylene oxidation and electrooxidation over Pt/YSZ-1, Pt/YSZ-2, Pt/YSZ-3 and Pt/YSZ-4

Assume all nanoparticles are spherical, non porous and uniform in shape with the average particle sizes deducted from ADF-STEMs as per Table 10-1 page 170.

All reaction rates are calculated based on the maximum rate at the highest temperature in each run at which high conversions are achieved within the temperature range of experiments

1- Weisz-Prater Criterion for Internal Mass Diffusion (Fogler, p839)

If $C_{WP} = \dfrac{-r'_{A(obs)}\,\rho_c R^2}{D_e C_{As}} < 1$, then internal mass transfer effects can be neglected.

$-r'_{A(obs)}$ = observed reaction rate, kmol/kg-cat·s

R = catalyst particle radius, m

ρ_c = solid catalyst density, kg/m^3; [ρ_c, for Pt = 21090 kg/m^3]

D_e = effective gas-phase diffusivity, m^2/s **[Fogler, p815]**

$= \dfrac{D_{AB}\phi_p\sigma_c}{\tau}$ where

D_{AB} = gas-phase diffusivity m^2/s; D_{AB}= 2.03×10^{-9} m^2/s for CO and 1.87×10^{-9} m^2/s for C_2H_4 **[Cussler, E. L. (1997). Diffusion: Mass Transfer in Fluid Systems (2nd ed.). New York: Cambridge University Press]**

ϕ_p = pellet porosity; σ_c =constriction factor; τ =tortuosity, all assumed to be unity for uniform spherical nonporous nanoparticles.

C_{As} = gas concentration of A at the catalyst surface, = 0.00003 kmol CO/m^3 and 0.00003 kmol C_2H_4/m^3

Pt/YSZ-4, R =(1.9/2) nm =0.95 nm for CO oxidation

$$C_{WP} = \frac{-r'_{A(obs)}\rho_c R^2}{D_e C_{As}} = ([9.0 \times 10^{-5} \text{ kmol-CO/kg-cat . s}]\times[\ 2.109\times10^4 \text{ kg-cat/m}^3] \times [\ 0.95 \times 10^{-9} \text{ m}]^2)/ ([2.03 \text{ x } 10^{-9} \text{ m}^2/\text{s}] \times [0.00003 \text{ kmol-CO/m}^3]) = \mathbf{2.8}\times \mathbf{10^{-5}} << \mathbf{1}$$

Pt/YSZ-4, R =(1.9/2) nm =0.95nm for C_2H_4 oxidation

$$C_{WP} = \frac{-r'_{A(obs)}\rho_c R^2}{D_e C_{As}} = [9.5 \times 10^{-5} \text{ kmol-}C_2H_4\text{/kg-cat . s}]\times[\ 2.109\times10^4 \text{ kg-cat/m}^3] \times [\ 0.95 \text{ x } 10^{-9} \text{ m}]^2 / ([1.87 \times 10^{-9} \text{ m}^2/\text{s}] \times [0.00003 \text{ kmol-}C_2H_4/\text{m}^3]) = \mathbf{3.2}\times \mathbf{10^{-5}} << \mathbf{1}$$

Similar calculations were performed to the rest of the catalysts and summary of results are in the following tables:

Table B-1: List of Weisz-Prater criterion for internal mass diffusion for CO oxidation and electrooxidation.

Catalyst	R (nm)	r_A for CO oxidation at T_{max} (mol/Kg cat.s)	C_{WP} for CO oxidation	r_A for CO electrooxidation at T_{max} (mol/Kg cat.s)	C_{WP} for CO electrooxidation
Pt/YSZ-1	3.35	7.4×10^{-5}	2.9×10^{-4}	NA	NA
Pt/YSZ-2	2.20	8.6×10^{-5}	1.4×10^{-4}	5.5×10^{-5}	9.2×10^{-4}
Pt/YSZ-3	1.50	8.9×10^{-5}	6.9×10^{-5}	8.2×10^{-5}	6.3×10^{-5}
Pt/YSZ-4	0.95	9.0×10^{-5}	2.8×10^{-5}	8.3×10^{-5}	2.6×10^{-5}

Table B-2: List of Weisz-Prater criterion for internal mass diffusion for C_2H_4 oxidation and electrooxidation.

Catalyst	R (nm)	r_A for C_2H_4 oxidation at T_{max} (mol/Kg cat.s)	C_{WP} for C_2H_4 oxidation	r_A for C_2H_4 electrooxidation at T_{max} (mol/Kg cat.s)	C_{WP} for C_2H_4 electrooxidation
Pt/YSZ-1	3.35	5.1×10^{-6}	8.0×10^{-5}	NA	NA
Pt/YSZ-2	2.20	9.4×10^{-5}	3.4×10^{-5}	4.9×10^{-5}	8.9×10^{-5}
Pt/YSZ-3	1.50	9.5×10^{-5}	1.6×10^{-5}	8.0×10^{-5}	6.8×10^{-5}
Pt/YSZ-4	0.95	9.5×10^{-5}	6.4×10^{-6}	8.9×10^{-5}	3.2×10^{-5}

2- Weisz-Hicks Criterion for Intraparticle mass and heat transfer Diffusion [Weisz-Hicks 1962 and Mears 1971]

$$\varphi = \frac{-r'_A \rho_c R^2}{C_A D_e} \exp\frac{\gamma\beta}{(1+\beta)} = C_{WP} \exp\frac{\gamma\beta}{(1+\beta)} \quad <1$$

$$\gamma = \frac{E_a}{R_g T}; \quad \beta = \frac{(-\Delta H_r) D_e C_A}{kT};$$

Ea: activation energy , J/mol

R_g: gas constant= 8.314 J/mol.K

T: preferably maximum temperature at which high reaction rates are observed, K

ΔH_r : heat of reaction = -283×10^3 J/mol for CO combustion and -1411 kJ/mol for ethylene combustion

k: catalyst thermal conductivity

Pt/YSZ-4 for CO oxidation

Ea = 31.1 kJ/mol

$T_{max} = T_{100} = 90^oC = 363K$

$\gamma = 31.3\times10^3$ J/mol /[8.314 J/mol.K × 363 K] =10.3

$\beta = [-283\times10^{3}\ J/mol \times 2.03\ x10^{-9}\ m^2/s \times 0.03\ mol/m^3]/[70\ J/m\cdot s\cdot K \times 363K] = -6.78\times10^{-10}$

$\varphi = 2.8\times 10^{-5} \times (0.99) = 2.7\times10^{-5} << 1$

Table B-3: List of Weisz-Hicks criterion for intraparticle mass and heat transfer diffusion for CO oxidation.

Catalyst	R (nm)	C_{WP}	T_{max} (K)	Ea kJ/mol	γ	β	φ
Pt/YSZ-1	3.35	2.9×10^{-4}	453	52.9	14.0	-5.4×10^{-10}	2.8×10^{-4}
Pt/YSZ-2	2.20	1.4×10^{-4}	388	47.4	14.7	-6.3×10^{-10}	1.3×10^{-4}
Pt/YSZ-3	1.50	6.9×10^{-5}	383	48.2	15.1	-6.4×10^{-10}	6.8×10^{-5}
Pt/YSZ-4	0.95	2.8×10^{-5}	363	31.3	10.3	-6.7×10^{-10}	2.7×10^{-5}

Pt/YSZ-4 for CO electrooxidation

Ea = 31.1 kJ/mol

$T_{max} = T_{100} = 90^{o}C = 363K$

$\gamma = 31.3\times10^{3}\ J/mol\ /[8.314\ J/mol\cdot K \times 363\ K] = 10.3$

$\beta = [-283\times10^{3}\ J/mol \times 2.03 \times10^{-9}\ m^2/s \times 0.03\ mol/m^3]/[70\ J/m.s.K \times 363K] = -6.78\times10^{-10}$

$\varphi = 2.8\times 10^{-5} \times (0.99) = 2.7\times10^{-5} << 1$

Table B-4: List of Weisz-Hicks criterion for intraparticle mass and heat transfer diffusion for CO electrooxidation.

Catalyst	R (nm)	C_{WP}	T_{max} (K)	Ea kJ/mol	γ	B	φ
Pt/YSZ-1	3.35	NA	NA	NA	NA	NA	NA
Pt/YSZ-2	2.20	9.2×10^{-4}	388	47.4	14.7	-6.3×10^{-10}	9.2×10^{-4}
Pt/YSZ-3	1.50	6.3×10^{-5}	383	48.2	15.1	-6.4×10^{-10}	6.2×10^{-5}
Pt/YSZ-4	0.95	2.6×10^{-5}	363	31.3	10.3	-6.7×10^{-10}	2.5×10^{-5}

Pt/YSZ-4 for C_2H_4 oxidation

Ea = 9.1 kJ/mol

$T_{max} = T_{100} = 100^{o}C = 373K$

$\gamma = 9.1\times10^{3}$ J/mol /[8.314 J/mol·K × 373 K] =2.9

$\beta = [-1411\times10^{3}$ J/mol × 1.87×10^{-9} $m^2/s \times 0.03$ mol/m^3]/[70 J/m·s·K × 373K] = -3.03×10^{-9}

$\varphi = 6.4\times10^{-6} \times (0.99) = 6.3\times10^{-6} << 1$

Table B-5: List of Weisz-Hicks criterion for intraparticle mass and heat transfer diffusion for C_2H_4 oxidation.

Catalyst	R (nm)	C_{WP}	T_{max} (K)	Ea kJ/mol	γ	β	φ
Pt/YSZ-1	3.35	8.0×10^{-5}	543	45.7	10.1	-2.0×10^{-9}	7.9×10^{-5}
Pt/YSZ-2	2.20	3.4×10^{-5}	513	42.4	9.9	-2.1×10^{-9}	3.3×10^{-5}
Pt/YSZ-3	1.50	1.6×10^{-5}	473	22	5.6	-2.3×10^{-9}	1.5×10^{-5}
Pt/YSZ-4	0.95	6.4×10^{-6}	373	9.1	2.9	-3.0×10^{-9}	6.3×10^{-6}

Pt/YSZ-4 for C_2H_4 electrooxidation

Ea = 12.5 kJ/mol

$T_{max} = T_{100} = 210^{o}C = 483K$

$\gamma = 12.5\times10^{3}$ J/mol /[8.314 J/mol·K × 483 K] =3.1

$\beta = [-1411\times10^{3}$ J/mol × 1.87×10^{-9} $m^2/s \times 0.03$ mol/m^3]/[70 J/m·s·K × 483K]= -2.3×10^{-9}

$\varphi = 3.2\times10^{-5} \times (0.99) = 2.7\times10^{-5} << 1$

Table B-6: List of Weisz-Hicks criterion for intraparticle mass and heat transfer diffusion for C_2H_4 electrooxidation.

Catalyst	R (nm)	C_{WP}	T_{max} (K)	Ea kJ/mol	γ	β	φ
Pt/YSZ-1	3.35	NA	NA	NA	NA	NA	NA
Pt/YSZ-2	2.20	8.9×10^{-5}	673	38.4	6.9	-1.6×10^{-9}	8.8×10^{-5}
Pt/YSZ-3	1.50	6.8×10^{-5}	533	30.7	6.9	-2.1×10^{-9}	6.7×10^{-5}
Pt/YSZ-4	0.95	3.2×10^{-5}	483	12.5	3.1	-2.3×10^{-9}	3.1×10^{-5}

All values obtained in Table B-1 to Table B-6 are far less than unity which indicates the absence of internal mass and heat-transfer resistances.

To insure that the catalyst temperature does not vary at the time of measurement, the temperature of the catalyst bed was held for 30 minutes to reach steady state before taking measurements, each measurement was repeated for 3 times to check stability, the total time of the 3 measurement is about 12-15 another minutes.

Three- phase boundary calculations of Pt/YSZ-1, Pt/YSZ-2, Pt/YSZ-3 and Pt/YSZ-4

Assume all nanoparticles are spherical and uniform in shape with the average particle sizes deducted from ADF-STEMs as per Table 10-1 page 170.

Calculation sample for Pt/YSZ-4:

Known parameters:

dp= 1.9 nm

dispersion= 51.8%

density of metal (Pt) = 21.09 $g \cdot cm^{-3}$

metal loading = 0.9%

mass of catalyst= 0.0525 g

Calculations:

mass of one particle = volume × density

$$Volume = \frac{4\pi D^3}{24}$$

$$Mass = \left(21.09 \frac{g}{cm^3} \times \frac{10^6 cm^3}{m^3} \right) \left(\frac{4\pi \left(1.9 \times 10^{-9} m\right)^3}{24} \right) = 7.57 \times 10^{-20} g$$

Active mass of surface metals = mass of catalyst × metal loading × dispersion

$$=0.0525 \times 0.009 \times 0.518 = 2.44 \times 10^{-4} \text{ g}$$

Number of surface particles = mass of all surface metals/ mass of one particle

$$= 2.44 \times 10^{-4} / 7.57 \times 10^{-20} = 3.23 \times 10^{-15} \text{ particles}$$

length of three phase boundary = circumference of one spherical particle x number of surface particles

$$= \pi \, d_p \times \text{number of surface particles}$$

$$= 3.14 \times 1.9 \times 10^{-9} \times 3.23 \times 10^{15} = 19.3 \times 10^{6} \text{ m}$$

Appendix C: Scholarly contributions

C.1 Refereed journal articles (published, accepted or submitted)

[1] **R. J. Isaifan,** E. A. Baranova, "Effect of ionically conductive supports on the catalytic activity of platinum and ruthenium nanoparticles for ethylene complete oxidation", *Catalysis Today* (2014) CATTOD-S-14-00030 (in press).

[2] S. Ntais, **R. J. Isaifan**, E. A. Baranova, "An X-ray photoelectron spectroscopy study of platinum nanoparticles on yttria-stabilized zirconia ionic support: Insight into metal support interaction", Accepted at the *Journal of Physical Chemistry* (2014) jp-2014-02113b.

[3] **R. J. Isaifan,** S. Ntais, E. A. Baranova, "Particle size effect on catalytic activity of carbon-supported Pt nanoparticles for complete ethylene oxidation", *Applied Catalysis A: General* 464 - 465 (2013) 87- 94.

[4] **R. J. Isaifan**, E. A. Baranova, "Catalytic electrooxidation of volatile organic compounds by oxygen-ion conducting ceramics in oxygen-free gas environment", *Electrochemistry Communications* 27 (2013) 164-167.

[5] H. Dole, **R. J. Isaifan**, F. M. Sapountzi, L. Lizarraga, D. Aubert, A. Princivalle, P. Vernoux, E. A. Baranova, "Low temperature toluene oxidation over Pt nanoparticles supported on yttria stabilized-zirconia", *Catalysis Letters* 143 (2013) 996-1002.

[6] **R. J. Isaifan,** H. Dole, E. Obeid, L. Lizarraga, P. Vernoux, E. A. Baranova, "Metal-support interaction of Pt nanoparticles with ionically and non-ionically conductive supports for CO oxidation", *Electrochemical and Solid State Lett*ers 15 (3) (2012) E14-E17.

[7] **R. J. Isaifan,** S. Ntais, M. Couillard, E. A. Baranova, "Size-dependent activity of Pt/yttria-stabilized zirconia catalyst for wireless electrooxidation of ethylene and carbon monoxide in oxygen free environment", submitted to the *Journal of Catalysis* (2014) JCAT-14-609.

[8] **R. J. Isaifan**, William D. Penwell, Joao O. C. Filizzola, Javier B. Giorgi, E. A. Baranova, "Platinum nanoparticles supported on $SmFeO_3$ novel perovskite group for carbon monoxide and ethylene oxidation", submitted to the *Journal of Applied Catalysis B* (2014) APCATB-S-14-02169.

[9] **R. J. Isaifan,** M. Couillard, E. A. Baranova," Particle size effect of Pt/yttria-stabilized zirconia on carbon monoxide methanation and preferential electrooxidation for hydrogen gas purification at low temperatures", to be submitted soon to the Journal of Power Sources.

C.2 Refereed journal transactions

[10] **R. J. Isaifan**, H. Dole, E. Obeid, L. Lizarraga, E. A. Baranova, P. Vernoux, "Catalytic Carbon Monoxide Oxidation over Size-Controlled Pt Nanoparticles in the Gas Phase and Elevated Temperatures", *ECS Transactions* 35 (28) (2011) 43.

C.3 Conference oral presentations

** presenting author*

[11] **R. J. Isaifan**, E. A. Baranova*, "Ionically and non-ionically conductive supports for ethylene complete oxidation over Pt and Ru nanoparticles", *The 11th European Congress on Catalysis-EuropaCat-XI*, Lyon, France, **2013**.

[12] M. Lortie, S. Ntais, **R. J. Isaifan,** E. A. Baranova*, "Reverse water gas shift reaction over Pt nanoparticles supported on oxygen ion conductive ceramics", *Electrochemical Society Conference*, San Francisco, USA, **2013**.

[13] S. Ntais, **R. J. Isaifan**, Elena A. Baranova*, "XPS studies of yttria-stabilized zirconia interfaced with Pt nanoparticles for carbon monoxide and ethylene electrooxidation", *Electrochemical Society Conference*, San Francisco, USA, **2013**.

[14] **R. J. Isaifan**, S. Ntais, M. Couillard, E. A. Baranova*, "Carbon monoxide and ethylene electro-oxidation by Pt nanoparticles/yttria stabilized zirconia catalysts in oxygen-free gas environment: Effect of Pt particle size", *International Workshop for Ionically Conductive Ceramics for Catalysis*, Lyon, France, **2013**.

[15] **R. J. Isaifan** and E. A. Baranova*, "Self-induced electrochemical promotion of platinum nanoparticles deposited on ionically conductive supports for ethylene complete oxidation", *The 62nd Canadian Chemical Engineering Conference*, Vancouver, Canada, **2012**.

[16] E. A. Baranova*, H. A.Dole and **R. J. Isaifan**, "Electrochemical promotion of Au and Pt nanoparticles for oxidation of volatile organic compounds at low temperature", *The 3rd International Symposium on Surface Imaging / Spectroscopy at the Solid / Liquid Interface*, Cracow, Poland, **2012**.

[17] **R. J. Isaifan,** H. Dole*, M. Lortie and E. A. Baranova, "Ethylene oxidation over size controlled nanoparticles deposited on different supports", *The 7th International Conference on Environmental Catalysis*, Lyon, France, 2012.

[18] H. Dole*, **R. J. Isaifan**, L. Lizarraga, P. Vernoux, E. A. Baranova, "Toluene oxidation over size-controlled Pt nanoparticles deposited on ionically and non-ionically conductive supports", *ECS Conference*, Seattle, USA, 2012.

[19] **R. J. Isaifan*,** E. A. Baranova, "Self-induced Electrochemical Promotion of ruthenium and platinum nanoparticles deposited on yttria- stabilized zirconia for ethylene complete oxidation", *The 2nd ECS Symposium*, Montreal, Canada, 2012.

[20] E. A. Baranova, P. Vernoux*, L. Lizarraga, E. Obeid, **R. J. Isaifan,** H. Dole, "Catalytic carbon monoxide oxidation over size-controlled Pt nanoparticles in the gas phase and elevated temperatures", *The 219th Electrochemical Society Conference*, Montreal, Canada, 2011.

C.4 Written work

[21] **R. J. Isaifan*,** "Synthesis of well defined size and shape nanoparticle using modified polyol reduction method", **Laboratory Manual**, Laboratory of Electrochemical Engineering, Chemical Engineering Department, Faculty of Engineering, University of Ottawa, Canada, 2011.

C.5 Poster presentations

[22] **R.J. Isaifan***, E. A. Baranova, H. A. Dole, "Electrochemical promotion of platinum nanoparticles supported on yttria stabilized zirconia", *The Electrochemical Society Symposium*, Queens University, Kingston, Canada, 2011.

[23] **R.J. Isaifan***, E. A. Baranova, H. A. Dole, "Electrochemical promotion of platinum nanoparticles supported on yttria stabilized zirconia", *The Annual Meeting of the Center for Catalysis Research and Innovation (CCRI)*, University of Ottawa, Ottawa, Canada, 2011.

[24] João O. C. Filizzola*, **R. J. Isaifan**, W. Penwell, J. Georgi, E. A. Baranova, Platinum nanoparticles supported on novel perovskite materials for oxidation of CO and C_2H_4, Science without Borders Symposium, University of Ottawa, Canada, 2013.

[25] **R.J. Isaifan***, E. A. Baranova, H. A. Dole, "Electrochemical promotion of platinum nanoparticles supported on yttria stabilized zirconia", *The Annual Meeting of the Center for Catalysis Research and Innovation (CCRI)*, University of Ottawa, Ottawa, Canada, 2013.

C. 6 Invited presentations and seminars

[26] **R. J. Isaifan***, "Self-induced electrochemical promotion of noble metals nanoparticles for environmentally important reaction systems", *University of Ottawa Department of Chemical and Biological Engineering Graduate Seminar Series*, May. **2014.**

[27] **R. J. Isaifan***, Elena A. Baranova, "Catalytic electrooxidation of volatile organic compounds by oxygen-ion conducting ceramics in oxygen-free gas environment", *University of Ottawa Centre for Catalysis Research and Innovation Technical Seminar*, Nov. **2013**.